The creation and use of a chemical kinetics code to model and understand the atmospheres of hot Jupiters

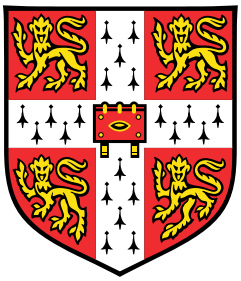

Richard John Hobbs

Institue of Astronomy
University of Cambridge

This dissertation is submitted for the degree of
Doctor of Philosophy

Robinson College September 2021

I would like to dedicate this thesis to my loving parents, Gillian and Ian, who supported my interests throughout my life, and my dearest partner Joanna, whose constant encouragement and love made this thesis possible.

I would like to thank my supervisors, Oliver Shorttle and Nikku Madhusudhan, for their knowledge and advice throughout all of my PhD, and Paul Rimmer for the scientific discussions we've had.

Declaration

I hereby declare that except where specific reference is made to the work of others, the contents of this dissertation are original and have not been submitted in whole or in part for consideration for any other degree or qualification in this, or any other university. This dissertation is my own work and contains nothing which is the outcome of work done in collaboration with others, except as specified in the text and Acknowledgements. This dissertation contains fewer than 60,000 words including appendices, bibliography, footnotes, tables and equations and has fewer than 150 figures.

Richard John Hobbs
September 2021

Published Content

This thesis is the result of my own work carried out at the University of Cambridge between October 2017 and September 2021. Parts of the work presented in this thesis have been published in refereed scientific journals. In all cases, the text in the thesis has been written by me and the figures presented in the chapters have been produced by me, unless explicitly stated otherwise.

Hobbs R., Rimmer P., Shorttle O., Madhusudhan N. (2021) 'Sulfur chemistry in the atmospheres of warm and hot Jupiters' MNRAS, 506(3):3186-3204

Hobbs R., Shorttle O., Madhusudhan N., Rimmer P. (2019) 'A chemical kinetics code for modelling exoplanetary atmospheres' MNRAS, 487(2):2242–2261

The creation and use of a chemical kinetics code to model and understand the atmospheres of hot Jupiters

Richard John Hobbs

Chemical compositions of exoplanets can provide key insights into their physical processes, and formation and evolutionary histories. Atmospheric spectroscopy provides a direct avenue to probe exoplanetary compositions. However, whether obtained in transit or thermal emission, spectroscopic observations probe limited pressure windows of planetary atmospheres and are directly sensitive to only a limited set of spectroscopically active species. It is therefore critical to have chemical models that can relate retrieved atmospheric compositions to an atmosphere's bulk physical and chemical state. To this end we present LEVI, a chemical kinetics code for modelling exoplanetary atmospheres.

LEVI is constructed as a eulerian solver of a series of coupled 1-D continuity equations for the evolution of molecular species. LEVI is able to calculate the gas phase hydrogen, oxygen, carbon, and nitrogen chemistry in hot Jupiters to produce abundance profiles of the planets' atmospheres. We perform extensive testing of LEVI to ensure its accuracy, including investigations of how both the boundary and initial conditions of the model could affect the final result, as well as comparing the thermochemical processes to the diffusional and photochemical processes. LEVI underwent benchmarking by testing it against already existing codes of the same type, to ensure the code was consistent with previously produced models.

We use LEVI to run a suite of models across a range of metallicities to produce the abundance of a number of molecules in any hot Jupiter's atmosphere. Our parameter sweep covers metallicities between 0.1x and 10x solar values for the C/H, O/H and N/H ratios, and equilibrium temperatures of hot Jupiters between 1000K and 2000K. We link this parameter sweep to hot Jupiter formation and migration models from previous works to produce predictions of the link between molecular abundance and planet formation pathways, for the spectrally active molecules H_2O, CO, CH_4, CO_2, HCN and NH_3. We investigate the detections of numerous molecules in the atmosphere of HD 209458b, and find that within the framework of our model, the abundance of these molecules best matches with a planet that formed by gravitational instability between the CO_2 and CO snowlines and underwent disk-free migration to reach its current location.

We next extend the underlying chemical network used in LEVI. We present and validate a new network of atmospheric thermo-chemical and photo-chemical sulfur reactions. Sulfur was chosen as the element to add due to its importance on planets such as Venus and the existence of previous studies that have shown that sulfur may be significant in hot Jupiter atmospheres. We use LEVI to investigate these reactions as part of a broader HCNO chemical network in a

series of hot and warm Jupiters. We also investigate how the inclusion of sulfur can manifest in a hot Jupiter's atmosphere indirectly. Sulfur chemistry can result in the depletion of many non-sulfur-bearing species, including CH_4, NH_3 and HCN, by several orders of magnitude.

In summary, we create a 1-D photochemical-kinetic model and show that it can be used to constrain the dynamics of exoplanet atmospheres and their origins. Some of the key directions for future development include expanding the sophistication of the underlying chemical networks, work begun by our introduction of sulfur, and exploring the possibility of 2-D and 3-D dynamical models, to account for zonal redistribution. More developed chemical networks allow us to better constrain the atmospheric chemistry, and thus the overall atmospheric composition, breaking existing degeneracies we highlight, while improving the treatment of the dynamics ensures our modelling gives a more accurate depiction of the disequilibrium chemistry taking place.

Table of contents

List of figures

List of tables

Chapter 1

Introduction

1.1 Motivation

Since the first exoplanets were discovered several decades ago (Campbell et al. 1988; Latham et al. 1989; Wolszczan and Frail 1992; Mayor and Queloz 1995), they have proved to be a constant source of interest and research for astronomers. The initial expectation of exoplanetary systems were that they would look rather similar to our own solar system, i.e., a set of small rocky planets near to the star, with a collection of larger gas giants further away. However, since the detection of a Jupiter mass planet at 0.05 AU, which is within the orbit of Mercury, around 51 Pegasi by Mayor and Queloz (1995), it has become clear that other planetary systems do not have to conform to the trends seen within our own. More than 4500 exoplanets have now been discovered covering the full spectrum of masses and orbital radii, including hot Jupiters, warm Neptunes, super Earths and mini Earths. The way in which these planets were detected can give us a lot of information about their physical and atmospheric properties. The most common ways of detecting exoplanets is via radial velocity measurements, which can give estimates of the planets mass and orbital radius, observing transits of the planet in front of its star, allowing for estimates of the planets radius and spectroscopic measurements of its atmosphere to take place, and direct imaging, in which the spectra of the planet can be directly observed. Combined with the vast number of detected exoplanets, these methods allow us to access a wealth of information about the planetary systems around other stars. The currently detected exoplanets are shown in Figure 1.1, separated by their method of detection. All these observations raise the question of the history of these planetary systems, i.e., what disk and planetary processes led to the present system architecture and planetary properties.

Exoplanets can broadly be split into two categories; Terrestrial planets, with a rocky core that comprises most of their mass and a thin atmosphere, and gas giant planets, with vast gaseous envelopes around a relatively small core. One sub-section of Jupiter-like planets

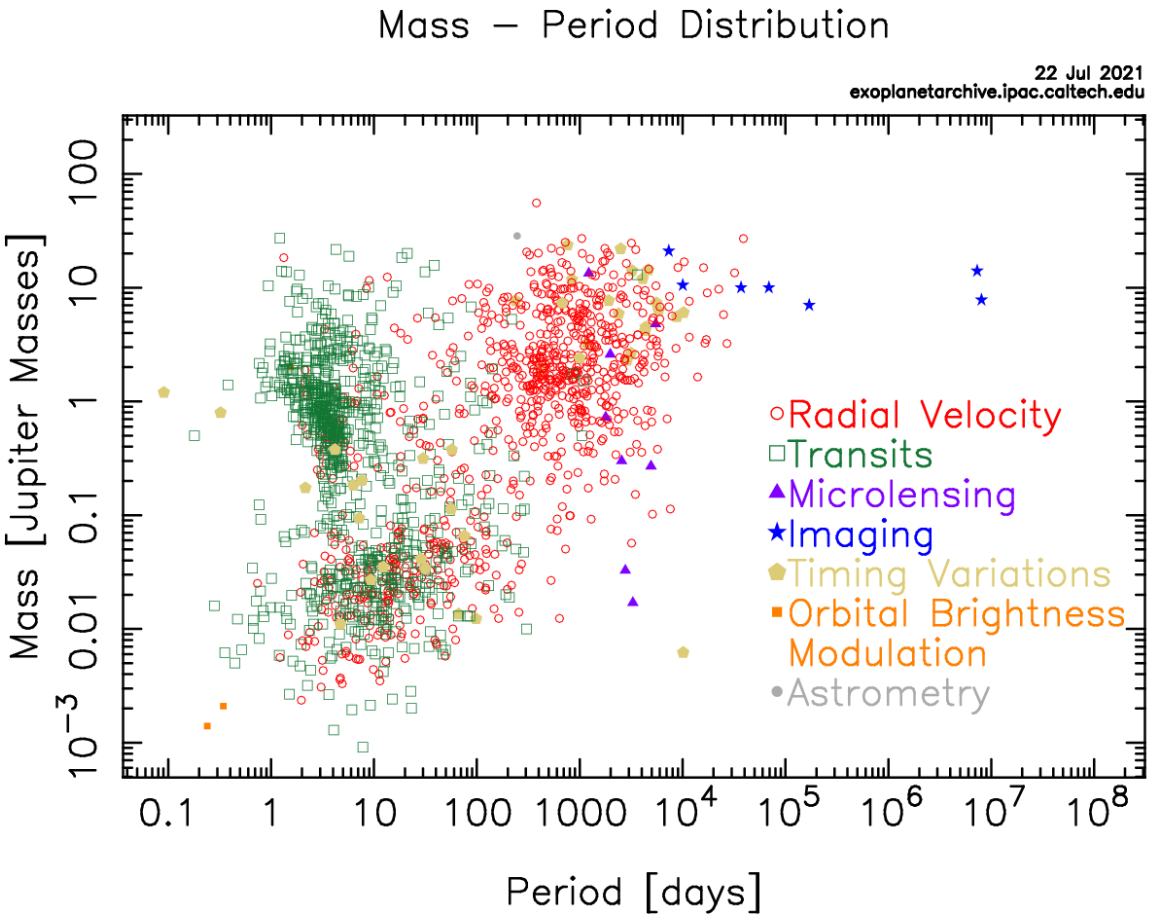

Fig. 1.1 The currently discovered exoplants as a function of their mass, orbital radius and method of detection. This data was extracted from the Exoplanet Archive (Akeson et al. 2013).

that are of particular interest are the so-called hot Jupiters. These are Jupiter mass planets that typically orbit within 0.1 AU of their host star, resulting in planetary temperatures above 1000K due to their proximity to their star. Current models suggest that these hot Jupiters could not have formed at their current locations; they must have migrated there from further out in the planetary system (e.g., Kley and Nelson 2012; Anderson et al. 2016; Bitsch et al. 2019; Teyssandier et al. 2019). Typically, these planets would have formed relatively near to their host star via core accretion or much further out via gravitational collapse (e.g., Lissauer and Stevenson 2007; Boley and Durisen 2010; Forgan and Rice 2011). These different formation locations can leave traces upon the bulk composition of the planet's atmosphere, altering the planets metallicity and the chemistry of its atmosphere (e.g., Öberg et al. 2011; Madhusudhan et al. 2016; Turrini et al. 2021).

Identifying and characterising features of exoplanets is the observational cornerstone to answering some of the biggest questions in planetary astrophysics: Within the field of giant planets major questions remain unresolved regarding their formation, composition, evolution during atmospheric escape, and how significant migration is in their history (Beaugé and Nesvorný 2012; Mordasini et al. 2016; Nelson et al. 2017; Dawson and Johnson 2018; McGuire et al. 2018). Both the location of where giant planets form and possible later migration through the proto-planetary disk may leave signs in the compositions of their atmospheres (e.g. Öberg et al. 2011; Moses et al. 2013; Madhusudhan et al. 2014a; Mordasini et al. 2016). Tracing giant planet migration history is also important for understanding terrestrial planet formation and survivability. This question is clearest for hot Jupiter systems, where the presumed inward migration of a Jupiter mass object may have significantly disrupted habitable zone planets (Del Popolo et al. 2005; Hands and Alexander 2016; Spalding and Batygin 2017; Sánchez et al. 2018).

Thus, the focus of this thesis is studying the atmospheric properties of hot Jupiters. They are interesting both for their own properties, such as their formation and migration history, as well as the implications they have for the survival of smaller bodies in the rest of the planetary system. Additionally, there is a plethora of real world data available to compare and validate our models against.

1.1.1 Hot Jupiter Formation

The location where a Jupiter-like planet forms around a star can leave traces upon the chemical composition of its atmosphere. Planets are formed out of the dust and gas surrounding their host star. Therefore, any variations in the composition of the gas or dust in the proto-planetary disk that depend on the distance from the star, should still be evident in the planet itself, depending on the ratio of dust to gas it is formed from (e.g.,Öberg et al. 2011; Helling et al.

2014; Madhusudhan et al. 2014a; Cridland et al. 2016; Madhusudhan et al. 2016; Mordasini et al. 2016; Booth et al. 2017).

At greater radial distances in the disk, various volatile species pass their snowlines, where they transition from the gas phase into being frozen as ice. In particular, oxygen rich species such as H_2O and CO_2 have their snowlines at higher temperatures (and therefore closer to the star) than CO: The water snowline is at $\sim$170 K, the CO_2 is at $\sim$ 80 K and the CO snowline is at $\sim$30 K (Martín-Doménech et al. 2014). Thus, the solids throughout most of the disk have sub-solar C/O ratios, and the gas has a super-solar C/O ratio. However, since the amount of H that is frozen is negligible compared to the metals, both the C/H and O/H ratios of the gas are sub-solar outside of the corresponding snowlines. In the same way, the N/H ratio in the gas becomes sub-solar once NH_3 freezes out at $\sim$100 K (Martín-Doménech et al. 2014).

There are two routes through which a gas giant is expected to form; core accretion closer to the star (Pollack et al. 1996; Lissauer and Stevenson 2007), and gravitational instability further from the star (Boss 2000; Gammie 2001; Boley 2009; Boley and Durisen 2010; Forgan and Rice 2011). The planet forms early and quickly in the gravitational instability scenario, accreting dust and gas almost equally. As such, it was typically expected to have a similar bulk composition to that of the disk as a whole, and therefore similar to the stellar metallicity (Boss 1997; Helled and Bodenheimer 2010). However, more recent works have shown that it is possible for planets formed via gravitational instability to have enriched or depleted metallicities based upon the size of the solids being accreted; if most solids are between 0.1m and 100m the resulting planet can become enriched, while if most solids are above 1km the planet may end up depleted (Helled et al. 2014). For the core accretion scenario a planet's resulting atmospheric metallicity is a more complicated function of planet location, being dependent on the solid to gas partitioning of elements. Most models of core accretion require several million years to form a rocky core and accrete a gaseous envelope (e.g., Pollack et al. 1996; Lissauer and Stevenson 2007; Kobayashi et al. 2011). The composition of the accreted gas is dependent upon the location of the forming planet within the disk; typically super-solar in the C/O ratio and sub-solar in the C/H, O/H and N/H. However, enrichment of the atmosphere by solids can also occur during atmospheric accretion, resulting in a variable overall composition (Pollack et al. 1996).

However, there are challenges to linking gas giant atmospheric composition directly to formation location. The presence of hot Jupiters suggests that giant planets can migrate through their system. This is because gaseous giant planets are not expected to form on such short period orbits (e.g., Mayor and Queloz 1995; Wu and Murray 2003; Wu and Lithwick 2011; Papaloizou et al. 2007). The accretion of solids (in the form of planetesimals or core erosion) onto the gas giant can result in a significantly different atmospheric composition, especially

if solid accretion occurs during migration. Accretion of solids typically results in planetary compositions that are solar or super-solar in O/H and C/H but sub-solar in C/O ratio, since the ice within the CO ice line is oxygen rich (e.g., Madhusudhan et al. 2014a, 2016). Additionally, radial drift of icy grains from the outer disk can supply volatiles to the inner disk (Booth et al. 2017). This results in the enrichment of volatiles at the snowlines of up to 10x C/H or O/H. This allows gas giants to become metal rich by directly accreting metal rich gas, and opens the possibility of planets with super-solar C/H and super-solar C/O. A schematic of the formation and migration processes of a hot Jupiter is shown in Figure 1.2.

Recently studies have also investigated how N/H ratios may vary in a planet's atmosphere based upon where the planet forms (Bosman et al. 2019; Öberg and Wordsworth 2019; Turrini et al. 2021). This additional parameter may help to break some of the degeneracy when examining the composition of giant planets, refining the estimates of where a particular planet may have formed.

Some recent studies have examined how the composition of a hot Jupiter may vary based upon its metallicity (Madhusudhan 2012; Moses et al. 2013; Tsai et al. 2017), and others have studied how these metallicities may change based upon where the hot Jupiter formed (Madhusudhan et al. 2014a; Cridland et al. 2020). However, very few have tried to link these two regimes such that it is possible to predict where a hot Jupiter formed based upon its composition, and those that have done so typically use local thermochemical equilibrium models to do so (Mordasini et al. 2016). However, purely equilibrium models are not sufficient to model the atmospheres of hot Jupiters.

When considering nitrogen bearing species, thermochemical models of Hot Jupiters with atmospheric temperatures above 700 K expect N_2 to be the dominant nitrogen bearing molecule at around 1 bar (e.g., Moses et al. 2011; Venot et al. 2012). N_2 is not detectable by spectral observations, which in principle makes determining the N/H ratio of hot Jupiter atmospheres challenging. However, there have been potential detections of the nitrogen bearing molecules NH_3 and HCN in the atmosphere of HD209458b, a planet whose temperature is far above 700 K (Giacobbe et al. 2021). This would only be possible if disequilibrium chemical effects, such as diffusion and photochemistry, were impacting the composition of the planet's atmosphere. As such, in this work, we will run a full suite of disequilibrium chemical models over the range of C/H, O/H and N/H ratios expected from planet formation models. In doing so we aim to more accurately link the observed molecular abundances of hot Jupiter observations to the planet's elemental composition, and thus to the planet's formation and migration history.

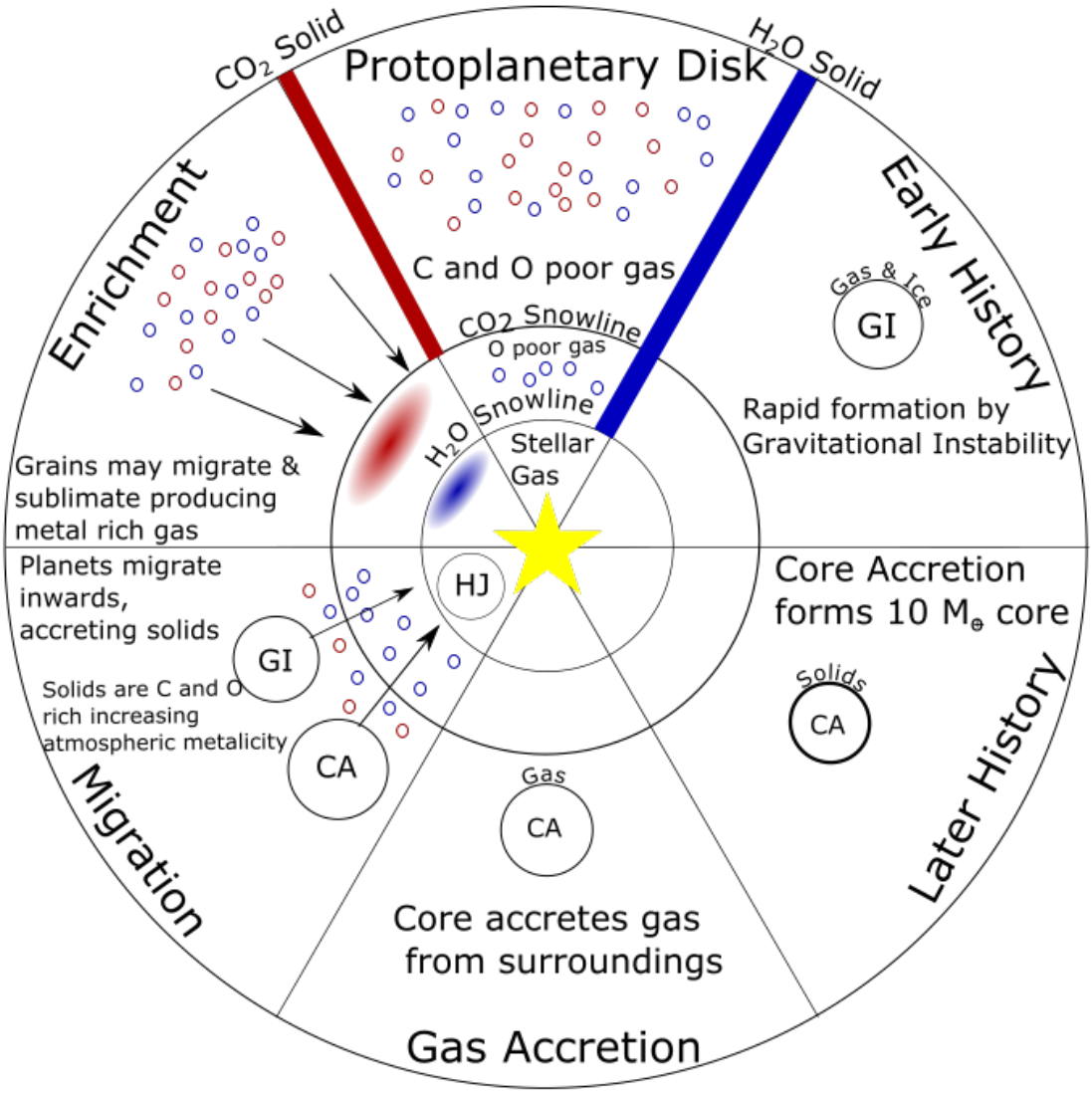

Fig. 1.2 A schematic showing the processes that result that in the formation, migration and metal enrichment of a hot Jupiter.

1.1.2 Hot Jupiter Observations

A key tool for characterising an exoplanet's atmosphere is its spectrum, observed via transits or thermal emission. The molecules in a planet's atmosphere absorb and emit light at particular frequencies, which can imprint a signature of the planet's atmosphere on the light received at Earth from the planet-star system. Thus, using what is known as retrieval models, it is possible to infer atmospheric chemistry based upon the features of the planet's transmission or emission spectrum (Seager and Sasselov 2000; Brown 2001; Deming et al. 2005; Grillmair et al. 2008; Seager and Deming 2010; Madhusudhan et al. 2016).

However, spectra only contain emission or absorption features for the spectrally active species present in a planet's atmosphere, and therefore provide only a partial view of atmospheric chemistry and dynamics. In addition, the observed transmission or emission spectrum comes from a narrow band of pressure ranges, generally between 1 - 10^{-3} bar, thus lacking sensitivity to chemistry in the rest of the atmosphere. Yet, with vertical mixing and diffusion transporting species through the atmosphere, chemistry at higher and lower pressures can contribute to atmospheric species in the observed pressure window. It is also possible for layers of clouds or hazes to block observations, resulting in muted spectral features that can imply incorrect abundances. This means that models are required to complete the picture of physical and chemical processes occurring in a planet from the limited spectroscopic detections.

At present, H_2O, Na and K are the most observed chemical species in hot Jupiter atmospheres using both space and ground based telescopes (Charbonneau et al. 2002; Redfield et al. 2008; Wyttenbach et al. 2015; Sing et al. 2016; Nikolov et al. 2018; Pinhas et al. 2019). Generally it has been found that H_2O abundances are low compared to expectations based upon our own solar system (Madhusudhan et al. 2014b; Barstow et al. 2017; Pinhas et al. 2019). However, thus far it has been unclear whether this is due to dearth of oxygen in their atmospheres, a high C/O ratio or another unknown factor. There have also been tentative detections of molecules such as CH_4, CO and NH_3 (Giacobbe et al. 2021), as well as HCN (MacDonald and Madhusudhan 2017b; Hawker et al. 2018; Giacobbe et al. 2021) and HS (Evans et al. 2018). However, these are not nearly as robust as the H_2O detections, and likely can not be until new, more precise observations are available from telescopes such as JWST and ARIEL.

1.1.3 Modelling Hot Jupiter Atmospheres

Atmospheric models can fill in details of atmospheric composition and structure that retrievals are not directly sensitive to, enabling physically and chemically informed interpolation and extrapolation of the retrieval observations. Improving the estimates of bulk atmospheric

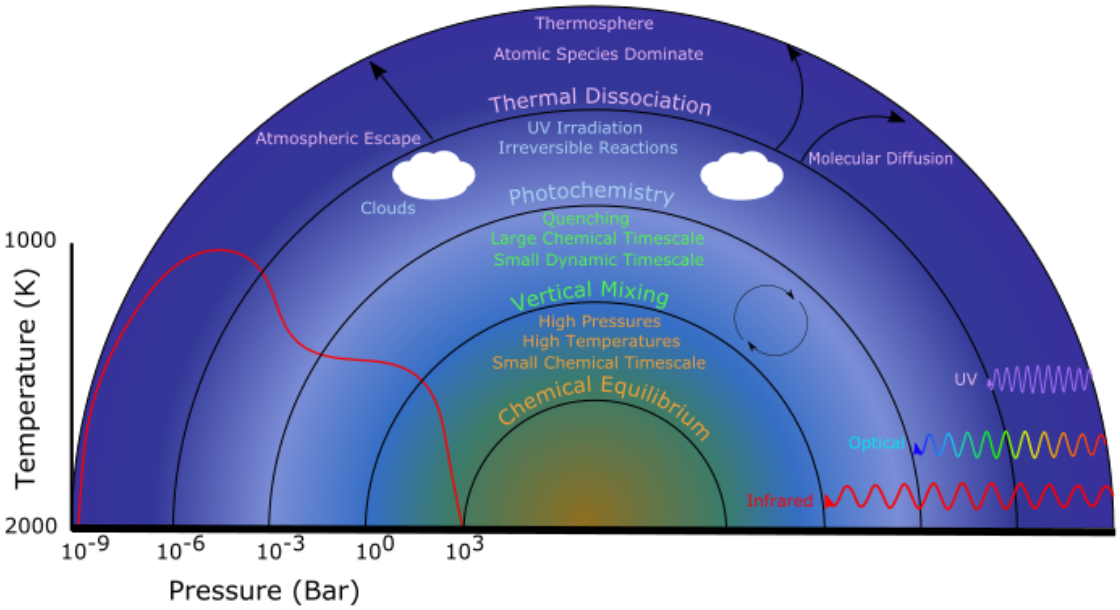

Fig. 1.3 A schematic of the interior of a hot Jupiter and some the processes that can take place in its atmosphere. The atmosphere is divided up into five approximate pressure windows based upon the dominant process within. An example of how the temperature within the planet is expected to vary with pressure is shown on the left side.

composition from retrievals is also then possible, by comparing the model atmosphere at different C/O and N/O ratios to the retrieved atmospheric abundances. Since the composition of planetary atmospheres may reflect when and where in a disk planets formed (Öberg et al. 2011; Madhusudhan et al. 2014a; Cleeves et al. 2018), these elemental ratios may ultimately provide a key insight into the history of planet formation.

To construct the chemical model, a network of atmospheric chemical reactions is compiled and used as input to a model that calculates the production and loss of all species in the atmosphere. This produces a profile of chemical abundances for an atmosphere in thermochemical equilibrium, such that the abundances of various species do not change over time. However, a planetary atmosphere may not be in local chemical equilibrium over its entire extent. It is expected that the deeper, hotter parts of the atmosphere ($P \gtrsim 0.1$ - 1 bar) approach thermochemical equilibrium, however, higher up (at lower pressures) various non-equilibrium processes can become significant. Therefore, to more accurately model atmospheric chemistry it is necessary to include the non-equilibrium processes that can dominate at lower pressures, such as vertical mixing and photo-chemistry (Cooper and Showman 2006; Moses et al. 2011, 2013). A schematic of the interior of a hot Jupiter, and the processes that can exist within, is shown in Figure 1.3.

Model	Network Basis	Diffusion	Photochemistry	Elements	Reactions	Molecules
Liang et al. (2003)	From Laboratory Measurements [1]	Yes	Yes	H/C/O	253	Unknown
Zahnle et al. (2009)	Zahnle et al. (1995)	Yes	Yes	H/C/O/N/S	507	49
Moses et al. (2011)	Gladstone et al. (1996)	Yes	Yes	H/C/O/N	1600	90
Venot et al. (2012)	From Combustion Studies	Yes	Yes	H/C/O/N	1918	104
Hu et al. (2012)	New	Yes	Yes	H/C/O/N/S	800	111
Rimmer and Helling (2016)	Stand2015	Yes	Yes	H/C/O/N/Metals	2980	162
Drummond et al. (2016)	Venot et al. (2012)	Yes	Yes	H/C/O/N	1918	104
Tsai et al. (2017)	Glassman et al. (2015)	Yes	No	H/C/O	300	29

Table 1.1 A comparison of the main features of a selection of non-equilibrium atmospheric chemistry codes in the literature.

Several models of exoplanetary atmospheric chemistry have been previously reported in the literature. While some focus purely on thermochemical equilibrium (Burrows and Sharp 1999; Lodders and Fegley 2002; Blecic et al. 2016), others have also sought to encapsulate the non-equilibrium chemistry occurring (i.e., Liang et al. 2003; Zahnle et al. 2009; Moses et al. 2011; Hu et al. 2012; Miller-Ricci Kempton et al. 2012; Venot et al. 2012; Rimmer and Helling 2016; Tsai et al. 2017). Table 1.1 shows a comparison of the processes included in a selection of chemical kinetics models. These models all work similarly, using a pressure - temperature (P-T) and eddy-diffusion (K_{zz}) profile as inputs to their codes to calculate abundance profiles of the atmosphere, with most of the differences between their predictions arising in their chemical network. Other inputs typically include the UV spectrum being applied to the top of the atmosphere for the purpose of calculating photochemistry, and the specific parameters of the planet being modelled, i.e., planetary gravity, albedo and orbital radius. Liang et al. (2003) first reported a photochemical model with H-C-O chemistry for a select set of species in highly irradiated atmospheres. Zahnle et al. (2009) investigated the effects of photochemistry on sulfur bearing molecules in hot Jupiters, and later warm Jupiters (Zahnle et al. 2016). This model was also adopted and furthered in Miller-Ricci Kempton et al. (2012). Moses et al. (2011) and Venot et al. (2012) both produced codes that focused on H-C-N-O photochemistry on hot Jupiters. Hu et al. (2012) created a model for the atmosphere of super-Earths, as well as incorporating the additional non-equilibrium effects that could occur on terrestrial planets. Rimmer and Helling (2016) focused on the effects that ions produced by lightning could have on the chemistry of hot Jupiters, as well as including a selection of metals in their network. Drummond et al. (2016) reported a model that self-consistently solved for both the P-T profile and chemical abundance profiles. Tsai et al. (2017) use a reduced chemical network to reproduce the results of Moses et al. (2011) and Rimmer and Helling (2016) for several hot Jupiters, and analyse the accuracy of the quenching approximation. These previous works use 1-D models, treating the entire atmosphere to a single vertical line. This allows for many simplifications, including using P-T profiles averaged for a specific location upon the planets surface (typically the

sub-stellar point or one of the terminators) and using eddy-diffusion as an approximation for the complex physics of atmospheric diffusion. These approximations inherently limit the accuracy of these models, and there have been some works that move beyond 1-D models. Agúndez et al. (2014) adapted the work of Venot et al. (2012) to report a 2-D model for hot Jupiters. 3-D General Circulation Models (GCMs) have also been used to model atmospheric effects, but typically use simpler chemical models (e.g., Drummond et al. 2018; Zhang and Showman 2018; Steinrueck et al. 2019). However, increasing the dimensionality of the models typically results in a decrease to their chemical complexity, as well as becoming more computationally expensive to run. Ultimately, all of these approaches, including the one presented in this work, represent a compromise between efficiency and complexity. Our goal in this work is to continue, and expand upon, the work done previously in this area. Initially, we will do this by creating a new chemical kinetics code such that we have a complete understanding of how and why it functions, and such that we can easily update and modify it in the future, with improvements and additions to improve its functionality.

1.1.4 Sulfur Chemistry in Hot Jupiter Atmospheres

Throughout the last few decades, chemical models of exoplanetary atmospheres have grown more detailed and complex. What had begun as equilibrium models containing limited molecular species made of only a few elements in small chemical networks (e.g., Lodders and Fegley 2002; Liang et al. 2003; Zahnle et al. 2009) have evolved into large photo-kinetic models containing hundreds of molecular species made of many elements in chemical networks with thousands of reactions (Moses et al. 2011; Venot et al. 2012; Rimmer and Helling 2016). One of the next steps in continuing this evolution is the inclusion of sulfur chemistry in these models.

Sulfur chemistry is known to play an important role in the atmospheric chemistry of planets in our solar system. In Earth's past, sulfate aerosols may have increased the albedo sufficiently to lead to the first Snowball Earth event (Macdonald and Wordsworth 2017), and sulfur isotope ratios combined with radiometric ageing can be used as a tracer of Earth's Great Oxidation Event (Hodgskiss et al. 2019). Sulfur photochemistry is thought to influence the production of hazes and clouds in the upper atmospheres of solar system planets such as Earth (Malin 1997), Venus (Zhang et al. 2012; Titov et al. 2018), Jupiter (Moses et al. 1995) and the moon Io (Irwin 1999). Similar hazes, expected to appear in the atmospheres of exoplanets (He et al. 2020), would greatly affect their observed spectra. This would limit our ability to examine their atmosphere, and make assessments of their habitability challenging (Gao et al. 2017). Although, it is also possible that detections of sulfur in exoplanet atmospheres would be capable of distinguishing an uninhabitable exo-Venus from a potentially habitable exo-Earth via key gas species such as SO_2, OCS and H_2S (Jordan et al. 2021).

Sulfur has also recently been of interest in the field of Jupiter-like exoplanets. A tentative detection of the mercapto radical, HS, in the atmosphere of the hot Jupiter WASP-121 b has been made (Evans et al. 2018). However, it is still uncertain whether the feature was in fact due to HS, or whether it was due to another unknown molecule. The warm Jupiter 51 Eri b has also been an excellent example of the importance of sulfur chemistry. Two groups have produced models of 51 Eri b's atmosphere, one study did not include sulfur chemistry (Moses et al. 2016) and the other did include sulfur chemistry (Zahnle et al. 2016). It was found in the work of Zahnle et al. (2016) that sulfur photo-chemistry in the atmosphere of the warm Jupiter 51 Eri b was the source of a large number of radicals that went on to catalyse other chemistry. This was a possible explanation for the differences in chemical abundance, especially in the CO_2 abundance, found for 51 Eri b between the sulfur-free models of Moses et al. (2016) and the sulfurous models of Zahnle et al. (2016). Thus, we believe that including sulfur chemistry in models of exoplanets, both terrestrial and gas-giant, would be valuable in obtaining more accurate pictures of their atmospheric composition. We will therefore include sulfur chemistry in our chemical network, to better analyse quantitatively the differences that sulfur makes, in addition to discovering how and why these differences occur.

There are several works that include sulfur chemistry for exoplanet atmospheres. We highlight a subset of these relevant for the atmospheric chemistry of gas giants. Hu et al. (2013) investigate the photochemistry of H_2S and SO_2 in terrestrial planets and conclude that their direct detection is unlikely due to the fact that these molecules are expected to undergo rapid photochemical conversion to elemental sulfur and sulfuric acid. Visscher et al. (2006) examine thermo-chemical sulfur chemistry for the hot, deep atmospheres of sub-stellar objects and find H_2S to be the dominant sulfur bearing gas. However, due to the high temperatures and pressures of the atmospheres they are studying, disequilibrium effects such as diffusion or photochemistry are not considered. Zahnle et al. (2009) investigate whether sulfur photochemistry could explain the hot stratospheres of hot Jupiters, and find that UV absorption of HS and S_2 may provide an explanation. Zahnle et al. (2016) also investigate whether sulfur could form photochemical hazes in the atmosphere of 51 Eri b, and under what conditions they could be formed. They find that sulfur clouds should appear on many planets where UV irradiation is weak. Wang et al. (2017) create synthetic spectra of their hot Jupiter atmospheric models to determine whether H_2S and PH_3 could be detected by JWST, and find that H_2S features should be observable for $T_{eq} > 1500$K. Gao et al. (2017) examine the effects of sulfur hazes on the reflected light from giant planets and find that the hazes would mask the presence of CH_4 and H_2O.

1.2 Thesis Outline

In this thesis, the work that has been accomplished during this PhD is presented. We show our creation of a new chemical code, and how we use it to answer a variety of questions surrounding the composition of hot Jupiter atmospheres. In this work we will focus on the questions of whether the formation location of a hot Jupiter can be determined by its current atmospheric composition, as well as how, and why, can sulfur chemistry change the composition of a hot Jupiters atmosphere.

In Chapter 2, we present the chemical kinetics code, LEVI, that was created during this PhD, and show its validation against other models. We describe in detail the mechanisms behind how and why the code works the way it does, and perform testing of how the initial conditions and boundary conditions may affect the final solution. We also perform a first look into how the metallicity of a hot Jupiter's atmosphere may effect the overall chemical composition of the planet.

In Chapter 3, we perform a detailed investigation into how atmospheric metallicities affect the chemical composition of a hot Jupiter atmosphere. We link these compositions to previously calculated formation models developed in previous studies, to create predictions of what the composition of a hot Jupiter should be for certain formation locations and migration pathways. We compare the actual H_2O water abundances detected within an ensemble of hot Jupiters to our compositional predictions. We find that every H_2O abundance lies within our predicted abundances for multiple formation pathways, confirming both our models' accuracy, and the need for additional molecular detections to decode the history of a migrating hot Jupiter. We also perform a case study upon the hot Jupiter HD 209458b, a hot Jupiter with multiple molecular detections, and find that within the framework of our models we expect that it formed via gravitational instability beyond the CO_2 snowline and within the CO snowline.

In Chapter 4, we expand the chemical network that we use through the inclusion of sulfur chemistry. We detail the sulfur molecules and reactions that were added, as well as explaining our choices for which reactions to include when multiple reaction coefficients had previously been calculated. We validated our new sulfur network against a range of previous models, including thermochemical equilibrium solvers and disequilibrium models. We showed how and why sulfur chemistry changes throughout the atmosphere of a hot Jupiter, as well as how varying the strength of both diffusion and UV irradiation can impact the distribution of sulfur bearing molecules throughout the atmosphere. We also investigated how the inclusion of sulfur impacted the abundances of other molecules throughout the atmosphere of a hot Jupiter, and found, and showed why, sulfur causes the abundances of CH_4, NH_3 and HCN to drop by several orders of magnitude around 10^{-3} bar. Additionally, we investigated previous claims of the importance of sulfur chemistry on the warm Jupiter 51 Eri b, and discovered that sulfur does

have a significant impact on the abundance of CO_2 in this planet's atmosphere, although we did not find as large a change as expected by previous works. The sulfur network produced in this chapter has also now gone on to be used by several other works to model sulfur chemistry in Venus and Venus-like planets (Rimmer et al. 2021; Jordan et al. 2021).

In Chapter 5, we give a summary of the work performed during this PhD and discuss the potential future research opportunities as a result of this work.

Chapter 2

A Chemical Kinetics Code for Modelling Exoplanetary Atmospheres

2.1 Introduction

In the following Chapter, we report a new code for 1-D modelling of chemistry in exoplanetary atmospheres, named LEVI. [1] The chemical processes that it can model include thermochemical equilibrium, eddy-diffusion, molecular diffusion, thermal diffusion and photochemistry. Through inputs in the form of pressure-temperature profiles, vertical mixing profiles, stellar properties, and a network of possible chemical reactions, the model can predict the mixing ratios of chemical species in a planet's atmosphere. Currently, the code uses a network that includes species comprised of H, C, O, N or He. The code is built to be modular in the chemical processes and reactions it can model, and the species it includes. We use this functionality to better understand the effects any of these components of the model can have on the chemistry of the atmosphere. Here, we focus on applying the code to the hydrogen rich atmospheres of hot Jupiters, although it can be generalised to apply to the atmospheres of terrestrial planets.

We demonstrate LEVI by applying it to two of the most studied hot Jupiters, HD 209458b and HD 189733b. HD 209458b and HD 189733b are excellent candidates for benchmarking LEVI as they are some of the best characterised planets (e.g., Seager and Sasselov 2000; Moses et al. 2013; Lewis et al. 2013; Liu and Showman 2013; Mayne et al. 2014; Schwarz et al. 2015; Amundsen et al. 2016; Brewer et al. 2017), and several previous chemical kinetics models have been applied to them. Between the two planets, a preliminary parameter space can be explored, comparing the differences between hot Jupiters with and without thermal inversions (where the temperature increases in the upper atmosphere instead of decreasing), the influence of strong

[1] Named after the Latin *Levis*, meaning light.

UV radiation, and the effects of an increase in a planet's effective temperature. In particular, HD 189733b is a very good candidate to study the effect of photochemistry, because of both the high stellar UV it receives, up to five times higher than HD 209458b, and the relatively low atmospheric temperature, at or less then 1000K at pressures less than 0.01 bar. HD 209458b was thought to have a temperature inversion (Knutson et al. 2008), although that is now debated (Diamond-Lowe et al. 2014; Schwarz et al. 2015). The temperature inversion is being kept in most of this work, both to match Moses et al. (2011) for benchmarking and to better investigate the effects of high temperature across the entire range of atmospheric pressure. We do, however, also use a P-T profile for HD 209458b that lacks a thermal inversion when comparing our model to a recent work that provides evidence of the presence of number of molecular species in it's atmosphere (Hawker et al. 2018).

In Section 2.2 the model and network being used for this code are described. Section 2.3 contains a validation against previously constructed codes and an examination of how the abundances of species in the atmosphere vary from thermochemical equilibrium due to vertical transport and photochemistry. Section 2.4 contains an exploration of the C/O and N/O parameter space. This is used to investigate how the bulk chemistry of an atmosphere can affect the mixing ratios of species within it, and to compare our model's predictions to evidence of species detected within HD 209458b. Section 2.5 contains a short summary and discussion of the results of this work.

2.2 The Atmospheric Model

Our model considers a 1-D plane-parallel atmosphere in hydrostatic equilibrium, with various processes affecting the chemistry. Using a given P-T profile, considerations of hydrostatic equilibrium, and the ideal gas law, the thermodynamic parameters of the atmosphere are determined. In this manner we follow the standard approach of existing chemical models (see Table 1.1) in using pre-determined profiles of both the temperature and vertical mixing strength, without self-consistently solving the radiative transfer equation.

We model chemical diffusion, photochemistry, and, as a limiting case, chemical equilibrium. Thermochemical equilibrium occurs once the rate of production and loss rate of every molecule due to chemical reactions is the same. Including diffusion, in the form of eddy, molecular or thermal diffusion, can lead to species being lifted from deep in the atmosphere into higher, cooler, layers or cause large, heavy, molecules to sink out of the upper atmosphere. Species that get lifted to higher atmosphere layers can have their abundance frozen in above thermochemical equilibrium values, since the time it takes for them to deplete back down to their equilibrium abundance is significantly longer than their resupply time from vertically mixing. This process is known as quenching. The eddy diffusion used is an approximation for atmospheric motion, so that the complex micro-physics of atmospheric mixing can be treated as a simple macroscopic process. In the upper atmosphere, high energy photons can cause some molecules to disassociate, and new species to form from the break-down products. The rate of these reactions is determined by the UV flux received by the planet.

LEVI solves a set of coupled differential equations that govern the chemical kinetics (described in Section 2.2.1) to obtain a steady-state solution for the chemical composition of the atmosphere. By dividing up the atmosphere into vertically distributed plane-parallel layers, these equations can be described in just one dimension. Each equation describes the time evolution of one species in the atmosphere due to production or loss from chemical interactions, or fluxes from other atmosphere layers. Other factors that could influence the evolution of the atmosphere, such as evaporation, atmospheric escape and geological outgassing are not currently implemented but, in the context of giant planets, these processes are in general not operating and/or are not chemically significant (Moses et al. 2011).

A steady-state solution to these equations is found by time-stepping the code using a second-order Rosenbrock solver (Rosenbrock 1963), from an initial guess for the chemical abundances, until the production and loss rates of every species in every atmosphere layer are balanced. For a closed system, in which there is no addition or removal of molecules into the system, this will produce a solution that is stable over large time periods.

The code is designed to be highly configurable, allowing modelling of a wide range of exoplanets. This includes atmospheric parameters such as elemental composition, the pressure-

temperature (P-T) profile of the atmosphere and the eddy diffusion coefficient. The stellar characteristics, such as the stellar spectrum and the planet-star separation, and the physical characteristics of the planet such as its surface gravity can also be changed as required to model different examples of hot Jupiters. The gravitational acceleration used throughout the atmosphere is an approximation of the average gravity, taken at the surface of the planet. For Jupiter-like planets, the 'surface' is taken to be at 1 bar. It is also possible to selectively exclude a subset of reactions, such as those that consider the effects of photochemistry, or the reactions of ions, to better understand the effects those reactions can have on the atmosphere. In addition, any reactions containing an undesired chemical species can be easily stripped away, to both further explore the atmospheric response to the presence of particular species, and to improve the computational runtime.

2.2.1 Model Setup

Here we describe the equations that govern the model being used, as well as the chosen boundary and initial conditions for the model.

Chemical Processes

The model used considers contribution from multiple processes, which can be described by a series of coupled one-dimensional continuity equations,

$$\frac{\partial n_i}{\partial t} = \mathscr{P}_i - \mathscr{L}_i - \frac{\partial \Phi_i}{\partial z}, \tag{2.1}$$

where n_i (m^{-3}) is the number density of species i, with $i = 1,...,N_i$, with N_i being the total number of species. $\mathscr{P}_i$ ($\mathrm{m}^{-3}\,\mathrm{s}^{-1}$) and $\mathscr{L}_i$ ($\mathrm{m}^{-3}\,\mathrm{s}^{-1}$) are the production and loss rates of the species i. ∂t (s) and ∂z (m) are the infinitesimal time step and altitude step respectively. Φ_i ($\mathrm{m}^{-2}\,\mathrm{s}^{-1}$) is the upward vertical flux of the species, given by,

$$\Phi_i = -(K_{zz} + D_i) n_t \frac{\partial X_i}{\partial z} + D_i n_i \left(\frac{1}{H_0} - \frac{1}{H} - \frac{\alpha_{T,i}}{T} \frac{dT}{dz} \right), \tag{2.2}$$

where X_i and n_t (m^{-3}) are the mixing ratio and total number density of molecules such that $n_i = X_i n_t$. The eddy-diffusion coefficient, K_{zz} ($\mathrm{m}^2\,\mathrm{s}^{-1}$), approximates the rate of vertical transport and D_i ($\mathrm{m}^2\,\mathrm{s}^{-1}$) is the molecular diffusion coefficient of species i. H_0 (m) is the mean scale height, H (m) is the molecular scale height, T (K) is the temperature, and $\alpha_{T,i}$ is the thermal diffusion factor. The equation for the molecular diffusion coefficient is adopted from

Chapman and Cowling (1970), where it is defined as,

$$D_i = \frac{3}{8n_t(\frac{1}{2}[d_i+d_t])^2}\left(\frac{k_bT(m_i+m_t)}{2\pi m_i m_t}\right)^{1/2}, \tag{2.3}$$

where m_i (kg) and d_i (m) are the mass and diameter of species i, respectively, and m_t (kg) and d_t (m) are the average mass and average diameter of all species in the atmosphere, respectively. The thermal diffusion factor is estimated from experimental and theoretical data from Chapman and Cowling (1970): for atomic hydrogen, $\alpha_{T,i} \approx -0.1(1-n_i/n_t)$; for He, $\alpha_{T,i} \approx 0.145(1-n_i/n_t)$; for H_2, $\alpha_{T,i} \approx -0.38$; and for all other molecules $\alpha_{T,i} \approx 0.25$. Under the assumption that the atmosphere can be approximated to an ideal gas, the total number density, n_t (m^{-3}), is

$$n_t = \frac{P(z)}{k_b\,T(z)}, \tag{2.4}$$

where P (Pa) and T (K) are the altitude dependent pressure and temperature, and k_b ($J\,K^{-1}$) is the Boltzmann constant.

The production and loss rates of species i can be calculated by considering all the reactions which include said species, (e.g. $n_i + n_{i'} \rightleftharpoons n_{i''} + n_{i'''}$), then finding the rate at which n_i is produced ($k_2 n_{i''} n_{i'''}$) and lost ($k_1 n_i n_{i'}$) in each reaction, where k_1 and k_2 are the rate of the forward and reverse reactions respectively, before summing over all such reactions such that,

$$\mathscr{P}_i - \mathscr{L}_i = \sum(k_2 n_{i'''} n_{i''} - k_1 n_i n_{i'}). \tag{2.5}$$

Atmospheric Profile

The physical characteristics of the atmospheres LEVI simulates have a profound impact on their chemistry. This is realised through a pressure-temperature (P-T) profile that describes the atmosphere being investigated. Currently, the P-T profiles are not calculated self-consistently, but instead use pre-calculated profiles as an input, typically derived from general circulation models and radiative transfer models. This simplification is typical for chemical kinetics models, since implementing radiative transfer to allow iterative recalculation of the P-T profile would significantly increase the runtime, in addition to the possibility of converging to a non-physical P-T profile and atmosphere chemistry. There have been other works investigating how having a self-consistent P-T profile may affect the results of chemical kinetics models. Drummond et al. (2016) found that for disequilibrium chemistry caused by strong $K_{zz} > 10^7$ $m^2\,s^{-1}$, self-consistent P-T profiles can vary by up to 100K. For the two test cases that we study

here, the hot Jupiters HD 189733b and HD 209458b, the P-T profiles are given in Figure 2.1a. We also consider an isothermal profile for reference.

The P-T and K_{zz} profiles for HD 209458b and HD 189733b that are used in most of this work have been adopted from Moses et al. (2011), with the origins of these profiles being estimated from the general circulation models of Showman et al. (2009a). The deepest layer of the atmosphere is chosen to be 10^3 bar, a pressure at which all species are expected to be in chemical equilibrium, while the highest atmosphere layer (10^{-8} bar) should be sufficient to cover the photochemical destruction and production region for all relevant molecules. For pressures below 10^{-7} bars, an ad-hoc approximation for the thermosphere is used based on the work of García Muñoz (2007), in which the atmospheric temperature increases rapidly up to an arbitrarily high value by 10^{-8} bar.

Actinic Flux

Many species in the atmosphere, upon absorbing a sufficiently energetic photon, can be photo-dissociated into a variety of species, including radicals. It is also possible for species to be photo-ionised, however we currently do not consider ions in our model. Since the rate of photo-dissociation is proportional to the number density of UV photons, it is necessary to define the actinic flux, the spherically integrated flux in any atmosphere layer due to irradiation from the host star. This can be calculated as,

$$F(\lambda, z) = F_0(\lambda)\, e^{-\tau(\lambda,z)/\mu_0}, \tag{2.6}$$

where F_0 (photons $\mathrm{m}^{-2}\,\mathrm{s}^{-1}\,\mathrm{nm}^{-1}$) is the flux at the top of the atmosphere (where by definition $\tau = 0$), μ_0 is angle of the path of sunlight, chosen to be 57.3^o as the mean zenith angle for the upper atmosphere (Hu et al. 2012). τ is the total optical depth, as a function of wavelength, integrated over all the atmosphere that the light passes through, calculated self-consistently and defined as,

$$\tau(\lambda, z) = \int_z^\infty n_i(z')\sigma_i(\lambda)dz', \tag{2.7}$$

where σ_i is the wavelength dependent cross-section of species. σ_i is found from the sum of the molecular absorption cross-section for photo-active species, $\sigma_a(\lambda)$, and the Rayleigh scattering cross section (Liou 2002),

$$\sigma_r(\lambda) = C_r \frac{8\pi^3 (m_r(\lambda)^2 - 1)^2}{3\lambda^4 N_s}, \tag{2.8}$$

where m_r is the real part of the refractive index of the molecule, and C_r is a corrective factor due to molecular anisotropy. N_s is the number density at STP (1 atm, 273.15 K). For most species C_r is approximately unity, apart from CO_2, for which C_r is approximately 1.14 (Sneep

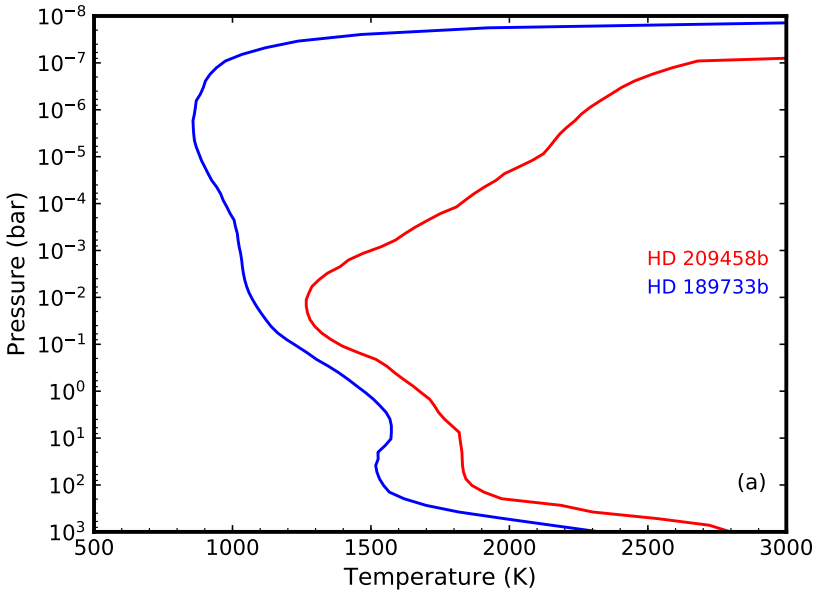

(a)

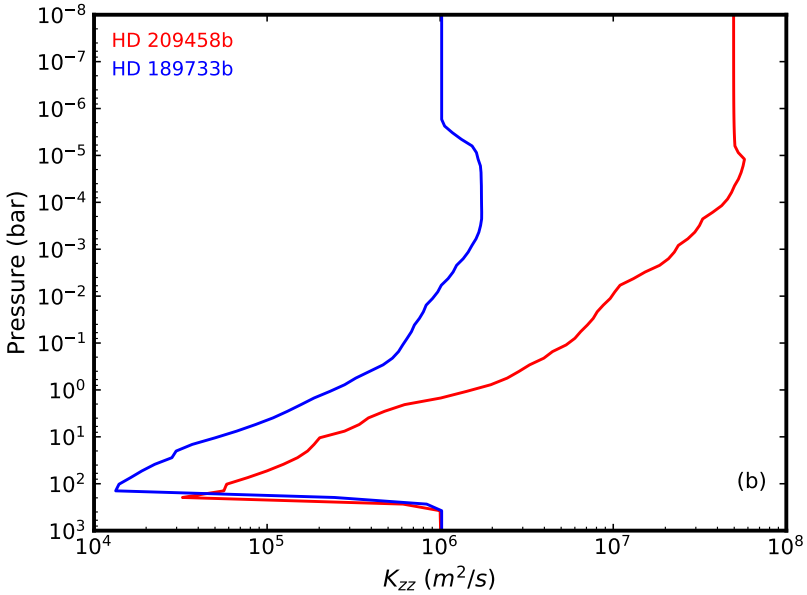

(b)

Fig. 2.1 Plot (a) are the Pressure-Temperature profiles for the average day-side of HD 209458b and HD 189733b assuming a solar composition atmosphere, adopted from Moses et al. (2011). At pressures below 10^{-7} bar an approximation for the thermosphere is used from García Muñoz (2007). Plot (b) displays the K_{zz} profiles that are being used for each planet, again drawn from Moses et al. (2011).

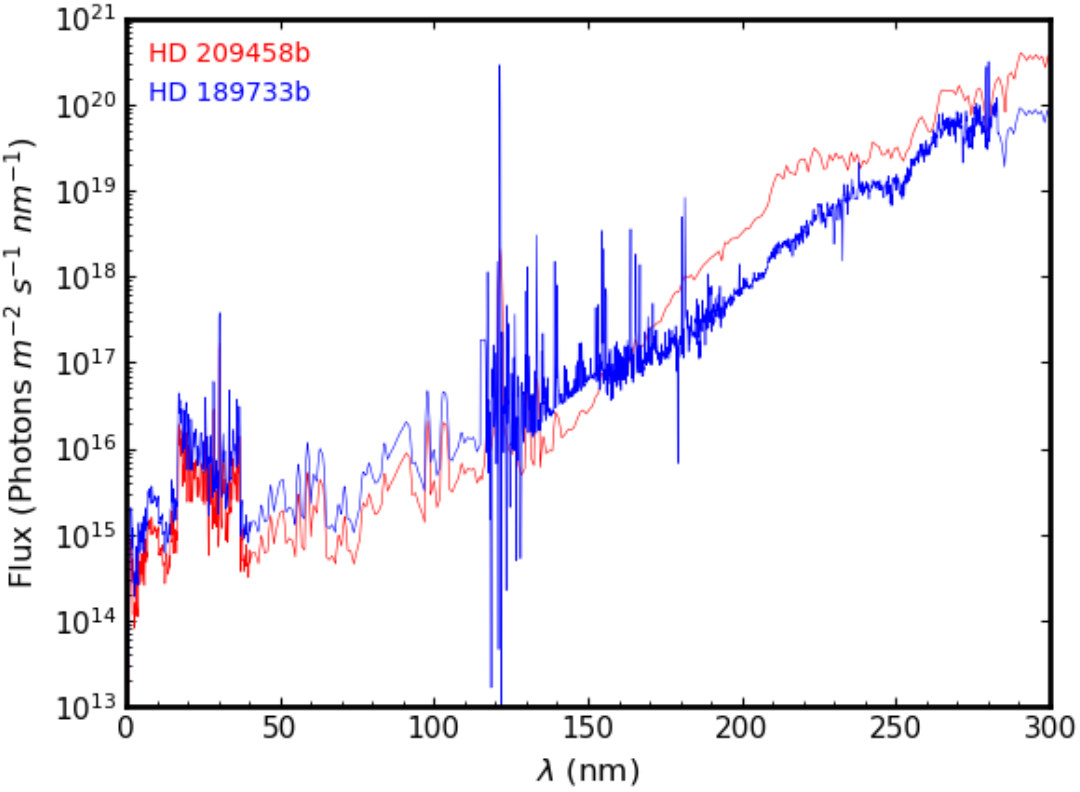

Fig. 2.2 The unattenuated UV fluxes applied to the top of the atmospheres of HD 189733b and HD 209458b. For HD 189733b the solar flux is used up to 115 nm and epsilon Eridani beyond that. For HD 209458b the solar flux is used. In both cases, the flux has been corrected to account for planet-star separation.

and Ubachs 2005). The refractive index can be approximated as that of the dominant species in the atmosphere, which for the atmospheres modelled in this work is H_2.

Very few stars have robust measurments of the UV spectrum at less than 100 nm, and therefore we have to use approximations for UV spectrum's of HD 209458 and HD 189733. The host star of HD 209458b is type G0V, similar to the sun, and therefore the spectrum used was the unattenuated solar flux at the top of the Earth's atmosphere, weighted by the relative flux received due to differing orbital radius between Earth and the sun ($d_\oplus$) and the planet and its host star (d_r), $(d_\oplus/d_r)^2$. For HD 209458b, d_r is approximately 0.047 AU.

HD 189733b orbits a star of type K1.5V. The closest analogue that could be found for this was the spectrum of epsilon Eridani, a K2V star, for wavelengths above 115 nm (Youngblood et al. 2016), and the solar flux below 115 nm. Since HD 189733b orbits at a distance of 0.031

AU, the spectrum is corrected to account for this in the same way as described above for HD 209458b.

Both these spectra are shown in Figure 2.2.

2.2.2 Chemical Network

LEVI is able to use an external chemical network to compute the reactions in the atmosphere, and the rate that at which they occur. In this work, the chemical network being used is a subset of the STAND2018 Atmospheric Chemical Network first developed in Rimmer and Helling (2016). The version being used is a H/C/N/O/He network, containing approximately 150 different chemical species and 1000 forward reactions. To improve the generality of the code it is possible to selectively disable certain reaction types, allowing the code to be applied to a much wider range of situations using the same network. The reactions that the model uses can be split into three general types: Bimolecular, termolecular and photochemical.

Bimolecular Reactions

The general form of a bimolecular reaction is,

$$A + B \rightarrow C + D, \tag{2.9}$$

for which the reaction rate is calculated using the generalised Arrhenius equation,

$$k = \alpha \left(\frac{T}{300} \right)^{\beta} \exp\left(-\frac{\gamma}{T} \right), \tag{2.10}$$

where k ($\mathrm{m^3\,s^{-1}}$) is the rate coefficient, T (K) is the temperature and α ($\mathrm{m^3\,s^{-1}}$), β and γ (K) are specific constants for each reaction, determined by fitting the Arrhenius equation to experimentally found or theoretically calculated values of k.

Termolecular Reactions

Termolecular reactions typically occur as either decomposition reactions,

$$A + M \rightarrow C + D + M, \tag{2.11}$$

or combination reactions,

$$A + B + M \rightarrow C + M, \tag{2.12}$$

where the M represents any third body that is involved in the reaction but is chemically unaffected as a result, often acting as either an energy source or sink for decomposition or combination reactions, respectively. To calculate the rate coefficients for these reactions, the Lindemann form is used (Lindemann et al. 1922); this form separates the rate constants into high and low pressure limits,

$$\begin{aligned} k_0 &= \alpha_0 \left(\frac{T}{300}\right)^{\beta_0} \exp\left(-\frac{\gamma_0}{T}\right), \\ k_\infty &= \alpha_\infty \left(\frac{T}{300}\right)^{\beta_\infty} \exp\left(-\frac{\gamma_\infty}{T}\right), \end{aligned} \tag{2.13}$$

with k_0 ($\mathrm{m^6\,s^{-1}}$ for combination or $\mathrm{m^3\,s^{-1}}$ for decomposition) as the low-pressure rate constant and k_∞ ($\mathrm{m^3\,s^{-1}}$ for combination or $\mathrm{s^{-1}}$ for decomposition) as the high-pressure rate constant. These can be combined to form an effective two-body reaction rate,

$$k = \frac{k_0[M]}{1 + \frac{k_0[M]}{k_\infty}}, \tag{2.14}$$

where $[M]$ ($\mathrm{m^{-3}}$) is the number density of the third species, where the third species can be any molecule in the atmosphere.

Reverse Reactions

It is necessary to consider that the reactions described in the previous sections will also occur in the opposite direction, i.e., the previous products will react together to form the reactants. The rate at which this happens can be calculated either with the Arrhenius equation, with the constants being determined experimentally as before, or by thermodynamically reversing the reaction (Burcat and Ruscic 2005). Due to the lack of experimental data for these reverse reactions, especially at the temperatures being considered, we are using thermodynamic reversal to determine the reaction rate.

The equation used to calculate the reverse reaction rate is,

$$\frac{k_f}{k_r} = K_c \left(\frac{k_b T}{P_0}\right)^{-\Delta\nu}, \tag{2.15}$$

in which k_f and k_r are the rate of the forward and reverse reactions, k_b is the Boltzmann constant, $\Delta\nu$ is the number of products minus the number of reactants, P_0 is the standard-state pressure

(which is 1 bar, under the ideal gas assumption). K_c is an equilibrium constant determined by,

$$K_c = \exp\left(-\frac{\Delta G^o}{\mathscr{R}T}\right), \tag{2.16}$$

where $\mathscr{R}$ is the gas constant and ΔG^o is the standard state gibbs free energy change on reaction, which expressed as enthalpy and entropy changes on reaction is,

$$\Delta G^o = \Delta H^o - T\Delta S^o, \tag{2.17}$$

with ΔH^o and ΔS^o as the standard state change in enthalpy and entropy, respectively, upon reaction. The enthalpy and entropy of each species can be calculated by a series in terms of the NASA polynomials,

$$\begin{aligned} \frac{H^o}{\mathscr{R}T} &= a_1 + \frac{a_2}{2}T + \frac{a_3}{3}T^2 + \frac{a_4}{4}T^3 + \frac{a_5}{5}T^4 + \frac{a_6}{T}, \\ \frac{S^o}{\mathscr{R}} &= a_1 lnT + a_2 T + \frac{a_3}{2}T^2 + \frac{a_4}{3}T^3 + \frac{a_5}{4}T^4 + a_7. \end{aligned} \tag{2.18}$$

The values for these polynomials were drawn from Burcat [2] whenever possible, and when not possible, used a modified Benson's method which calculates the polynomials based upon the chemical bonds in the species, described in the Appendix of Rimmer and Helling (2016).

Photochemistry

The rate of photo-dissociation for photochemically active molecules is also calculated. The molecular absorption cross-sections, σ_a (m^2), for these molecules were drawn primarily from PhIDRates [3], apart from C_4H_2 and C_4H_4, which were not in this database. These two molecules used the cross-sections from the MPI-Mainz-UV-VIS Spectral Atlas of Gaseous Molecules [4]. These cross-sections are often temperature dependant, but there is a significant lack of data at high temperatures, and so often the cross-sections we use are measured at room temperature. There has been some work done in identifying the UV cross-section for CO_2 at high temperatures (Venot et al. 2013, 2018), in which several orders of magnitude difference were found in the absorption cross-section, resulting in significant differences to the computed chemical composition. This emphasises the need for more high temperature cross-sections to accurately compute the photo-chemistry occuring in hot Jupiter atmospheres. The cross-sections were divided into 3000 bins, each 0.1 nm wide, to cover the approximately 300 nm

[2] http://garfield.chem.elte.hu/Burcat/burcat.html
[3] http://phidrates.space.swri.edu/
[4] www.uv-vis-spectral-atlas-mainz.org

range over which most cross-sections are defined. The photo-dissociation rate is then,

$$k = t_f \int \sigma_a(\lambda) F(\lambda, z) d\lambda \tag{2.19}$$

with $F(\lambda, z)$ as the actinic flux as described in 2.2.1, and t_f a dimensionless factor accounting for the fraction of time the atmosphere being modelled spends receiving stellar irradiation. This is 0 or 1 for a tidally locked planet's night and day sides respectively, and on average 1/2 for a planet with a day-night cycle. Photo-dissociation reactions are not reversed, since, while it is possible for reactions of this form to occur, they occur too slowly to have any impact on the atmosphere.

2.2.3 Numerical Method

Here we describe how the governing equations presented in the previous section are discretised into a form that can be solved numerically.

Discretisation

Equation 2.1 can be rewritten in a discrete form that allows it to be solved numerically,

$$\frac{\Delta n_{i,j}}{\Delta t} = \mathscr{P}_{i,j} - \mathscr{L}_{i,j} - \frac{\Phi_{i,j+1/2} - \Phi_{i,j-1/2}}{\Delta z}, \tag{2.20}$$

where, as previously, the subscript i refers to the i^{th} species. The subscript j represents the j^{th} layer in the atmosphere, and takes values from $j = 1,\ldots,N_z$, with N_z being the total number of atmosphere layers. The diffusion terms have subscripts $j+1/2$ and $j-1/2$ and thus are defined to be at the upper and lower boundary of each layer. Here it has been assumed that only adjacent layers will contribute to the incoming fluxes, as a first-order treatment of diffusion is being used (Hu et al. 2012). The layer thickness is given by Δz. Equation 2.2 can be similarly discretised to

$$\begin{aligned}\Phi_{i,j\pm1/2} = \mp(K_{zz,j\pm1/2} + D_{i,j\pm1/2})\, n_{t,j\pm1/2}\, \frac{X_{i,j\pm1} - X_{i,j}}{\Delta z} \\ + D_{i,j\pm1/2}\, n_{i,j\pm1/2} \left[\frac{(m_{t,j\pm1/2} - m_i) g}{k_b T_{j\pm1/2}} \mp \frac{\alpha_{T,i}}{T_{j\pm1/2}} \frac{T_{j\pm1} - T_j}{\Delta z} \right],\end{aligned} \tag{2.21}$$

in which any $Y_{j\pm1/2}$ has been approximated to $(Y_{j\pm1} + Y_j)/2$. $m_{t,j}$ is the mean mass of atmosphere layer j, and m_i is the mass of species i, g is the gravitational acceleration, and k_b is the Boltzmann constant. Now, it is possible to combine Equation 2.20 and 2.21 to form a set of

ordinary differential equations with time as the independent variable,

$$\frac{\Delta n_{i,j}}{\Delta t} = \mathscr{P}_{i,j} - \mathscr{L}_{i,j} + \frac{1}{\Delta z_{j-1/2}}[(k^{-}_{i,j+1/2}\frac{n_{t,j+1/2}}{n_{t,j+1}})\, n_{i,j+1} - (k^{+}_{i,j+1/2}\frac{n_{t,j+1/2}}{n_{t,j}} + k^{-}_{i,j-1/2}\frac{n_{t,j-1/2}}{n_{t,j}})\, n_{i,j} + (k^{+}_{i,j-1/2}\frac{n_{t,j-1/2}}{n_{t,j-1}})\, n_{i,j-1}], \quad (2.22)$$

in which

$$k^{\pm}_{j+1/2} = \frac{K_{zz,j+1/2} + D_{i,j+1/2}}{\Delta z_j} \pm \frac{D_{i,j+1/2}}{2\Delta z_j}\left[\frac{(m_{t,j} - m_i)g\,\Delta z_j}{k_b T_{j+1/2}} - \frac{\alpha_{T,i}}{T_{j+1/2}}(T_{j+1} - T_j)\right] \quad (2.23)$$

We define the atmosphere layers to be spaced equally in log pressure, and thus to find the corresponding altitude hydrostatic equilibrium is assumed,

$$P(z) = P_0\, e^{\frac{-m(z)gz}{k_b T(z)}}, \quad (2.24)$$

with m as the mean mass of the molecules in an atmosphere layer, found by $\sum_i m_i n_i$, where m_i is the mass of a molecule of species i. g is the surface gravity, defined for gas giants as the gravity at 1 bar, which is set to 10 $\mathrm{m\,s^{-2}}$ for an isothermal profile, 21.4 $\mathrm{m\,s^{-2}}$ for HD 189733b and 9.36 $\mathrm{m\,s^{-2}}$ for HD 209458b in accordance with Moses et al. (2011). The size of the atmospheric layers are recalculated at every time step to ensure the atmosphere stays in hydrostatic equilibrium, since the mass of each layer varies as the system evolves.

Solver

LEVI uses a semi-implicit second-order Rosenbrock solver to find a steady-state solution to Equation 2.22, (Rosenbrock 1963). Verwer et al. (1999) show that the second-order Rosenbrock solver is stable over large range of step-sizes. This property of the solver is ideal for chemical kinetics, where step-sizes can range over many orders of magnitude due to the possibility of chemical reactions which have sub-microsecond timescales and diffusion which can occur over timescales of hundreds of years. The general differential equation is,

$$\frac{dn}{dt} = f(n), \quad (2.25)$$

where n is the dependent variable, t is the independent variable and $f(n)$ is some general function of n. The Rosenbrock solver provides a solution to Equation 2.25 in the form,

$$\begin{aligned} n_{k+1} &= n_k + 1.5\Delta t g_1 + 0.5\Delta t g_2, \\ (\mathbf{I} - \gamma\Delta t\mathbf{J})g_1 &= f(n_k), \\ (\mathbf{I} - \gamma\Delta t\mathbf{J})g_2 &= f(n_k + \Delta t g_1) - 2g_1, \end{aligned} \tag{2.26}$$

where Δt is the size of the time-step, chosen by the solver as described in Equation 2.31, γ is a scaler constant, suggested by Verwer et al. (1999) to be $\gamma = 1 + 1/\sqrt{2}$ for stability, the subscript k denotes the k^{th} step in the solver, $\mathbf{I}$ is the identity matrix, and

$$\mathbf{J} \equiv \frac{\partial f}{\partial n}|_{n_k}, \tag{2.27}$$

is the Jacobian matrix evaluated at n_k.

To solve Equation 2.26 it is necessary to invert the Jacobian matrix, which is one of the most expensive parts of the calculations, and so we focused on making this as efficient as possible. The Jacobian takes the form of a tridiagonal block matrix of total size $N_i N_z$, the product of the total number of species and the total number of atmosphere layers. The construction of this matrix is presented in equation 2.28. The diagonal blocks, B, of the Jacobian are made up of square matrices of size N_i that describe the interactions between species in the same atmosphere layer. The off-diagonal blocks, A and C, also matrices of size N_i, represent the effects of adjacent atmosphere layers via diffusion. The subscripts for the A, B and C matrices show which atmosphere layer they represent.

$$J = \begin{bmatrix} B_1 & C_1 & 0 & 0 & \dots & 0 & 0 & 0 & 0 \\ A_2 & B_2 & C_2 & 0 & \dots & 0 & 0 & 0 & 0 \\ 0 & A_3 & B_3 & C_3 & \dots & 0 & 0 & 0 & 0 \\ 0 & 0 & A_4 & B_4 & \dots & 0 & 0 & 0 & 0 \\ \vdots & \vdots & \vdots & \vdots & \ddots & \vdots & \vdots & \vdots & \vdots \\ 0 & 0 & 0 & 0 & \dots & B_{N_z-3} & C_{N_z-3} & 0 & 0 \\ 0 & 0 & 0 & 0 & \dots & A_{N_z-2} & B_{N_z-2} & C_{N_z-2} & 0 \\ 0 & 0 & 0 & 0 & \dots & 0 & A_{N_z-1} & B_{N_z-1} & C_{N_z-1} \\ 0 & 0 & 0 & 0 & \dots & 0 & 0 & A_{N_z} & B_{N_z} \end{bmatrix} \tag{2.28}$$

By comparison of equations 2.5, 2.22, 2.25, and 2.27, it can be seen that

$$\begin{aligned} A &= \frac{k^{-}_{i,j+1/2}\, n_{t,j+1/2}}{dz_{j-1/2}\, n_{t,j+1}}, \\ C &= \frac{k^{+}_{i,j-1/2}\, n_{t,j-1/2}}{dz_{j-1/2}\, n_{t,j-1}}, \\ B &= -\left(\frac{k^{+}_{i,j+1/2}\, n_{t,j+1/2}}{dz_{j-1/2}\, n_{t,j}} + \frac{k^{-}_{i,j-1/2}\, n_{t,j-1/2}}{dz_{j-1/2}\, n_{t,j}}\right) \\ &\quad + \frac{\partial}{\partial n_j}\left(\sum\left(k_2\, n_{i''}\, n_{i'''} - k_1\, n_i\, n_{i'}\right)\right). \end{aligned} \tag{2.29}$$

As a result, both A and C are purely diagonal matrices, while B is a full matrix with each position describing how one species reacts with another in the same layer.

To invert this Jacobian, we use the method of inverting a tridiagonal matrix described in Hubeny and Mihalas (2014), with a generalisation to block tridiagonal by treating each matrix element in the inversion method as a full matrix. As a result, only the three N_i size matrices are ever kept in the memory, which is much less expensive than trying to invert the complete $N_i N_z$ matrix.

Convergence

There are several conditions that must be satisfied before the run is considered to be complete and have reached steady-state. These are that both the relative change, $\Delta n = \frac{|n_{i,j,k+1} - n_{i,j,k}|}{n_{i,j,k}}$, and the rate of relative change, $\frac{\Delta n}{\Delta t}$ of mixing ratios in the atmosphere, are sufficiently small that running the code further would produce no significant change.

To ensure that each step is correctly approaching steady-state, several conditions are checked after every time-step. If the conditions are passed then the solver continues, otherwise, the latest solution is discarded and the step-size is reduced, before re-running the solver. The conditions are that every species has a positive number density and that the truncation error, ε is sufficiently small.

The truncation error is found by calculating the difference between second-order solution and the first-order solution, $n^1_{k+1} = n_k + \Delta t g_1$, such that,

$$\varepsilon = |n_{k+1} - n^1_{k+1}|. \tag{2.30}$$

Since the timescales being modelled can vary over many orders of magnitude, having a time-step that is self-adjusting is vital to allowing the code to have a reasonable runtime. The

truncation error can thus be used as a cheap local error estimation to control the step size,

$$\Delta t_{k+1} \sim \Delta t_k (1/\varepsilon)^{0.5}. \tag{2.31}$$

2.2.4 Initial and Boundary Conditions

Initial Conditions

In the present work we focus on hydrogen-rich gas giant atmospheres. Our baseline model uses solar elemental abundances, from Asplund et al. (2009). In Section 2.4 we also explore the effects of variation in the C/O and N/O ratios. In Asplund et al. (2009) the solar abundances are given as fractions of the number of hydrogen molecules, while for LEVI the elemental abundances have been transformed to the fraction of the total number of molecules (i.e., the mixing ratio), enabling easier description of non-hydrogen dominated atmospheres. The ratio of elemental atoms to the total number of molecules therefore starts as: $X_{\rm H} = 1.707$, $X_{\rm He} = 0.145$, $X_{\rm C} = 4.594 \times 10^{-4}$, $X_{\rm N} = 1.154 \times 10^{-4}$ and $X_{\rm O} = 8.359 \times 10^{-4}$. When calculating solar abundances all H is assumed to be in the form of H_2, thus leading to a $X_{\rm H}$ that is greater than one. This gives a C/O ratio of 0.55 and a N/O ratio of 0.138.

When choosing the initial conditions, conservation of mass is ensured by summing over the product of the species present (n_i) and the number of atoms of x contained by n_i ($A_{i,x}$),

$$\sum_i A_{i,x} n_i = X_x. \tag{2.32}$$

The initial chemistry of the atmosphere is chosen as a set of species that contain all the elements in the atmosphere, then by using Equation 2.32 for each element to solve for the species' initial abundance and setting the initial abundance of all other species in the network to zero. To simplify solving Equation 2.32, we picked the initial species set to be small molecules, so that dividing the elements between them would be straightforward.

With this approach, there are still a range of viable starting conditions for the atmospheric mixing ratio and it is important to demonstrate that model convergence is not affected by this decision, although computational speed is, typically slowing down the run-time by up to a factor of five. A comparison of the steady state solution for a 1500 K isotherm without diffusion or photochemistry, emerging from a choice of three initial atmospheric species sets is shown in the first plot of Figure 2.3, with the initial species sets being: (1) H_2, CO, OH and NH_3; (2) H_2, CH_4, H_2O and N_2; and (3) atomic H, C, O, and N. Having the initial species set being elements in their atomic form provides a starting condition of extreme disequilibrium, compared to starting with molecules that are expected to dominate the steady-state atmosphere, as in the other two starting conditions. There is no noticeable difference between the three sets of mixing

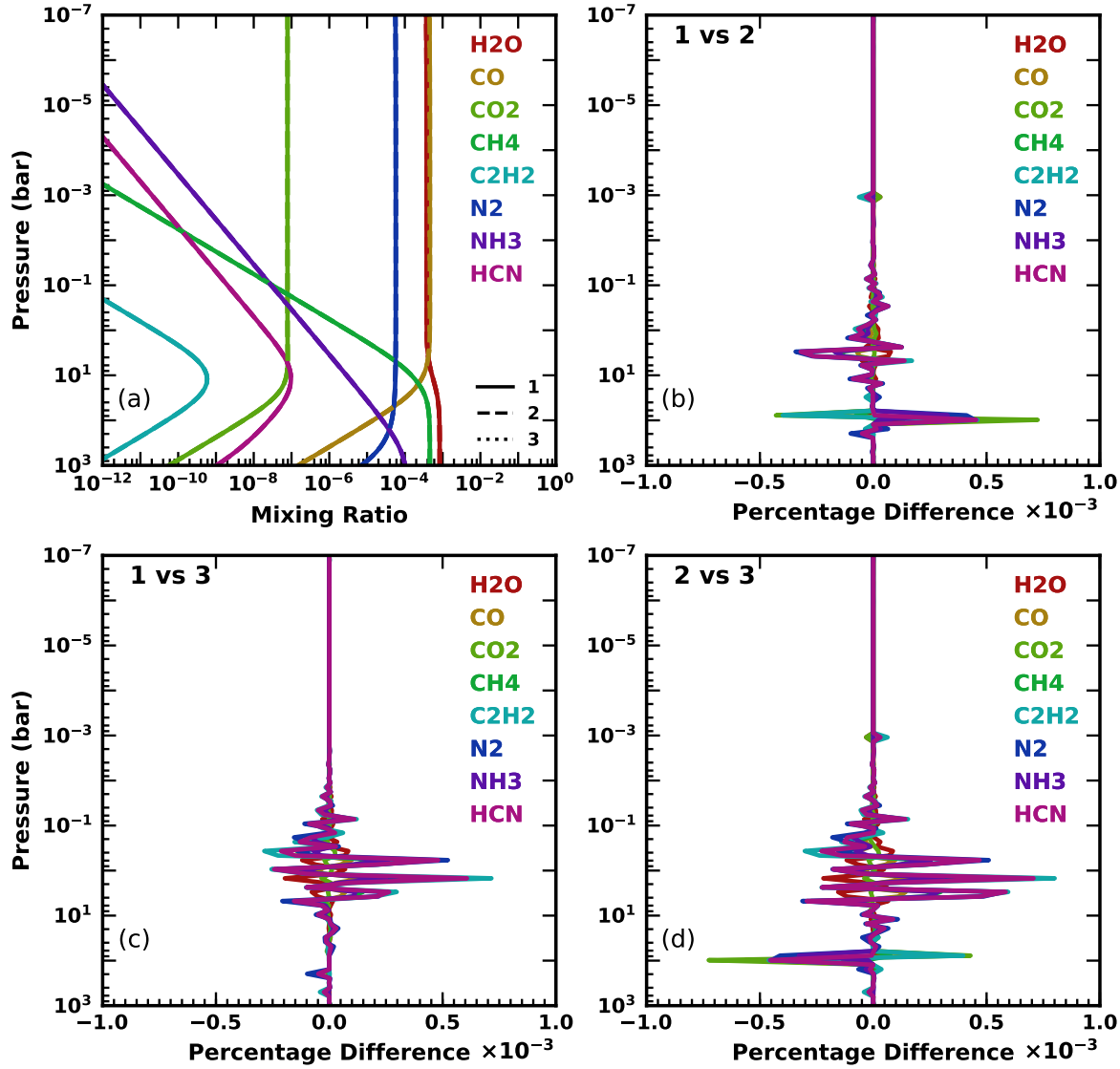

Fig. 2.3 An investigation of the effect of initial conditions on atmospheric chemistry. The sets of initial species are: H_2, CO, OH and NH_3 (Solid lines, labeled 1; H_2, CH_4, H_2O and N_2 (Dashed lines, labeled 2; and elements in their atomic form (Dotted lines, labeled 3. In this example a 1500K isotherm was used, with no diffusion or photochemistry. Plot a) shows all three starting conditions, while b), c) and d) each show the percentage difference between two of the starting options.

ratios, confirming that the steady-state solution is independent of the choice of atmospheric species used to initialise the calculation. The time taken to reach this steady state, however, is significantly different between the three sets, with set (1) taking four and three times as long as sets (2) and (3) respectively, in this scenario. This is because the close the initial guess for the atmospheric composition is to steady state, the faster steady state is reached. Set (1) is very dissimilar to steady state, and therefore takes the longest to reach it. Plots b), c) and d) of Figure 2.3 show the accuracy to which each of the three different initial conditions are the same. In all cases there was less than a 10 ppm difference between any two starting sets of molecules, thus suggesting that the solutions these initial sets produce are functionally identical.

Boundary Conditions

It is necessary to specify boundary conditions at the minimum and maximum pressures chosen for the simulation. There are a variety of choices available, depending both on the type of planet and the range of pressures being explored.

For terrestrial exoplanets, the lower boundary conditions usually model any surface-atmosphere interaction, so typical boundary conditions can include permanently assigning a species an abundance at the surface to model a large reservoir, or a flux to describe surface emission and deposition. For the upper atmosphere a flux due to atmospheric escape is common (Hu et al. 2012).

Gas-giant exoplanets have no solid surface at the lower boundary, thus the boundary conditions are either chemical equilibrium or zero flux. The upper boundary condition could be atmospheric escape or, if the upper boundary is deep enough in the atmosphere, zero flux. In general, atmospheric escape does not significantly affect the mass of the atmosphere (Linsky et al. 2010; Murray-Clay et al. 2009). For a boundary in chemical equilibrium, the assumption is that layers deeper in the atmosphere have a chemical timescale much shorter than the dynamical timescale, so the boundary would be in chemical equilibrium. A zero flux, or closed boundary, assumes that the deeper layers are chemically identical to the bottom layer in the calculation, such that there will be no chemical consequence to flow of molecules across the layer boundaries.

The effect of setting different lower boundary conditions are explored in the left plot in Figure 2.4, which shows the difference between equilibrium (dashed lines) and zero flux (solid lines) boundary conditions. It can be seen that there is a slight difference in the mixing ratios as a result of these boundary condition changes, especially to N_2. To better quantify this change, the right plot in Figure 2.4 shows the percentage difference between zero flux and equilibrium boundary conditions for a 1500 K isotherm was used, with 1×10^6 $m^2\,s^{-1}$ K_{zz} and no photochemistry. Throughout most of the atmosphere the difference in abundance

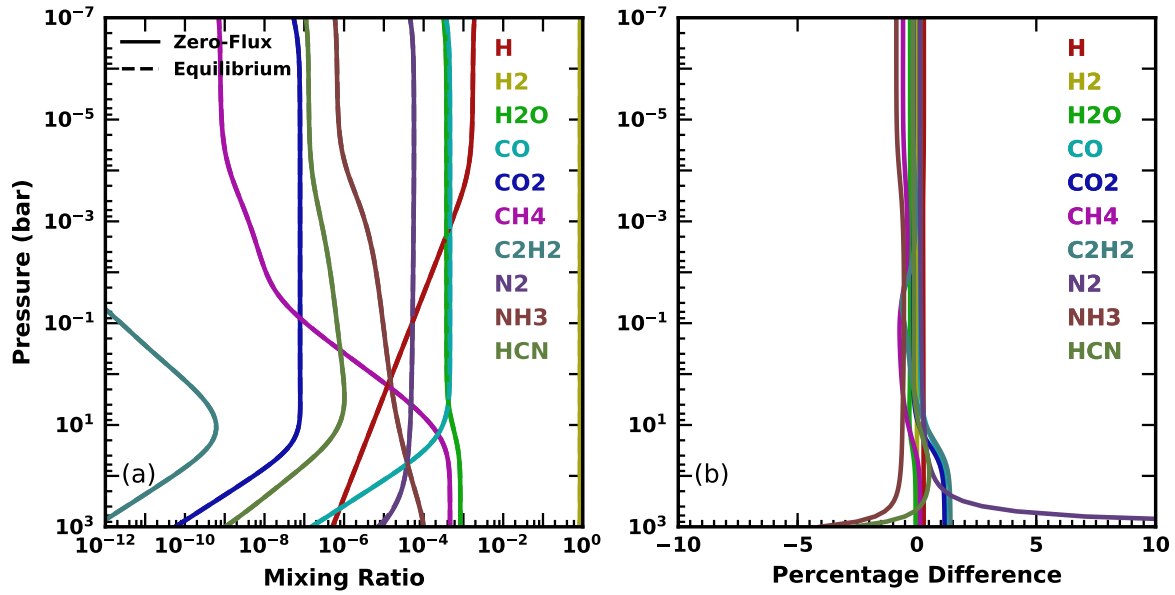

Fig. 2.4 The difference in steady-state atmospheric chemistry based on the lower boundary condition. In this example a 1500 K isotherm was used, with 1×10^6 $m^2 s^{-1}$ K_{zz} and no photochemistry. Plot (a) shows a comparison of the atmospheric chemistry between the two boundary conditions, while (b) shows the percentage difference in the abundances of a zero-flux boundary condition compared to a equilibrium boundary condition.

is less than one percent, however closer to the lower boundary it can increase up to 10%. Thus, it is clear that the boundary conditions can have a much more significant impact upon atmospheric abundances than the initial conditions, although even a 10% change is negligible when considering the precision with which the abundance of these molecules can be detected in exoplanet atmospheres, which is typically only to within an order of magnitude. Since it is possible for diffusion to drive even the deepest layers slightly away from equilibrium, zero flux boundary conditions were chosen for this work, to prevent a disparity between the boundary layer and the layer above. As a result, zero flux conditions were also chosen for the upper boundary, to ensure conservation of mass in the atmosphere.

2.3 Validation and Testing

In this section we apply our model to the atmospheres of several hot Jupiters. We first compare our models of HD 209458b to that of previous codes (Moses et al. 2011 and Venot et al. 2012) for validation. We then investigate the effects of disequilibrium chemistry on the atmospheric chemistry of hot Jupiters and discuss why these effects occur. We also show the fastest reaction pathway the model takes for several important net reactions in the atmosphere. These pathways are found by use of a code that traces the reactions that lead from the products to the reactants, and identifying the route that has the fastest overall reaction rate.

2.3.1 Validation

We chose HD 209458b as one of the best candidates for benchmarking LEVI, due to both the well characterised spectral observations of its atmosphere (MacDonald and Madhusudhan 2017b; Hawker et al. 2018; Welbanks et al. 2019; Giacobbe et al. 2021) and the existence of several previous chemical models that have predicted atmospheric compositions for this planet (Moses et al. 2011, Venot et al. 2012, Agúndez et al. 2014, Rimmer and Helling 2016, Tsai et al. 2017). The results produced by this code are compared to the disequilibrium models of HD 209458b of both Moses et al. (2011) and Venot et al. (2012) (Figure 2.5). Like LEVI, both other models do not self-consistently calculate the P-T profile, but rather use a fixed input. The species chosen for the comparison are H_2, H and H_2O (Figure 2.5a), CO, CH_4 and CO_2 (Figure 2.5b), and N_2, NH_3 and HCN (Figure 2.5c). These species are expected to be some of the most abundant (e.g. Swain et al. 2009; MacDonald and Madhusudhan 2017b), and several have strong spectral signatures.

Looking at the comparison plots in Figure 2.5, it can be seen that for most species there is no significant difference between LEVI and Venot et al. (2012), or between LEVI and Moses et al. (2011). In the deep atmosphere there are some slight differences in the abundances of many molecules. These differences are not significant, and are likely a consequence of slightly differing P-T profiles, thermodynamic coefficients, and choices of initial elemental ratios. For example, Moses et al. (2011) and Venot et al. (2012) model a lower-oxygen atmosphere, because they have considered 20% of the oxygen abundance to be sequestered in silicates.

One of the largest differences between the models is for NH_3, where there is an half an order-of-magnitude lower quenching abundance of NH_3 for LEVI compared to Moses et al. (2011), while LEVI predicts nearly a hundred times more NH_3 at 10^{-6} bar. Compared to Venot et al. (2012), LEVI predicts a nearly identical quenching abundance of NH_3, and almost ten thousand times more NH_3 at 10^{-6} bar. These differences are due to a high degree of uncertainty in the rate of the pathway that converts NH_3 to N_2:

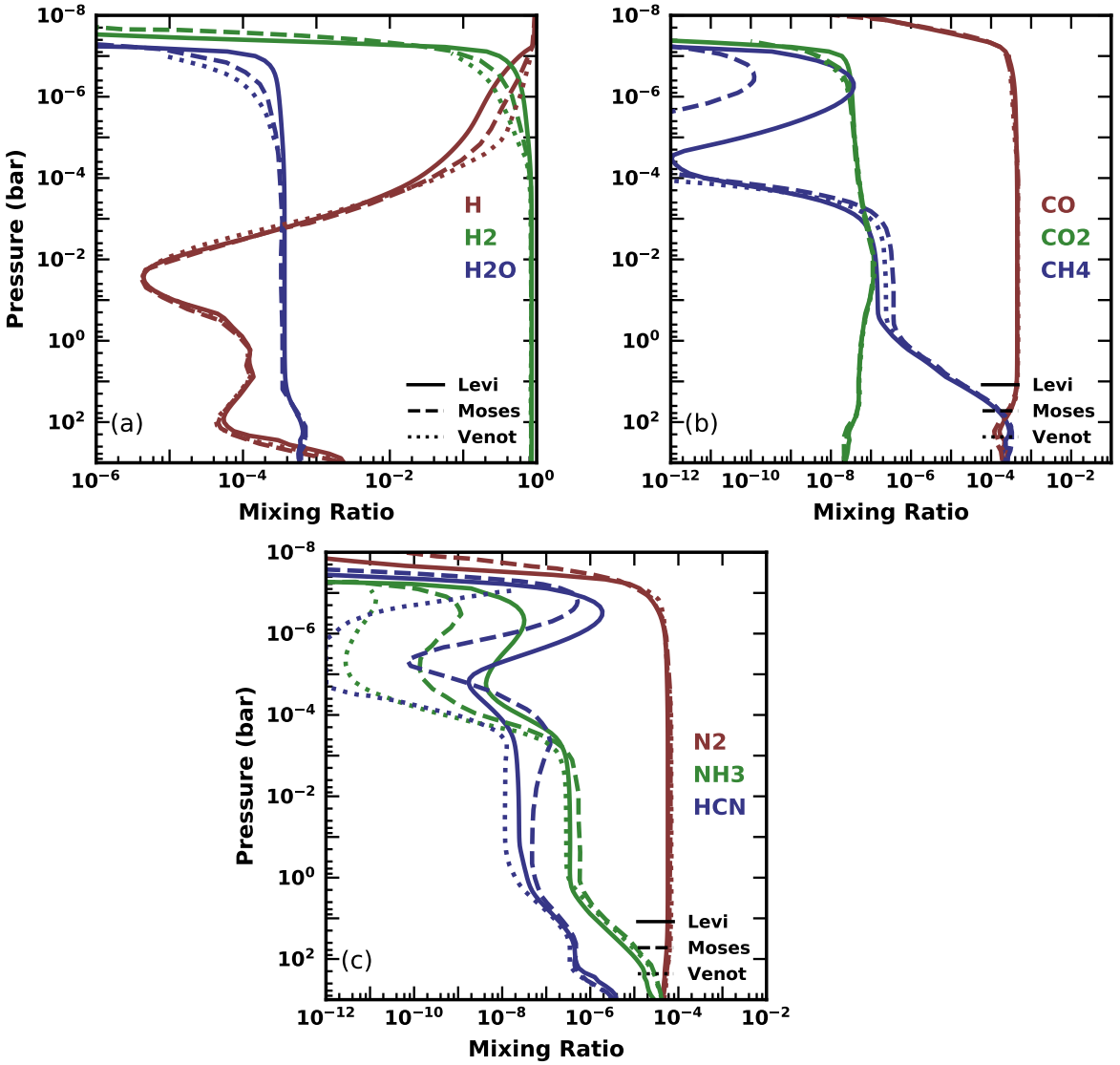

Fig. 2.5 A comparison of models of the atmosphere of HD 209458b for a selection of major molecules in the atmosphere. The solid line is the model described in this paper, the dashed line is the model created by Moses et al. (2011) and the dotted line is the code described in Venot et al. (2012).

$$\begin{aligned} \mathrm{H_2 + M} &\longrightarrow \mathrm{H + H + M} \\ 2(\mathrm{H + NH_3} &\longrightarrow \mathrm{NH_2 + H_2}) \\ 2(\mathrm{H + NH_2} &\longrightarrow \mathrm{HN + H_2}) \\ \mathrm{2\,HN} &\longrightarrow \mathrm{N_2 + 2\,H} \\ \textbf{Net}: \mathrm{2\,NH_3} &\longrightarrow \mathrm{N_2 + 3\,H_2}, \end{aligned} \tag{2.33}$$

The observed difference in the quenching location of CH_4 arises for similar reasons. In the network used by LEVI, there are several pathways that convert CH_4 into CO, one of which has a highly uncertain reaction rate (Rimmer and Helling 2016), and can explain the nearly 1 dex and 0.5 dex higher quenching abundance of CH_4 seen in Moses et al. (2011) and Venot et al. (2012), respectively, than in LEVI. The large differences in abundance seen in HCN between the three models throughout the atmosphere are due to high degrees of uncertainty in the rate constants of many of the reactions that include HCN.

To conclude, LEVI can reproduce the composition of HD 209458b predicted by several other chemical models. While there are still some significant differences in abundances of several highly abundant species in exoplanet atmospheres, these are the result of uncertainties in rate constants and absorption cross-sections, which differ between the models. Only new experiments and calculations of the rate constants and absorption cross-sections will help resolve these differences.

2.3.2 Equilibrium vs. Diffusion vs. Photochemistry

In this section the effects of the three main chemical processes that occur in atmospheres are compared and contrasted. Thermochemical equilibrium, diffusion in the form of molecular, thermal and eddy-diffusion and photochemistry can all combine to play an important role in determining the distribution of observable species in exoplanet atmospheres, and thus should be considered when investigating the chemistry of these exoplanets. Chemical equilibrium is expected to dominate in the lower atmosphere, up to a few bars, due to the high temperatures and pressure. Diffusion effects then take over for some species between approximately 1-10^{-4} bars, and photochemistry dominates above this. At higher altitudes, in the thermosphere, it is sufficiently hot that most species thermally dissociate down to their base elements. We apply our code to the hot Jupiters HD 209458b and HD 189733b and discuss how and why the equilibrium and disequilibrium models diverge. We run three model scenarios, with the results presented in Figure 2.6: no-diffusion, no-photochemistry (solid lines); with diffusion, but no-photochemistry (dashed lines); with diffusion and photochemistry (dotted lines). Results similar to these have also been produced by previous 1-D chemical codes (e.g. Zahnle et al.

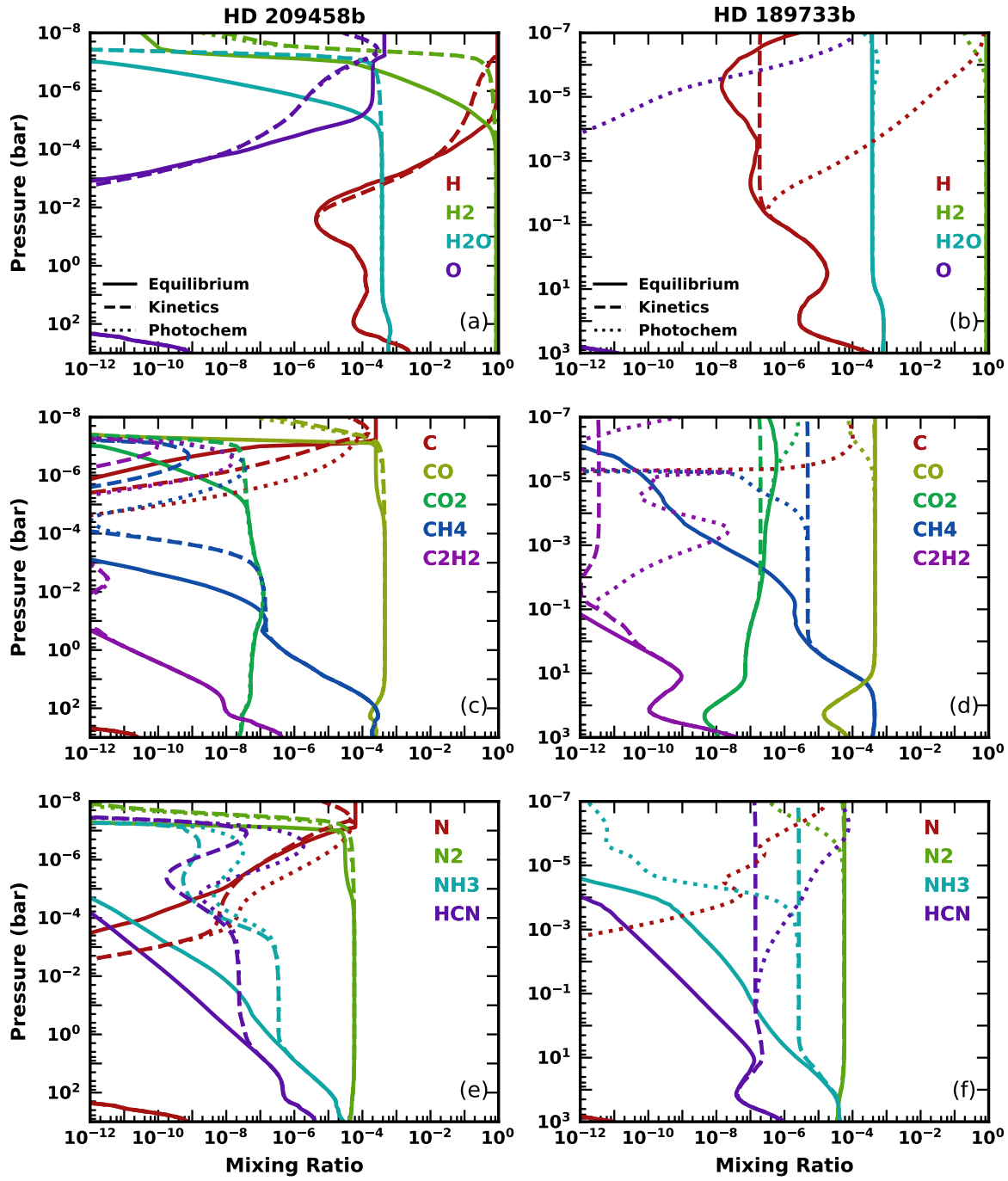

Fig. 2.6 Abundance profiles for several species on HD 290458b (left) and HD 189733b (right) for purely equilibrium chemistry (solid lines), diffusion (dashed line) and both diffusion and photochemistry (dotted line). The P-T and the K_{zz} profiles for these models are shown in Figures 2.1a and 2.1b.

2009; Moses et al. 2011; Hu et al. 2012; Venot et al. 2012; Rimmer and Helling 2016; Tsai et al. 2017).

Equilibrium

In the deepest regions of the atmospheres of the planets being investigated, below 1 bar, the high temperature and pressure may produce an atmosphere in chemical equilibrium. The relative abundances of species at chemical equilibrium depend on the P-T profile. For the investigated planets, at solar composition, we find that CH_4 and H_2O dominate over CO, and NH_3 approaches the abundance of N_2, while higher in the atmosphere this trend is reversed (Heng and Tsai 2016). When solving for equilibrium analytically, this same trend is found. In the observable region of the atmosphere, approximately 1 - 10^{-4} bar for emission spectroscopy, CO is the dominant carbon species, with most of the remaining oxygen ending up in H_2O, and N_2 is the dominant nitrogen species.

On HD 209458b, the thermosphere begins around 10^{-7} bar, causing most species to dissociate down to their base atomic forms. The thermosphere of HD 189733b does not begin until a higher altitude, so no thermal dissociation can be seen for this planet in Figure 2.6. Notable for comparison later on are the abundances of HCN and NH_3 in the observable region of the atmosphere; in this equilibrium scenario they are very minor constituents, far below detectable limits (HCN or NH_3 abundances at least 1% of the H_2O abundance) for solar composition (MacDonald and Madhusudhan 2017b).

Diffusion

The inclusion of diffusion, the dashed lines in Figure 2.6, leads to some significant deviations from chemical equilibrium. At very high pressures, the temperature is high enough that the chemical time-scale of the reactions is much shorter than the dynamical time-scale, and therefore the atmosphere at these levels is still in chemical equilibrium, as predicted. However, as the pressure and temperature decrease, and reaction rates drop due to the decreased rates of molecule-molecule interactions, the rate of some reactions drop sufficiently such that the time-scale of dynamic motion is now shorter than that of chemical interaction. This results in quenching at the pressure level where the two time-scales are equal, with the species abundance being effectively frozen in at this point and this chemistry being transported higher into the atmosphere by eddy diffusion. This process leads to the possibility of significantly different abundances of some species in the observable region of the atmosphere, compared to chemical equilibrium.

Figure 2.6 shows a number of species being affected by quenching in observable regions of the atmosphere, including CH_4, HCN and NH_3. NH_3 is of particular note on both HD 209458b and HD 189733b, as quenching may increase its abundance to the point where it can be distinguished in the atmospheric spectra of a hot Jupiter, making it potentially detectable (MacDonald and Madhusudhan 2017b).

On HD 209458b the high temperatures lead to a shorter reaction timescale compared to the mixing timescale, implying that the condition for chemical equilibrium is satisfied until much lower pressures in the atmosphere, compared to HD 189733b where quenching occurs deeper in the atmosphere. HD 189733b has many species at their quenched abundance throughout the upper atmosphere. This is due to the the planet's upper atmosphere not having a thermal inversion below the thermosphere, so the chemical timescale monotonically increases with decreasing pressure. On the other hand, HD 209458b does have a thermal inversion, so the chemical timescale can decrease with decreasing pressure, and so the upper atmosphere may begin to return to chemical equilibrium.

Photochemistry

The dotted lines in Figure 2.6 show how the inclusion of photochemistry affects the atmosphere. The photolysis of CO, H_2O, N_2, NH_3 and CH_4 drive most of the photochemical reactions that occur in the upper atmosphere.

The destruction of H_2O by a UV photon into OH and H, as deep as 0.1 bar, sets up the reaction that turns H_2 into H:

$$\begin{aligned} H_2O + h\nu &\longrightarrow OH + H \\ H_2 + OH &\longrightarrow H_2O + H \\ \textbf{Net}: H_2 + h\nu &\longrightarrow 2H. \end{aligned} \tag{2.34}$$

This reaction provides a large pool of highly reactive hydrogen radicals that can diffuse to both higher and lower altitudes to cause a chain of further reactions, drastically altering the composition of the upper atmosphere. On HD 209458b the rate of this reaction is low compared to the rate of dissociation of molecules due to the high temperatures in the upper atmosphere, and so little difference can be seen between the case with and without photochemistry. As evidenced in Figure 2.6a and 2.6b, H_2O is not permanently depleted from the atmosphere until much lower pressures due to it being replenished as fast as it is destroyed.

The photolysis of CO can produce C and O radicals that can also contribute to the destruction of H_2. Like H_2O, CO is also being replenished quickly, in this case by a reaction between CH_4 and H_2O:

$$
\begin{aligned}
2(\mathrm{H_2} + \mathrm{M} &\longrightarrow 2\,\mathrm{H} + \mathrm{M}) \\
\mathrm{H_2O} + \mathrm{H} &\longrightarrow \mathrm{OH} + \mathrm{H_2} \\
\mathrm{CH_4} + \mathrm{H} &\longrightarrow \mathrm{H_2} + \mathrm{CH_3} \\
\mathrm{CH_3} + \mathrm{OH} &\longrightarrow \mathrm{CH_2O} + \mathrm{H_2} \\
\mathrm{H} + \mathrm{CH_2O} &\longrightarrow \mathrm{H_2} + \mathrm{CHO} \\
\mathrm{H} + \mathrm{CHO} &\longrightarrow \mathrm{CO} + \mathrm{H_2} \\
\textbf{Net} : \mathrm{CH_4} + \mathrm{H_2O} &\longrightarrow \mathrm{CO} + 3\,\mathrm{H_2}.
\end{aligned}
\tag{2.35}
$$

However, as Figure 2.6d shows, on HD 189733b the formation of CO is not efficient enough to prevent loss of CO above 10^{-5} bar and so some of the carbon can end up in other species, e.g., CO_2 and HCN. On HD 209458b, the temperature, and thus the reaction rates, are high enough to keep replenishing CO until pressures as low as 10^{-7} bar.

The C radicals from the photolysis of CO often end up producing CH_4:

$$
\begin{aligned}
\mathrm{CO} + h\nu &\longrightarrow \mathrm{C} + \mathrm{O} \\
\mathrm{C} + \mathrm{H_2} &\longrightarrow \mathrm{CH} + \mathrm{H} \\
\mathrm{CH} + \mathrm{H_2} &\longrightarrow \mathrm{CH_2} + \mathrm{H} \\
\mathrm{CH_2} + \mathrm{H_2} &\longrightarrow \mathrm{CH_3} + \mathrm{H} \\
\mathrm{CH_3} + \mathrm{H_2} &\longrightarrow \mathrm{CH_4} + \mathrm{H} \\
\textbf{Net} : \mathrm{CO} + 4\,\mathrm{H_2} &\longrightarrow \mathrm{CH_4} + \mathrm{O} + 4\,\mathrm{H},
\end{aligned}
\tag{2.36}
$$

which leads to the increase of methane seen on HD 209458b. CH_4 is, in turn, susceptible to destruction by H radicals, thus leading to an overall decrease in methane if sufficient H is produced by the photo-dissociation of H_2O, as discussed earlier, and as can be seen at 10^{-5} bar on HD 189733b.

CO_2 is not greatly affected by photochemistry since its production is based upon fast reactions between H_2O and CO, both of which are largely constant until high in the atmosphere. In the upper atmosphere of HD 189733b, some of the CO is transformed into CO_2

C_2H_2 is an important byproduct of photochemistry. The carbon atoms released from dissociation of CH_4 or CO are reprocessed to form C_2H_2. This is the result of a highly efficient pathway:

$$\begin{aligned}
\mathrm{CO} + h\nu &\longrightarrow \mathrm{C} + \mathrm{O} \\
\mathrm{C} + \mathrm{H_2} &\longrightarrow \mathrm{CH} + \mathrm{H} \\
\mathrm{CH} + \mathrm{H_2} &\longrightarrow \mathrm{CH_2} + \mathrm{H} \\
\mathrm{CH_4} + h\nu &\longrightarrow \mathrm{CH_3} + \mathrm{H} \\
\mathrm{CH_3} + \mathrm{M} &\longrightarrow \mathrm{CH_2} + \mathrm{H} + \mathrm{M} \\
\mathrm{CH_2} + \mathrm{CH_2} &\longrightarrow \mathrm{C_2H_2} + \mathrm{H_2} \\
\textbf{Net} : \mathrm{CO} + \mathrm{CH_4} + 2\,\mathrm{H_2} &\longrightarrow \mathrm{C_2H_2} + 4\,\mathrm{H},
\end{aligned} \tag{2.37}$$

which leads to many orders of magnitude more C_2H_2, on both HD 209458b and HD 189733b, than otherwise expected if there was no UV flux.

Photo-chemistry can also speed up the reaction converting NH_3 to HCN,

$$\begin{aligned}
\mathrm{NH_3} + h\nu &\longrightarrow \mathrm{NH_2} + \mathrm{H} \\
\mathrm{NH_2} + h\nu &\longrightarrow \mathrm{HN} + \mathrm{H} \\
\mathrm{H} + \mathrm{NH} &\longrightarrow \mathrm{H} + \mathrm{H} + \mathrm{N} \\
\mathrm{CH_4} + \mathrm{M} &\longrightarrow \mathrm{CH_3} + \mathrm{H} + \mathrm{M} \\
\mathrm{CH_3} + \mathrm{N} &\longrightarrow \mathrm{HCN} + \mathrm{H_2} \\
2(\mathrm{H} + \mathrm{H} + \mathrm{M} &\longrightarrow \mathrm{H_2} + \mathrm{M}) \\
\textbf{Net} : \mathrm{NH_3} + \mathrm{CH_4} &\longrightarrow \mathrm{HCN} + 3\,\mathrm{H_2},
\end{aligned} \tag{2.38}$$

causing a significant increase in the amount of HCN. On HD 209458b this proceeds to the point where HCN is the second most abundant carbon and nitrogen bearing molecule in the atmosphere, and on HD 189733b it is the most abundant carbon and nitrogen bearing molecule. This reaction also causes the large decrease of NH_3 seen in the upper atmosphere of HD 189733b, compared to models without photochemistry. Although loss processes exist for HCN, the products are normally not very stable, and often form HCN upon their destruction. The result is that destruction reactions are inefficient in regulating HCN's abundance, especially with other pathways forming it fast enough to replenish any loss.

2.4 Exploration of the Chemical Parameters

In this section we perform an initial exploration into the parameter space of the C/O ratio and N/O ratio, and consider how it may effect the detectability of certain species in exoplanet atmospheres. Apart from where stated otherwise, these models use the P-T profile and K_{zz} profile described in Section 2.2.1, the initial atmospheric composition of H_2, CO, OH and NH_3 as described in Section 2.2.4 and the zero-flux boundary conditions from Section 2.2.4. Finally, we use a new P-T profile for HD 209458b (Figure 2.11 that does not contain a thermal inversion to investigate the C/O and N/O ratios that would best fit with new evidence of multiple species on HD 209458b.

2.4.1 The C/O and N/O Ratio

Throughout our previous models we have used a solar composition for the atmospheres of the planets being investigated (Section 2.2.4). However, there is evidence that some hot Jupiters have C/O ratios substantially different from solar values, between $0.05 < C/O < 1$ compared to the solar value of C/O = 0.55 (Madhusudhan et al. 2011, Stevenson et al. 2014). A planet's composition depends on many factors, mainly arising from its formation and migration history. Thus knowledge of the atmospheric composition of a planet can lead to insights into it's past (Öberg et al. 2011, Madhusudhan et al. 2014b, Mordasini et al. 2016). One way of finding an atmosphere's molecular composition is through consideration of the effects that a change in elemental composition would have upon species in that atmosphere.

In this section we independently vary the C/O and N/O ratios for a planet otherwise equivalent to HD 189733b. We investigate the effects that the elemental composition has upon the abundance of a number of species in the atmosphere, how it affects the possibility of detecting some of these species and thus how easily detectable are these changes in composition. We explore a parameter space in which the total amount of carbon and nitrogen can vary between 0.1 and 10 times solar. This corresponds to an atomic C/O ratio varying between 0.055 and 5.5, and an N/O ratio varying between 0.0138 and 1.38. The atomic fraction of oxygen is always kept constant, with the change in carbon or nitrogen abundance being accounted for by an equivalent but opposite change in the total amount of hydrogen. We pick 100 mbar as the pressure being investigated since both emission and transmission spectra are sensitive to the abundance of species at this pressure. These models use the P-T and K_{zz} profile of HD 189733b from Figures 2.1a and 2.1b, which at 0.1 bar corresponds to a temperature of 1200 K and 7×10^5 m^2 s^{-1}.

In Figure 2.7 and 2.8 maps of the abundance of C and O species are shown as a function of atmospheric composition. None of the species show any strong dependence on the amount of

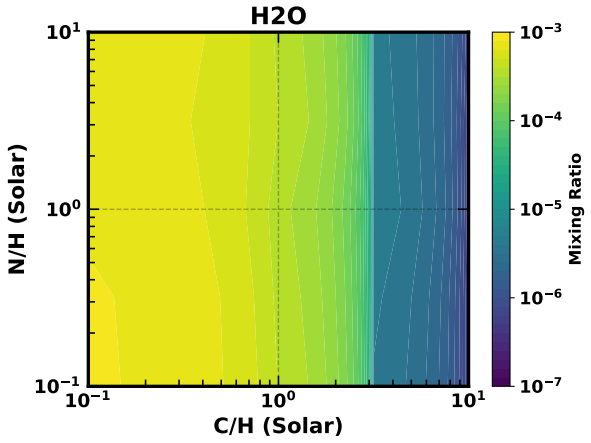

(a)

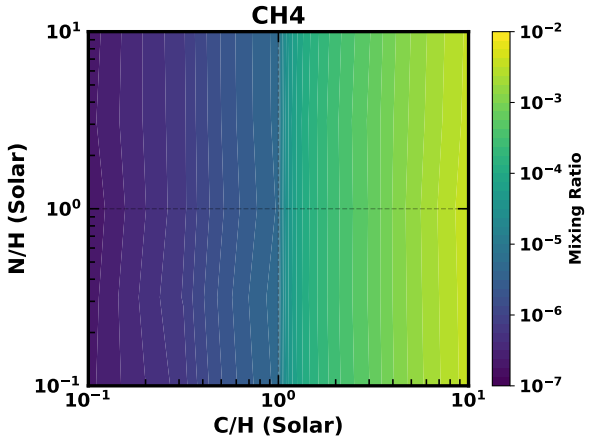

(b)

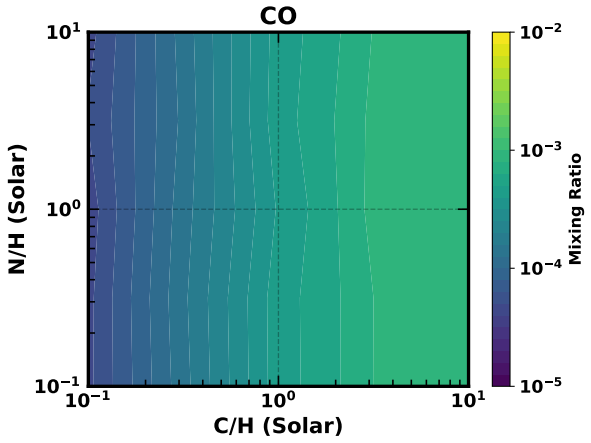

(c)

Fig. 2.7 Abundance variations of H_2O (top), CH_4 (middle) and CO (bottom) on HD 189733b at 0.1 bar for the parameter space in which the amount of nitrogen and carbon in the atmosphere varies between 0.1 and 10 times the solar amount. These models use the P-T and diffusion profile from Figure 2.1a and 2.1b for HD 189733b.

N in the atmosphere. In hydrogen dominated atmospheres, the abundances of H_2O, CH_4 and CO are primarily determined by the equation:

$$CH_4 + H_2O \rightleftharpoons CO + 3\,H_2 \tag{2.39}$$

which at 100 mbar in the atmosphere of HD 189733b favours the formation of CO. At solar C, a C/O ratio of 0.55, this means that CO is the primary carbon carrier and H_2O contains most of the remaining oxygen. Since there is nearly twice as much oxygen as carbon in the atmosphere, CO and H_2O have very similar abundances. For sub-solar carbon, there is less CO, and thus less oxygen bound to CO, resulting in an increase of H_2O. Once C/O > 1 (1.8× solar carbon), oxygen, not carbon, is now the limiting factor in producing CO, and so the abundance of water quickly drops as there is very little oxygen available to form it. Much of the excess carbon ends up in CH_4, resulting in a sharp increase in its abundance. In Figure 2.8a, we can see how CO_2 is also affected indirectly by Equation 2.39; while there is excess oxygen not bound to CO, its abundance is directly related to the amount of carbon, however once C/O > 1, then the majority of the oxygen is bound to CO, and the abundance of CO_2 drops off rapidly. Larger hydrocarbons can also be very strongly affected by the variation in carbon, with the abundance of C_2H_2 changing by more than eight orders of magnitude for only two orders of magnitude change in carbon.

In Figure 2.9 the variation of the three major nitrogen species within the parameter space is shown. The abundance of N_2 has no dependence on carbon, while both NH_3 and HCN do. This is because of the fast reaction,

$$\begin{aligned}
H_2 + M &\longrightarrow H + H + M \\
CH_4 + H &\longrightarrow CH_3 + H_2 \\
H + NH_3 &\longrightarrow NH_2 + H_2 \\
H + NH_2 &\longrightarrow HN + H_2 \\
H + HN &\longrightarrow N + H + H \\
N + CH_3 &\longrightarrow HCN + H_2 \\
\textbf{Net}: NH_3 + CH_4 &\longrightarrow HCN + 3\,H_2,
\end{aligned} \tag{2.40}$$

thus causing the abundance of NH_3 and HCN to have a dependence on the amount of carbon in the atmosphere. This dependence is particularly strong when C/O > 1, since there can now be an excess of CH_4, without it being converted into CO. More CH_4 therefore leads to more NH_3 being converted into HCN. As expected, all the nitrogen species have a strong dependence on the amount of nitrogen in the atmosphere, though HCN has a weaker dependence than the

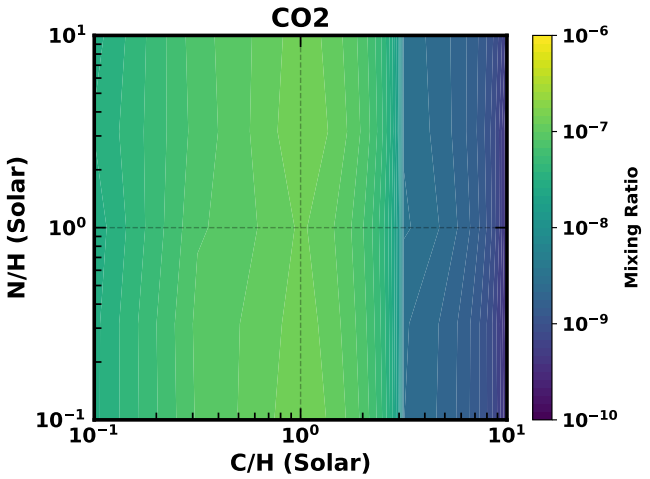

(a)

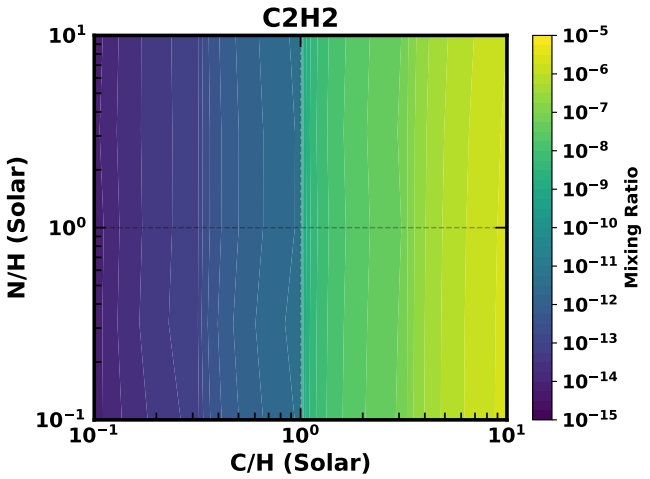

(b)

Fig. 2.8 Abundance variations of CO_2 (top), C_2H_2 (bottom) on HD 189733b at 0.1 bar for the parameter space in which the amount of nitrogen and carbon in the atmosphere varies between 0.1 and 10 times the solar amount. These models use the P-T and diffusion profile from Figure 2.1a and 2.1b for HD 189733b.

others, due to carbon often being the limiting factor for its abundance. Many of these same trends for variation in the C/O ratio are seen in Madhusudhan (2012).

In Figure 2.10, the ratios of NH_3 and HCN to H_2O are shown, since this is what determines the observability of these species in exoplanet atmospheres. Since both NH_3 and H_2O decrease with increasing carbon, the overall increase in NH_3/H_2O is due to the more rapid decrease of H_2O. Having HCN and NH_3 abundances at least 1% that of H_2O is predicted to be needed to detect either of these molecules (MacDonald and Madhusudhan 2017b). Given this, Figure 2.10 suggests that the amount of nitrogen is not very significant in the detection of these species, whereas C/O > 1 is almost always essential. However, exceptionally large amounts of nitrogen in the atmosphere can overcome this and allow detection of HCN and NH_3 at slightly lower C/O ratios, although typically we would not expect much more than five times solar nitrogen in a hot Jupiters atmosphere (Turrini et al. (2021)).

2.4.2 Molecular Detections on HD 209458b

The emission spectra of HD 209458b was initially thought to contain evidence for a thermal inversion in the atmosphere (Knutson et al. 2008), and so far in this work we have modelled it's atmosphere as such to enable validation of the code. More recent studies, however, have found that HD 209458b should not have a thermal inversion (Diamond-Lowe et al. 2014), and it seems valuable for us to examine how this changes the predicted abundance profiles for species in its atmosphere. In addition, recent work in the literature presents evidence of CO, H_2O and HCN in the atmosphere of HD 209458b (Hawker et al. 2018). Hawker et al. (2018) find the best fit mixing abundance of HCN to be 10^{-5}, with a minimum mixing ratio of $10^{-6.5}$. They also find H_2O and CO mixing ratios consistent with previous values of approximately $10^{-5\pm0.5}$ and $10^{-4\pm0.5}$ respectively (Madhusudhan et al. 2014a; MacDonald and Madhusudhan 2017a; Brogi and Line 2019).

In this section we used a model P-T profile for the day-side of HD 209458b, without a thermal inversion (Gandhi and Madhusudhan 2017). For the deep adiabatic region of the atmosphere, above 100 bars, we use the same values as the earlier P-T profile for HD 209458b, translated by 100 K for a smooth connection (Figure 2.11). The same K_{zz} profile and UV flux for HD 209458b from earlier are used, seen in Figure 2.1b and Figure 2.2 respectively.

In Figure 2.12 the chemical abundance profiles for the new P-T profile of HD 209458b are compared with those from the old P-T profile. In the lower atmosphere, where the P-T profile is largely unchanged, there is very little difference between the old and new mixing ratios. In the upper atmosphere the lower temperature of the new P-T profile, due to the lack of a thermal inversion, means that some species that would otherwise be depleted by the higher

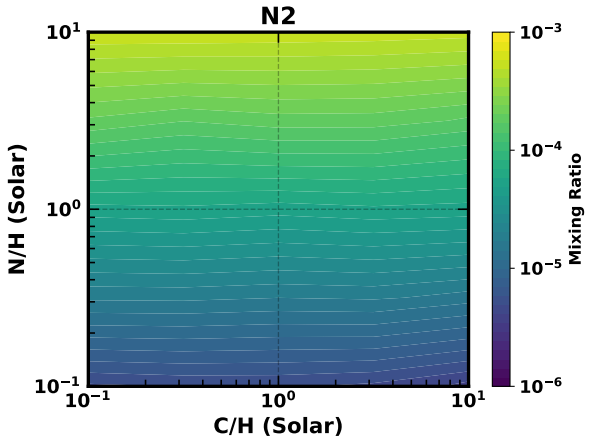

(a)

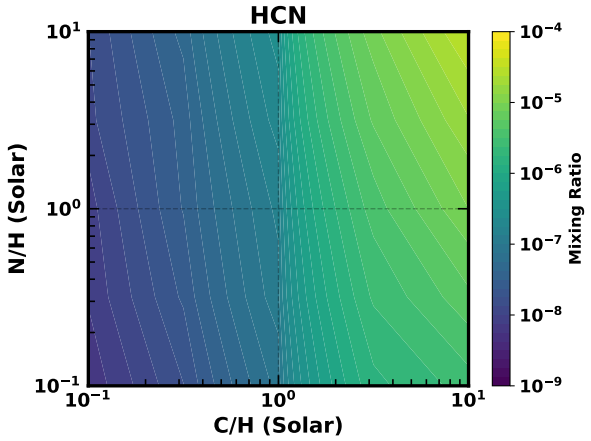

(b)

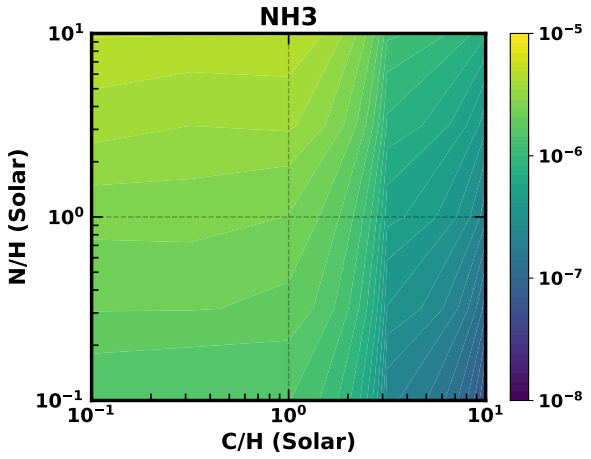

(c)

Fig. 2.9 Abundance variations of N_2 (top), HCN (middle) and NH_3 (bottom) on HD 189733b at 0.1 bar for the parameter space in which the amount of nitrogen and carbon in the atmosphere varies between 0.1 and 10 times the solar amount. These models use the P-T and diffusion profile from Figure 2.1a and 2.1b for HD 189733b.

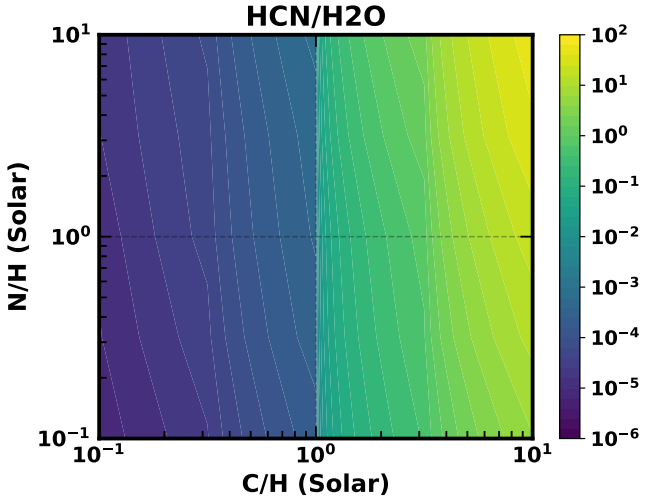

(a)

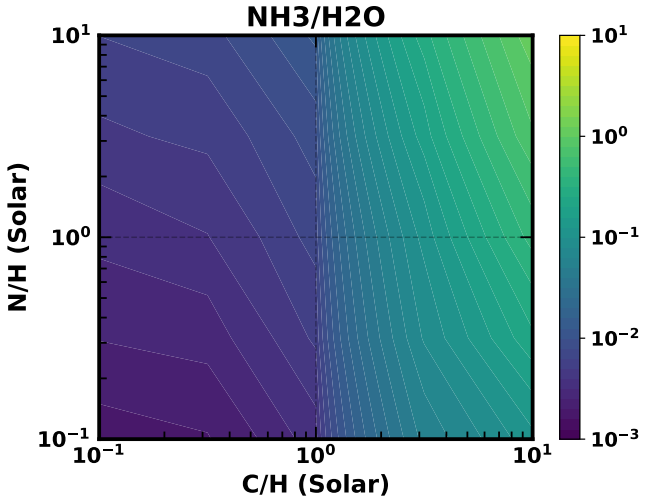

(b)

Fig. 2.10 Variations in the ratio of HCN and NH_3 to H_2O, top and bottom respectively, on HD 189733b at 0.1 bar for the parameter space in which the amount of nitrogen and carbon in the atmosphere varies between 0.1 and 10 times the solar amount. These models use the P-T and diffusion profile from Figure 2.1a and 2.1b for HD 189733b.

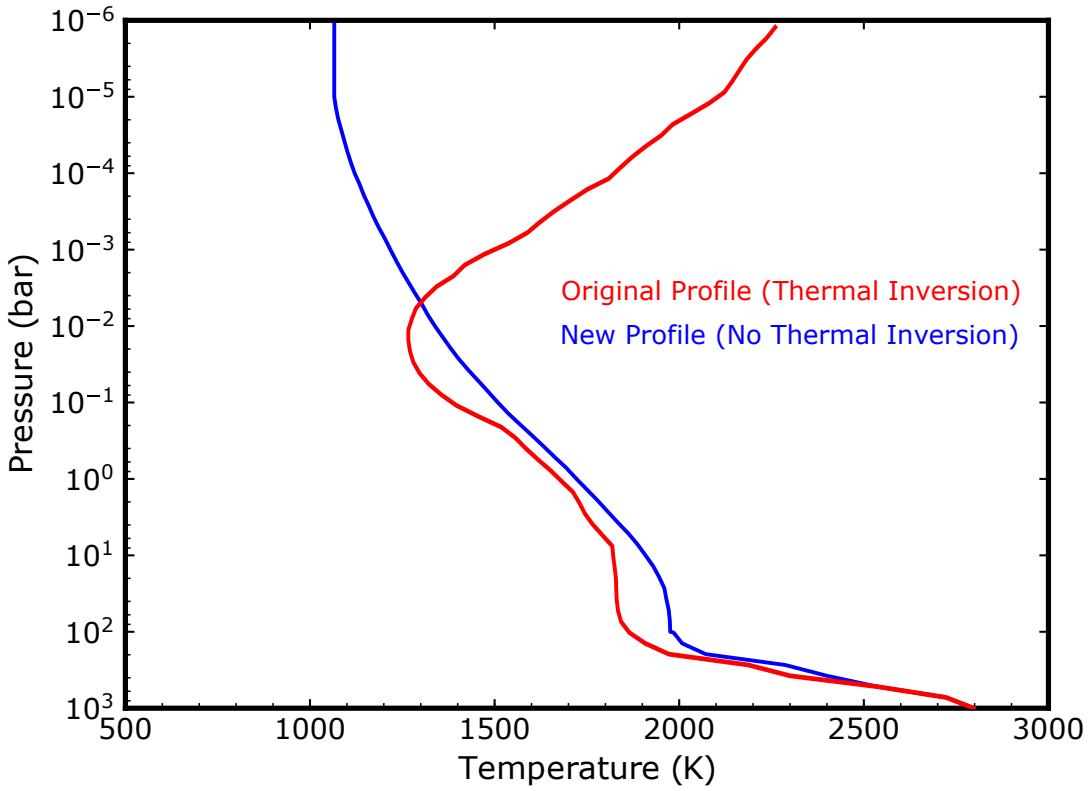

Fig. 2.11 The Pressure-Temperature profile for the average day-side of HD 209458b, with and without a thermal inversion in the atmosphere.

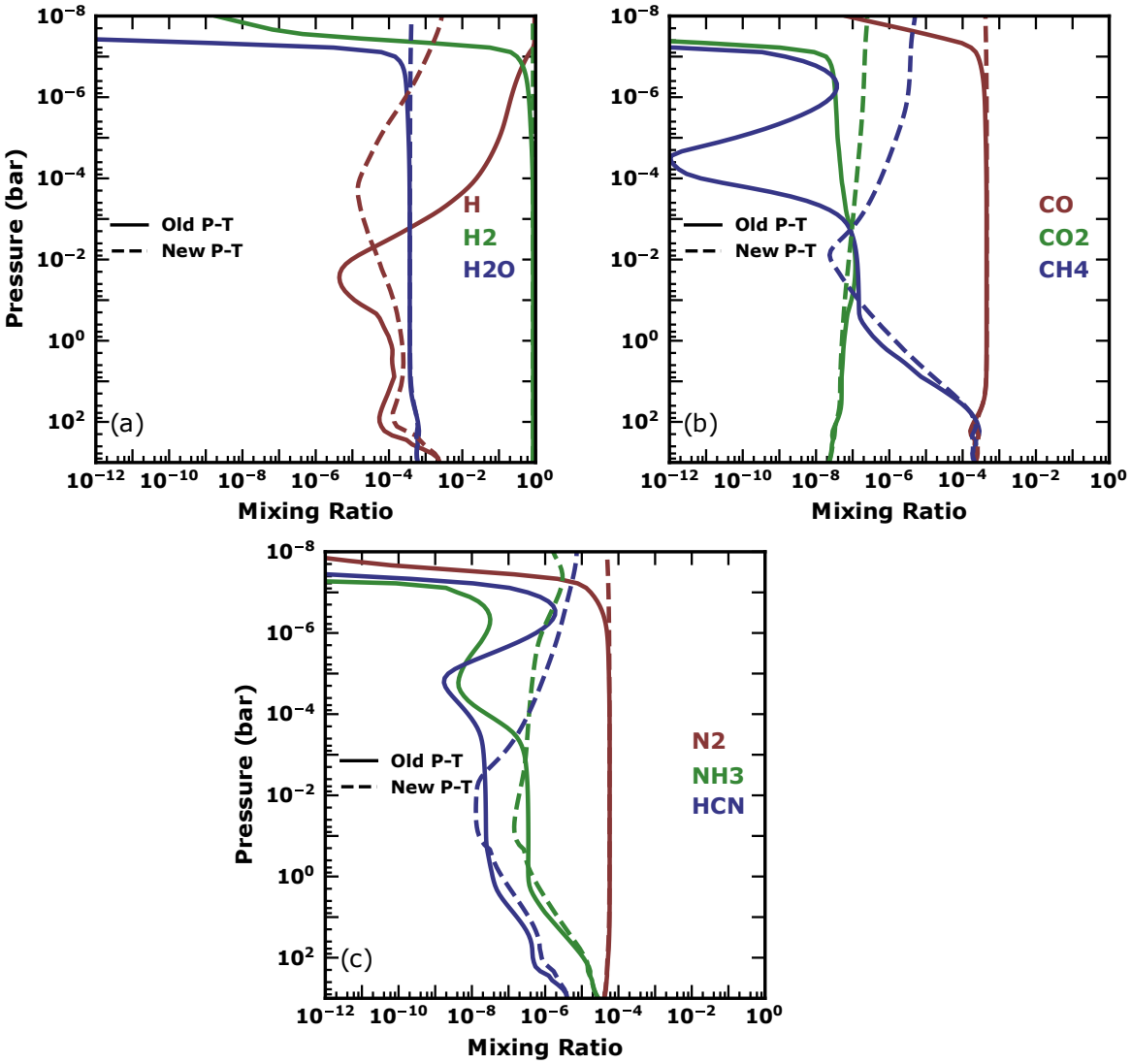

Fig. 2.12 A comparison of the chemistry in the atmosphere of HD 209458b for two temperature profiles. The solid lines use a P-T profile with no thermal inversion, from Figure 2.11, while the dashed lines use a P-T profile with a thermal inversion, from Figure 2.1a

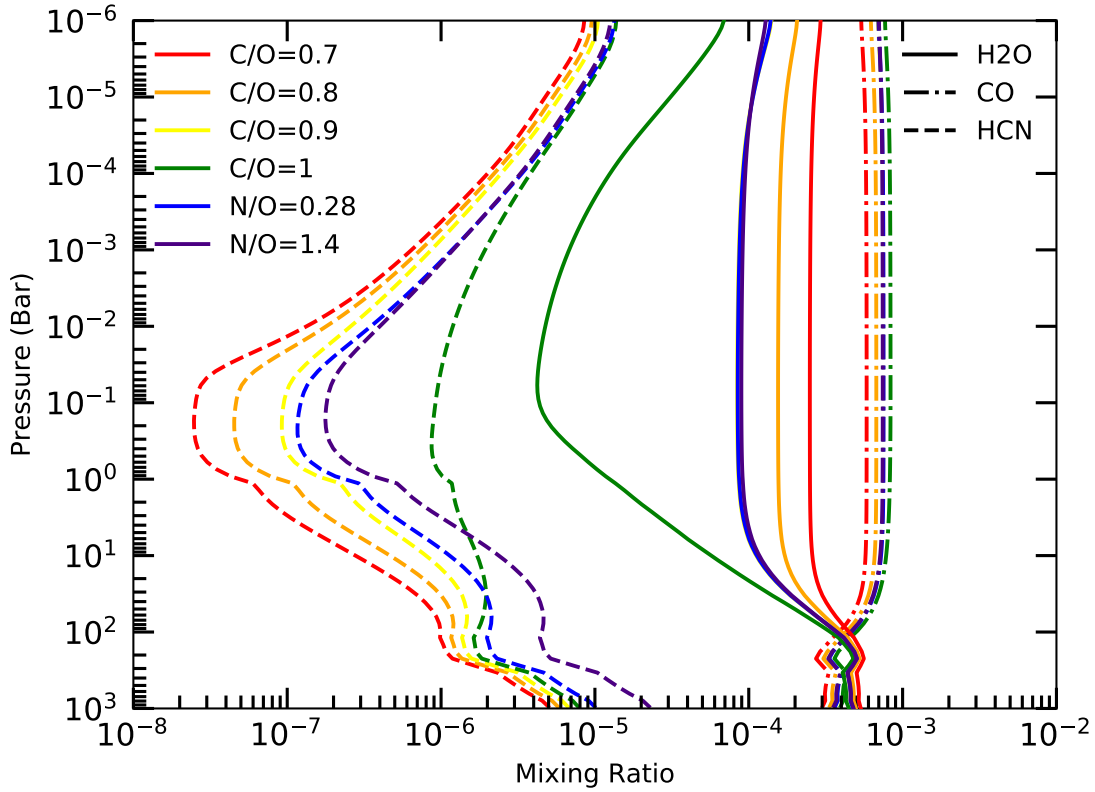

Fig. 2.13 The mixing ratios of CO, HCN and H_2O on HD 209458b, using the P-T profile from Figure 2.11. Each of the molecules are displayed at different C/O and N/O ratios. The C/O ratio is 0.9 for the two N/O ratios shown.

temperatures, such as HCN or CH_4, are present in greater quantities. For HCN and CH_4 this results in an increase in abundance of nearly two orders of magnitude at 10^{-3} bar.

In Figure 2.13 the abundance profiles for CO, HCN and H_2O are displayed for a range of C/O ratios. We can compare the mixing ratios of these species between 10^{-1} and 10^{-3} bar in our models to the estimated abundances from Hawker et al. (2018). The abundance of CO provides little information since across all C/O ratios being modelled it stays at approximately 10^{-3}, consistent with the expected value. HCN provides more information, with a C/O $\gtrsim 0.9$ required to pass the minimum estimated mixing ratio of $10^{-6.5}$, and a C/O = 1.2 (not shown in Figure 2.13) is required for HCN to match the best fit abundance of 10^{-5}. However, H_2O provides an upper limit of C/O ≈ 1; higher C/O than this quickly depletes H_2O below 10^{-6}. As such, it is clear that alterations to the C/O ratio by itself may not be sufficient to explain the observed abundances.

In Figure 2.13 we also included two models in which we increased the N/O ratio by two times (N/O = 0.28) and ten times (N/O=1.4) the solar value, to discover the effect this has on the abundance of these molecules. For these models, we kept C/O = 0.9. Increasing the amount of nitrogen in the atmosphere by two times solar increases the HCN abundance by approximately a third at 10^{-3} bar. Further increases to the amount of nitrogen in the atmosphere do little to the abundance of HCN since the amount of free carbon is the limiting factor beyond this. The N/O ratio has no significant effect on the abundance of either CO or H_2O.

Through comparison of our model and the expected molecular abundances of HD 209458b we can produce some initial constraints for the C/O and N/O ratio of this hot Jupiter: a 0.9 $\lesssim$ C/O $\gtrsim$ 1, and preferentially N/O > 1. However, varying C/O and N/O is not sufficient to match the estimated best fit abundance of HCN, which lies outside the range that these two parameters alone can explore. In particular, there are a number of other important parameters that could and should also be varied, such as the K_{zz} strength, the atmospheric metallicity and the P-T profile. It is expected that increasing K_{zz} and the N/H ratios would assist in increasing the HCN abundance towards the estimated best fit value. This full sweep of parameter space is, however, beyond the scope of this work, but provides a good basis for future investigations.

2.5 Conclusion

In this work, we present a new one-dimensional diffusion and photochemistry code, named LEVI, currently able to model gaseous chemistry in hot Jupiter atmospheres via solving of the continuity equation. We focus on H, C, O and N chemistry, using a chemical network that contains over 1000 reactions and 150 species. Through inputs in the form of a pressure - temperature profile, an eddy diffusion profile and a UV stellar flux, the code can calculate steady state abundance profiles for all species over the desired pressure range.

LEVI was validated against the disequilibrium chemistry models produced by Moses et al. (2011) and Venot et al. (2012); For HD 209458b the abundance profiles of species that LEVI produced matched closely with those of the other two models, with any differences being a consequence of the slightly differing input parameters, such as the elemental abundance distribution and some reaction rate constants. We discussed how the differing P-T profiles of HD 209458b and HD 189733b affected equilibrium chemistry in their atmosphere, and noted that, in pure chemical equilibrium, neither HCN nor NH_3 would be detectable. Eddy-diffusion and photochemistry were also included, and we discussed how they affected the chemistry of the atmospheres, as well as how the chemistry of the two planets atmospheres compared to each other. Of particular note was that the quenching caused by eddy-diffusion is capable of raising the abundance of NH_3 and HCN to potentially detectable levels.

The influence of the parameter space of the C/O and N/O ratio on the abundance of various molecules at 100 mbar in the atmosphere of HD 189733b was investigated. It was found that species that contained C or O were strongly affected by variations in the C/O ratio, while other molecules were weakly affected, if at all. In general, only species that contain nitrogen are affected by changes to the N/O ratio. We also looked at how the fractions NH_3/H_2O and HCN/H_2O varied with the atmospheric composition, an important fraction in determining whether it is possible to detect these molecules. We found that when trying to detect NH_3 or HCN, the quantity of carbon in the atmosphere is much more important than the amount of nitrogen. At a solar N/O ratio, sub-solar carbon would make detecting either of these molecules near impossible, however with at least 5 times solar nitrogen in the atmosphere, NH_3 and HCN could be detected with only 0.5 times and 0.8 times solar carbon respectively. In an atmosphere with a deficit of nitrogen, less than two times solar carbon would make detecting either of these molecules possible.

Recent literature (Diamond-Lowe et al. 2014) has suggested that HD 209458b does not contain a thermal inversion. Other work (Madhusudhan et al. 2014a; MacDonald and Madhusudhan 2017a; Brogi and Line 2019; Hawker et al. 2018) has found evidence for CO, H_2O and HCN with best fit mixing ratios of approximately $10^{-4\pm0.5}$, $10^{-5\pm0.5}$ and 10^{-5} respectively, and with a minimum mixing ratio of HCN at $10^{-6.5}$. We applied our model to HD 209458b,

using a new P-T profile without a thermal inversion, to discover which C/O and N/O ratios could best fit with these observations. A C/O > 1 resulted in a significant depletion of H_2O. To obtain at least the minimum mixing ratio of HCN, a C/O $\gtrsim$ 0.9 was required. A large N/O ratio, ten times solar or more, can help increase the HCN abundance closer to the best fit value, but it results in much smaller increases compared to increasing the C/O ratio. Further testing with both these parameters and others are outside the scope of this work, and have been left for future investigations.

Chapter 3

Molecular Tracers of Planet Formation in the Atmospheres of Hot Jupiters

3.1 Introduction

In this Chapter, we focus on linking the chemical composition of a hot Jupiter's atmosphere to its metallicity, and thus its migration and formation history. To do so, we run a full suite of disequilibrium chemical models over the range of C/H, O/H and N/H ratios expected from planet formation models. In doing so we aim to more accurately link the observed molecular abundances of past and future hot Jupiter observations to the planet's atmospheric composition. Thus we can discover the planet's past evolution, from its formation location to its current position around its host star.

In Section 3.2.1 we provide details of the chemical kinetics code we are using to create our models, as well as the atmospheric parameters of the hot Jupiters we are modelling. We present the results of these models in Section 3.3. In Section 3.4 we discuss the results of our models, and compare them with different formation scenarios from previous works, as well as comparing detections on real hot Jupiters to our models. We discuss our findings and review our work in Section 3.6.

3.2 Methods

3.2.1 The Atmospheric Model

In this work, as in the previous chapter, we will continue to limit our network to exploring the chemistry of H, He, C, N, O species. It is possible that species containing other elements could affect the results produced. In particular, previous studies have discovered sulfur chemistry can have a catalytic effect on CNO chemistry, able to deplete the abundance of molecules such as NH_3, HCN and CH_4 by several orders of magnitude (Zahnle et al. 2016). We explore how sulfur may effect the composition of hot and warm Jupiter atmospheres next chapter. However, the inclusion of these species goes beyond the scope of this chapter's work.

Unlike in the previous chapter, we do not use precalculated K_{zz} profiles, instead we calculate the profile iteratively and self-consistently using the equations described in Zhang and Showman (2017) and Komacek et al. (2019):

$$K_{zz} \sim \frac{W^2}{\tau_{\text{chem}}^{-1} + \frac{W}{H}}, \tag{3.1}$$

where $H = RT/g$ is the scale height of the atmosphere, with R being the gas constant, T being the temperature at the pressure being calculated and g being the gravitational acceleration of the planet. τ_{chem} is the timescale of chemical interactions, and is equal to:

$$\tau_{\text{chem}} = \frac{[X]}{d[X]/dt}, \tag{3.2}$$

where $[X]$ is the abundance of some molecule X, and W is the vertical wind speed, where $\frac{W}{H} \sim \frac{U}{a}$. Here, a is the radius of the planet, and U is the characteristic horizontal wind-speed, defined as

$$U \sim \frac{2\gamma U_{\text{eq}}}{\alpha + \sqrt{\alpha^2 + 4\gamma^2}}, \tag{3.3}$$

where U_{eq} is the speed of the maximum cyclostophic wind, defined as

$$U_{\text{eq}} = \frac{a}{\tau_{\text{adv,eq}}}, \tag{3.4}$$

and the dimensionless parameters α and γ are defined as

$$\alpha = 1 + \frac{\Omega\, \tau_{\text{wave}}^2}{\tau_{\text{rad}}\, \Delta \ln p}, \tag{3.5}$$

$$\gamma = \frac{\tau_{\text{wave}}^2}{\tau_{\text{rad}}\,\tau_{\text{adv,eq}}\,\Delta \ln p}. \tag{3.6}$$

Ω is the planet's rotation rate, set equal to the orbital period in this work since we assume hot Jupiters are always tidally locked. $\Delta \ln p$ is the pressure difference between the pressure of interest and the deep atmosphere, where the day and night temperatures are the same. The timescales in the above equations are: the Kelvin wave propagation time across a hemisphere;

$$\tau_{\text{wave}} = a/NH, \tag{3.7}$$

where N is the Brunt-Väisälä frequency, the radiative timescale;

$$\tau_{\text{rad}} = \frac{p\,c_p}{4\,g\,\sigma\,T^3}, \tag{3.8}$$

where c_p is the specific heat capacity of the atmosphere, and σ is the Stefan-Boltzmann constant. Lastly, the advective timescale that a cyclostrophic wind induced by the day-night temperature difference in radiative equilibrium would have is;

$$\tau_{\text{adv,eq}} = a\sqrt{\frac{2}{R\,k_b\,T_{eq}\,\Delta \ln p}}, \tag{3.9}$$

where k_b is the Boltzmann constant and T_{eq} is the equilibrium temperature of the planet.

We also use a variable parametisation for the P-T profile of the atmosphere using the equations described in Guillot (2010). The temperature of the atmosphere is parametised as;

$$T^4 = \frac{3}{4}T_{\text{int}}^4\left(\frac{2}{3}+\tau\right) + \frac{3}{4}T_{\text{irr}}^4 f\left(\frac{2}{3} + \frac{\mu_*}{\gamma} + \left(\frac{\gamma}{3\,\mu_*} - \frac{\mu_*}{\gamma}\right)\exp\left(-\frac{\gamma\,\tau}{\mu_*}\right)\right). \tag{3.10}$$

Here, $\mu_* = \cos\theta_* = 1/\sqrt{3}$, where θ_* is the incidence angle for radiation, $\gamma = \kappa_{\text{v}}/\kappa_{\text{th}}$ is the ratio between the mean visual (κ_{v}) and thermal (κ_{th}) opacities, and τ is the optical depth. We chose the values for the visual and thermal opacities to be $4\times10^{-3}\,\text{cm}^2\,\text{g}^{-1}$ and $10^{-2}\,\text{cm}^2\,\text{g}^{-1}$ respectively, approximately the values for HD 209458b (Guillot 2010). $f = 1/2$ is a flux factor for isotropic radiation averaged over the day-side of the planet. The interior temperature is set to be $T_{\text{int}} = 300\,\text{K}$ and the irradiation temperature is $T_{\text{irr}} = \sqrt{2}\,T_{\text{eq}}$, where T_{eq} is the equilibrium temperature of the planet. For T_{eq} we assume the planet has an albedo of 0 and efficient energy redistribution.

We use the values for solar metallicity from Asplund et al. (2009). This gives an elemental ratio, as a fraction of the total number of molecules, of: $X_{\text{H}_2} = 0.5\times X_{\text{H}} = 0.8535$, $X_{\text{He}} = 0.145$, $X_{\text{C}} = 4.584\times10^{-4}$, $X_{\text{O}} = 8.359\times10^{-4}$, $X_{\text{N}} = 1.154\times10^{-4}$. In our models, we independently

alter the metallicity between 0.1× and 10× these solar values for each of C, O, N. He is kept constant, and H_2 is altered such that X_{H_2}, X_{He}, X_C, X_O and X_N sum to unity.

The equilibrium temperatures of the modelled hot Jupiters range across five temperatures between 1000 K and 2000 K, although we only show the two extremes in this work. To produce a suite of models over the full range of bulk compositions, we ran our model for each point in a $9 \times 9 \times 9$ grid in the C/H, O/H and N/H parameter space, for each planetary equilibrium temperature being investigated. This produced a total of 729 models per modelled planet, with data points for X/H equally spaced in logspace between 0.1× and 10× the solar values for X/H.

It is worth noting that due to our prescription for K_{zz}, the different equilibrium temperatures of our hot Jupiter models will result in different K_{zz} values. While this masks the exclusive effect of temperature as a variable in setting the chemistry of hot Jupiter atmospheres, our primary aim is to model realistic variations in hot Jupiter atmospheric chemistry due to compositional differences. Therefore, a sweep of orbital radius (and therefore temperature and K_{zz}), explores the range of hot Jupiter atmosphere chemistry for a given composition.

3.2.2 Planet Composition Models

In this section we discuss how different formation and migration mechanisms may lead to different metallicities in the atmosphere of a hot Jupiter. Throughout this work we use metallicity to refer to the full suite of C/H, O/H and N/H ratios. The following formation and migration pathways came from three different works; Madhusudhan et al. (2014a), Booth et al. (2017) and Turrini et al. (2021).

The work of Madhusudhan et al. (2014a) does not consider nitrogen composition, however, they do consider the widest range of formation scenarios of the studies we consider. They model hot Jupiters that formed via core accretion and then migrated via both in-disk and disk-free migration, as well as hot Jupiters that formed via gravitational instability before migrating disk-free. This produces a wide range of potential C/O ratios for a hot Jupiter, based upon its history.

Madhusudhan et al. (2014a) found that hot Jupiters formed by core accretion between 2 AU and 20 AU before undergoing disk migration had $1 < [O/H] < 10$, and $1 < [C/H] < 5$, with a C/O ratio that was always sub-solar. Hot Jupiters that formed by core accretion but then underwent disk-free migration fall into two regimes. Those that formed closer in have slightly super-solar C/H and O/H, up to [C/H] =2 and [O/H]=4, but still sub-solar C/O, while those that formed further away, beyond the CO_2 snowline, had sub-solar C/H and O/H, down to [C/H]=0.6 and [O/H]=0.4, but a super-solar C/O ratio. Lastly, planets that formed beyond the CO_2 snowline but within the CO snowline by gravitational instability and then migrated inwards also tend

a (AU)	[C/H]	[O/H]	[N/H]
5	0.93	1.06	1.02
12	1.33	1.28	1.09
19	1.77	1.85	1.35
50	3.23	3.70	1.89
100	4.67	5.19	2.43
130	7.33	8.33	3.65

Table 3.1 A summary of the expected bulk compositions of a hot Jupiter from Turrini et al. (2021). The planet starts migrating from 6 different formation locations, accreting solids as it travels inwards until its final position at 0.04AU.

to have either super-solar metallicity but a sub-solar C/O ratio or sub-solar metallicity with a super-solar C/O ratio. However, if they formed beyond the CO snowline, beyond ∼100 AU, they can be any metallicity within our parameter space, but at a solar C/O ratio.

The work of Booth et al. (2017) also does not consider nitrogen in their models. However, their models of chemical enrichment by pebble drift result in compositions in regions of the parameter space that were forbidden by previous works. Through the accretion of metal rich gas the composition of a gas giant could end up with a [C/H] ratio up to 5, and a C/O ratio between solar and 1. For Jupiters forming within the CO_2 snowline, they tend to find metallicities of [O/H] = 2 and between 2 < [C/H] < 3, thus producing super-solar C/O ratios in these high metallicity planets. For planets forming beyond the CO_2 snowline, most formation locations result in a C/O ratio of 1, along the entire parameter space of metallicities.

Turrini et al. (2021) do not consider as wide a range of migration routes as the previous works we have compared to, but they do include the nitrogen in their models as a possible way of breaking the degeneracy arising from the consideration of only the C/O ratio. They consider 6 different formation locations for a hot Jupiter that forms via core accretion and subsequently migrates through the disk to an orbital radius of 0.04 AU, accreting solids along the way. How these formation locations relate to the atmospheric C/H, O/H and N/H ratios compared to their solar values is summarised in Table 3.1. While we acknowledge that our planetary models orbit at slightly wider radii (between 0.08 AU and 0.3 AU) compared to the 0.04 AU in the work of Turrini et al. (2021), we assume that any change in the atmospheric composition due to these small differences in migration distance will be sufficiently small to ignore.

A summary of the different metallicities expected from these formation models can be seen in Figure 3.1.

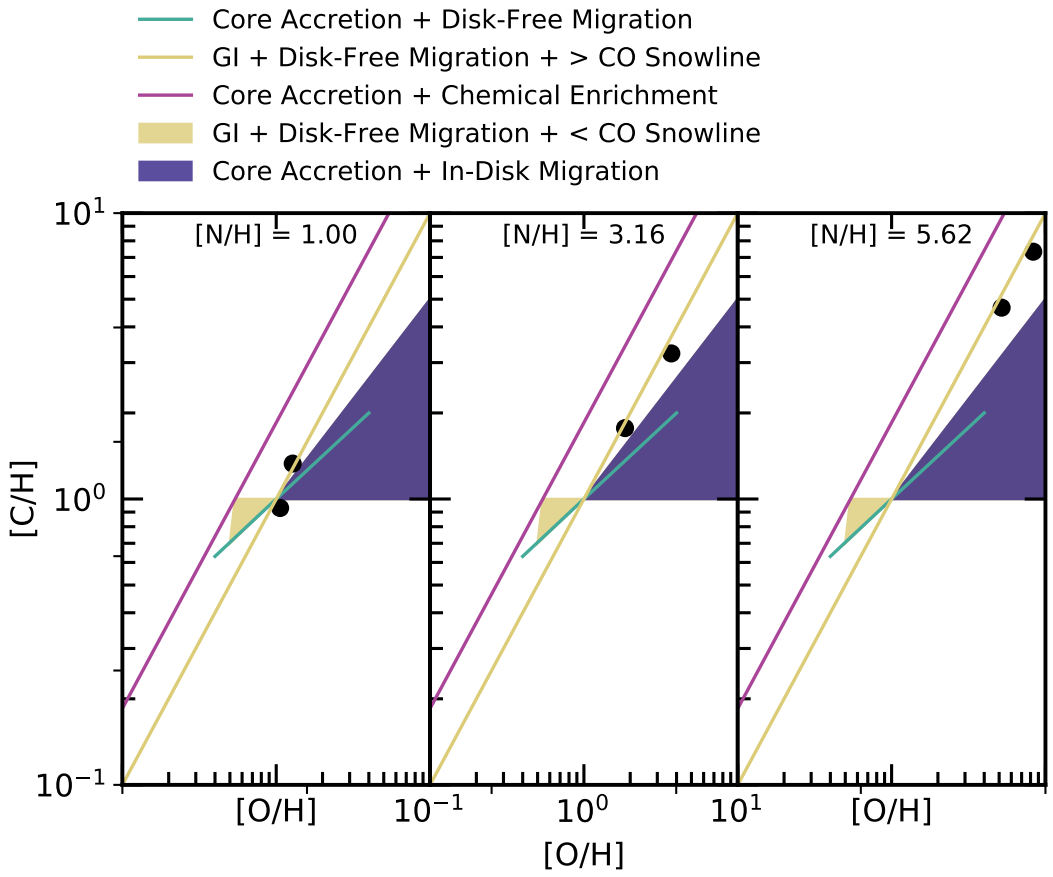

Fig. 3.1 The different ranges of metallicities expected from several formation models. The red, blue and green lines cover the core accretion and gravitational instability models from Madhusudhan et al. (2014a), the purple lines covers the pebble accretion and enrichment models from Booth et al. (2017), and the black dots are the metallicities expected from the six formation locations for core accretion in Turrini et al. (2021). Gravitational instability from within the CO snowline also covers the entire metallicity range of core accretion with in-disk migration, but can't be easily seen due to overlap.

3.3 Model Results

In this section we present the results of our suite of chemical models. We compute models over a grid of C/H, O/H and N/H ratios for two hot Jupiters. We discuss example hot Jupiters at two equilibrium temperatures; 1000 K and 2000 K. These planets correspond to an orbital radius of 0.3 AU and 0.08 AU around a Sun-like star respectively, assuming an albedo of 0 and efficient energy redistribution. We show the resultant P-T profiles for these planets in Figure 3.2 and the K_{zz} profiles in Figure 3.3.

We show our results in Figures 3.4 - 3.9 presented below. In these figures, we show the C/O ratios of 0.25, 0.54 (solar) and 1 as lines on the figure to assist in determining the abundances at these values. Additionally, we split each figure into three regimes; abundances above 10^{-6} which should be detectable, abundances between 10^{-6} and 10^{-10} which we may one day be able to detect and abundances below 10^{-10} which we never expect to be detectable (Greene et al. 2016). All these results are shown for a pressure of 10^{-3} bar, the pressure at which observations of the molecules we model are sensitive to in hot Jupiter atmospheres (Madhusudhan 2019). Throughout this section we use the convention that X/H refers to the absolute value, while [X/H] refers to a value normalised to solar.

3.3.1 H_2O Abundance

In Figure 3.4 we show how the abundance of water varies over our chosen parameter space. Water's abundance is primarily determined by O/H, however for C/O ratio values greater than 1, a decrease in the abundance of water can be seen (Madhusudhan 2012; Moses et al. 2013). This is because water does have a weak dependence on the C/H ratio; as the C/O ratio approaches 1, the fraction of O in CO becomes increasingly significant, leaving less O to form H_2O. While C/O < 1, we see a range in H_2O abundances between 10^{-5} at [O/H] = 0.1 and 10^{-2} at [O/H] = 10 for both temperature models. For C/O ratios greater than 1, the H_2O abundance on the 1000 K hot Jupiter slowly decreases down to 10^{-6} as the C/O ratio increases, while on the 2000 K hot Jupiter, the H_2O drops by several orders of magnitude immediately.

For planets with a C/O ratio close to 1, H_2O is a good measure of the C/O ratio in our two hot Jupiter models. This is because H_2O becomes increasingly dependent on the C/O ratio once the ratio approaches or exceeds 1. However, for C/O ratios that exceed 1, H_2O would cease to be a useful tool for analysis in our 2000K model as its abundance would drop below detectable limits. At C/O ratios less than 0.25, the H_2O abundance tends to depend only on the O/H ratio, becoming a worse measure of the C/O ratio. As expected for H_2O, it is independent of the N/H ratio. There are no N-bearing species that contain O that are of sufficient abundance to impact the sequestration of O in H_2O. Thus, H_2O has no use in determining the N/H ratio.

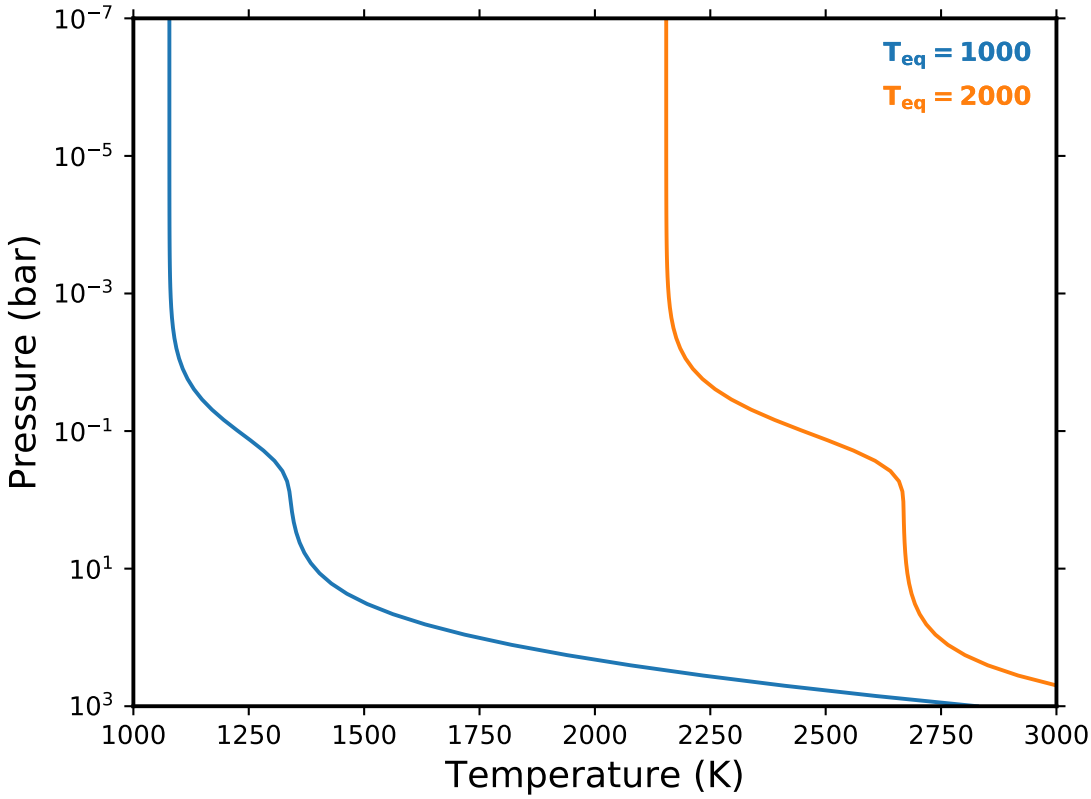

Fig. 3.2 The P-T profiles being used in this work. Both were created using the expression presented in Section 3.2.1, with an equilibrium temperature of 1000 K or 2000 K.

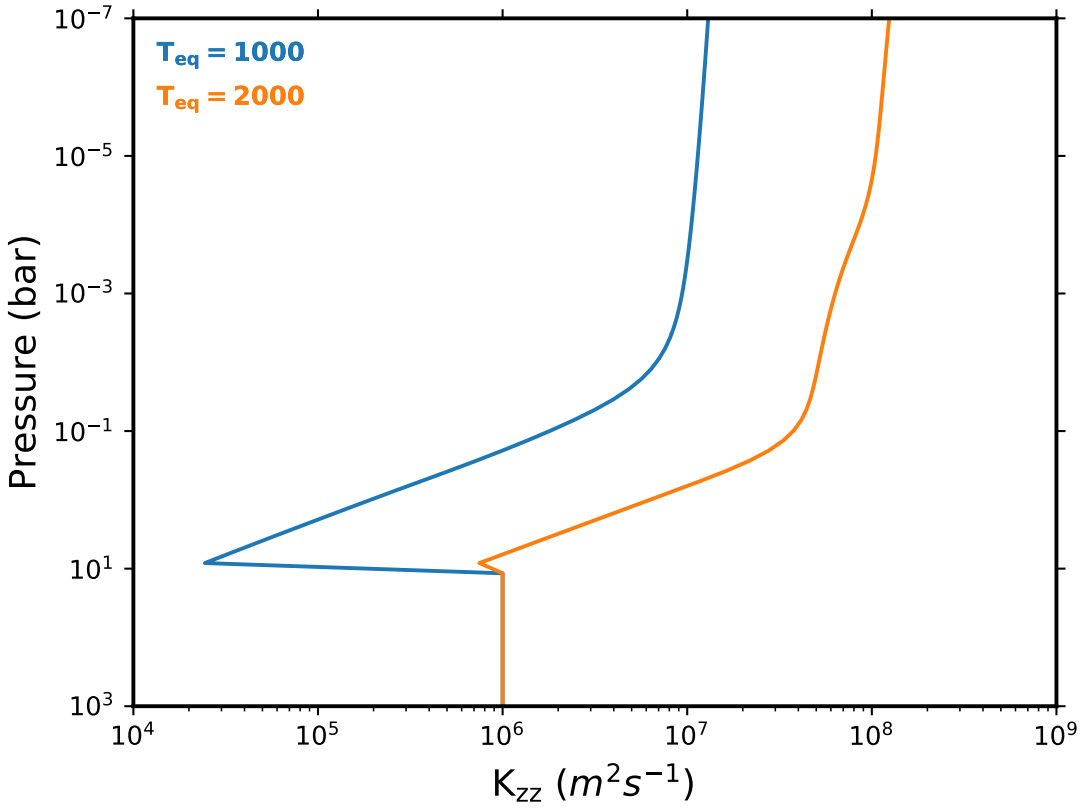

Fig. 3.3 The K_{zz} profiles being used in this work. Both were created using the expression presented in Section 3.2.1, with an equilibrium temperature of 1000 K or 2000 K.

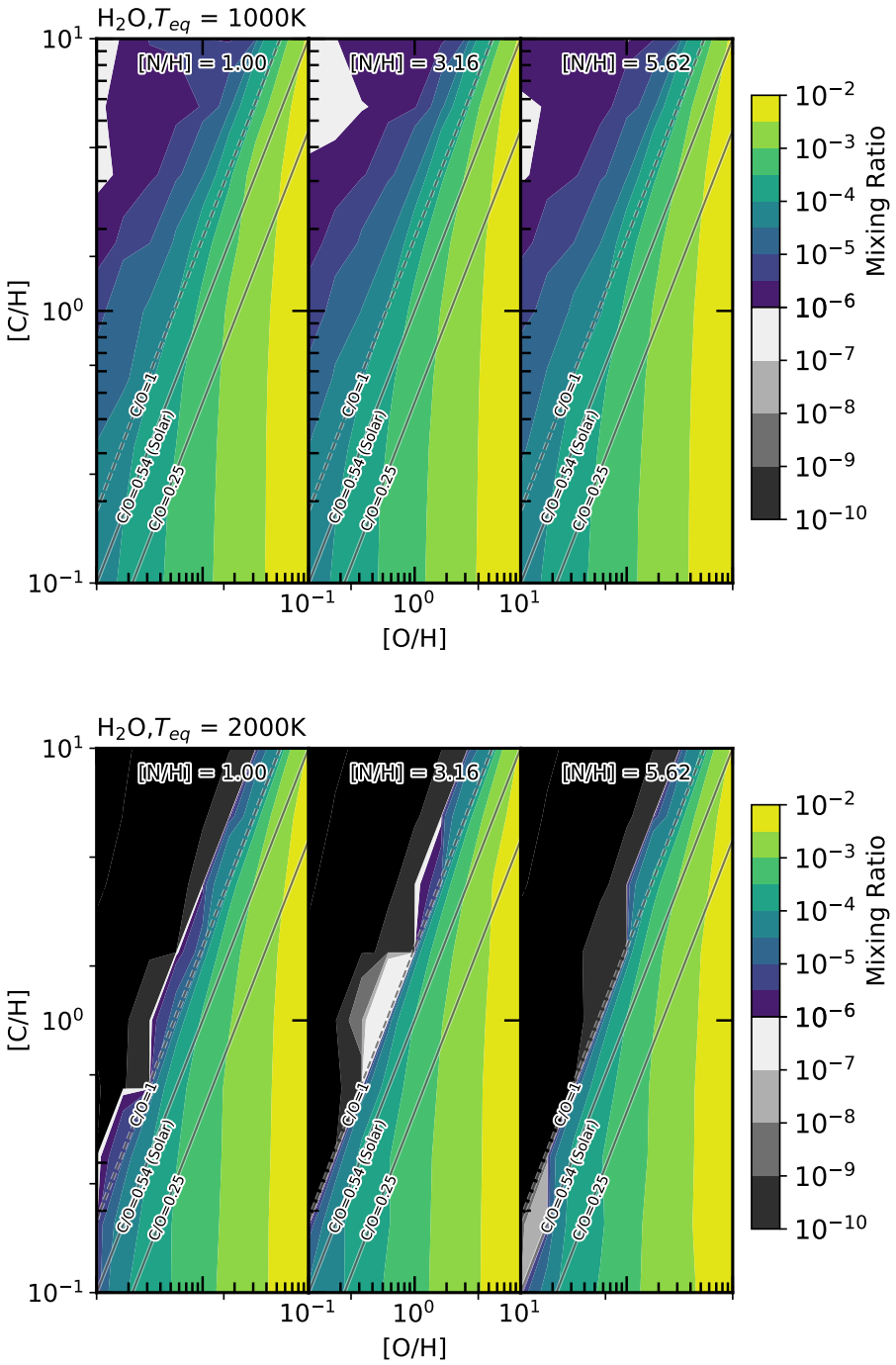

Fig. 3.4 The abundance of H_2O for two hot Jupiters, one with a 1000 K equilibrium temperature (top) and one with a 2000 K equilibrium temperature (bottom). The variation in abundance of H_2O is shown against the atmospheric C/H and O/H ratios normalised to solar values. The C/O ratios of 0.25, 0.54 (solar) and 1 are shown on each plot to assist visualisation. Additionally, we consider three atmospheric N/H ratios normalised to solar; 1, 3.2 and 5.6. These are shown from left to right on the figures above.

3.3.2 CO Abundance

Figure 3.5 shows how the abundance of CO varies across the composition parameter space. CO is directly dependent upon both the O/H and C/H ratios. However, the way it is dependent can be quite useful for determining planetary composition. For a C/O ratio less than 1, the CO abundance is near independent of the O/H ratio, while for a C/O ratio greater than 1, the CO abundance is near independent of the C/H ratio. This is because for C/O < 1, CO is the primary carbon carrier, and as long as there is more oxygen than carbon, increasing the amount of oxygen does not assist in creating more CO. This relationship is reversed for ratios of C/O > 1. Since there are very few formation models that result in a C/O > 1, we can see that CO provides a good measure of the C/H ratio, especially considering that it is predicted to be one of the most abundant species in hot Jupiter atmospheres. In our modelled atmospheres, we find that the abundance of CO varies between 10^{-5} for [O/H] = 0.1 and [C/H] = 0.1, and 10^{-2} for [O/H] = 10 and [C/H] = 10. Once again, we see little effect of the N/H ratio on the abundance of CO. While molecules like HCN could theoretically take more of the available carbon as the N/H ratio increases, we find that even with [N/H] = 10, the HCN abundance is still a small fraction of the CO abundance and thus doesn't diminish the atmospheric CO reservoir in any significant way.

3.3.3 CH_4 Abundance

The variation in the methane abundance across our parameter space is shown in Figure 3.6. We find CH_4 has a positive dependence upon the C/H ratio and a negative dependence upon the O/H ratio for the two hot Jupiters we model. This is due to CO sequestering a greater fraction of the carbon as the amount of available O in the atmosphere increases. Unlike H_2O and CO, methane's abundance also has a strong temperature dependence. At 1000 K, CH_4 has a maximal abundance of 10^{-2} in the high C/H, low O/H regime, with a minimal abundance of 10^{-8} in the low C/H, high O/H regime. By comparison, at 2000 K, the maximum and minimum abundance of methane is 10^{-6} and 10^{-16} respectively. Methane's abundance is approximately unchanging along lines of constant C/O ratio, making it an excellent check to confirm the values of the C/O first expected by examining CO and H_2O. However, it will likely be impossible to detect CH_4 on the hotter hot Jupiters; in our 2000 K model, for a C/O < 1, methane's abundance is typically below 10^{-9}. This is far below the estimates we have for the detectable limits of molecules. The strong dependence of the CH_4 abundance on temperature does make it a good proxy for the temperature, but a poor tool for examining the metallicity of the very hot Jupiters.

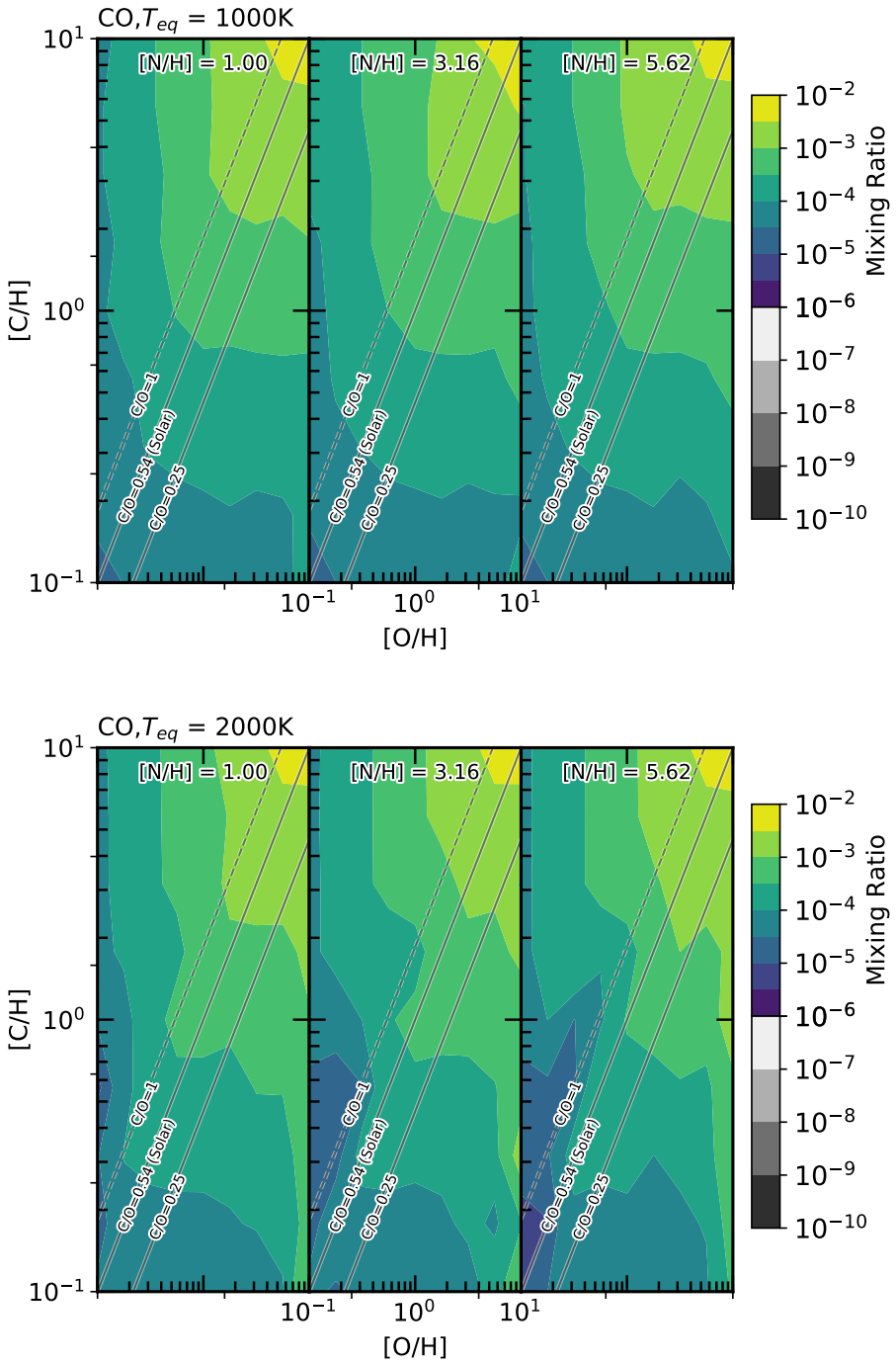

Fig. 3.5 The abundance of CO for two hot Jupiters, one with a 1000 K equilibrium temperature (top) and one with a 2000 K equilibrium temperature (bottom). The variation in abundance of CO is shown against the atmospheric C/H and O/H ratios normalised to solar values. The C/O ratios of 0.25, 0.54 (solar) and 1 are shown on each plot to assist visualisation. Additionally, we consider three atmospheric N/H ratios normalised to solar; 1, 3.2 and 5.6. These are shown from left to right on the figures above.

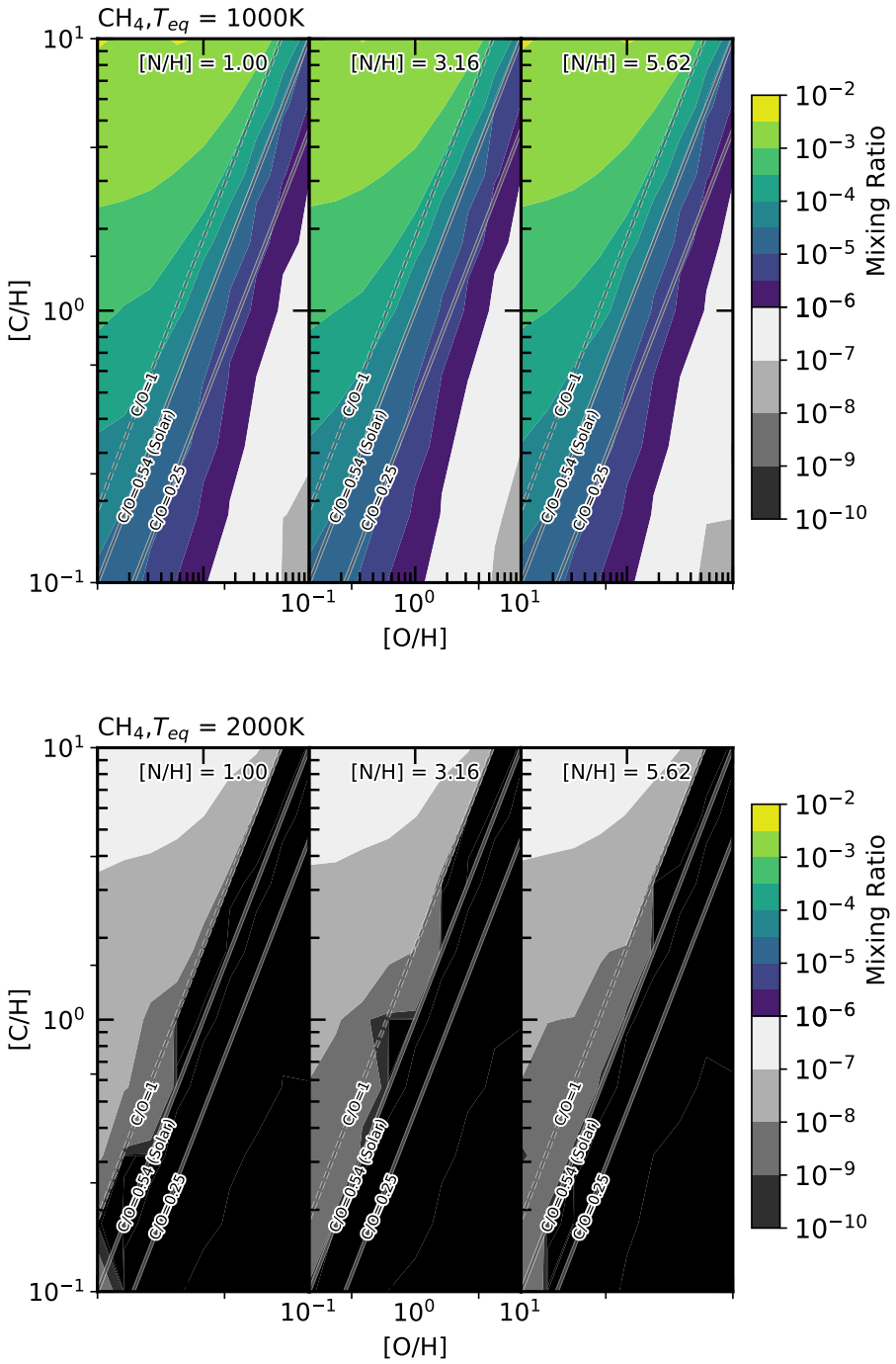

Fig. 3.6 The abundance of CH_4 for two hot Jupiters, one with a 1000 K equilibrium temperature (top) and one with a 2000 K equilibrium temperature (bottom). The variation in abundance of CH_4 is shown against the atmospheric C/H and O/H ratios normalised to solar values. The C/O ratios of 0.25, 0.54 (solar) and 1 are shown on each plot to assist visualisation. Additionally, we consider three atmospheric N/H ratios normalised to solar; 1, 3.2 and 5.6. These are shown from left to right on the figures above.

3.3.4 CO_2 Abundance

We show the range of CO_2 abundances in Figure 3.7. We find that CO_2 is very strongly dependent on the O/H ratio, but only weakly dependent on the C/H ratio in our models. However, there is a significant decrease in CO_2 abundance when the C/O ratio crosses from less than 1 to greater than 1. This is because the majority of the oxygen is sequestered the form of CO, leaving little for other oxygen bearing species. The range of CO_2 abundances in both temperature cases are similar for C/O ratios less than 1, ranging between 10^{-9} and 10^{-4}. Though for C/O > 1, CO_2 follows a similar pattern to H_2O, for T_{eq} = 2000 K there is a rapid decline in abundance as the C/O ratio increases, while for T_{eq} = 1000 K the decline is much slower. CO_2 is a poor diagnostic tool by itself, with a large range of both C/H and O/H ratios corresponding to a single abundance.

3.3.5 HCN Abundance

In Figure 3.8 we present the range of HCN abundances across our parameter space. Unlike in the previous figures in this section, we have replaced the O/H ratio on the x-axis with the N/H ratio, with three values for the O/H ratio chosen to examine. As expected, HCN is strongly dependent on both the C/H and N/H ratios at the temperatues we model. While some dependence on the O/H ratio is also observed, this is merely an artifact of the O/H ratio affecting the overall C/O ratio.

We see a rapid increase in the abundance of HCN in the atmosphere for C/O ratios greater than 1. This is because the most abundant carbon carrier, CO, is no longer limited by the available carbon in the atmosphere, but by the available oxygen at these ratios. Thus, additional HCN can form due to the excess carbon available. Both planetary temperatures modelled have similar maximum abundances for HCN, at around 10^{-4}, at 10 [N/H] and C/O $\ll$ 1. For C/O less than 1, we find that for lower temperatures we expect HCN abundances around 10^{-7}. For the hotter temperatures the HCN abundance is much lower, around 10^{-11}. The HCN abundance can function as a way of tracing the N/H ratio, however, for C/O < 1, highly sensitive measurements will be needed to detect such a low abundance.

3.3.6 NH_3 Abundance

In Figure 3.9 we present how the NH_3 abundance varies across our parameter space. As expected, NH_3 is dependent on the N/H ratio. We find that NH_3 is also dependent on the C/H and O/H ratio to a small extent, however this is mainly a function of the global C/O ratio, not the individual ratios themselves. Where the C/O ratio is greater than 1, we see large abundances

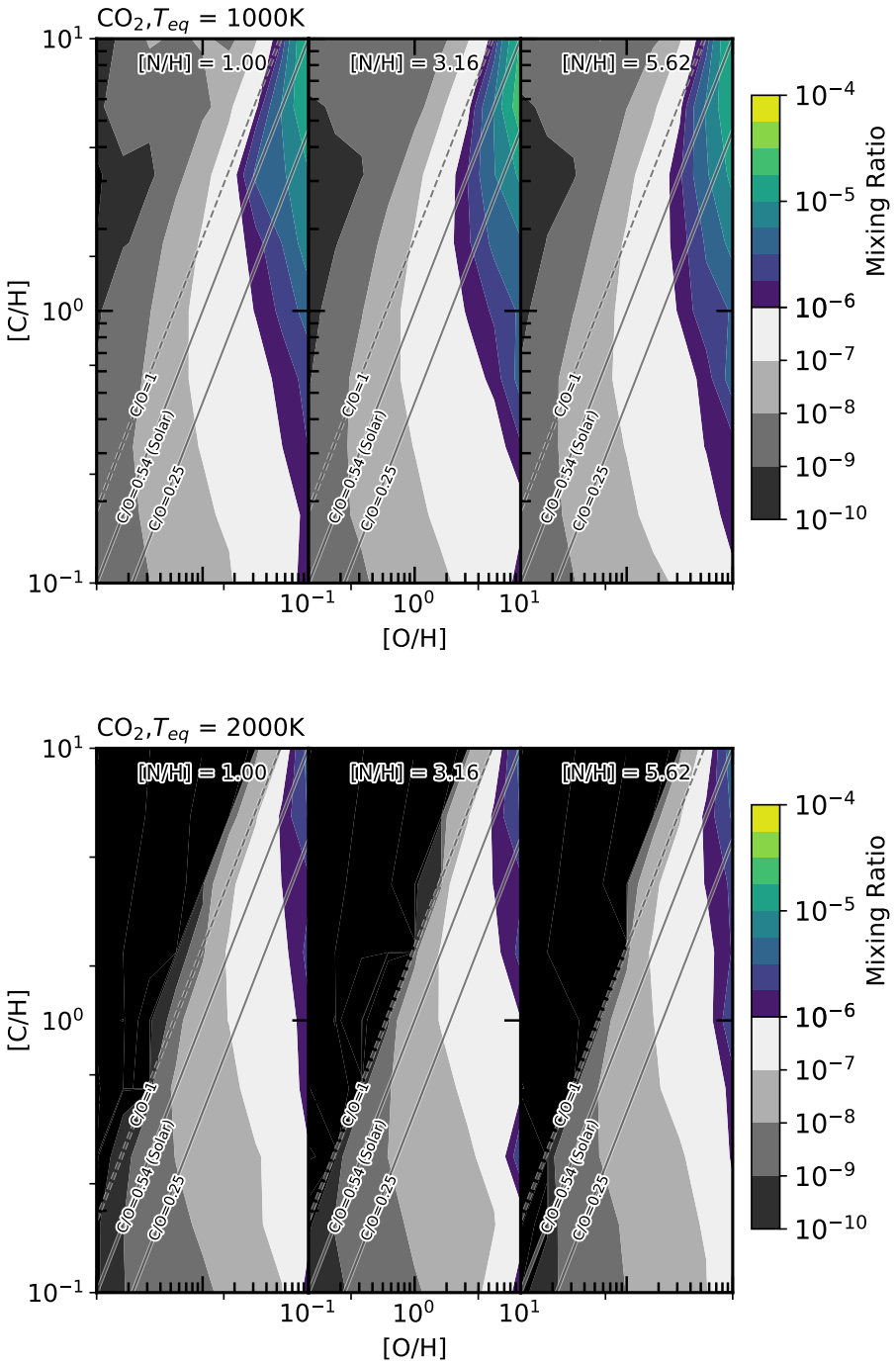

Fig. 3.7 The abundance of CO_2 for two hot Jupiters, one with a 1000 K equilibrium temperature (top) and one with a 2000 K equilibrium temperature (bottom). The variation in abundance of CO_2 is shown against the atmospheric C/H and O/H ratios normalised to solar values. The C/O ratios of 0.25, 0.54 (solar) and 1 are shown on each plot to assist visualisation. Additionally, we consider three atmospheric N/H ratios normalised to solar; 1, 3.2 and 5.6. These are shown from left to right on the figures above.

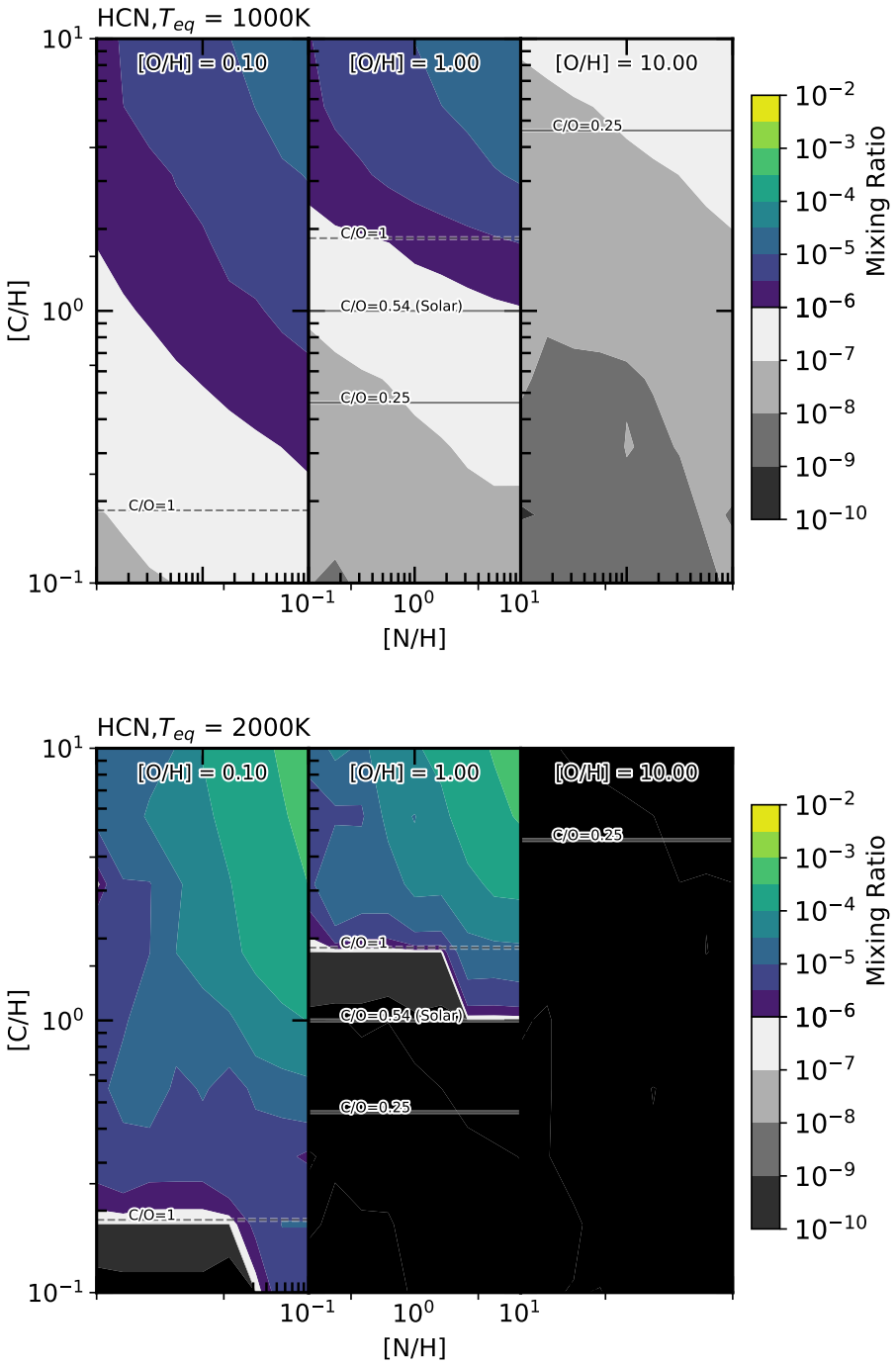

Fig. 3.8 The abundance of HCN for two hot Jupiters, one with a 1000 K equilibrium temperature (top) and one with a 2000 K equilibrium temperature (bottom). The variation in abundance of HCN is shown against the atmospheric C/H and N/H ratios normalised to solar values. The C/O ratios of 0.25, 0.54 (solar) and 1 are shown on each plot to assist visualisation. Additionally, we consider three atmospheric O/H ratios normalised to solar; 0.1, 1 and 10. These are shown from left to right on the figures above.

of HCN, limiting the amount of available N to form NH_3. We also see large differences in ammonia abundance between the two temperature models. At lower temperatures, with C/O < 1, the ammonia abundance varies between 10^{-5} and 10^{-4}. While in our higher temperature model we find approximately five orders of magnitude less ammonia in the atmosphere, between 10^{-10} and 10^{-9} for C/O < 1. The abundance of NH_3 is a useful tool to determine the N/H ratio for cooler planets, as long as sufficiently sensitive measurements to detect it in the atmosphere can take place.

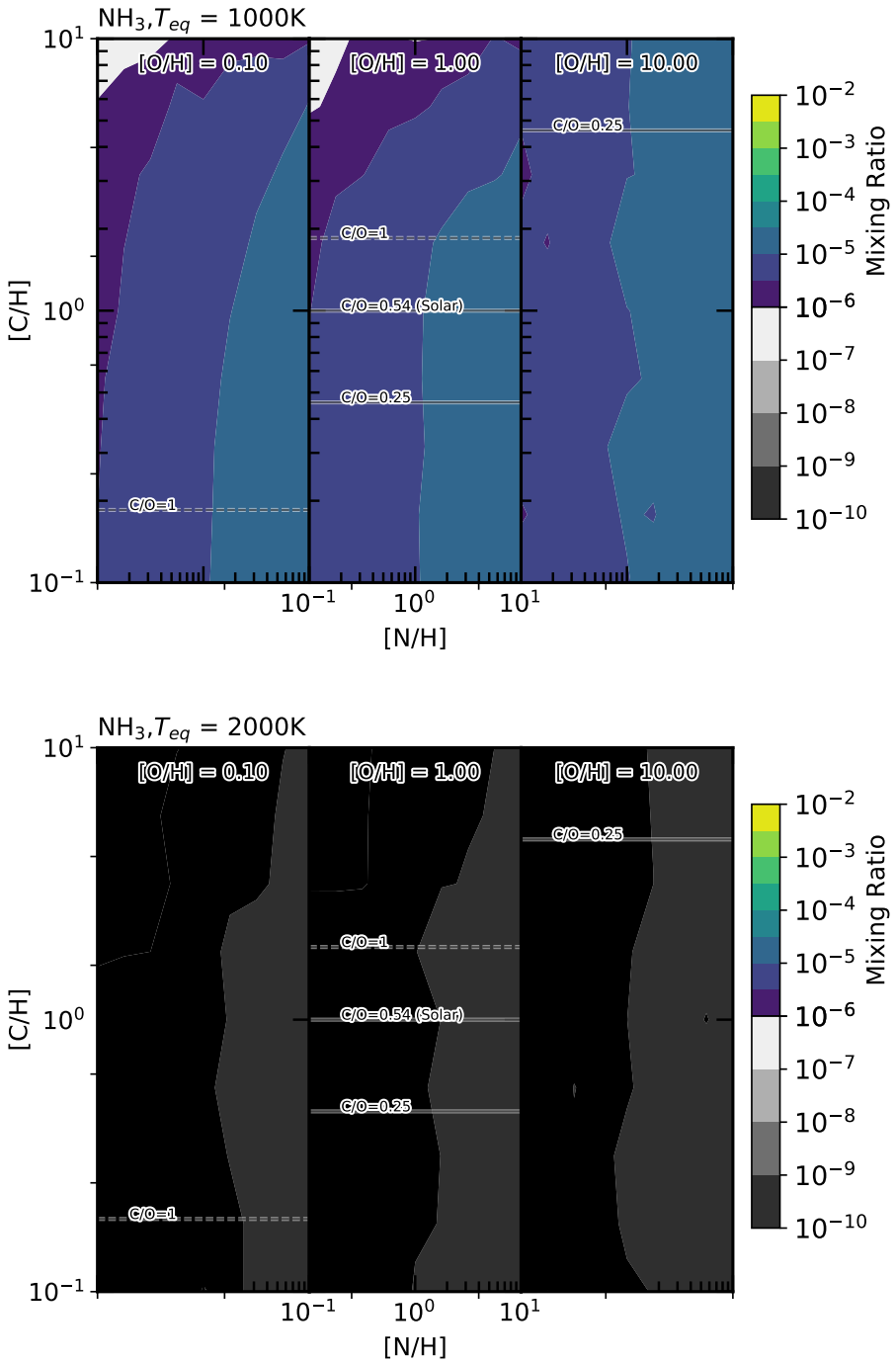

Fig. 3.9 The abundance of NH_3 for two hot Jupiters, one with a 1000 K equilibrium temperature (top) and one with a 2000 K equilibrium temperature (bottom). The variation in abundance of NH_3 is shown against the atmospheric C/H and N/H ratios normalised to solar values. The C/O ratios of 0.25, 0.54 (solar) and 1 are shown on each plot to assist visualisation. Additionally, we consider three atmospheric O/H ratios normalised to solar; 0.1, 1 and 10. These are shown from left to right on the figures above.

Molecule	$\log(X_{\mathrm{Max}}, X_{\mathrm{Min}})$, 1000 K	$\log(X_{\mathrm{Max}}, X_{\mathrm{Min}})$, 2000 K
H_2O	(-2, -3.3)	(-2, -4)
CO	(-2.2, -3.2)	(-2, -3.3)
CH_4	(-5, -6)	(-13, -14)
CO_2	(-4, -7)	(-5, -7)
HCN	(-7, -8)	(-10, -12)
NH_3	(-4.3, -5.3)	(-9.3, -10.3)

Table 3.2 The expected abundances for six molecules in the atmospheres of two hot Jupiters, one with $T_{eq} = 1000$ K and the other with $T_{eq} = 2000$ K, for a gas giant formed by core accretion that migrated within the disk, or a gas giant formed by gravitational instability between the CO_2 and CO snowline that migrated disk-free, from the work of Madhusudhan et al. (2014a).

3.4 Comparison with Formation and Migration Models

In this section we use our results from the previous section in conjunction with the formation models of previous works (Madhusudhan et al. 2014a; Booth et al. 2017; Turrini et al. 2021). We compare the metallicity ranges these works predict for different formation and migration models to the parameter figure in the previous section. This gives us an abundance range, for each of the six molecules investigated previously, for each formation and migration model. Thus we can define what our model predicts the atmospheric composition of a hot Jupiter will be based upon where the planet formed and how it migrated.

3.4.1 Planetary Carbon and Oxygen Abundances due to Migration

From the work of Madhusudhan et al. (2014a), we first look at the migration mechanism of a hot Jupiter formed via core accretion with subsequent disk migration to its current location. This migration pathway leads to expected [C/H] ratios between 1 and 5, and [O/H] ratios between 1 and 10, and that the C/O ratio is always less than solar. In Table 3.2 we show the range of expected chemical abundances of the six molecules we investigated in the previous section for this elemental parameter space.

We split planets formed by core accretion that then underwent disk-free migration into two groups: those that formed beyond the CO_2 snowline, with sub-solar C/H and O/H and those that formed within the CO_2 snowline, with super-solar C/H and O/H. From Madhusudhan et al. (2014a), planets that formed within the CO_2 snowline, have allowed metallicities along the straight line between [C/H] and [O/H] equal to 1, and [C/H] = 2 and [O/H] = 4, and planets that formed beyond the CO_2 snowline have allowed metallicities along the straight line between [C/H] and [O/H] equal to 1, and [C/H] = 0.6 and [O/H] = 0.4. Madhusudhan et al. (2014a) did

Molecule	1000 K	2000 K
Within the CO_2 snowline	$\log(X_{\rm Max}, X_{\rm Min})$	$\log(X_{\rm Max}, X_{\rm Min})$
H_2O	(-2.3, -3.3)	(-2, -4)
CO	(-3, -3.2)	(-2, -3.3)
CH_4	(-4, -6)	(-13, -15)
CO_2	(-5, -7)	(-6, -8)
HCN	(-7, -8)	(-11, -12)
NH_3	(-4.3, -5.3)	(-9.3, -10.3)
Beyond the CO_2 snowline		
H_2O	(-3, -4)	(-3, -5)
CO	(-3.3, -3.5)	(-3, -3.3)
CH_4	(-4, -5)	(-8, -11)
CO_2	(-6, -8)	(-7, -9)
HCN	(-6, -7)	(-9, -11)
NH_3	(-4.3, -5.3)	(-9.3, -10.3)

Table 3.3 The expected abundances for six molecules in the atmospheres of two hot Jupiters, one with $T_{eq} = 1000$ K and the other with $T_{eq} = 2000$ K, for a gas giant formed by core accretion that underwent disk-free migration, from the work of Madhusudhan et al. (2014a). We split the formation location of the planet into two groups: Within the CO_2 snowline and beyond the CO_2 snowline.

not consider the N/H in their models, and so we choose to use N/H = 1 for the comparisons here. We present the expected abundance for these planets in Table 3.3.

Lastly from the work of Madhusudhan et al. (2014a), we consider planets formed via gravitational instability that then migrate inwards disk-free. There are again two regions to consider for this formation-migration mechanism: those planets that formed within the CO snowline and those that formed outside the CO snowline. The composition of those planets that formed by gravitational instability within the CO snowline is similar to those formed by core accretion with in-disk migration, however the potential metallicity also extends into sub-solar metallicity with super-solar C/O ratio. Those that formed beyond the CO snowline have a near solar C/O ratio, but with any metallicity within our parameter space, producing a wide range of possible abundances. We present the expected abundance ranges for both of these cases in Table 3.4.

We summarise the resulting atmospheric chemistry at 10^{-3} bar for our 1000 K and 2000 K hot Jupiters following formation and migration from these five different scenarios in Figure 3.10. Overall what we see is significant overlap between formation location and migration types investigated here. This was expected based upon the overlapping metallicities that we drew from Madhusudhan et al. (2014a). We can still draw some important insights from this data though.

Molecule	1000 K	2000 K
Within the CO snowline	$\log(X_{\rm Max}, X_{\rm Min})$	$\log(X_{\rm Max}, X_{\rm Min})$
H_2O	(-2, -4)	(-2, -4)
CO	(-2.2, -3.5)	(-2, -4)
CH_4	(-3.3, -6)	(-8.5, -14)
CO_2	(-4, -7.5)	(-5, -10)
HCN	(-6, -8)	(-6, -12)
NH_3	(-4.3, -5.3)	(-9.3, -10.3)
Beyond the CO snowline		
H_2O	(-2, -5)	(-2, -5)
CO	(-2.5, -5)	(-2, -4.5)
CH_4	(-4, -5)	(-12, -13)
CO_2	(-4, -9)	(-5, -10)
HCN	(-6.3, -7)	(-10, -11)
NH_3	(-4.3, -5.3)	(-9.3, -10.3)

Table 3.4 The expected abundances for six molecules in the atmospheres of two hot Jupiters, one with $T_{eq} = 1000$ K and the other with $T_{eq} = 2000$ K, for a gas giant formed by gravitational instability and underwent disk-free migration from the work of Madhusudhan et al. (2014a). We split this formation mechanism for those planets formed outside of the CO snowline and those that formed within the CO snowline but beyond the CO_2 snowline.

H_2O: We find that high H_2O abundances in our models, between 10^{-2} and 10^{-3}, can be found for a hot Jupiter that formed at any location, and is independent of the equilibrium temperature of the hot Jupiter. However, very low H_2O abundances were unique to planets that had formed further out, at least beyond the CO_2 snowline for both core accretion and gravitational instability formation models. This is because these formation locations resulted in either low O/H ratio or a high C/O ratio, both of which cause low H_2O abundances.

CO: Similar to H_2O, our model predicts high CO abundances in both cases are able to occur regardless of where the hot Jupiter formed. However, we once again find that very low CO abundances are only expected for planets that formed further out, either by core accretion beyond the CO_2 snowline or by gravitational instability beyond the CO snowline for our 1000K model, or any location of gravitational instability for our 2000K model. This is due to low C/H and O/H ratios, irrespective of the C/O ratio.

CH_4: For our 2000K temperature hot Jupiter, we never expect CH_4 to be detectable, with abundances always far below 10^{-6}. For our cooler 1000K hot Jupiter, methane abundances can be high, up to 10^{-4} for planets formed by core accretion with disk-free migration or gravitational instability beyond the CO snowline. We expect to see the highest CH_4 levels in the case of the 1000K hot Jupiter that formed between the CO_2 and CO snowlines, possibly approaching an abundance of 10^{-3}. This is because this is the model with the highest C/O ratio,

on which the CH_4 ratio strongly depends. For our 1000K hot Jupiter, we only find methane abundances below 10^{-5} for planets that formed close in by core accretion, either within the CO_2 snowline and then migrated disk-free or those that underwent in-disk migration, or formed within the CO snowline by gravitational instability. It is possible then that detections of low levels of CH_4 could also function in helping determine where a hot Jupiter formed.

CO_2: For core accretion, our models find higher levels of CO_2 are associated with a planet that formed further in, with both the maximum and minimum levels of CO_2 increasing by up to two orders of magnitude as we move from the more distant formation models to the closer ones. However, planets that formed by gravitational instability, can contain a range of CO_2 levels that encompasses the entire range of all the other models, requiring other features to break the degeneracy here.

HCN: For our 2000K temperature hot Jupiter, we predict HCN abundances below 10^{-8}, and thus very unlikely to be detectable, for every model except one. We find that our 2000K hot Jupiter formed by gravitational instability between the CO_2 and CO snowlines can have HCN abundances as high as 10^{-6}. In the atmosphere of our 1000K hot Jupiter, we only find high levels of HCN in the model of core accretion and then disk-free migration for planets that formed beyond the CO_2 snowline and gravitational instability within the CO snowline. This is because these are the only models with a significantly super-solar C/O ratio, which favours the production of HCN.

NH_3: Ammonia levels cover the same range in every model, with no expected metallicity to be extreme enough to find significantly different NH_3 levels. However, for our 2000K temperature hot Jupiter, the abundance of NH_3 in their atmospheres is expected to be below 10^{-8}, and thus not detectable. For the 1000K hot Jupiter, NH_3 is expected to be detectable at around 10^{-5} bar.

3.4.2 Chemical Enrichment of Hot Jupiters

The work of Booth et al. (2017) looks at the chemical enrichment by pebble drift of gas giants formed by core accretion. For planets formed within the CO_2 snowline this results in $2 <$ [C/H] < 3 and [O/H] = 2 and for planets formed beyond the CO_2 snowline this can result in any metallicity within our parameter space, but with a C/O = 1. The abundances our model predicts for this formation and migration scenario are in Table 3.5. We summarise the resulting atmospheric chemistry in 1000 K and 2000 K hot Jupiters following formation and migration from these two different scenarios in Figure 3.10.

Overall what we see is that only a few molecules in chemically enriched planets' atmospheres stand out as tracers of these planets' pasts. Regardless of temperature, H_2O, CO, CO_2 and NH_3 all lie within the ranges of expected abundances discussed in the previous section.

Molecule	1000 K	2000 K
Within the CO_2 snowline	$\log(X_{\rm Max}, X_{\rm Min})$	$\log(X_{\rm Max}, X_{\rm Min})$
H_2O	(-3, -4.3)	(-3, -4)
CO	(-2.5, -3.2)	(-2.3, -3.3)
CH_4	(-4, -5)	(-12, -13)
CO_2	(-6, -7)	(-6, -7)
HCN	(-5, -7)	(-9, -10)
NH_3	(-4.3, -5.3)	(-9.3, -10.3)
Beyond the CO_2 snowline		
H_2O	(-3, -4.3)	(-3, -5)
CO	(-2, -5)	(-2, -4.3)
CH_4	(-3, -4)	(-7, -9)
CO_2	(-5, -9)	(-6, -9)
HCN	(-5, -7)	(-4, -7)
NH_3	(-4.3, -5.3)	(-9.3, -10.3)

Table 3.5 The expected abundances for six molecules in the atmospheres of two hot Jupiters, one with $T_{eq} = 1000$ K and the other with $T_{eq} = 2000$ K, using the models of chemical enrichment by Booth et al. (2017). We split the formation location of the planet into two groups: Within the CO_2 snowline and beyond the CO_2 snowline.

For only the hotter Jupiters, we find that chemical enrichment of planets formed beyond the CO_2 snowline leads to large elevations in the expected abundance of HCN. Also, our predicted CH_4 abundance levels in planets chemically enriched by pebble drift that formed beyond the CO_2 snowline are at least half an order of magnitude above values expected by other formation models, making it the best contender for a chemical enrichment tracer.

There are a number of tracers to distinguish where a planet that was known to have been chemically enriched was formed. Both H_2O and CO abundances in enriched planets that formed beyond the CO_2 snowline are expected to be able to reach significantly lower values than in a planet formed within the CO_2 snowline. In hotter Jupiters, HCN can help distinguish to two formation areas, however in cooler hot Jupiters there is a full overlap in the expected abundances of HCN from both locations. CH_4 likely works as the best tracer however. Regardless of temperature, there is no overlap in expected abundance of CH_4 between the two formation areas, with significantly higher CH_4 always being expected for a planet that formed beyond the CO_2 snowline.

3.4.3 Tracers of Nitrogen Chemistry

Turrini et al. (2021) select six formation locations in conjunction with a core accretion and in-disk migration model to produce the final metallicity of a hot Jupiter. These values are

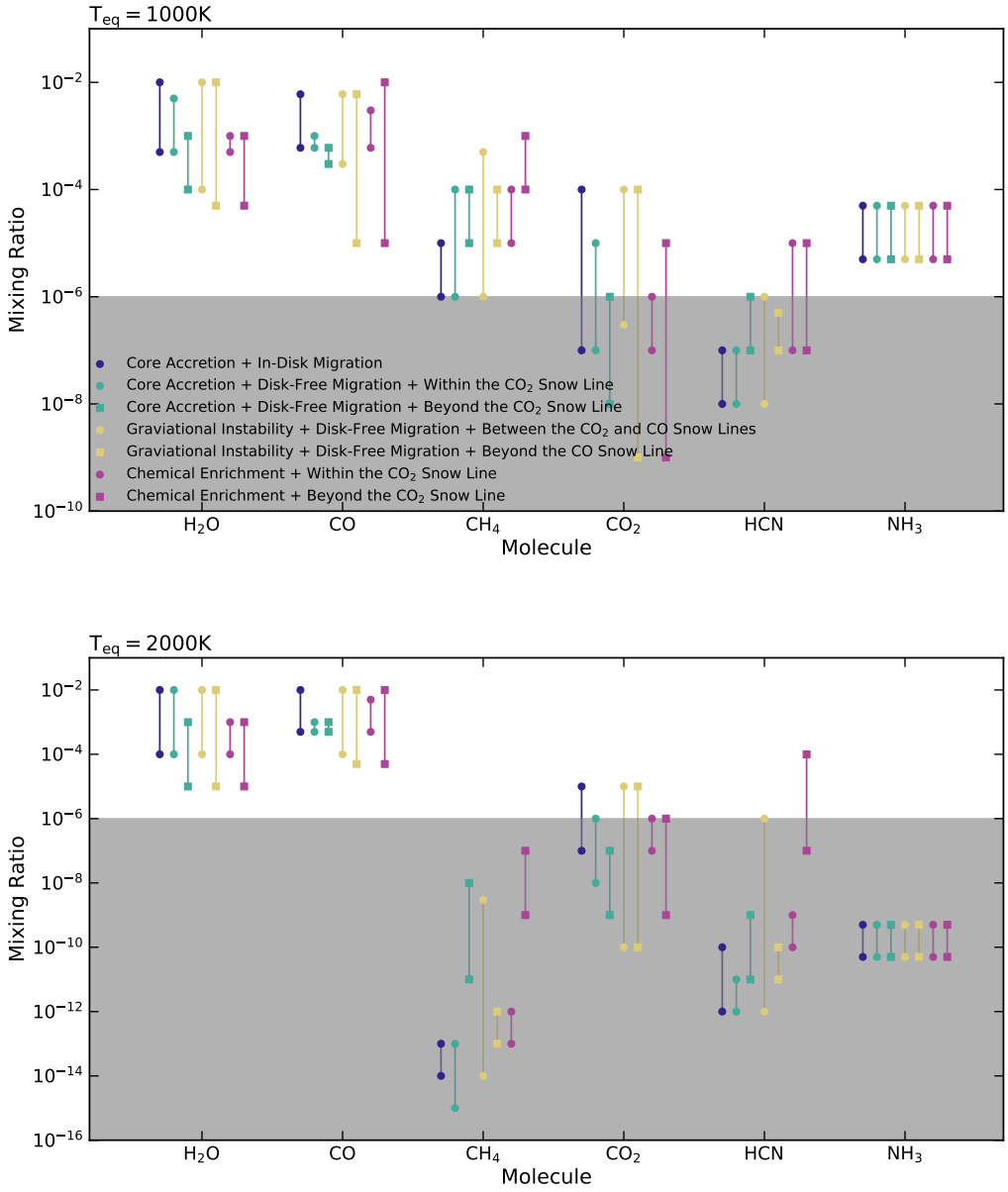

Fig. 3.10 A comparison of the abundances of six molecules that our models predict, based upon the metallicities resulting from the five different formation and migration mechanisms discussed in Madhusudhan et al. (2014a) and two different formation locations from Booth et al. (2017), for the two different planet temperatures we investigate. The red, blue and green ranges correspond to work from Madhusudhan et al. (2014a) while the purple ranges correspond to work from Booth et al. (2017). The range of abundances we see for each species for each formation model is due to the spread of metallicity possible from those models. The grey zone below 10^{-6} marks the region in which abundances are expected to be too low to be detectable.

Molecule	5AU	12AU	19AU	50AU	100AU	130AU
1000 K	$\log(X)$	$\log(X)$	$\log(X)$	$\log(X)$	$\log(X)$	$\log(X)$
H_2O	-3.3	-3.2	-3.1	-3.0	-2.7	-2.5
CO	-3.4	-3.2	-3.1	-2.7	-2.7	-2.5
CH_4	-4.4	-4.5	-4.2	-4.7	-5	-5.1
CO_2	-6.7	-6.5	-6.1	-5.5	-5.2	-5.0
HCN	-6.5	-6.2	-6.3	-6.3	-6.1	-6.0
NH_3	-5.1	-5.1	-5.0	-5.0	-4.7	-4.7
2000 K						
H_2O	-3.3	-3.3	-3.0	-2.3	-2.3	-2.3
CO	-3.3	-3.3	-3.0	-3.0	-2.5	-2.3
CH_4	-12	-12	-12	-12	-12	-12
CO_2	-7.3	-7.0	-7.0	-6.3	-6.0	-5.3
HCN	-10.3	-10.3	-10.3	-10.2	-10.1	-10
NH_3	-10.2	-10.1	-10	-10	-9.7	-9.5

Table 3.6 The expected abundances for six molecules in the atmospheres of two hot Jupiters, one with $T_{eq} = 1000\,\mathrm{K}$ and the other with $T_{eq} = 2000\,\mathrm{K}$, using the models from Turrini et al. (2021). We split the table into columns of formation location of the planet, using the metallicity of these planets shown in Table 3.1 in conjunction with our models to produce the abundances shown in this table.

shown in Table 3.1. We tabulate the molecular abundance our model predicts for each planetary formation location in Table 3.6.

As expected, the monotonic increase in the metallicity of hot Jupiters as formation distance increases, translates to a similar monotonic increase for each of the six molecules we examine. This is shown in Figure 3.11. Notably, the molecules H_2O, CO, CH_4 and CO_2 all change by approximately an order of magnitude across the range of formation locations. This should be sufficient for detections of these molecules in a planet's atmosphere to link quite accurately to the planet's C/O ratio and where it formed. However, HCN and NH_3 have a significantly smaller range of possible abundances. This makes it much harder to be able to link the detection of nitrogen species to the planet's N/H ratio and where it may have formed, especially due to the current scarcity in nitrogen species detected and HCN being below the detectable limit regardless of planetary temperature.

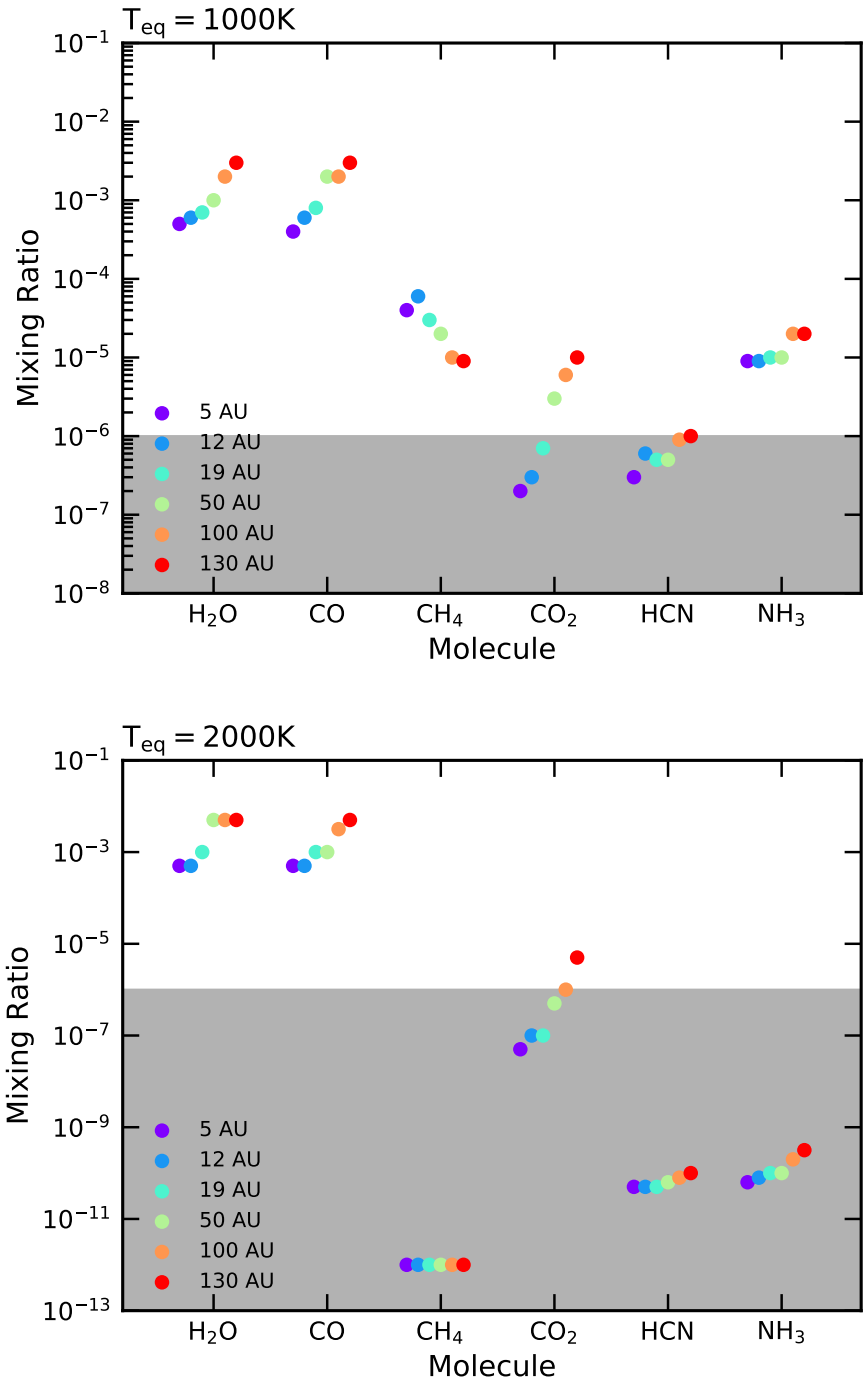

Fig. 3.11 A comparison of the abundances of six molecules that our models predict for the different formation locations presented in Turrini et al. (2021), for hot Jupiters at two equilibrium temperatures. The grey zone below 10^{-6} marks the region in which abundances are expected to be too low to be detectable.

Planet Name	M_P (M_J)	T_{eq} (K)	$\log(X_{H_2O})$
WASP-107b	0.12	740	$-2.87^{+0.95}_{-0.73}$
HD 189733b	1.14	1200	$-4.66^{+0.35}_{-0.33}$
KELT-11b	0.20	1300	$-3.60^{+0.60}_{-0.70}$
HAT-P-1b	0.53	1320	$-2.54^{+0.75}_{-0.67}$
WASP-43b	2.03	1440	$-3.68^{+0.92}_{-0.88}$
HD 209458b	0.69	1450	$-4.54^{+0.33}_{-0.27}$
WASP-17b	0.51	1740	$-3.84^{+1.27}_{-0.51}$
WASP-19b	1.14	2050	$-3.43^{+0.47}_{-0.52}$

Table 3.7 A table of the H_2O abundances detected in hot Jupiters with equilibrium temperatures between 1000 K and 2000 K. The values for KELT-11b come from Changeat et al. (2020), while all the others were drawn from Welbanks et al. (2019).

3.5 A Comparison with Retrieved Abundances in Hot Jupiters' Atmospheres

In this section we examine an ensemble of H_2O detections made in the atmospheres of hot Jupiters, and compare the detected values to our models predictions. We also perform a case study of the hot Jupiter HD 209458b to determine whether our models can predict where the planet formed and how it migrated.

3.5.1 H_2O Abundances

In Table 3.7 we tabulate 8 hot Jupiters whose detected water abundance has been determined to within an order of magnitude.

All eight planets have their water abundance fall within the ranges predicted by our models. However, HD 189773b and HD 209458b have notably lower H_2O abundances than any of the other planets. While the other planets could have formed and migrated by any of the mechanisms discussed in the previous section, our models suggest that HD 189733b and HD 209458b would have had to have formed farther out to obtain their current water abundances. Which mechanism is still not precisely determined, but either core accretion, with or without chemical enrichment, beyond the CO_2 snowline or gravitational instability beyond the CO snowline are the only ways to produce such low water mixing ratios within our models.

Molecule	Emission (Gandhi et al. 2019)	Transmission (Welbanks et al. 2019)	Transmission (Giacobbe et al. 2021)	Matching Formation Models
H_2O	$-4.11^{+0.91}_{-0.3}$	$-4.54^{+0.33}_{-0.27}$	-3.92	All
CO	$-2.16^{+0.99}_{-0.47}$		-2.85	All
CH_4			-2.33	$\sim$ CE-B or GI-B
CO_2			-4.28	CA-ID or GI
HCN			-4.07	$\sim$ CA-DF-B or $\sim$ CE or $\sim$ GI-B
NH_3			-3.89	$\sim$ All
C/O ratio	$0.99^{+0.01}_{-0.02}$			CE or GI-B

Table 3.8 A summary of the retrieved values of molecular abundances in the atmosphere of HD 209458b from a number of recent studies. The matching formation models column refers to the formation models we compared to in Section 3.4. The abbreviations are: CE: Chemical Enrichment. CE-B: Chemical Enrichment beyond the CO_2 snowline. These models came from Booth et al. (2017). CA-ID: Core Accretion with In Disk migration. CA-DF-B: Core Accretion with Disk-Free Migration from beyond the CO_2 snowline. GI: Gravitational Instability. GI-B: Gravitational Instability between the CO_2 and CO snowlines. These models came from Madhusudhan et al. (2014a).

3.5.2 Case Study: HD 209458b

HD 209458b is one of the most studied hot Jupiters, with multiple molecules potentially detected within its atmosphere. In particular, H_2O, CO and the C/O ratio on the day-side of the planet have been retrieved by Gandhi et al. (2019), and at the day-night terminator we can find values for the H_2O abundance in Welbanks et al. (2019) and the H_2O, CO, CH_4, CO_2, HCN and NH_3 abundance from Giacobbe et al. (2021). These values are summarised in Table 3.8.

Based upon General Circulation Models (GCM) of HD 209458b (Showman et al. 2009b), we can use our 2000 K model as an approximation to the day-side of the planet, and our 1000 K model as an approximation to the terminator of the planet.

Comparing the retrieved values from the day-side emission spectra in Gandhi et al. (2019) to our results, we see that the detected values for H_2O and CO fall within the range of any of the formation models we considered. However, their retrieved C/O ratio of approximately 1 was only possible in one of the scenarios we investigated: Chemical enrichment via pebble drift, as discussed in Booth et al. (2017).

Next we compare our results to the retrieved abundances from the terminator transmission spectra of HD 209458b in Giacobbe et al. (2021). Both the H_2O and CO results are on the boundary of being possible with any formation model, but they do favour core accretion and chemical enrichment beyond the CO_2 snowline or any formation location by gravitational instability. All of the other abundances of retrieved molecules from Giacobbe et al. (2021) are higher than any our models predict. However, this difference is generally no more than half an order of magnitude, and so we will compare to the formation pathways that produce

results closest to the retrieved values. It is likely that these differences arise from either margins of error within the retrieved values, or simplifications within our own models when trying to model the complex chemistry of hot Jupiters. The retrieved value for methane in Giacobbe et al. (2021) is approximately half an order of magnitude above our values of CH_4 for chemical enrichment beyond the CO_2 snowline and gravitational instability between the CO_2 and CO snowlines. However, it is several orders of higher than any other formation pathway, thus suggesting that for CH_4, HD 209458b was unlikely to have formed via any other mechanism. The retrieved abundance for CO_2 falls within the predicted abundances for a planet forming via core accretion with in-disk migration, and for a planet forming via gravitational instability. The retrieved HCN abundance lies above any of our models predictions, but is within half an order of magnitude of values predicted by core accretion and disk-free migration beyond the CO_2 snowline, any location of chemical enrichment, or gravitational instability between the CO_2 and CO snowlines. Lastly, the NH_3 results from Giacobbe et al. (2021) are also higher than any of our modelled results, however this could be accounted for by variations in the N/H ratio. Regardless, any formation model could be responsible for producing the observed NH_3 values.

Overall, the likely formation location and migration mechanism for HD 209458b seems to be narrowed down significantly. The most likely pathway is forming between the CO_2 and CO snowlines by gravitational instability, since this fits with every detected feature. It is also possible the that HD 209458b formed beyond the CO_2 snowline and was then chemically enriched by pebble accretion, with only the CO_2 abundance from Giacobbe et al. (2021) not supporting this formation mechanism. However, because the detection significance of CO_2 in Giacobbe et al. (2021) was very low, it is likely that this value has a significant error to it, and may actually line up with our predictions.

3.6 Conclusion

In this work we have explored the carbon, oxygen and nitrogen compositional parameter space for a hot Jupiter, and seen how these predicted abundances may relate to the formation location of the planet. By expanding upon the work in the previous chapter we have run a suite of 1500 models of our chemical kinetics code. We did this for a generic hot Jupiter orbiting at two possible distances from a sun-like star, encompassing a range of atmospheric elemental compositions between 0.1x and 10x the solar values for carbon, oxygen and nitrogen. We compare our parameter space to the formation and migration models of three previous works (Madhusudhan et al. 2014a; Booth et al. 2017; Turrini et al. 2021) to create a frame work of how the abundance of six of the major species in a hot Jupiter atmosphere might be linked to where the planet formed.

We find that, as expected, there is a large degree of degeneracy when trying to link a planet's atmospheric composition to its formation location, however we do obtain some insights that may assist in narrowing down the history of a hot Jupiter. Using the relationship between formation and metallicity shown in Madhusudhan et al. (2014a) we find that low CO_2 and H_2O abundances are expected only in planets forming beyond the CO_2 snowline. We also find that low CH_4 abundances on the cooler hot Jupiters are only expected for a planet forming within the CO_2 snowline or by gravitational instability beyond the CO_2 snowline. Additionally, we find that our models predict high HCN abundances for planets that formed beyond the CO_2 snowline via core accretion before undergoing disk-free migration, or by gravitational instability between the CO_2 and CO snowlines.

We also considered the possibility of chemical enrichment of hot Jupiters as presented in Booth et al. (2017). We find the best way to determine if a hot Jupiter had been chemically enriched was via an elevated CH_4 abundance within the enriched planet's atmosphere. The formation location of a chemically enriched planet could best be identified via the CO or CO_2 abundance, both of which would be lower in a planet that formed beyond the CO_2 snowline.

Using the work of Turrini et al. (2021), we investigated whether having the N/H ratio as a chemical parameter could allow us to gain insights into where a hot Jupiter formed. In general we find that this is not the case. Species that do not contain nitrogen are generally unaffected by changes to the N/H ratio. Additionally, the range of N/H ratios predicted by Turrini et al. (2021) only covers between $1 < [N/H] < 3$, which does not have a very significant impact even on those species that do contain nitrogen.

We compared an ensemble of retrieved water abundances on hot Jupiters from Welbanks et al. (2019) to the water abundances we predicted using our models. We found that all the detected abundances lay within our predictions, but with the water abundance being the only

value given, it was almost impossible to distinguish which formation mechanism may have lead to that abundance. Thus we conclude that water alone makes a poor diagnostic tool.

Finally we performed a case study on the hot Jupiter HD 209458b, using detections from Gandhi et al. (2019), Welbanks et al. (2019) and Giacobbe et al. (2021). We found the our model predicted gravitational instability between the CO_2 and CO snowlines as the most likely formation method for this planet. However, core accretion beyond the CO_2 snowline followed by chemical enrichment by pebble drift also matched with all but one molecular detection, and thus could also be a contender for how HD 209458b was formed.

To improve our ability to predict formation mechanisms further, we either need additional, more accurate molecular abundance measurements on hot Jupiters, and to expand the functionality of our code. One way of doing this could be the creation of synthetic spectra based upon the atmospheric compositions our model predicts. These can be compared with both real spectra, to assist in determining the accuracy of our models, and to synthetic spectra from models across the range of elemental composition, to determine how precise the retrieved spectra must be to distinguish between the different models. The upcoming launch of satellites such as the James Web Space Telescope (JWST) should help in providing a more accurate picture of the composition of a hot Jupiter. To improve chemical models of hot Jupiters, inclusion of other elements such as sulfur may assist in making the models more accurate representations of hot Jupiters.

Chapter 4

Sulfur Chemistry in the Atmospheres of Warm and Hot Jupiters

4.1 Introduction

The focus of this Chapter is to continue this evolution of the chemical network used by LEVI. We do so by introducing a new element, sulfur, to the model and to the network described in Chapter 2. In this chapter we apply the network to hot and warm Jupiters. By doing so, we can investigate the importance of sulfur in the atmospheres of exoplanets in both the context of sulfur itself and the way it impacts carbon and oxygen chemistry. We revisit 51 Eri b, studied previously by Zahnle et al. (2016) and Moses et al. (2016), with our own model, as well as the hot Jupiter HD 209458b, to determine whether we can identify what role sulfur plays in the chemistry of both warm and hot Jupiters.

We begin with a brief overview of the model we're using. In Section 4.3 we validate our network for pure thermo-chemical equilibrium and compare our model against the sulfur model of Wang et al. (2017) and Zahnle et al. (2016). Section 4.4 contains our analysis of the sulfur chemistry occurring in the atmospheres of hot Jupiters, and shows which pathways in our network lead to such chemistry occurring. In Section 4.5, we examine how sulfur can affect the chemistry of other, non-sulfur species in both warm and hot Jupiters. We discuss our findings and review what we have discovered in Section 4.6.

4.2 Model Details

In previous Chapters, we used a subset of the STAND2019 network. This was the STAND2015 network first developed in Rimmer and Helling (2016) plus the additional reactions from Rimmer and Rugheimer (2019). We limited the network to only reactions with neutral species containing hydrogen, carbon, nitrogen and oxygen, and used it in conjunction with LEVI to model hot Jupiter atmospheres.

As part of this work we have developed a new addition to this network, comprised of an additional 185 reactions and 30 species that include the element sulfur. Our sulfur species include molecules that contain up to 2 H, 3 C, 3 O and 2 S, except for the allotropes of sulfur that include up to S_8. These species are tabulated in Table 4.1. The reactions we have added were mainly drawn from the NIST chemical kinetics database [1], with the full tabulation of both reactions and sources available in the table of Appendix A.2.

We applied a sensible selection criterion when choosing which sources of the rate constants to use for each reaction. Where possible, we selected rate constants that had been measured experimentally, rather than theoretically. This network was intended to be able to apply to hot Jupiters, whose temperatures can reach several thousand Kelvin. As such, we aimed to pick rate constants that had been measured over a range of temperatures, ideally to temperatures that are realistic for a hot Jupiter, i.e., 2000 K. Unfortunately, many reactions have only been measured at room temperature, resulting in currently unavoidable limitations to the accuracy of these rate constants. Finally, we in general picked the more recently measured rate constants when there were multiple measurements made for a single reaction. In some cases, the rate constants of both the forward and reverse reaction were available. In these cases, we picked the rate constants for the reaction with the smaller energy barrier, and used this as the forward reaction, and used thermodynamic reversal to obtain the rates for the reverse reaction. We took the estimated rate constants of sulfur allotrope polymerisation from Moses et al. (2002) and several carbon mono-sulphide, CS, reactions from the KIDA database (Wakelam et al. 2012) [2]. These reactions are thermodynamically reversed using the NASA7 polynomials from Burcat [3], with the full method for these reversals detailed in Chapter 2. There are no polynomials for the species CS_2OH, H_2C_3S and HSNO, so we do not reverse the reactions that include these species. We also include the photodissociation cross-sections for 17 reactions involving eleven sulfur species: S_2, S_3, S_4, H_2S, SO, SO_2, SO_3, S_2O, OCS, CS_2 and CH_3SH. The photo-dissociation cross-section, $\Sigma_{i\rightarrow j}$ (m^2) is equal to $\sigma_{a,i} \times q_{a,i\rightarrow j}$, where $\sigma_{a,i}$ (m^2) is the absorption cross-section and $q_{a,i\rightarrow j}$ is the quantum yield. The wavelengths $i = 1$ Å and

[1] https://kinetics.nist.gov/kinetics/
[2] http://kida.astrophy.u-bordeaux.fr/
[3] http://garfield.chem.elte.hu/Burcat/burcat.html

Table 4.1 Chemical names of the sulfur species used in the network

Species	Chemical Name
S	Sulfur
S_2	Disulfur
S_3	Trisulfur
S_4	Tetrasulfur
S_5	Pentasulfur
S_6	Hexasulfur
S_7	Heptasulfur
S_8	Octasulfur
HS	Mercapto Radical
H_2S	Hydrogen Sulfide
H_2S_2	Hydrogen Disulfide
CS	Carbon Sulfide
CS_2	Carbon Disulfide
CS_2OH	Thioxomethyl Radical
HCS	Thioformyl Radical
OCS	Carbonyl Sulfide
H_2CS	Thioformaldehyde
H_2C_3S	Tricarbon Monosulfide
CH_3SH	Mercaptomethane
HSNO	Thionylimide
SO	Sulfur Monoxide
SO_2	Sulfur Dioxide
SO_3	Sulfur Trioxide
S_2O	Disulfur Monoxide
HSO	Sulfenate
HSO_2	Sulfinate
HSO_3	Bisulfite
HOSO	Hydroperoxysulfanyl
HSOO	HSOO

$j = 10000$ Å are the range over which we use these cross-sections. The cross-sections for H_2S, SO, SO_2, OCS, CS_2 and CH_3SH were taken from PhIDrates [4], the cross-sections for S_3, S_4 and S_2 from the MPI-Mainz-UV-VIS Spectral Atlas of Gaseous Molecules[5] and the cross-section for S_2 from the Leiden database (Heays et al. 2017).

Here we define which parameters are consistent throughout all models, and what changes are applied to specific models. In all of our models:

- We set the boundary conditions at the top and bottom of the atmosphere to be zero-flux, such that there is no interaction with the atmosphere outside of our model
- When we apply a UV flux to our atmospheres, we choose a mean zenith angle of 57.3° (Zahnle et al. 2008; Hu et al. 2012)
- We model the planet as if its day-side is always facing the star it orbits, i.e. it's tidally locked, such that it experiences an uninterrupted flux. When modelling a far out planet, such as 51 Eri b, this assumption breaks down and so we halve the flux to account for rotation.

Most of our models use a solar metallicity, with values from Asplund et al. (2009). This gives an elemental ratio, as a fraction of the total number of molecules, of: $X_{H_2} = 0.5 \times X_H = 0.8535$, $X_{He} = 0.145$, $X_C = 4.584 \times 10^{-4}$, $X_O = 8.359 \times 10^{-4}$, $X_N = 1.154 \times 10^{-4}$, $X_S = 2.250 \times 10^{-5}$. When we alter the metallicity, we proportionally change the amount of C, O, N and S in the atmosphere. He is kept constant, and H_2 is altered such that the ratios sum to unity.

There are also parameters that vary between each model. This includes: the pressure-temperature (P-T) profile, the gravity of the planet, the eddy-diffusion profile applied to the model and the spectral irradiance applied to the top of the atmosphere. An overview of these differences can be seen in Table 4.2.

[4] https://phidrates.space.swri.edu/
[5] www.uv-vis-spectral-atlas-mainz.org

Case	Analogue Planet	T-profile K	Gravity cm s^{-2}	K_{zz}-profile cm^2 s^{-1}	Metallicity	TOA Spectral Irradiance photons cm^{-2} s^{-1} Å^{-1}
Figure 4.1	Hot Jupiter	1400	1000	None	Solar	None
Figure 4.2	Hot Jupiter	2000	1000	10^9	Solar	800× Solar
Figure 4.3	WASP-121 b	Evans et al. (2018)	875	10^9	[M/H] = 1.3	5300× Solar
Figure 4.4	Hot Jupiter	Multiple	1000	None	Solar	None
Figure 4.5	Hot Jupiter	Multiple	1000	10^9	Solar	10× Solar
Figure 4.6	Hot Jupiter	1200	1000	Multiple	Solar	10× Solar
Figure 4.7	Hot Jupiter	1200	1000	10^9	Solar	Multiple
Figure 4.8	HD 209458 b	Moses et al. (2011)	936	Moses et al. (2011)	Solar	800× Solar
Figure 4.16	51 Eri b	Moses et al. (2016)	3200	10^7	Solar	Moses et al. (2016)

Table 4.2 Model Parameters

4.3 Validation of the Network

In this section we test our model by applying it to the atmospheres of several hot Jupiters. We compare the thermochemistry of our model to an equilibrium solver, FastChem. We also compare and contrast our complete model to a previous sulfur models produced by Wang et al. (2017) and Zahnle et al. (2016).

4.3.1 Equilibrium Comparison

As a first step of validating our new sulfur network, we chose to consider our results when only allowing thermochemistry, with no disequilibrium chemistry. We compare to the analytical equilibrium output of FastChem, a chemical equilibrium solver produced by Stock et al. (2018). In this comparison, we chose to compare a hot Jupiter atmosphere model with an isothermal temperature of 1400 K. The results of this are shown in Figure 4.1, where we display only the important sulfur species for comparison. We have a near perfect match compared to the analytic output for every species except for HS, which we slightly under-produce, and OCS, which we slightly over-produce.

We expect the causes for these slight dissimilarities to be due to differences in the thermochemical constants we use to reverse our reaction rates. We use the NASA7 polynomials from Burcat [6] to calculate our Gibbs free energy, while Stock et al. (2018) drew theirs from thermochemical databases, e.g., Chase (1998).

Overall, it can be seen that the thermochemistry of our sulfur network is an excellent match to the analytical solution of FastChem. The slight differences seen between the two models are not large enough to significantly impact the chemistry occurring in the atmosphere. Additionally, at a practical level, the difference seen between the models would not be detectable with present observations.

4.3.2 Comparison with Previous Sulfur Networks

The model of Wang et al. (2017) was used to create synthetic spectra to determine whether JWST could detect sulfur and phosphorous species in the atmosphere of giant planets. We make comparisons between our new network and the output of their model for sulfur species.

In Figure 4.2, the comparison is made for a hot Jupiter model with an atmosphere at an equilibrium temperature of 1400 K, a $K_{zz} = 10^9\,\mathrm{cm^2\,s^{-1}}$. In this figure, most of the atmosphere shown is dominated by the effects of thermochemistry, with only the very top possibly being

[6] http://garfield.chem.elte.hu/Burcat/burcat.html

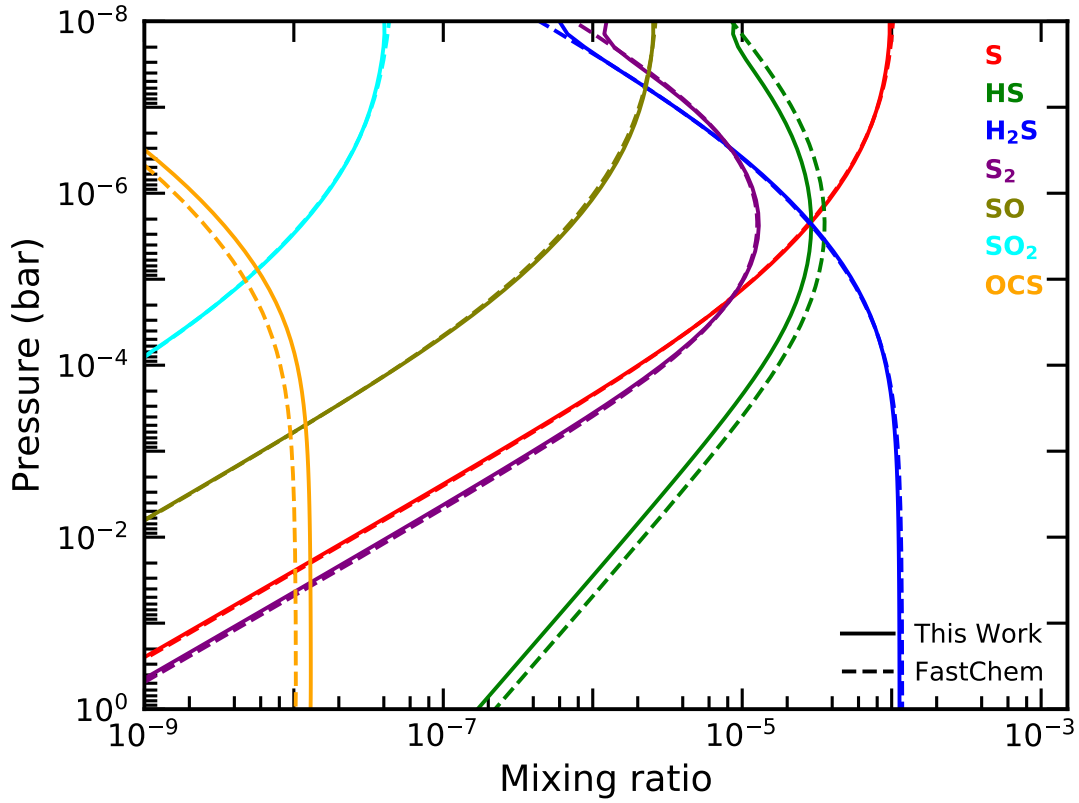

Fig. 4.1 The abundances of significant sulfur bearing species for a purely thermochemical chemistry calculation, taking place in a hot Jupiter atmosphere model that is isothermal at 1400 K, has a gravity of $10\,\mathrm{m\,s^{-2}}$ and a metallicity $5\times$ solar. It has no diffusion or UV spectrum applied to the atmosphere. The solid lines are the output of the model being discussed in this work, while the dashed lines are from the analytical equilibrium solver of FastChem (Stock et al. 2018).

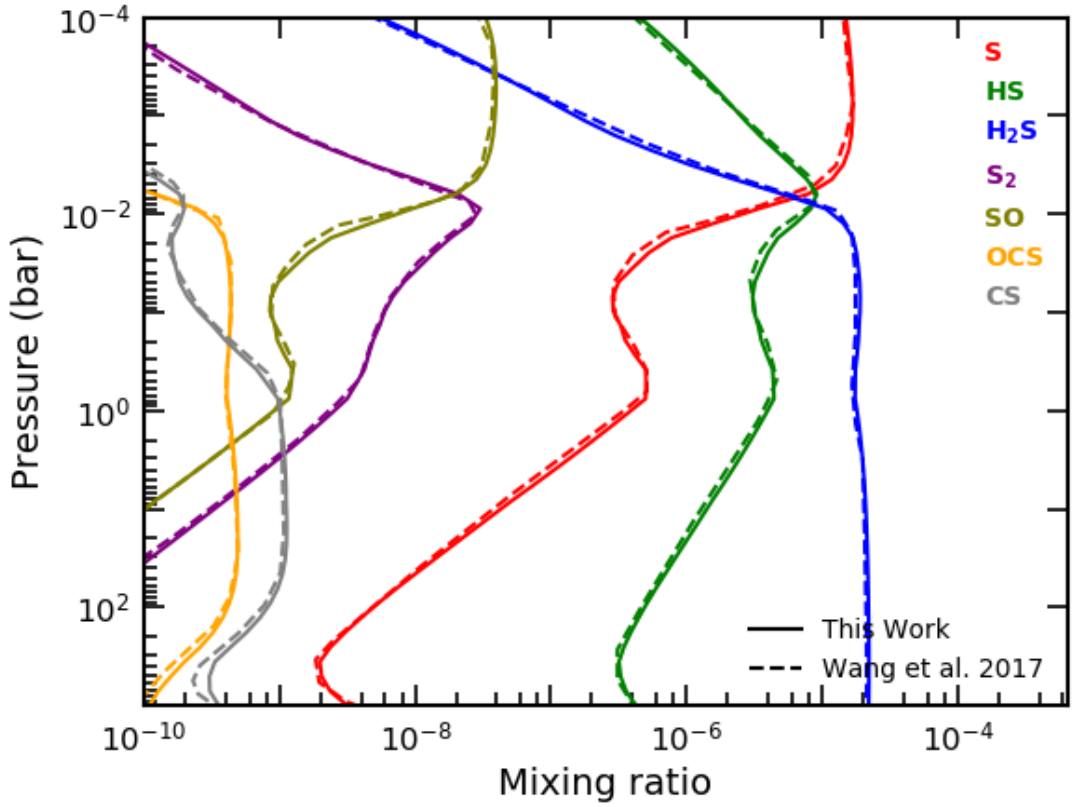

Fig. 4.2 A comparison between our network (solid lines) and one presented in Wang et al. (2017) (dashed lines) for a hot Jupiter model. This atmosphere has an equilibrium temperature of 2000 K, a gravity of $10\,\mathrm{m\,s^{-2}}$, $K_{zz} = 10^9\,\mathrm{cm^2\,s^{-1}}$ and with a solar metallicity.

effected by the disequilibrium effects of diffusion. We compare the abundances of the seven most abundant sulfur species, S, S_2, HS, H_2S, SO, OCS and CS.

Throughout the entire atmosphere we see an excellent match between our own model and that of Wang et al. (2017), with the abundance of every species matching very closely between the models. With this, we have firmly validated the thermochemistry of our new sulfur network. Wang et al. (2017) did not include considerations of photochemistry in their model, and so further tests are required to validate the sulfur photochemistry in our model.

In Figure 4.3 we show our model for the hot Jupiter WASP-121 b, and compare to the abundance profile presented in Evans et al. (2018), which was produced by the model of Zahnle et al. (2016). This hot Jupiter is modelled with a metallicity of 20× solar and constant $K_{zz} = 10^9\,\mathrm{cm^2\,s^{-1}}$. The model in Evans et al. (2018) used an F6V host star, however we were unable to gain access to the spectrum used in this work, so we approximate it as a solar host star, with its spectrum scaled as if it were the size and temperature of WASP-121.

We can broadly split the atmosphere in this figure into two regimes. The first is deep in the atmosphere where the pressure is greater than 10^{-3} bar, and where thermochemical effects are expected to be more important. The second is at pressures less than 10^{-3} bar where we expect disequilibrium effects such diffusion and photochemistry to dominate.

In the deep atmosphere, Figure 4.3 shows that our model has close agreement with the model of Evans et al. (2018), with a difference in predicted abundances of less than 50% between the models. We observe a systematic under-abundance of S-bearing species in our model compared with that of Evans et al. (2018). As the non-S species match closely, this likely reflects a slightly different atmospheric composition being used. More significant differences can be seen in the upper atmosphere, with most of the displayed species varying by several orders of magnitude between the models. We expect this to be primarily due to the difference in the stellar spectrum being applied to this atmosphere. It can be seen in Figure 4.3 that the general shape of the abundance profiles are very similar, except that our model predicts photochemistry to begin deeper into the atmosphere, a result consistent with the stronger UV spectrum of a G2V star penetrating further. The only other major difference seen in this figure is the profile of S in the upper atmosphere. We believe this to be as a result of differences in how the models treat molecular diffusion.

Our new network has also been used in Rimmer et al. (2021) to model sulfur chemistry on Venus. The model in that work produces results very similar to the observations of Venus's atmosphere, suggesting that the network is valid down to temperatures in the middle atmosphere of Venus; as low as 200 K.

In conclusion, after comparing our new sulfur model against the sulfur models from Wang et al. (2017) and Evans et al. (2018), we see both similarities and differences in the way we treated thermochemistry and photochemistry. We are confident in the accuracy of our thermochemistry after comparisons with the chemical equilibrium solver in Section 4.3.1. Also, our thermochemical results are very similar to those seen in Evans et al. (2018). Comparing photochemistry is more difficult, but overall the structure of the abundance profiles suggests the photochemistry between this work and Evans et al. (2018) is similar. The discrepancies that can be seen are likely due to differences in UV cross-sections and stellar spectrum.

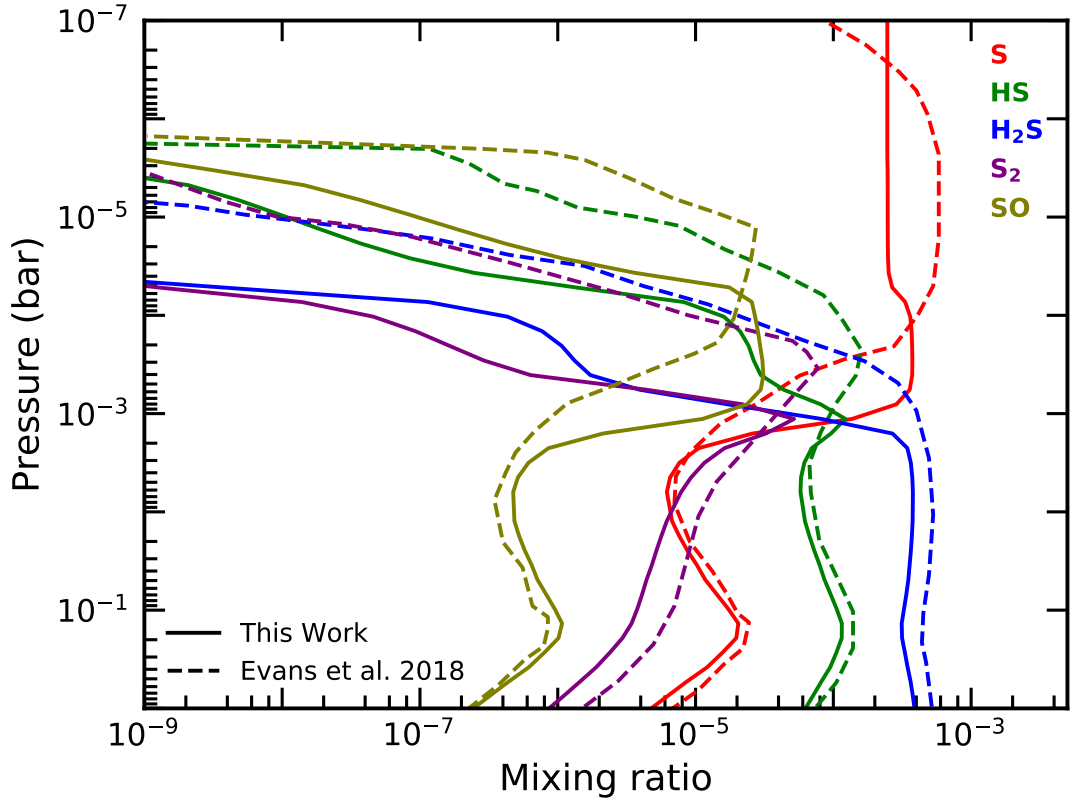

Fig. 4.3 A comparison between our network (solid lines) and the one presented in Evans et al. (2018) (but created by the network of Zahnle et al. (2016)) (dashed lines) for a model of WASP-121 b. The P-T profile for this model is taken from Evans et al. (2018), with constant $K_{zz} = 10^9\,\mathrm{cm^2\,s^{-1}}$, a gravity of $8.75\,\mathrm{m\,s^{-2}}$ and a metallicity $20\times$ solar. The UV spectrum applied to the top of the atmosphere is $5300\times$ Earth's insolation.

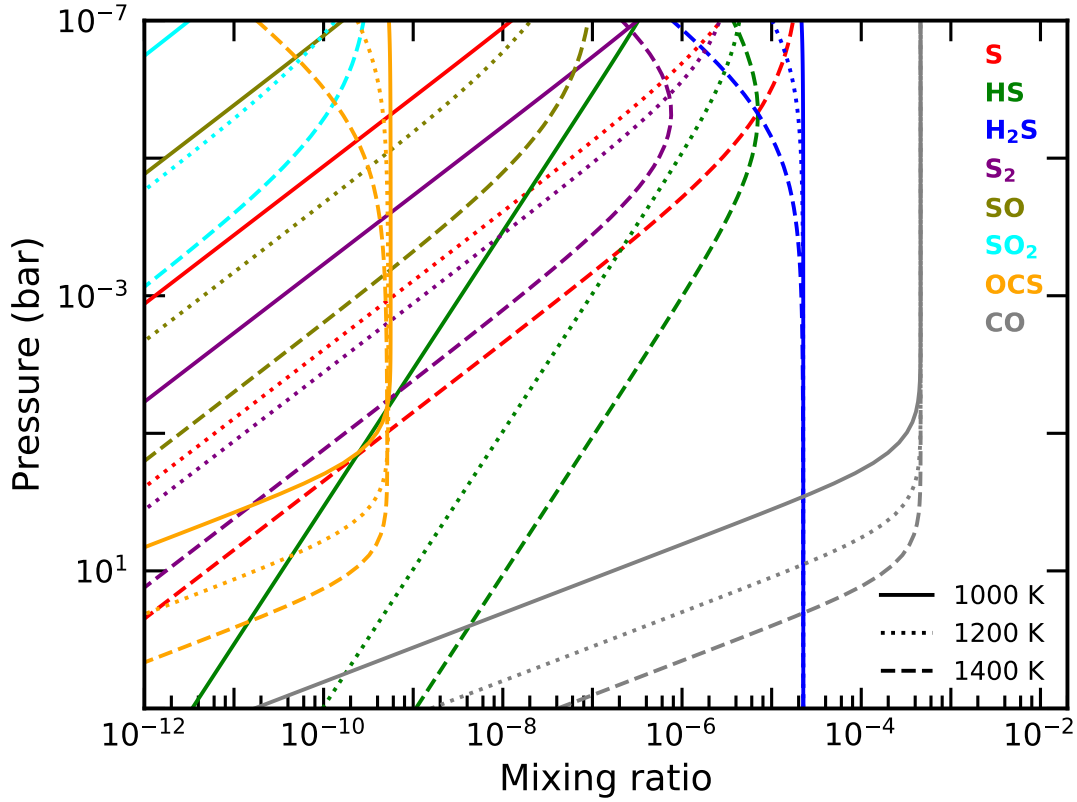

Fig. 4.4 Sulfur chemistry in three isothermal (1000K, 1200K and 1400K) hot Jupiter atmospheres in local thermodynamic equilibrium. This atmosphere has a solar metallicity and a gravity of $10\,\mathrm{m\,s^{-2}}$. It has no diffusion or photochemistry applied to it.

4.4 Sulfur in Hot Jupiters

In this section, we investigate sulfur chemistry in the atmosphere of hot Jupiters. We identify the major sulfur species throughout the atmosphere, and note how and why the abundance of these species change. We consider this change in relation to both the planet's temperature and other properties such as diffusion.

4.4.1 Local Thermochemical Equilibrium

To begin with, we investigate the simplest scenario for sulfur chemistry in hot Jupiters: An isothermal atmosphere model that is purely in local thermochemical equilibrium, without any form of diffusion or photochemistry.

In Figure 4.4 we show comparisons of three isothermal atmospheres in chemical equilibrium. The isothermal temperatures of these atmospheres are 1000 K (solid), 1200 K (dotted) and 1400 K (dashed). All three have a solar metallicity and a gravity of $10\,\mathrm{m\,s^{-2}}$. We plot carbon monoxide, CO, and sulfur bearing species that have a mixing ratio greater than 10^{-10} at any point in the atmosphere. In this manner we can show the full scope of sulfur chemistry throughout the entire atmosphere.

The first point of note is the preference of sulfur to form H_2S. At all temperatures shown, H_2S is the primary carrier of sulfur throughout the majority of the atmosphere, with an abundance of 2×10^{-5} for most of the deep atmosphere. It is only at low pressures along the hottest isotherms where this changes, with the primary sulfur carrier becoming atomic S. The reactions that set these abundances are

$$\begin{aligned} \mathrm{S} + \mathrm{H_2} &\rightarrow \mathrm{H} + \mathrm{HS} \\ \mathrm{HS} + \mathrm{H_2} &\rightarrow \mathrm{H} + \mathrm{H_2S} \\ 2\,\mathrm{H} + \mathrm{M} &\rightarrow \mathrm{H_2} + \mathrm{M} \\ \textbf{Net}: \mathrm{S} + \mathrm{H_2} &\rightarrow \mathrm{H_2S}. \end{aligned} \tag{4.1}$$

High temperatures favour the left hand side of this net equation, preferring to dissociate H_2S to its constituent H_2 and S. In comparison, high pressures favour the formation of H_2S from H_2 and S. This is why S becomes the most abundant sulfur species only at very low pressures along the high temperature isotherms.

The mercapto radical involved in this reaction, HS, is also of interest, as it acts as an intermediary between S and H_2S. HS forms a steady pool that quickly reacts to either S or H_2S, depending on which is more thermodynamically favoured. Generally, the higher temperature atmospheres favour HS. In all three models, lower pressure increases the abundance of HS. This is unsurprising since, as previously mentioned, the higher temperature and lower pressure favour the dissociation of the large pool of H_2S, creating more HS as a result. Although, at the very top of the atmosphere, above 10^{-7} bar, this changes. Here, the abundance of HS in the 1400 K atmosphere decreases with pressure and drops below the abundance of HS in the 1200 K atmosphere. This result arises from atomic S now being the primary sulfur carrier, since its production is favoured by both temperature and pressure. With the majority of sulfur now being in S, the equilibrium abundance of HS decreases.

Both sulfur oxides, SO and SO_2, follow similar patterns throughout the atmosphere. They increase in abundance with decreasing pressure, and are more abundant in higher temperature atmospheres. There are two dominant production pathway for SO. At high pressures in the lower temperature atmospheres, the pathway is

$$\begin{aligned} H_2O + M &\rightarrow OH + H + M \\ H_2S + H &\rightarrow H_2 + HS \\ HS + H &\rightarrow S + H_2 \\ S + OH &\rightarrow H + SO \\ \textbf{Net} : H_2S + H_2O &\rightarrow 2H_2 + SO, \end{aligned} \tag{4.2}$$

while in the higher temperature atmosphere, or in any of the modelled atmospheres at low pressures, the pathway is

$$\begin{aligned} H_2O + M &\rightarrow OH + H + M \\ OH + H &\rightarrow O + H_2 \\ H_2S + O &\rightarrow H + HSO \\ HSO &\rightarrow H + SO \\ H + H + M &\rightarrow H_2 + M \\ \textbf{Net} : H_2S + H_2O &\rightarrow 2H_2 + SO. \end{aligned} \tag{4.3}$$

In both pathways, the net reaction is unchanged, with the only differences being in the route taken in the pathway.

For SO_2 the pathways are

$$\begin{aligned} H_2O + H &\rightarrow OH + H \\ SO + OH &\rightarrow HOSO \\ HOSO &\rightarrow SO_2 + H \\ H + H + M &\rightarrow H_2 + M \\ \textbf{Net} : SO + H_2O &\rightarrow SO_2 + H_2, \end{aligned} \tag{4.4}$$

for the deep atmosphere, or more directly

$$\begin{aligned} H + H_2O &\rightarrow OH + H_2 \\ SO + OH &\rightarrow SO_2 + H \\ \textbf{Net} : SO + H_2O &\rightarrow SO_2 + H_2, \end{aligned} \tag{4.5}$$

for the upper atmosphere.

The sulfur molecules HSO and HOSO referenced in these pathways are not shown in Figure 4.4 due to their very low abundance. The production of both SO and SO_2 starts with the destruction of H_2S by an oxygen atom, O. This produces the short lived species HSO

that quickly dissociates into SO. SO subsequently reacts with the hydroxyl radical, OH. At pressures greater than 10^{-1} bar, this reaction forms the very short lived species HOSO, that then dissociates into SO_2. At pressures less than 10^{-1} bar, SO and OH react directly to form SO_2. The production of SO is significantly faster than the reaction rate of SO with OH. As a result, the equilibrium abundance of SO is much larger than that of SO_2. Near the top of the atmosphere, above 10^{-6} bar in the 1400 K isothermal atmosphere, the abundances of SO and SO_2 stop increasing with decreasing pressure. This happens due to the H_2S abundance dropping. It is now no longer as available to start the production pathway of SO and SO_2.

The pathway producing the sulfur molecule OCS is

$$\begin{aligned} H_2S + H &\rightarrow HS + H_2 \\ HS + CO &\rightarrow OCS + H \\ \textbf{Net} : H_2S + CO &\rightarrow OCS + H_2. \end{aligned} \tag{4.6}$$

In the deep atmosphere, below 10^{-1} bar, the abundance of OCS is controlled by the abundance of CO. Above this pressure, there is a zone for which both H_2S and CO have a constant abundance. This leads OCS to stay at a constant abundance at these pressures. Above 10^{-4} bar for the 1400 K atmosphere, and 10^{-6} bar for the 1200 K atmosphere, the drop in the abundance of H_2S results in the mixing ratio of OCS decreasing at a similar rate.

The allotrope of sulfur, S_2, is produced by the pathway

$$\begin{aligned} H_2S + H &\rightarrow HS + H_2 \\ HS + S &\rightarrow S_2 + H \\ \textbf{Net} : H_2S + S &\rightarrow S_2 + H_2. \end{aligned} \tag{4.7}$$

Thus, the abundance of S_2 is controlled by the abundance of S and HS (and therefore H_2S). This results in a general increase of abundance as pressure decreases. The exception is for the case of the 1400 K isotherm, where the drop in abundance of H_2S and HS above 10^{-6} bar leads to a decrease in the mixing ratio of S_2.

4.4.2 Disequilibrium

The atmospheres of most planets are not in chemical equilibrium at low pressure ($< 10^{-3}$ bar). Therefore it is important to consider how the disequilibrium effects of diffusion and photochemistry can impact the expected sulfur chemistry in a planet's atmosphere. The lowest pressure shown for our disequilibrium figures is 10^{-7} bar. This is theoretically high enough in the atmosphere that sulfur-ionizing photons could form an ionosphere. The consideration of

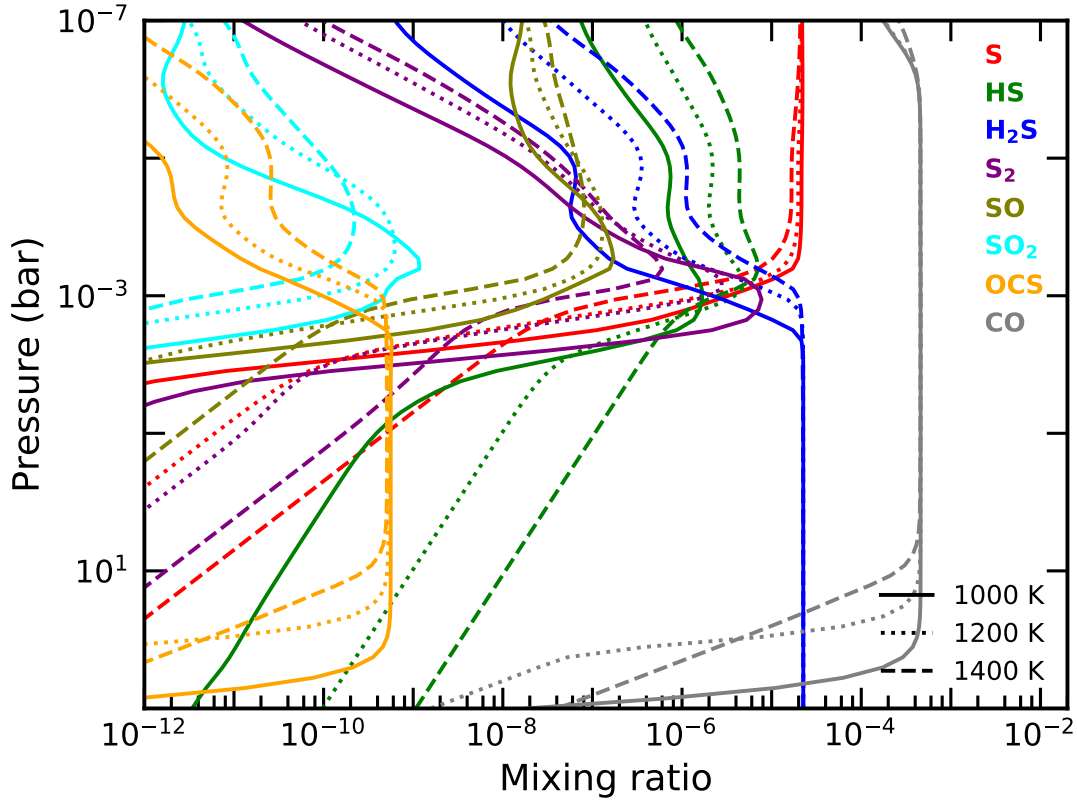

Fig. 4.5 Sulfur chemistry in three isothermal (1000K, 1200K and 1400K) hot Jupiter atmospheres in steady-state. This atmosphere has a solar metallicity, a gravity of $10\,\mathrm{m\,s^{-2}}$, constant $K_{zz} = 10^9\,\mathrm{cm^2\,s^{-1}}$ and a UV flux $10\times$ Earth's.

ion-chemistry is outside the scope of this work, but it is important to note that the top of our modelled atmospheres do not include this effect.

In Figure 4.5 we show the same three isothermal atmospheres as in the previous section: isotherms of 1000 K (solid), 1200 K (dotted) and 1400 K (dashed). Once again, all three have a solar metallicity and a gravity of $10\,\mathrm{m\,s^{-2}}$. All of these atmospheres now have a constant eddy diffusion $K_{zz} = 10^9\,\mathrm{cm^2\,s^{-1}}$. They also have a UV spectrum applied to the top of the atmosphere of $10\times$ Earth's received solar flux.

In the deep atmosphere, below about 10^{-1} bar, the abundances are near identical to the equilibrium results presented in the previous section. At this depth, the high pressure ensures that the reaction rates are fast enough that the disequilibrium effects of diffusion and photo-dissociation do not have a significant impact on the chemistry previously presented.

Higher in the atmosphere, above 10^{-3} bar, we start to see the significance of disequilibrium chemistry. Many of the sulfur molecules are susceptible to photo-dissociation.

Once again H_2S is of particular note. At 10^{-3} bar it is rapidly dissociated by free H radicals that are produced by photolysis, and then diffuse down from higher in the atmosphere

$$\begin{aligned} H_2O + h\nu &\rightarrow OH + H \\ H_2 + OH &\rightarrow H_2O + H \\ H_2S + H &\rightarrow HS + H_2 \\ HS + H &\rightarrow S + H_2 \\ \textbf{Net} &: H_2S \rightarrow S + H_2. \end{aligned} \tag{4.8}$$

This effect occurs at all temperatures. Although, in the colder models, we see the abundance of H_2S driven much further away from its equilibrium value, by more than two orders of magnitude, compared to the hotter models. This is because of the longer chemical timescales at lower temperatures, which slows the recombination reactions. Overall, the rapid destruction of H_2S allows for full dissociation to atomic S. This results in S being the primary sulfur species at all temperatures and pressures above 10^{-3} bar.

The production of a large available pool of S has knock-on effects for the abundance of SO and SO_2. Above 10^{-3} bar the abundance of SO is controlled by the reaction chain of

$$\begin{aligned} SO + h\nu &\rightarrow S + O \\ H_2O + h\nu &\rightarrow OH + H \\ S + OH &\rightarrow SO + H \\ H + H + M &\rightarrow H_2 + M \\ \textbf{Net} &: H_2O \rightarrow H_2 + O, \end{aligned} \tag{4.9}$$

and SO_2 by a very similar chain

$$\begin{aligned} SO_2 + h\nu &\rightarrow SO + O \\ H_2O + h\nu &\rightarrow OH + H \\ SO + OH &\rightarrow SO_2 + H \\ H + H + M &\rightarrow H_2 + M \\ \textbf{Net} &: H_2O \rightarrow H_2 + O. \end{aligned} \tag{4.10}$$

Overall, both these reaction pathways act as a dissipative cycle that increases the abundance of atomic O in the atmosphere, while preventing SO and SO_2 from being permanently dissociated. The abundances of both SO and SO_2 are primarily determined by the amount of atomic S in the atmosphere. As a result the abundances of SO and SO_2 are nearly temperature

independent throughout the upper atmosphere: SO reaches abundances around 10^{-7}, while SO_2 is never greater than 10^{-9}.

S_2 is significantly affected by the introduction of disequilibrium chemistry. The large increase in both HS and S around 10^{-3} bar greatly boosts its production through the reaction

$$S + HS \rightarrow S_2 + H. \tag{4.11}$$

This is particularly prominent in the lower temperature isotherms. In the 1000 K atmosphere, the abundance of S_2 reaches nearly 10^{-5} (compared to only 10^{-10} at the same pressure and temperature in the local thermochemical equilibrium case). However, above 10^{-3} bar, it is rapidly photo-dissociated into S + S. The outcome is a quick drop-off in its abundance at all temperatures.

OCS is not greatly affected by the introduction of disequilibrium chemistry. Its abundance is still determined by the pathway shown in equation 4.6.

4.4.3 Diffusion Strength

It is important to understand how our choices for the parameters of the disequilibrium chemistry can affect the overall distribution of sulfur chemistry in planetary atmospheres. To that end, in Figure 4.6, we compare three atmospheric models of a 1200 K isothermal hot Jupiter with different strengths of eddy-diffusion, K_{zz}. We do so to test the sensitivity of sulfur chemistry to the strength of the vertical mixing in the atmosphere. We chose to use two extremes of diffusion, $K_{zz} = 10^6\,\mathrm{cm^2\,s^{-1}}$ (dashed) and $K_{zz} = 10^{12}\,\mathrm{cm^2\,s^{-1}}$ (solid), to understand the limiting cases for diffusion. We also include the previously used average case of $K_{zz} = 10^9\,\mathrm{cm^2\,s^{-1}}$ (dotted) as a comparison.

Immediately seen is that the weakest mixing, $K_{zz} = 10^6\,\mathrm{cm^2\,s^{-1}}$, does not differ greatly from the intermediate case of $K_{zz} = 10^9\,\mathrm{cm^2\,s^{-1}}$. This suggests that $K_{zz} = 10^9\,\mathrm{cm^2\,s^{-1}}$ is already sufficiently low that eddy-diffusion is having little effect upon sulfur chemistry.

For the strongest diffusion, $K_{zz} = 10^{12}\,\mathrm{cm^2\,s^{-1}}$, there are several significant differences to the abundance of sulfur molecules. Most of these effects stem from the diffusion quenching the H_2S, such that it stays as the most abundant sulfur molecule up until 10^{-5} bar. This results in a lower atomic S abundance, which has a knock-on effect of also lowering the abundance of both SO and SO_2.

The sulfur allotrope S_2 is also significantly affected by the stronger diffusion. Its abundance between 10^{-1} bar and 10^{-4} bar drops by up to two orders of magnitude compared to the weaker diffusion cases. This is largely caused by the S_2 diffusing higher into the atmosphere where it can be photo-dissociated, which causes the drop-off in abundance from 10^{-1} bar. Above

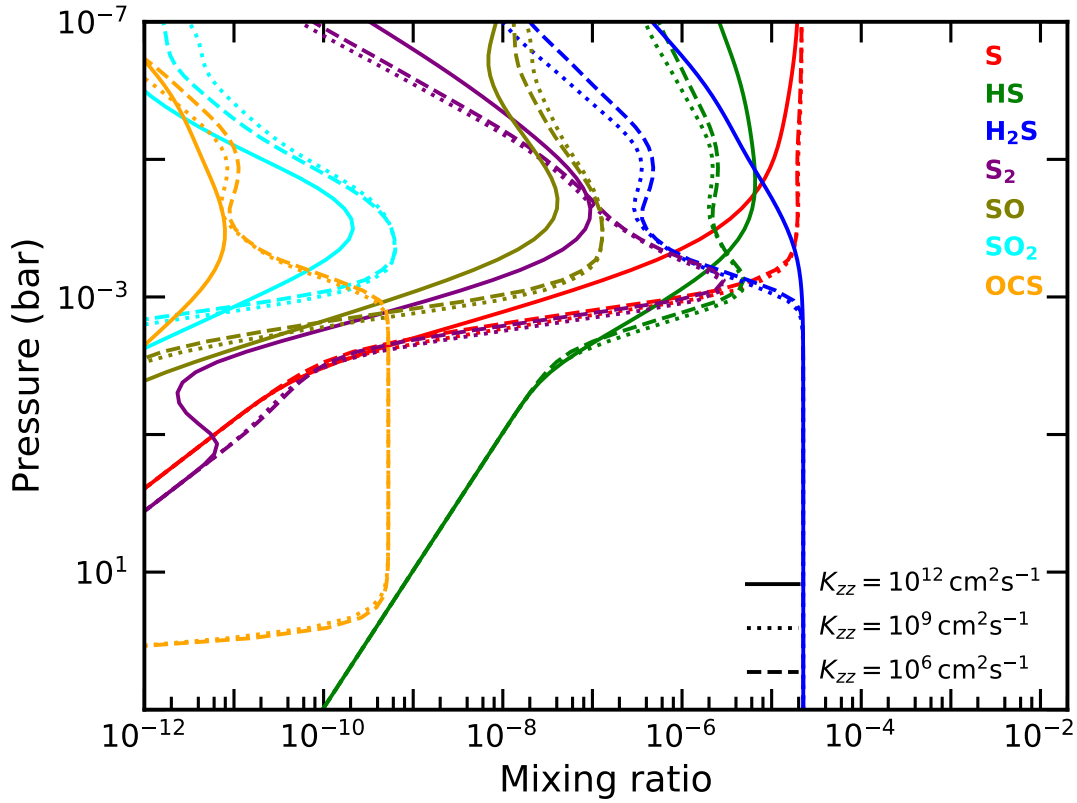

Fig. 4.6 Sulfur chemistry in a 1200 K isothermal hot Jupiter atmosphere. This model explores the sensitivity of sulfur chemistry to the strength of the vertical mixing, by comparing models with three different K_{zz} values. This atmosphere has a solar metallicity, a gravity of $10\,\mathrm{m\,s^{-2}}$ and has a UV spectrum $10\times$ Earth's applied to it.

10^{-4} bar, the stronger diffusion lifts the abundance of S_2 faster than it can be dissociated, to mixing ratios slightly above that of the weaker diffusion models.

Overall, the strength of the vertical mixing does not have much impact on most sulfur molecules. This conclusion is in line with previous studies by Zahnle et al. (2009) and Zahnle et al. (2016), in which they found that vertical mixing was only significant in lower temperatures due to how fast sulfur reactions occur. The atmospheres being studied in this work are sufficiently hot that the atmosphere reaches a steady-state balance between the thermochemical and photo-chemical elements. The effects of diffusion are thus negated unless the value of K_{zz} is increased to extreme values. At these extremes, the strong mixing may be able to keep H_2S detectable higher in the atmosphere, but strong mixing also significantly suppresses the abundance of S_2, preventing its abundance from reaching detectable levels.

4.4.4 UV Strength

We next examine how altering the strength of the UV flux being applied to the top of the model can alter the sulfur chemistry. While this is not a very realistic change to be made independent of all other parameters, (since the flux strength is most commonly set by the distance of the planet from the star, which would greatly impact the atmosphere's temperature), it is important to understand our network's sensitivity to changes in the rate of photochemistry. As such, we present three different models of a hot Jupiter with a 1200 K isothermal atmosphere in Figure 4.7. Two have extremes of UV irradiation at 100× Earth's (solid) and 1× Earth's (dashed). The other has 10× Earth's (dotted) irradiation, the same as previously used in this section.

Most species show no change deep in the atmosphere, below the 10^{-2} bar level. No species show any difference below 10^{-1} bar. This shows that even for extreme irradiation, the deepest parts of the atmosphere are difficult to move away from thermochemical equilibrium.

The species primarily affected by the change in UV flux is H_2S. Its abundance drops by an order of magnitude at 10^{-3} bar for the highest flux compared to the lowest flux. This also greatly impacts S at the same pressure. Its abundance is up to five orders of magnitude greater for the greatest flux compared to the smallest. This difference is only seen for a small pressure window however, and the abundance of S is very similar across all three fluxes above 10^{-4} bar.

In this same pressure window, the greater availability of S caused by the stronger flux allows the abundance of both SO and SO_2 to grow much larger than in the models with weaker fluxes. However, above 10^{-4} bar this is reversed as the available S becomes similar in all three models, resulting in the strongest UV model depleting SO and SO_2 by about an order of magnitude compared to the weakest UV model.

The comparative abundance of S_2 goes through several phases. Deep in the atmosphere, around 10^{-1} bar, the stronger UV flux can penetrate deep enough to begin to dissociate it into

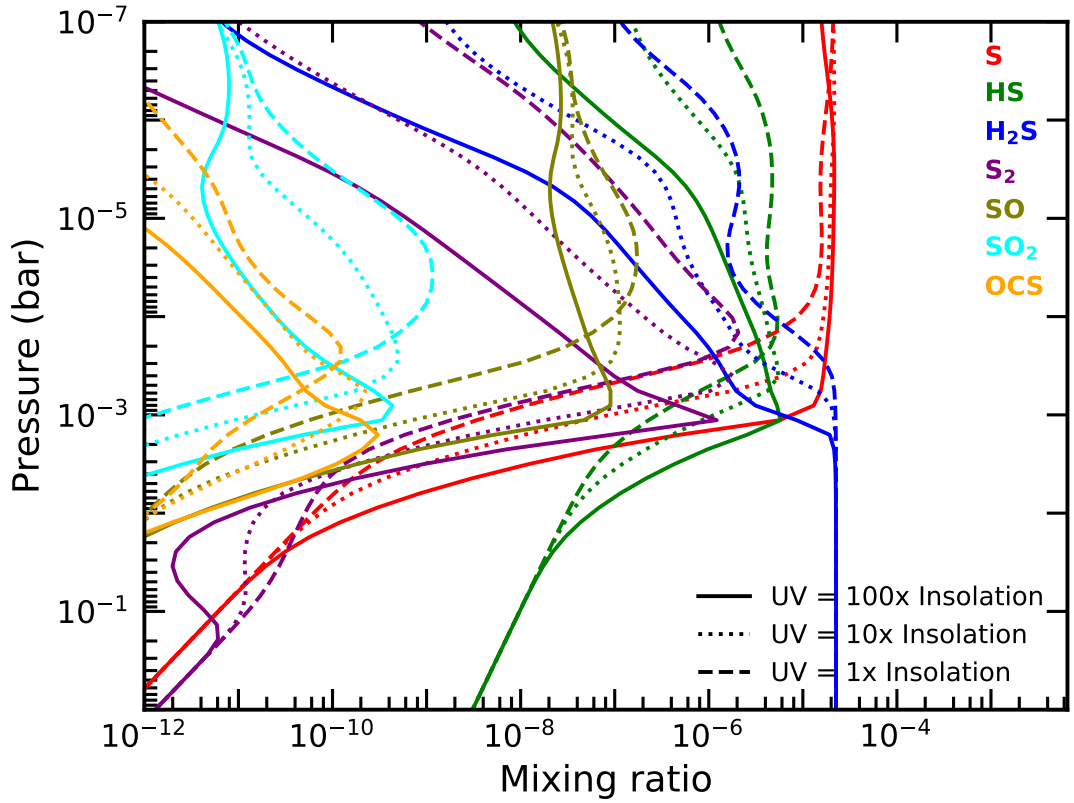

Fig. 4.7 Sulfur chemistry in a 1200 K isothermal hot Jupiter atmosphere. This model explores the sensitivity of sulfur chemistry to the strength of the UV flux, by comparing models with three different strength of UV. This atmosphere has a solar metallicity, $K_{zz} = 10^9\,\mathrm{cm^2\,s^{-1}}$ and a gravity of $10\,\mathrm{m\,s^{-2}}$.

S + S. However, not far above this, around 10^{-2} bar, the excess S that is produced by H_2S dissociation in the stronger UV cases is sufficient to boost the production of S_2 above its rate of photo-dissociation. Thus we see more S_2 in the stronger UV model, up until between 10^{-3} bar and 10^{-4} bar when the availability of atomic S equalises across all three models. Above this, the stronger UV flux once again dominates in dissociating S_2, resulting in its abundance being several orders of magnitude lower than in the weak UV model.

Overall, the strength of the UV flux simply shifts the abundance profiles deeper into the atmosphere. This happens because the stronger flux can penetrate deeper, with an increase of two orders of magnitude in UV flux able to push the profiles of sulfur molecules one order of magnitude deeper in pressure into the atmosphere.

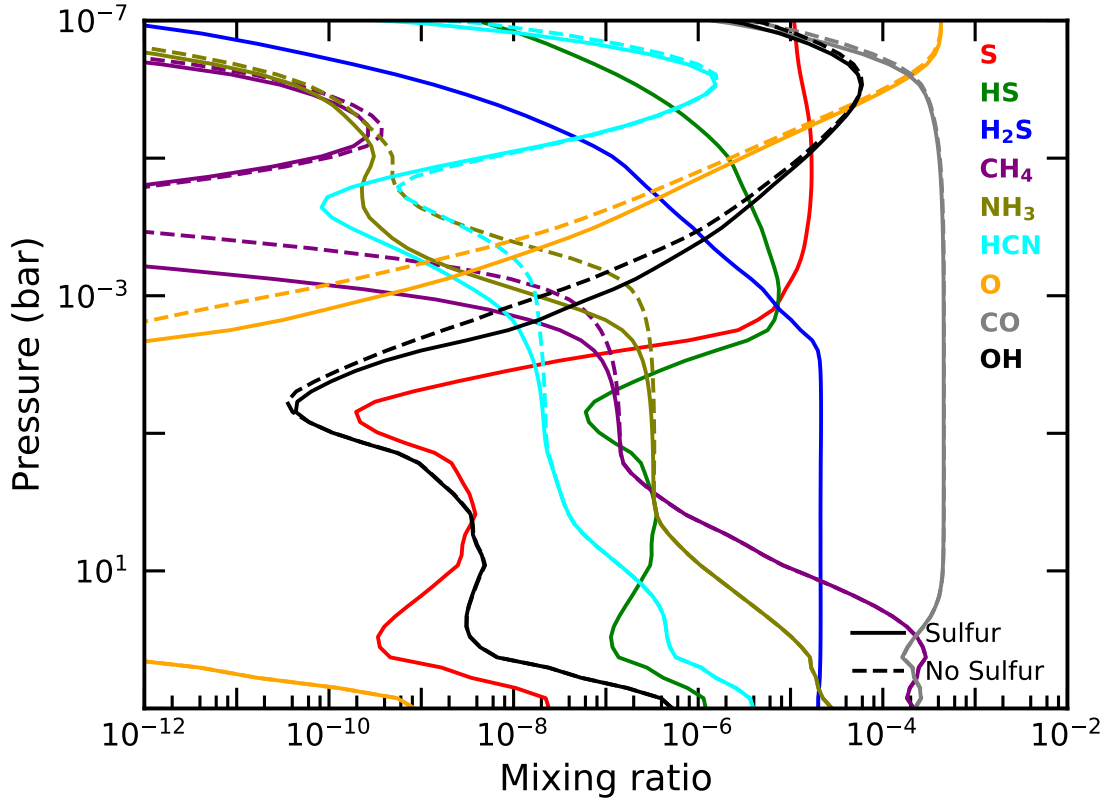

Fig. 4.8 A comparison of the abundance profiles for the hot Jupiter HD 209458b both with (solid lines) and without (dashed lines) our new sulfur network being included. This model uses the pressure - temperature profile and K_{zz} profile from Moses et al. (2011). It has solar metallicity, a gravity of $9.36\,\mathrm{m\,s^{-2}}$ and has a UV spectrum $800\times$ Earth's applied to it.

4.5 The Impact of Sulfur's Inclusion on Atmospheric Chemistry

In this section we investigate what effect the sulfur chemistry has upon the modelled composition of both the hot Jupiter HD 209458b and the warm Jupiter 51 Eri b. We compare atmospheric models of these planets with and without sulfur included in our network. In this way we isolate sulfur's impact, and examine the pathways in our network that lead to these chemical differences occurring.

4.5.1 HD 209458 b

We chose to examine the effects of sulfur chemistry on the atmosphere of the well studied hot Jupiter, HD 209458b. We have previously investigated this planet with LEVI in Chapter 2, and we return to it again. We do so now with our updated chemical model to discover how the inclusion of sulfur chemistry affects the predicted abundance profiles of this hot Jupiter's atmosphere.

As can be seen in Figure 4.8, we see no difference due to the inclusion of sulfur below 1 bar, in the deep atmosphere of the planet. At this depth, the abundance of the main sulfur species is set by the same reaction path as shown in Reaction 4.1. These reactions are very rapid and interactions with other species are slow by comparison, preventing sulfur from having any effect on CNO chemistry in the deep atmosphere.

Higher in the atmosphere, around 10^{-3} bar, sulfur has a much more significant effect on the CNO chemistry. In Figure 4.8, it can be seen that at this pressure the inclusion of sulfur decreases the predicted abundance of NH_3, CH_4 and HCN by up to two orders of magnitude.

Through a thorough and careful analysis of the fastest reaction pathways that cause the destruction of NH_3, CH_4 and HCN, we can identify how and why sulfur causes these differences. Figure 4.8 shows that sulfur chemistry changes where these three molecules stop being quenched. Molecules stop being quenched when the chemical timescale of the rate limiting step in the fastest destruction pathway becomes faster than the dynamical timescale in that region of the atmosphere. By examining this region for NH_3, CH_4 and HCN, and how it changes location with the inclusion of sulfur, we can determine why sulfur chemistry effects the abundance of CNO species within the atmosphere of a hot Jupiter. We use the chemical timescale as

$$\tau_{chem} = \frac{[X]}{d[X]/dt}, \tag{4.12}$$

where $[X]$ is the number density of the molecule we are investigating, either NH_3, CH_4 or HCN. $d[X]/dt$ is the change in number density of X with time, which is approximately the reaction rate of the rate limiting step in the fastest destruction pathway of $[X]$. We treat the dynamic timescale as

$$\tau_{dyn} = \frac{H_0 dH}{K_{zz}}, \tag{4.13}$$

where H_0 is the scale height of the atmosphere, dH is the thickness of one atmospheric layer in our model, and K_{zz} is the eddy-diffusion (Visscher and Moses 2011).

The most efficient pathway for the destruction of NH_3 leads the nitrogen to end up in the stable molecule N_2, via the following scheme:

$$
\begin{aligned}
2\,(\mathrm{NH_3} + \mathrm{H} &\rightarrow \mathrm{NH_2} + \mathrm{H_2}) \\
2\,(\mathrm{NH_2} + \mathrm{H} &\rightarrow \mathrm{NH} + \mathrm{H_2}) \\
\mathrm{NH} + \mathrm{H} &\rightarrow \mathrm{N} + \mathrm{H_2} \\
\mathrm{NH} + \mathrm{H_2O} &\rightarrow \mathrm{HNO} + \mathrm{H_2} \\
\mathrm{HNO} + \mathrm{H} &\rightarrow \mathrm{NO} + \mathrm{H_2} \\
\mathrm{NO} + \mathrm{N} &\rightarrow \mathrm{N_2} + \mathrm{O}\,(\mathrm{RL}) \\
\mathrm{O} + \mathrm{H_2} &\rightarrow \mathrm{OH} + \mathrm{H} \\
\mathrm{OH} + \mathrm{H_2} &\rightarrow \mathrm{H_2O} + \mathrm{H} \\
2\,(\mathrm{H_2} + \mathrm{M} &\rightarrow \mathrm{H} + \mathrm{H} + \mathrm{M}) \\
\textbf{Net}: 2\,\mathrm{NH_3} &\rightarrow \mathrm{N_2} + 3\,\mathrm{H_2},
\end{aligned}
\tag{4.14}
$$

with the reaction marked with (RL) being the rate limiting step in the pathway. We show the chemical timescales of each of the main steps in this pathway in Figure 4.9, as well as the dynamic timescale, all as a function of pressure. We compare these rates for both an atmosphere including sulfur and a sulfur free atmosphere. When we examine where τ_{chem} of the rate limiting step, NO + N $\rightarrow$ N_2 + O, becomes shorter than τ_{dyn}, we see a significant pressure difference between the sulfur and sulfur-free cases being examined. This pressure difference matches up precisely to where we see NH_3 quenching end in Figure 4.8; around 10^{-3} bar with sulfur, and 3×10^{-4} bar without sulfur.

The presence of NO in the rate limiting step is why the inclusion of sulfur significantly effects its timescale. Figure 4.9 also includes the timescale of NO photodissociation, and it can be seen that the presence of sulfur increases the timescale of this reaction by many orders of magnitude between 10^{-3} and 10^{-2} bar. This large slowing in the destruction of NO results in significantly more NO available in the atmosphere, greatly increasing the rate of the rate limiting step, resulting in the difference in the location of the end of quenching between the two models, and the lower abundance of NH_3 seen in the sulfur-containing model of HD 209458b.

The difference in the photochemical rate of NO arises from the UV shielding by sulfur molecules. In particular, we find that H_2S is responsible for most of the additional UV shielding when sulfur is introduced to the atmosphere. This can be seen in Figure 4.10 where we show the UV flux at different pressure levels, and compare to the same atmosphere but with transparent H_2S. We find that H_2S causes the available flux around 10^{-3} bar to drop by tens of orders of magnitude, depending on the wavelengths being examined. Thus H_2S blocks a large fraction of the incoming UV light, allowing NO to survive until higher in the atmosphere compared to a sulfur free atmosphere.

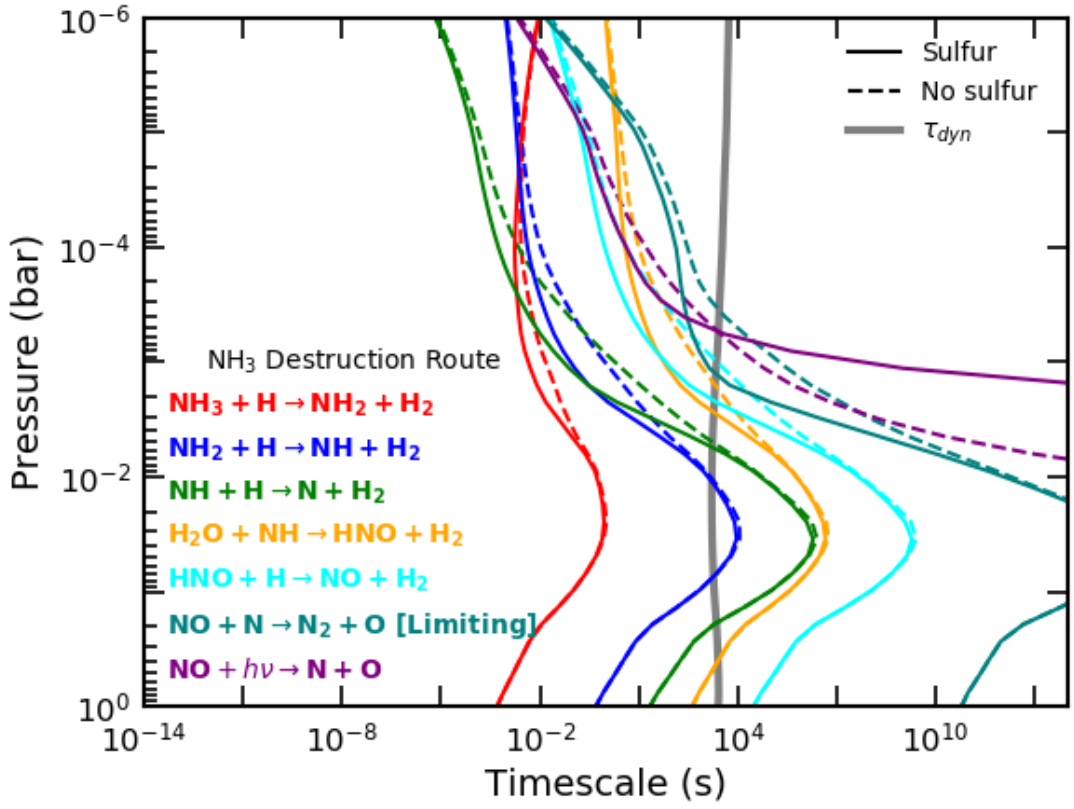

Fig. 4.9 A comparison of the chemical timescales in the most efficient pathway to destroy NH_3 in the atmosphere of HD 209458b, for both an sulfur-containing and a sulfur-free atmosphere. The dynamic timescale is also shown in this figure. The pressure at which the rate limiting step occurs on a shorter timescale than the dynamic timescale is where we expect to see quenching of NH_3 end in the atmosphere of HD 209458b. The increase in the timescale of the photodissociation of NO with the inclusion of sulfur is responsible for the difference in where the rate limiting drops below the dynamic timescale.

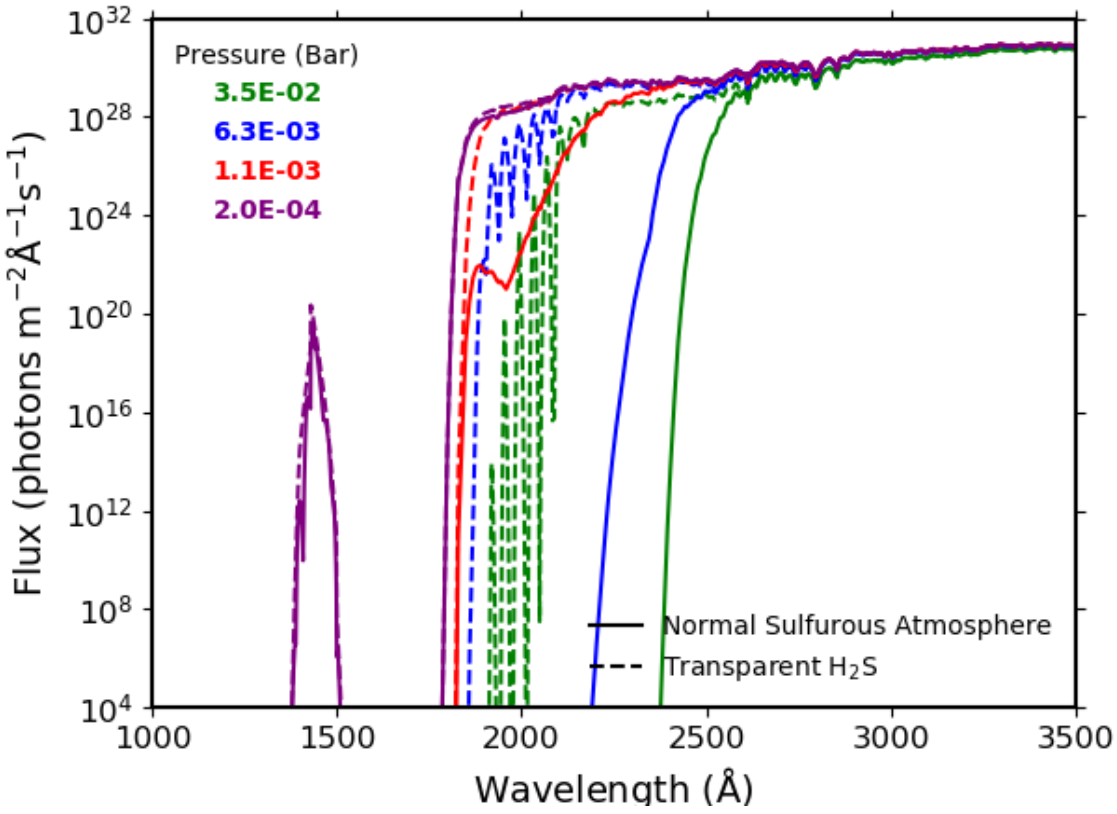

Fig. 4.10 The apparent flux at different pressures within the atmosphere of a sulfur-containing HD 209458b. To show the effect of sulfur shielding in this atmosphere, we compare the normal flux to the flux if H_2S was transparent.

When we examine the dominant destruction pathway for CH_4, we find that the carbon tends to end up in CO via;

$$\begin{aligned} CH_4 + H &\rightarrow CH_3 + H_2 \\ CH_3 + OH &\rightarrow CH_2O + H_2 \,(\mathrm{RL}) \\ CH_2O + H &\rightarrow CHO + H) \\ CHO + H &\rightarrow CO + H_2 \\ H_2O + H &\rightarrow OH + H_2 \\ 2\,(H_2 + M &\rightarrow H + H + M) \\ \textbf{Net} : CH_4 + H_2O &\rightarrow CO + 3\,H_2, \end{aligned} \tag{4.15}$$

with the reaction marked as (RL) again being the rate limiting step in the this reaction pathway. We show the main timescales of this reaction pathway in Figure 4.11. Once again we see the rate limiting step's timescale become smaller than the dynamic timescale at different pressures in a sulfur-containing vs. a non-sulfur-containing atmosphere. The explanation for this lies within a different set of reactions:

$$\begin{aligned} SO + h\nu &\rightarrow S + O \\ O + H_2 &\rightarrow OH + H \\ S + OH &\rightarrow SO + H. \end{aligned} \tag{4.16}$$

In a sulfur-containing atmosphere, the photodissociation of SO produces O significantly faster than any other reaction between 10^{-3} and 10^{-4} bar. This results in a corresponding rate increase in the reaction $O + H_2 \rightarrow OH + H$. The timescales of both of these reactions are also shown in Figure 4.11. The result of these rate increases can be seen in Figure 4.8, where both O and OH have their abundances increased by at least an order of magnitude around 10^{-3} bar. The rate limiting step in the destruction of CH_4 is dependant on the OH abundance. Thus, the consequence of an increase in OH abundance is that the timescale of the rate limiting step in a sulfur-containing atmosphere becomes shorter than the dynamic timescale deeper in the atmosphere. This leads to the quenching of CH_4 ending deeper in the atmosphere, and the difference in abundance between sulfur-containing and non-sulfur-containing atmosphere, as seen in Figure 4.8.

We have found the most efficient pathway for the destruction of HCN to be via the route:

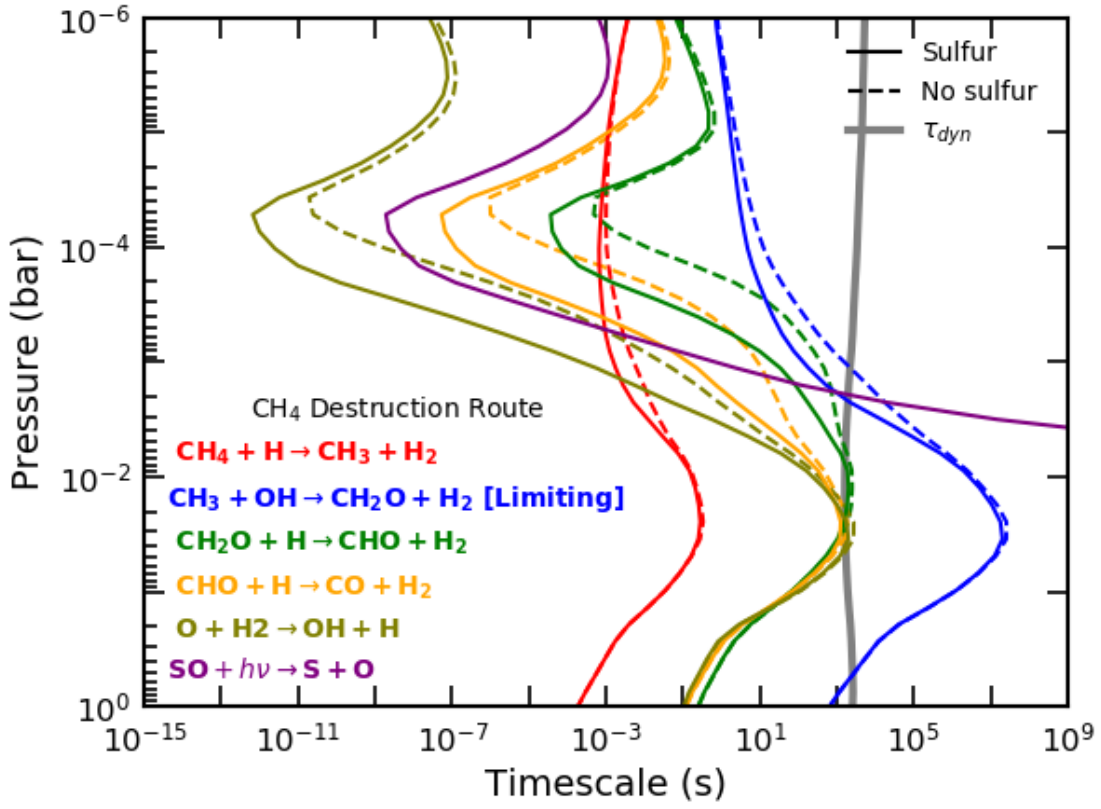

Fig. 4.11 A comparison of the chemical timescales in the most efficient pathway to destroy CH_4 in the atmosphere of HD 209458b, for both an sulfur-containing and a sulfur-free atmosphere. The dynamic timescale is also shown in this figure. The pressure at which the rate limiting step occurs on a shorter timescale than the dynamic timescale is where we expect to see quenching of CH_4 end in the atmosphere of HD 209458b. The photodissociation of SO causes a 30× increase in available O, which greatly increases the rate that O becomes OH, and thus is responsible for the change in the rate limiting step of this reaction pathway.

$$\begin{aligned}
\mathrm{HCN} + \mathrm{M} &\rightarrow \mathrm{HNC} + \mathrm{M} \\
\mathrm{HNC} + \mathrm{OH} &\rightarrow \mathrm{HNCO} + \mathrm{H}\,(\mathrm{RL}) \\
\mathrm{HNCO} + \mathrm{H} &\rightarrow \mathrm{CO} + \mathrm{NH_2} \\
\mathrm{NH_2} + \mathrm{H_2} &\rightarrow \mathrm{NH_3} + \mathrm{H} \\
\mathrm{H_2O} + \mathrm{H} &\rightarrow \mathrm{OH} + \mathrm{H_2} \\
\textbf{Net} : \mathrm{HCN} + \mathrm{H_2O} &\rightarrow \mathrm{CO} + \mathrm{NH_3},
\end{aligned} \tag{4.17}$$

with the rate limiting step marked as (RL). The rates for this pathway are shown in Figure 4.12. The explanation for the difference in abundance of HCN in sulfur-containing and non-sulfur-containing atmospheres follows the same reasoning as for CH_4. Once again, the rate limiting step contains OH, and thus Reactions 4.16 explain why the inclusion of sulfur increases the abundance of OH, and thus the increase the rate at which HCN is destroyed.

Overall, the change in the abundance of both HCN and CH_4 with the inclusion of sulfur show the catalytic role that sulfur chemistry can have in planetary atmospheres (as also noted by Zahnle et al. 2016).

Figure 4.8 shows that, at pressures lower than 10^{-5} bar, the effects of sulfur once again become insignificant. Above this height, H_2S begins to drop in abundance, making the shielding of NO less effective. This results in the sulfur-containing and non-sulfur-containing photodissociation rates of NO approach similar rates once more, such that the overall destruction rate of NH_3 is now approximately the same in both models. Additionally, above this height, SO is no longer the fastest producer of O, with other reactions such as OH photodissociation becoming more dominant. As such, both sulfur-containing and non-sulfur-containing destruction rates of CH_4 and HCN become similar. In consequence, the very upper atmospheres of hot Jupiters that contain sulfur look nearly indistinguishable from those without sulfur.

There is potential for detecting the differences caused by the inclusion of sulfur in hot Jupiters' atmospheres. There has already been evidence for CH_4 (Guilluy et al. 2019) and HCN (Hawker et al. 2018; Cabot et al. 2019) detections in the atmosphere's of hot Jupiters. Most retrievals identify species, and their abundances, around the pressure of 10^{-3} bar. Thus, it should be possible to detect the drop in abundance of these molecules due to sulfur. However, the pressure range over which there is an identifiable difference due to sulfur is rather limited. Any investigated spectra of this planet would need to be very precise, more so than any currently obtainable, and thus we will need to rely on future facilities with greater resolving power (e.g., JWST, ARIEL) Tsai et al. 2021.

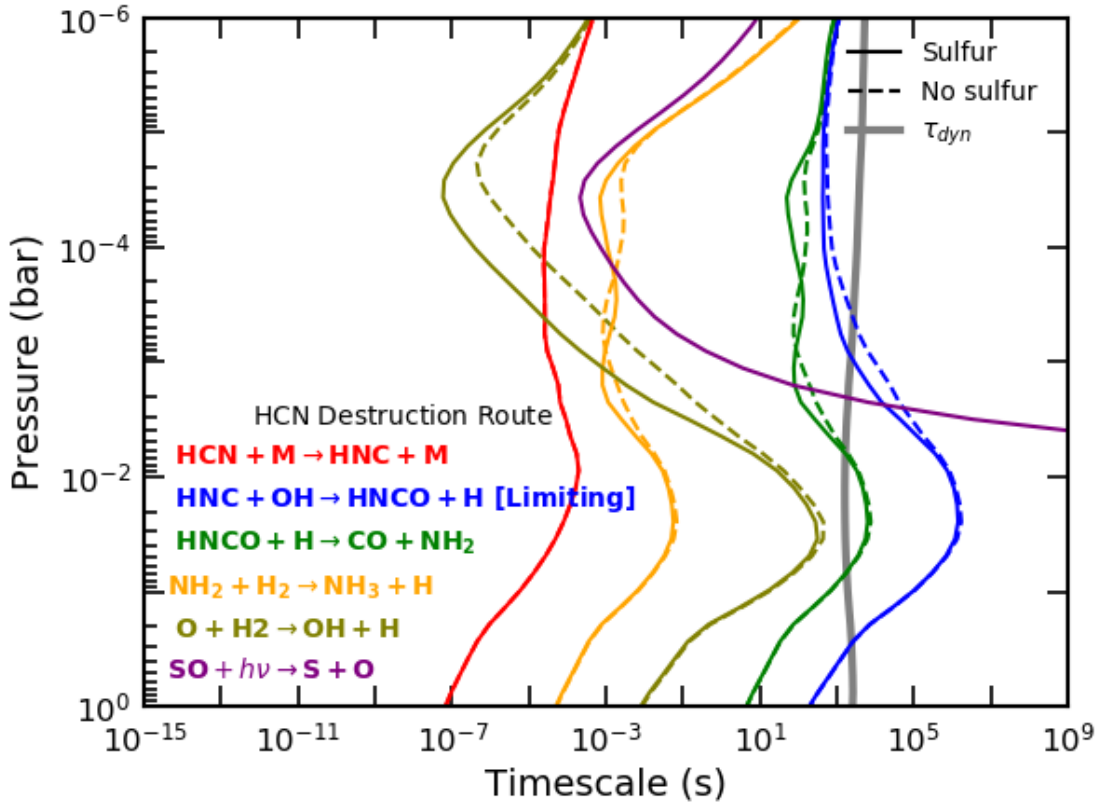

Fig. 4.12 A comparison of the chemical timescales in the most efficient pathway to destroy HCN in the atmosphere of HD 209458b, for both an sulfur-containing and a sulfur-free atmosphere. The dynamic timescale is also shown in this figure. The pressure at which the rate limiting step occurs on a shorter timescale than the dynamic timescale is where we expect to see quenching of HCN end in the atmosphere of HD 209458b. The photodissociation of SO causes a 30× increase in available O, which greatly increases the rate that O becomes OH, and thus is responsible for the change in the rate limiting step of this reaction pathway.

4.5.2 Warm Jupiters

Previously, there has been discussion in the literature about how sulfur on warm Jupiters may affect the abundance of species in the atmosphere of these planets. Of particular note is the warm Jupiter 51 Eri b, which both Moses et al. (2016) and Zahnle et al. (2016) have modelled in the past. Moses et al. (2016) ran models without any sulfur in the atmosphere, while Zahnle et al. (2016) ran models with sulfur. Both works studied the chemistry of 51 Eri b in great detail, both with and without sulfur. What is of particular interest though are the differences found between the two models. As Moses et al. (2016) notes, they find up to two orders of magnitude more CO_2 than Zahnle et al. (2016) for otherwise identical conditions. Thus, our focus in this section will be on examining the warm Jupiter 51 Eri b with both our sulfur-containing and non-sulfur-containing models to determine if sulfur is responsible for this difference, and, if it is, why.

To begin this section, we directly compare our model for the atmosphere of 51 Eri b to that of Moses et al. (2016) and Zahnle et al. (2016) as a benchmark for whether differences in the models themselves could be responsible for the difference in CO_2 abundance. The P-T profile for 51 Eri b is shown in Figure 4.13. In Figure 4.14 we compare our sulfur free model to the model from Moses et al. (2016), using the pressure temperature profile, K_{zz} profile and stellar UV flux also from Moses et al. (2016). In Figure 4.15 we compare our sulfur-containing model to the model from Zahnle et al. (2016). We use the same temperature profile and UV flux, but with a constant $K_{zz} = 10^7\,\mathrm{cm^2\,s^{-1}}$ to match the conditions used in Zahnle et al. (2016). The atmosphere of 51 Eri b in both models is treated as having solar metallicity and a constant gravity of $32\,\mathrm{m\,s^{-2}}$. Since the temperature of 51 Eri b falls below 500 K, the lower limit for convergence of our model, LEVI, we solve for this atmosphere using ARGO, a code developed by Rimmer and Helling 2016, that is better suited to model lower temperature atmospheres.

Figure 4.14 shows a close match between our model and that of Moses et al. (2016) for the carbon species, though we do find significantly less NH_3 and significantly more OH due to rate differences between our networks. Our comparison with Zahnle et al. (2016) in Figure 4.15 shows large differences of at least an order of magnitude in the abundance of all of the sulfur species. Additionally, throughout much of the lower atmosphere, below 10^{-4} bar, we find nearly an order of magnitude more CO_2 than Zahnle et al. (2016). This negates most of the difference in abundance of CO_2 that we initially expected to find between sulfur-containing and non-sulfur-containing models in the deeper atmosphere when comparing Moses et al. (2016) and Zahnle et al. (2016).

However, in Figure 4.16 we compare two models, with and without sulfur, both using a constant $K_{zz} = 10^7\,\mathrm{cm^2\,s^{-1}}$. Our results clearly show that while the CO_2 abundance in both models below 10^{-4} bar are similar, above this pressure, significant differences appear. In a

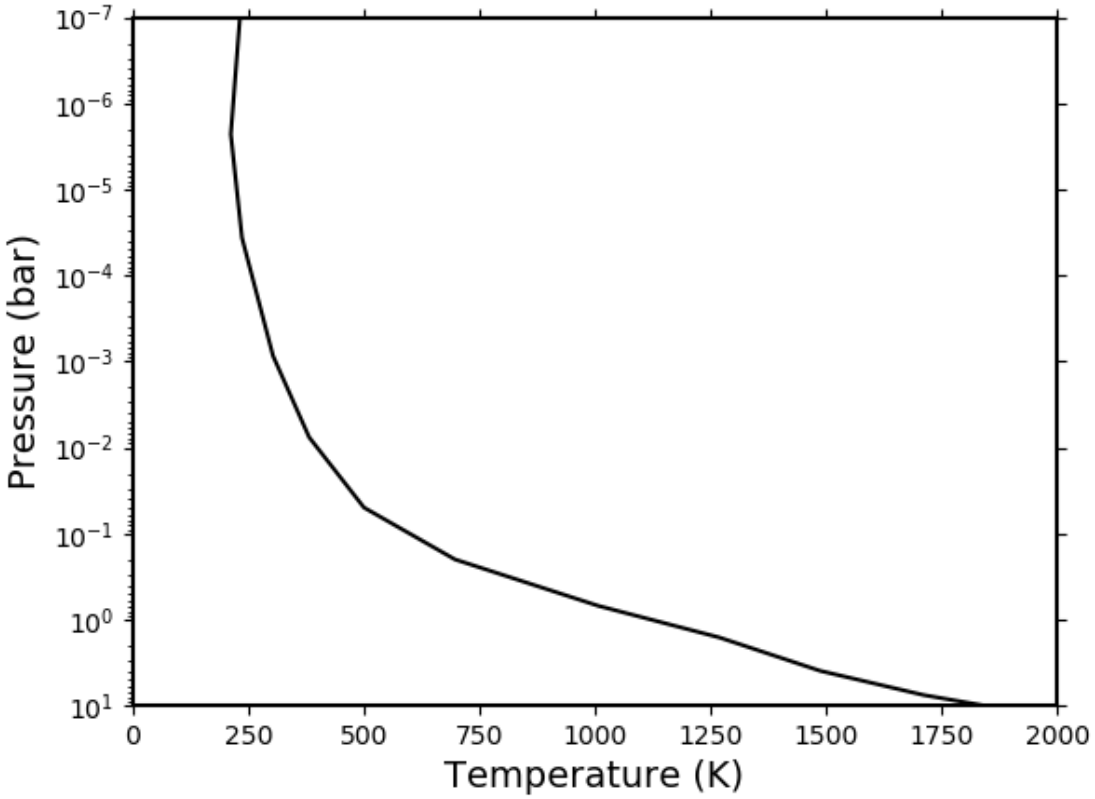

Fig. 4.13 The P-T profile of 51 Eri b, based upon the profile shown in Moses et al. (2016).

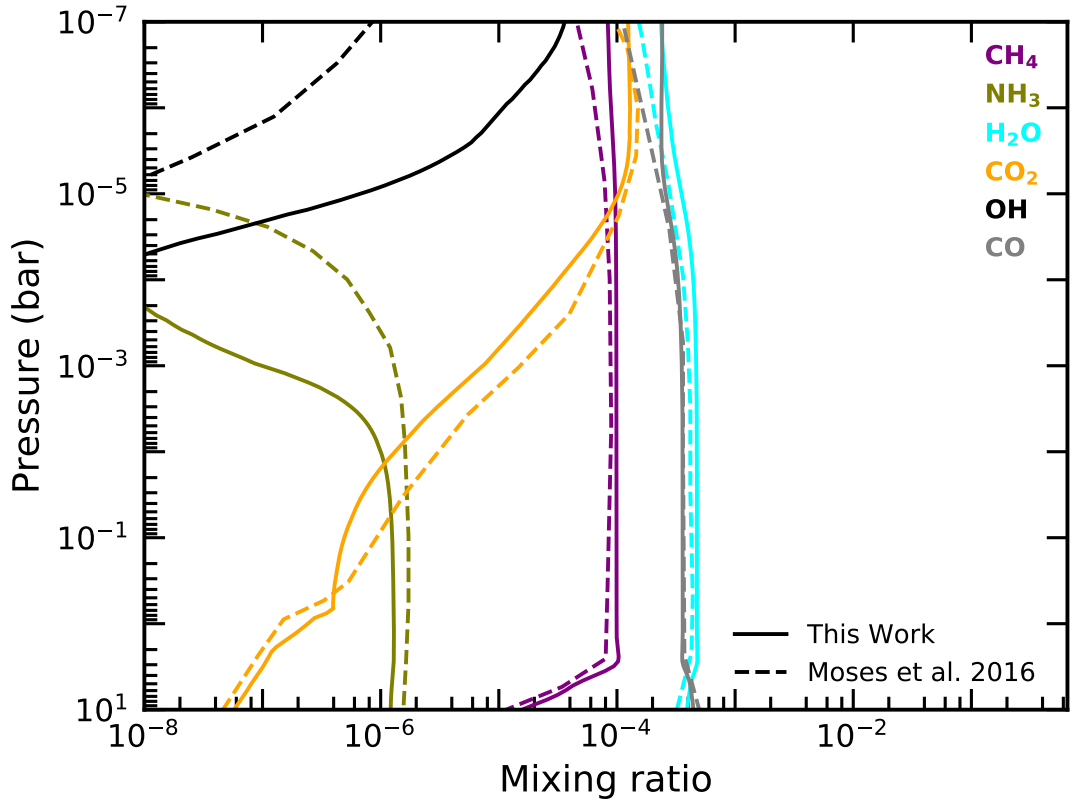

Fig. 4.14 A comparison of the abundance profiles for the warm Jupiter 51 Eri b. The solid lines are the sulfur free model from this work and the dashed lines are the model from Moses et al. (2016). We used the temperature profile, K_{ZZ} profile and UV flux profile from Moses et al. (2016). The planet has a gravity of $32\,\mathrm{ms}^{-2}$ and a solar metallicity.

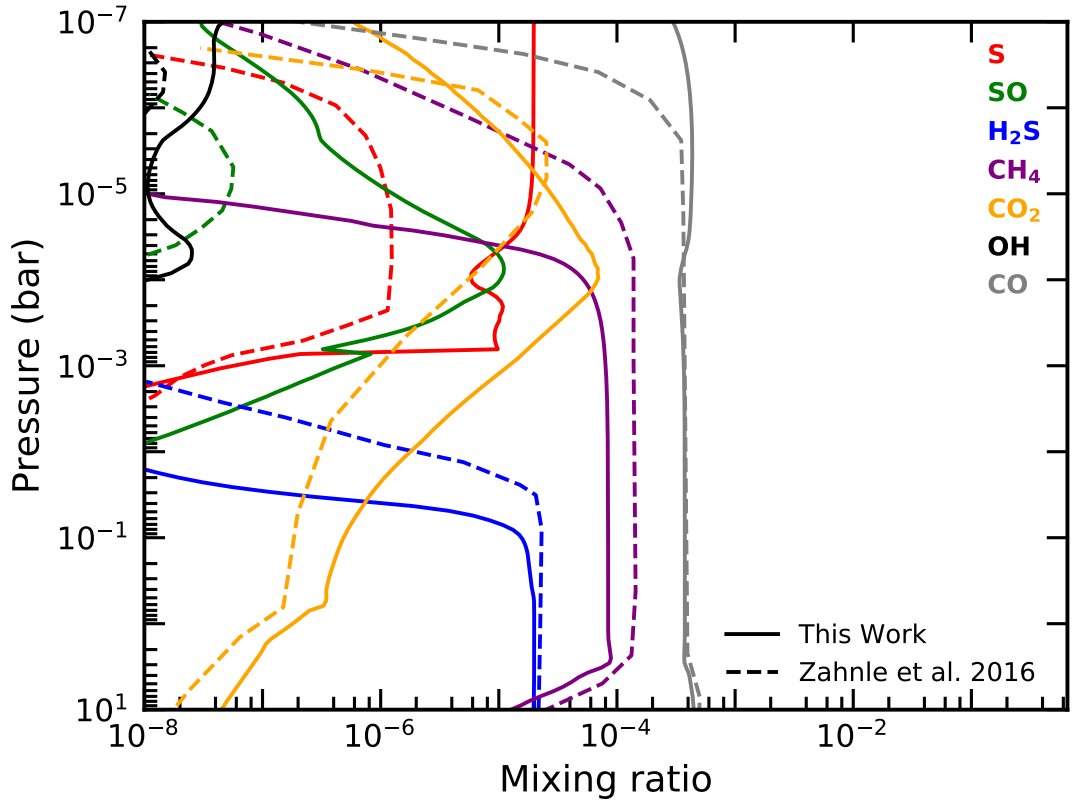

Fig. 4.15 A comparison of the abundance profiles for the warm Jupiter 51 Eri b. The solid lines are the sulfur-containing model from this work and the dashed lines are the model from Zahnle et al. (2016). We used the temperature profile and UV flux profile from Moses et al. (2016), and used a constant $K_{zz} = 10^7\,\mathrm{cm^2\,s^{-1}}$. The planet has a gravity of $32\,\mathrm{m\,s^{-2}}$ and a solar metallicity.

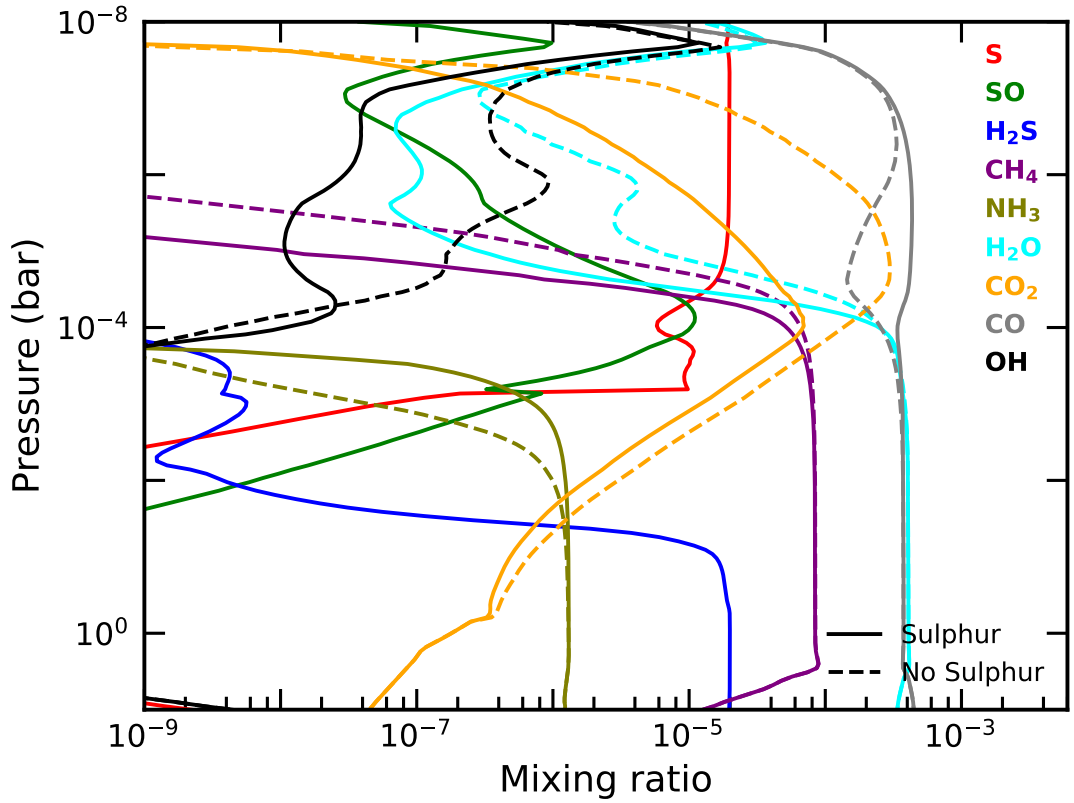

Fig. 4.16 A comparison of the abundance profiles for a warm Jupiter model both with (solid lines) and without (dashed lines) our new sulfur network being included. This warm Jupiter uses the P-T profile and UV spectrum from Moses et al. (2016). It has a gravity of $32\,\mathrm{m\,s^{-2}}$, a solar metallicity and a constant $K_{zz} = 10^7\,\mathrm{cm^2\,s^{-1}}$.

sulfur-containing atmosphere CO_2 is significantly depleted, with its peak abundance five times less than in a non-sulfur-containing atmosphere. This is less than the difference seen between Zahnle et al. (2016) and Moses et al. (2016). Our results for CO_2 overall agree better with Moses et al. (2016), both with and without sulfur. However, the reason for the decrease in CO_2 abundance with the inclusion of sulfur is the effect of the products of H_2S photo-dissociation on the abundance of OH. Both with and without sulfur, CO_2 is produced by the following reactions

$$\begin{aligned} H_2O + h\nu &\rightarrow OH + H, \\ CO + OH &\rightarrow CO_2 + H, \\ H + H + M &\rightarrow H_2 + M \\ \textbf{Net}: H_2O + CO + h\nu &\rightarrow CO_2 + H_2. \end{aligned} \tag{4.18}$$

The destruction is also the same regardless of the presence of sulfur, through the photo-dissociation of CO_2. What does change is the abundance of OH, which is consumed by reacting with S via

$$\begin{aligned} H_2S + h\nu &\rightarrow HS + H, \\ HS + H &\rightarrow H_2 + S, \\ S + OH &\rightarrow SO + H. \end{aligned} \tag{4.19}$$

The SO will diffuse upward, where it will photo-dissociate, releasing more atomic sulfur which will consume more hydroxyl radicals. It is this effect of the sulfur chemistry on the hydroxyl radicals that causes the lower abundance of CO_2 when sulfur is included. The destruction of OH via the photochemical properties of H_2S explains the shift of the peak of CO_2 to higher pressures when sulfur is present.

There is one other feature of note, the H_2O spike near 10^{-8} bar. This occurs because our constant K_{zz} places the CO homopause at $\sim 10^{-7}$ bar. As the CO drops off, it stops effectively self-shielding, and so CO is easily dissociated into C(^{1}D) and O(^{1}D). The O(^{1}D) reacts with H_2 to form H_2O. H_2O is preserved at this height, because its destruction forms OH which quickly reacts with H_2 to reform H_2O

$$H_2 + OH \rightarrow H_2O + H. \tag{4.20}$$

This reaction dominates instead of the reaction CO + OH $\rightarrow$ CO_2 + H (See Reaction 4.18) since the depletion of CO due to molecular diffusion means that it is no longer as efficient. This leads to H_2O peaking at $\sim 10^{-8}$ bar. It drops off above this height because of a combination of molecular diffusion of H_2O and photochemical destruction of OH.

4.6 Summary and Discussion

Our goal in this work was to construct a complete sulfur chemical network that would primarily function for the high temperatures of hot Jupiters, but that should be applicable over a large range of temperatures. By combining this network with our chemical kinetics code, LEVI, and the H/C/O/N network STAND2019 from Rimmer and Helling (2016) and Rimmer and Rugheimer (2019) we gained the ability to find the steady-state solutions for chemical abundance in the atmospheres of a variety of hot Jupiters. We validated our new network against similar previously published models to identify the similarities and differences. We investigated the primary pathways of sulfur chemistry over a range of hot Jupiter models, and examined how the abundance of sulfur species changed with variations to the model. We also compared how the inclusion of sulfur into a hot Jupiter's atmosphere can affect the abundance of other, non-sulfur species, potentially altering these species detectability.

We started by validating our network against previous models, including the work of Wang et al. (2017) and the work presented in Evans et al. (2018) (but made by Zahnle et al. 2016). We found our results matched nearly perfectly with Wang et al. (2017) (Figure 4.2), but their work only explored pressures higher than 10^{-4} bar, and so photochemistry was not considered. Similarly, we find that our results matched well with Evans et al. (2018) below 10^{-4} bar (Figure 4.3). However, in the upper atmosphere, we find the species' abundances follow the same general trends, but at significantly different pressures. This is inferred to be most likely due to different choices in the UV flux applied to the model.

Across a range of isothermal hot Jupiter atmospheres, we investigated the most abundant sulfur species and how this varies with the model's parameters. In our disequilibrium atmosphere model (Figure 4.5) we found that from the bottom of the atmosphere until between 10^{-2} and 10^{-3} bar, H_2S contains nearly all of the atmosphere's sulfur. Above this, H_2S is destroyed by photochemically produced H radicals that cause atomic S to become the primary sulfur carrier for the rest of the atmosphere. Other sulfur molecules of note are S_2 and HS. S_2 builds up significantly around 10^{-3} bar, particularly on slightly cooler hot Jupiters, where for a brief pressure window it is the most abundant sulfur species. The mercapto radical, HS, is one of the few sulfur molecules whose presence may have already been detected on an exoplanet (Evans et al. 2018). We find that it builds up strongly around 10^{-3} bar, especially along isotherms > 1200 K, with a maximum abundance of 4×10^{-3} seen in our model in Figure 4.5.

We also examined the sensitivity of sulfur chemistry to variations in both the strength of the vertical mixing (Figure 4.6) and the strength of the UV flux (Figure 4.7) applied to the atmosphere. We found that weakening the diffusion had little effect on the sulfur species. Stronger mixing increased the abundance of H_2S above 10^{-3} bar, while decreasing the abundance of S and S_2. The effect of stronger UV irradiation is primarily to dissociate

photosensitive molecules deeper into the atmosphere. Species such as H_2S were up to two orders of magnitude less abundant at 10^{-3} bar in more highly irradiated models.

Most sulfur species are not easily detected in exoplanet atmospheres, but that does not mean that sulfur chemistry does not matter for atmospheric retrievals. Our models have shown that the presence of sulfur in both hot and warm Jupiter atmospheres can significantly change the abundance of other, more easily detected, molecules. Of particular note are the differences we have found to the abundances of CH_4, HCN and NH_3 in hot Jupiters by including S in the network, as well as CO_2 in warm Jupiters. We found this was due to the catalytic properties of sulfur chemistry (also seen in Zahnle et al. 2016) for CH_4 and HCN, and due to the photo-shielding effect of H_2S for NH_3. At around a pressure of 10^{-3} bar in a atmospheric model of HD 209458b (Figure 4.8), the abundances of NH_3, CH_4 and HCN in a sulfurous atmosphere dropped by several orders of magnitude when compared to their abundances in a non-sulfurous atmosphere. This is a very large change, but it occurs over a very narrow pressure window. If this intersects with the detectable range made by observations, it would be a significant and noticeable effect. But, if the detection occurred at location higher or lower in the atmosphere, no change would be noticed compared to a sulfur free case. It is also very likely that the location at which sulfur chemistry impacts these molecules is dependant upon many of the planet's parameters: The planet's temperature and metallicity, as well as the diffusion strength or the incoming UV flux. More testing and modelling is required to discover exactly how these parameters will alter sulfur's effect upon these molecules.

The effect of sulfur upon CO_2 in warm Jupiters is also important, first noticed when comparing the sulfurous (Zahnle et al. 2016) and non-sulfurous (Moses et al. 2016) models of 51 Eri b. We find our network predicts up to five times less CO_2, due to sulfur, above 10^{-4} bar. Below this pressure, the loss of CO_2 is present, but less significant. In this section of the upper atmosphere, we predict approximately a factor of five more CO_2 compared to the model in Zahnle et al. (2016). These differences in the models are again down to uncertainties in the rate constants used for our sulfur reactions.

Current observations may struggle to distinguish the effects of sulfur we predict in both hot and warm Jupiters. However, it is important that observations from the next generation of telescopes take these effects into account, since they can significantly alter the composition of the atmosphere. An understanding of the precise effects of sulfur can be difficult to reach, due to how many uncertainties there are in the reaction rate constants within the network. As we have shown, these rates can greatly affect not just other sulfur species, but other detectable species within the atmosphere. New measurements of the rate constants of these sulfur reactions need to take place to truly be able to constrain the exact effect that sulfur can have. Some of the most important reactions discussed within this work still have large divergences between their

different measurements. We discuss where some of these reactions' rate constants come from in Appendix A.1.

Finally, it is important to consider that while it is difficult to identify the bulk sulfur abundance without the detection of sulfur species, the effect of sulfur upon other species can be used as a method to constrain the sulfur abundance. There of course would be a large degree of degeneracy in this parameter, but it could work as a first step to limiting the sulfur abundance of exo-planets to realistic values.

Chapter 5

Summary and Future Research

As the study of exosolar systems, and the planets within them, progresses, it is clear that we must use all the tools at our disposal to understand them. By investigating the bulk and atmospheric properties of exoplanets, we can learn not only about the planet being studied, but also gain insight into the history of these planetary systems. Of particular interest are the exoplanets known as hot Jupiters. Since hot Jupiters are not expected to have formed in-situ, they must have migrated through their proto-planetary system. This will have left traces upon the planet that, if detected, could help to fill in the picture of the systems history. Using the retrieved spectra of hot Jupiters, studies have already detected small molecules, including H_2O and CH_4, in these planets' atmospheres. However, to link these detections back to the planet's physical properties, and thus to its history, models of the planet's atmosphere are needed. The creation and use of a model of the chemistry and composition of hot Jupiters' atmospheres was the aim of this thesis.

In Chapter 2 we presented the details behind how the atmospheric model we created functions. This began with a set of coupled one-dimensional continuity equations for the time evolution of species in the atmosphere based upon their production and loss rates, and their vertical flux. We defined and described the components of each term in this equation, including;

- Thermochemical reactions that came from an external chemical network, and whose rates depends upon the pressure and temperature of the atmosphere
- Photochemical reactions whose rates depend upon an external UV flux
- Eddy diffusion and molecular diffusion

We explained in detail how we discretised this equation to make it computer solvable, using a semi-implicit second order Rosenbrock solver to obtain a converged steady-state solution for the atmospheric abundance profile for the atmosphere.

We showed our initial testing of the code, including checking that the initial conditions did not effect the converged solution, as well as how changing the boundary conditions would effect the solution. We also showed our codes validation against several other chemical codes, and found that we could reproduce their results within a small error margin.

We also performed some initial exploration of hot Jupiter atmospheres using our model. We compared how the introduction of disequilibrium effects such as diffusion and photochemistry into an atmospheric model of HD 209458b and HD 189733b changes the steady-state results of their atmospheres. We also modelled how changing the metallicity of the atmosphere changes the abundance of the molecules in the atmosphere. We identified that the C/H ratio is important for setting the abundance of any molecule that included carbon or oxygen, and that the abundance of many molecules changed rapidly across the C/O = 1 line, due to the sequestration of carbon in CO when C/O < 1 and oxygen in CO when C/O > 1. We found that the N/H ratio was only important for setting the abundance of molecules that contained nitrogen.

In Chapter 3 we investigated the links between how a hot Jupiter's formation and migration history may alter its atmospheric metallicity and thus the composition of its atmosphere. We presented the variation in the abundance of six different molecules in a hot Jupiter's atmosphere across a metallicity parameter space varying between $0.1\times$ and $10\times$ the solar O/H, C/H and N/H ratio. We linked our parameter models with formation and migration models produced by previous works. We compared the metallicities expected from these formation models and mapped them across our parameter models to produce molecular abundance ranges for each formation and migration model.

We then used the retrieved molecular abundances from an ensemble of hot Jupiters to test whether our models could predict where a hot Jupiter may have formed and from where it migrated. The detected water abundance across eight hot Jupiters all lay within the ranges our model predicted, however, all but two values fell within the ranges predicted by multiple formation models, limiting the potential to determine their histories. We also performed a more detailed case study of the hot Jupiter HD 209458b. When we compared the abundance of the six molecules detected within its atmosphere to our models predictions, we found that the best formation and migration model that fitted with our model was for it to have formed between the CO_2 and CO snowlines by gravitational instability and migrated disk-free.

In Chapter 4 we expanded the network our code uses to include molecules that contain the element sulfur. Sulfur is an element expected to be an important component in the atmospheres of hot Jupiters, particularly for the formation of hazes and clouds. We validated this new addition to the network by comparing it to previous works that contain the sulfur molecules. We investigated how changing the planetary temperature, diffusion strength and UV insolation

changed the composition of sulfur molecules in the hot Jupiter's atmosphere, and identified the chemical pathways that are responsible for these changes.

We compared the abundance profiles of the hot Jupiter HD 209458b and the warm Jupiter 51 Eri b both with and without sulfur, to identify the impact sulfur's inclusion has on atmospheric chemistry. In the atmosphere of HD 209458b we found that sulfur's inclusion decreased the abundance of CH_4, NH_3 and HCN by several orders of magnitude around 10^{-3} bar. We investigated in detail why this occurred, by examining the timescales of the reactions that led to these species' destruction, and how they changed when sulfur was included. In the atmosphere of 51 Eri b, we also found that the inclusion of sulfur decreased the abundance of CO_2 by several orders of magnitude in the upper atmosphere, a result that lines up with differences noticed between two previous studies upon this planet.

Overall, we have achieved our goal of constructing a chemical kinetics code able to model the atmospheres of hot Jupiters. We have validated the code thoroughly multiple times to ensure the accuracy of the model. We have shown how codes such as this can be used in conjunction with spectral data and formation models to analysis the history of the hot Jupiter. Also, we have used the code to show the impact of sulfur chemistry on the composition of the atmospheres of hot and warm Jupiters.

There are, however, still many limitations to our models, and many locations in which they could be improved. One of the most prominent is our use of either pre-calculated or analytical P-T profiles, neither of which represent the true form of the planets P-T profile. To more accurately achieve this, we would need to include an iterative radiative transfer calculation to create a self-consistent P-T profile for the chemical abundance profile we calculated. Another limitation is in our rate constants. As discussed in detail in Chapter 4, the rates in many of our most important reactions have large degrees of uncertainty in them. Additionally, for many reactions, both with and without sulfur, we have had to extrapolate their reaction rates far beyond the temperatures for which they were measured.

5.1 Future Research Possibilities

In this thesis we have shown the development and implementation of a code that can be used to model hot Jupiter atmospheres and output predictions of the abundance profiles of their atmospheres. It can already model equilibrium, kinetic and photochemistry for carbon, oxygen, nitrogen and sulfur chemistry. However, there are still many directions available to expand the uses of this code. The first such directly relates to the work already done. In Chapter 3 we consider variations to C/H, O/H and N/H ratios to identify how molecular abundance depends on the metallicity. However, in Chapter 4 we both introduce a new element, sulfur, into

the network, and show that it significantly impacts the abundance of several molecules at the pressures that we were considering in Chapter 3. Additionally, the work of Turrini et al. (2021) already considers how the S/H ratio in a hot Jupiter's atmosphere would vary based upon its formation location. Therefore, a natural research direction would be to create a metallicity parameter sweep model across the C/H, O/H, N/H and S/H ratios.

Another direction in which our work is already moving, is in the immediate application of our sulfur network to solar system science in the form of Venus studies. These studies have begun in Rimmer et al. (2021), and their continuation will be important in understanding the chemistry of similar exoplanets in the future.

The creation of synthetic spectra from our abundance profiles would allow a much more direct way of comparing our models to the observed spectra from exoplanets. One use of these synthetic spectra could be examining how sensitive a telescope would need to be to detect a certain change in the abundance of different chemical species.

Another logical direction would be to expand the complexity of the code. Clouds and hazes are already known to be important in hot Jupiter atmospheres (i.e., Zahnle et al. 2016), thus the inclusion of condensation in the code's functions could be valuable. Expanding the chemical network further used could also be valuable. The next most abundant element in hot Jupiter atmospheres is phosphorous. Phosphorus chemistry be valuable for detecting life on terrestrial planets (Glaser et al. 2020) and in the future, may be detectable in the atmospheres of hot Jupiters (Visscher et al. 2006). Also valuable could be the inclusion of metals or metal-containing molecules such as Na, TiO and VO. These are known to be important absorbers that can exist in hot Jupiter atmospheres (e.g., Fortney et al. 2006; Burrows et al. 2007, and will be necessary to include for the purposes of creating accurate synthetic spectra of hot Jupiters.

A potential route to pursue in the future would be head beyond 1-D models, into 2-D or 3-D chemical models. This would allow us to capture more of the complex dynamics that can take place in the atmosphere of a planet, such as better incorporation of day/night cycles, and the implication of longitudinal and latitudinal winds. Since hot Jupiters are generally tidally locked, a strong longitudinal wind is expected, that would likely result in a form of longitudinal quenching between the hot day-side and the cold night-side. This would be particularly important to understand when comparing our models to transmission spectra, that retrieve abundances from the terminator of the planet, since it is uncertain how the resupply and loss due to these dynamics would impact the chemical abundances at the planets terminator.

The last major direction would be modelling the atmospheres of planets smaller than hot Jupiters. Creating atmospheric models of terrestrial planets is an important step in preparation for the next generation of space telescopes, such as JWST. These telescopes should be able to obtain sufficiently detailed spectro-graphic data from smaller planets to retrieve the composition

of their atmospheres. Therefore it is important that chemical models exist to understand the composition of the atmospheres of terrestrial planets, and to discover whether these compositions are naturally occurring, or whether they might be the result of life's processes. Once again, sulfur chemistry is of particular interest since we currently have only a few tentitive detections of sulfur molecules in exoplanet atmospheres (Evans et al. 2018). Since telescopes such as JWST may be able to detect sulfur molecules in exoplanet atmosphere, it is vital that we have models available able to interpret what this chemistry would mean for the composition of the planet, and what it implies for the habitability of the planet as a whole.

References

Agúndez, M., Parmentier, V., Venot, O., Hersant, F., and Selsis, F. (2014). Pseudo 2D chemical model of hot-Jupiter atmospheres: application to HD 209458b and HD 189733b. A&A, 564:A73.

Akeson, R. L., Chen, X., Ciardi, D., Crane, M., Good, J., Harbut, M., Jackson, E., Kane, S. R., Laity, A. C., Leifer, S., Lynn, M., McElroy, D. L., Papin, M., Plavchan, P., Ramírez, S. V., Rey, R., von Braun, K., Wittman, M., Abajian, M., Ali, B., Beichman, C., Beekley, A., Berriman, G. B., Berukoff, S., Bryden, G., Chan, B., Groom, S., Lau, C., Payne, A. N., Regelson, M., Saucedo, M., Schmitz, M., Stauffer, J., Wyatt, P., and Zhang, A. (2013). The NASA Exoplanet Archive: Data and Tools for Exoplanet Research. PASP, 125(930):989.

Amano, A., Yamada, M., Hashimoto, K., and Sugiura, K. (1983). Kinetic Feature of the Reaction between Methanethiol and Hydrogen Atoms. *NIPPON KAGAKU KAISHI*, 1983(3):385–393.

Amundsen, D. S., Mayne, N. J., Baraffe, I., Manners, J., Tremblin, P., Drummond, B., Smith, C., Acreman, D. M., and Homeier, D. (2016). The UK Met Office global circulation model with a sophisticated radiation scheme applied to the hot Jupiter HD 209458b. A&A, 595:A36.

Anderson, K. R., Storch, N. I., and Lai, D. (2016). Formation and stellar spin-orbit misalignment of hot Jupiters from Lidov-Kozai oscillations in stellar binaries. MNRAS, 456(4):3671–3701.

Asplund, M., Grevesse, N., Sauval, A. J., and Scott, P. (2009). The Chemical Composition of the Sun. ARA&A, 47(1):481–522.

Atkinson, R., Baulch, D. L., Cox, R. A., Crowley, J. N., Hampson, R. F., Hynes, R. G., Jenkin, M. E., Rossi, M. J., and Troe, J. (2004). Evaluated kinetic and photochemical data for atmospheric chemistry: Volume I - gas phase reactions of O_x, HO_x, NO_x and SO_x species. *Atmospheric Chemistry and Physics*, 4(6):1461–1738.

Atkinson, R., Baulch, D. L., Cox, R. A., Hampson, R. F., Kerr, J. A., and Troe, J. (1992). Evaluated Kinetic and Photochemical Data for Atmospheric Chemistry: Supplement IV. IUPAC Subcommittee on Gas Kinetic Data Evaluation for Atmospheric Chemistry. *Journal of Physical and Chemical Reference Data*, 21(6):1125–1568.

Barstow, J. K., Aigrain, S., Irwin, P. G. J., and Sing, D. K. (2017). A Consistent Retrieval Analysis of 10 Hot Jupiters Observed in Transmission. ApJ, 834(1):50.

Bauer, S., Jeffers, P., Lifshitz, A., and Yadava, B. (1971). Reaction between CO and SO2 at elevated temperatures: A shock-tube investigation. *Symposium (International) on Combustion*, 13(1):417 – 425. Thirteenth symposium (International) on Combustion.

Beaugé, C. and Nesvorný, D. (2012). Multiple-planet Scattering and the Origin of Hot Jupiters. ApJ, 751:119.

Bitsch, B., Izidoro, A., Johansen, A., Raymond, S. N., Morbidelli, A., Lambrechts, M., and Jacobson, S. A. (2019). Formation of planetary systems by pebble accretion and migration: growth of gas giants. A&A, 623:A88.

Black, G., Jusinski, L., and Slanger, T. (1983). Rate coefficients for CS reactions with O2, O3 and NO2 AT 298 K. *Chemical Physics Letters*, 102(1):64 – 68.

Blecic, J., Harrington, J., and Bowman, M. O. (2016). TEA: A Code Calculating Thermochemical Equilibrium Abundances. ApJ, 225:4.

Blitz, M. A., Hughes, K. J., Pilling, M. J., and Robertson, S. H. (2006). Combined Experimental and Master Equation Investigation of the Multiwell Reaction H + SO2. *The Journal of Physical Chemistry A*, 110(9):2996–3009.

Boley, A. C. (2009). The Two Modes of Gas Giant Planet Formation. ApJ, 695(1):L53–L57.

Boley, A. C. and Durisen, R. H. (2010). On the Possibility of Enrichment and Differentiation in Gas Giants During Birth by Disk Instability. ApJ, 724(1):618–639.

Booth, R. A., Clarke, C. J., Madhusudhan, N., and Ilee, J. D. (2017). Chemical enrichment of giant planets and discs due to pebble drift. MNRAS, 469(4):3994–4011.

Bosman, A. D., Cridland, A. J., and Miguel, Y. (2019). Jupiter formed as a pebble pile around the N_2 ice line. A&A, 632:L11.

Boss, A. P. (1997). Giant planet formation by gravitational instability. *Science*, 276:1836–1839.

Boss, A. P. (2000). Possible Rapid Gas Giant Planet Formation in the Solar Nebula and Other Protoplanetary Disks. ApJ, 536(2):L101–L104.

Bradley, J. N., Trueman, S. P., Whytock, D. A., and Zaleski, T. A. (1973). Electron spin resonance study of the reaction of hydrogen atoms with hydrogen sulphide. *Journal of the Chemical Society, Faraday Transactions 1: Physical Chemistry in Condensed Phases*, 69:416–425.

Brewer, J. M., Fischer, D. A., and Madhusudhan, N. (2017). C/O and O/H Ratios Suggest Some Hot Jupiters Originate Beyond the Snow Line. AJ, 153:83.

Brogi, M. and Line, M. R. (2019). Retrieving temperatures and abundances of exoplanet atmospheres with high-resolution cross-correlation spectroscopy. AJ, 157(3):114.

Brown, T. M. (2001). Transmission Spectra as Diagnostics of Extrasolar Giant Planet Atmospheres. ApJ, 553:1006–1026.

Bulatov, V., Vereshchuk, S., Dzegilenko, F., Sarkisov, O., and Khabarov, V. (1990). Photooxidative conversion of H2S in the presence of O2 and NO2. *KHIMICHESKAYA FIZIKA*, 9(9):1214–1223.

Burcat, A. and Ruscic, B. (2005). Third Millennium Ideal Gas and Condensed Phase Thermochemical Database for Combustion with Updates from Active Thermochemical Tables.

Burrows, A., Hubeny, I., Budaj, J., Knutson, H. A., and Charbonneau, D. (2007). Theoretical Spectral Models of the Planet HD 209458b with a Thermal Inversion and Water Emission Bands. ApJ, 668(2):L171–L174.

Burrows, A. and Sharp, C. M. (1999). Chemical Equilibrium Abundances in Brown Dwarf and Extrasolar Giant Planet Atmospheres. ApJ, 512:843–863.

Cabot, S. H. C., Madhusudhan, N., Hawker, G. A., and Gandhi, S. (2019). On the robustness of analysis techniques for molecular detections using high-resolution exoplanet spectroscopy. MNRAS, 482(4):4422–4436.

Campbell, B., Walker, G. A. H., and Yang, S. (1988). A Search for Substellar Companions to Solar-type Stars. ApJ, 331:902.

Changeat, Q., Edwards, B., Al-Refaie, A. F., Morvan, M., Tsiaras, A., Waldmann, I. P., and Tinetti, G. (2020). KELT-11 b: Abundances of Water and Constraints on Carbon-bearing Molecules from the Hubble Transmission Spectrum. AJ, 160(6):260.

Chapman, S. and Cowling, T. G. (1970). *The mathematical theory of non-uniform gases. an account of the kinetic theory of viscosity, thermal conduction and diffusion in gases*. Cambridge University Press.

Charbonneau, D., Brown, T. M., Noyes, R. W., and Gilliland, R. L. (2002). Detection of an Extrasolar Planet Atmosphere. ApJ, 568:377–384.

Chase, M. (1998). *NIST-JANAF Thermochemical Table*. American Institute of Physics.

Chung, K., Calvert, J. G., and Bottenheim, J. W. (1975). The photochemistry of sulfur dioxide excited within its first allowed band and the forbidden band. *International Journal of Chemical Kinetics*, 7(2):161–182.

Cleeves, L. I., Öberg, K. I., Wilner, D. J., Huang, J., Loomis, R. A., Andrews, S. M., and Guzman, V. V. (2018). Constraining Gas-phase Carbon, Oxygen, and Nitrogen in the IM Lup Protoplanetary Disk. ApJ, 865:155.

Cooper, C. S. and Showman, A. P. (2006). Dynamics and Disequilibrium Carbon Chemistry in Hot Jupiter Atmospheres, with Application to HD 209458b. ApJ, 649:1048–1063.

Cooper, W. F. and Hershberger, J. F. (1992). An infrared laser study of the atomic oxygen (3P) + carbon disulfide reaction. *The Journal of Physical Chemistry*, 96(13):5405–5410.

Craven, W. and Murrell, J. N. (1987). Trajectory studies of S + O2 and O + S2 collisions. *J. Chem. Soc., Faraday Trans. 2*, 83:1733–1741.

Cridland, A. J., Pudritz, R. E., and Alessi, M. (2016). Composition of early planetary atmospheres - I. Connecting disc astrochemistry to the formation of planetary atmospheres. MNRAS, 461(3):3274–3295.

Cridland, A. J., van Dishoeck, E. F., Alessi, M., and Pudritz, R. E. (2020). Connecting planet formation and astrochemistry. C/Os and N/Os of warm giant planets and Jupiter analogues. A&A, 642:A229.

Cupitt, L. and Glass, G. (1970). Reaction of atomic oxygen with hydrogen sulphide. *Transactions of the Faraday Society*, 66:3007–3015.

Cupitt, L. and Glass, G. (1975). Reactions of sh with atomic oxygen and hydrogen. *Int. J. Chem. Kinet.;(United States)*, 7(Suppl 1).

Dawson, R. I. and Johnson, J. A. (2018). Origins of Hot Jupiters. ARA&A, 56:175–221.

Del Popolo, A., Ercan, N., and Yeşilyurt, I. S. (2005). Orbital migration and the period distribution of exoplanets. A&A, 436:363–372.

Deming, D., Brown, T. M., Charbonneau, D., Harrington, J., and Richardson, L. J. (2005). A New Search for Carbon Monoxide Absorption in the Transmission Spectrum of the Extrasolar Planet HD 209458b. ApJ, 622:1149–1159.

Demore, W., Sander, S., Golden, D., Hampson, R., Kurylo, M., Howard, C., Ravishankara, A., Kolb, C., and Molina, M. (1997). Chemical kinetics and photochemical data for use in stratospheric modeling. *JPL Publication*, 90.

Diamond-Lowe, H., Stevenson, K. B., Bean, J. L., Line, M. R., and Fortney, J. J. (2014). New Analysis Indicates No Thermal Inversion in the Atmosphere of HD 209458b. ApJ, 796(1):66.

Dorthe, G., Caubet, P., Vias, T., Barrere, B., and Marchais, J. (1991). Fast flow studies of atomic carbon kinetics at room temperature. *The Journal of Physical Chemistry*, 95(13):5109–5116.

Drummond, B., Mayne, N. J., Baraffe, I., Tremblin, P., Manners, J., Amundsen, D. S., Goyal, J., and Acreman, D. (2018). The effect of metallicity on the atmospheres of exoplanets with fully coupled 3D hydrodynamics, equilibrium chemistry, and radiative transfer. A&A, 612:A105.

Drummond, B., Tremblin, P., Baraffe, I., Amundsen, D. S., Mayne, N. J., Venot, O., and Goyal, J. (2016). The effects of consistent chemical kinetics calculations on the pressure-temperature profiles and emission spectra of hot Jupiters. A&A, 594:A69.

Du, S., Francisco, J. S., Shepler, B. C., and Peterson, K. A. (2008). Determination of the rate constant for sulfur recombination by quasiclassical trajectory calculations. *The Journal of chemical physics*, 128(20):204306.

Evans, T. M., Sing, D. K., Goyal, J. M., Nikolov, N., Marley, M. S., Zahnle, K., Henry, G. W., Barstow, J. K., Alam, M. K., Sanz-Forcada, J., Kataria, T., Lewis, N. K., Lavvas, P., Ballester, G. E., Ben-Jaffel, L., Blumenthal, S. D., Bourrier, V., Drummond, B., García Muñoz, A., López-Morales, M., Tremblin, P., Ehrenreich, D., Wakeford, H. R., Buchhave, L. A., Lecavelier des Etangs, A., Hébrard, É., and Williamson, M. H. (2018). An Optical Transmission Spectrum for the Ultra-hot Jupiter WASP-121b Measured with the Hubble Space Telescope. AJ, 156(6):283.

Forgan, D. and Rice, K. (2011). The Jeans mass as a fundamental measure of self-gravitating disc fragmentation and initial fragment mass. MNRAS, 417(3):1928–1937.

Fortney, J. J., Cooper, C. S., Showman, A. P., Marley, M. S., and Freedman, R. S. (2006). The Influence of Atmospheric Dynamics on the Infrared Spectra and Light Curves of Hot Jupiters. ApJ, 652(1):746–757.

Gammie, C. F. (2001). Nonlinear Outcome of Gravitational Instability in Cooling, Gaseous Disks. ApJ, 553(1):174–183.

Gandhi, S. and Madhusudhan, N. (2017). GENESIS: new self-consistent models of exoplanetary spectra. MNRAS, 472:2334–2355.

Gandhi, S., Madhusudhan, N., Hawker, G., and Piette, A. (2019). HyDRA-H: Simultaneous Hybrid Retrieval of Exoplanetary Emission Spectra. AJ, 158(6):228.

Gao, P., Marley, M. S., Zahnle, K., Robinson, T. D., and Lewis, N. K. (2017). Sulfur Hazes in Giant Exoplanet Atmospheres: Impacts on Reflected Light Spectra. AJ, 153(3):139.

García Muñoz, A. (2007). Physical and chemical aeronomy of HD 209458b. Planet. Space Sci., 55(10):1426–1455.

Garland, N. L. (1998). Temperature dependence of the reaction: SO+O2. *Chemical Physics Letters*, 290(4):385 – 390.

Giacobbe, P., Brogi, M., Gandhi, S., Cubillos, P. E., Bonomo, A. S., Sozzetti, A., Fossati, L., Guilluy, G., Carleo, I., Rainer, M., Harutyunyan, A., Borsa, F., Pino, L., Nascimbeni, V., Benatti, S., Biazzo, K., Bignamini, A., Chubb, K. L., Claudi, R., Cosentino, R., Covino, E., Damasso, M., Desidera, S., Fiorenzano, A. F. M., Ghedina, A., Lanza, A. F., Leto, G., Maggio, A., Malavolta, L., Maldonado, J., Micela, G., Molinari, E., Pagano, I., Pedani, M., Piotto, G., Poretti, E., Scandariato, G., Yurchenko, S. N., Fantinel, D., Galli, A., Lodi, M., Sanna, N., and Tozzi, A. (2021). Five carbon- and nitrogen-bearing species in a hot giant planet's atmosphere. Nature, 592(7853):205–208.

Gladstone, G. R., Allen, M., and Yung, Y. L. (1996). Hydrocarbon Photochemistry in the Upper Atmosphere of Jupiter. Icarus, 119:1–52.

Glaser, D. M., Hartnett, H. E., Desch, S. J., Unterborn, C. T., Anbar, A., Buessecker, S., Fisher, T., Glaser, S., Kane, S. R., Lisse, C. M., Millsaps, C., Neuer, S., O'Rourke, J. G., Santos, N., Walker, S. I., and Zolotov, M. (2020). Detectability of Life Using Oxygen on Pelagic Planets and Water Worlds. ApJ, 893(2):163.

Glassman, I., Yetter, R., and Glumac, N. (2015). *Combustion*. Academic Press.

Goumri, A., Rocha, J.-D. R., Laakso, D., Smith, C. E., and Marshall, P. (1999). Characterization of Reaction Pathways on the Potential Energy Surfaces for H + SO2 and HS + O2. *The Journal of Physical Chemistry A*, 103(51):11328–11335.

Goumri, A., Rocha, J.-D. R., and Marshall, P. (1995). Kinetics of the Recombination Reaction SH + O2 + Ar: Implications for the Formation and Loss of HSOO and SOO in the Atmosphere. *The Journal of Physical Chemistry*, 99(27):10834–10836.

Greene, T. P., Line, M. R., Montero, C., Fortney, J. J., Lustig-Yaeger, J., and Luther, K. (2016). Characterizing Transiting Exoplanet Atmospheres with JWST. ApJ, 817(1):17.

Grillmair, C. J., Burrows, A., Charbonneau, D., Armus, L., Stauffer, J., Meadows, V., van Cleve, J., von Braun, K., and Levine, D. (2008). Strong water absorption in the dayside emission spectrum of the planet HD189733b. Nature, 456:767–769.

Grosch, H., Fateev, A., and Clausen, S. (2015). UV absorption cross-sections of selected sulfur-containing compounds at temperatures up to 500 °C. J. Quant. Spec. Radiat. Transf., 154:28–34.

Guillot, T. (2010). On the radiative equilibrium of irradiated planetary atmospheres. A&A, 520:A27.

Guilluy, G., Sozzetti, A., Brogi, M., Bonomo, A. S., Giacobbe, P., Claudi, R., and Benatti, S. (2019). Exoplanet atmospheres with GIANO. II. Detection of molecular absorption in the dayside spectrum of HD 102195b. A&A, 625:A107.

Hands, T. O. and Alexander, R. D. (2016). There might be giants: unseen Jupiter-mass planets as sculptors of tightly packed planetary systems. MNRAS, 456:4121–4127.

Hawker, G. A., Madhusudhan, N., Cabot, S. H. C., and Gandhi, S. (2018). Evidence for Multiple Molecular Species in the Hot Jupiter HD 209458b. ApJ, 863(1):L11.

He, C., Horst, S., Lewis, N., Yu, X., Moses, J., McGuiggan, P., Marley, M., Kempton, E., Moran, S., Morley, C., and Vuitton, V. (2020). Sulfur Promotes Haze Formation in Warm CO_2-Rich Exoplanet Atmospheres. In *AAS/Division for Planetary Sciences Meeting Abstracts*, volume 52 of *AAS/Division for Planetary Sciences Meeting Abstracts*, page 403.04.

Heays, A. N., Bosman, A. D., and van Dishoeck, E. F. (2017). Photodissociation and photoionisation of atoms and molecules of astrophysical interest. A&A, 602:A105.

Helled, R. and Bodenheimer, P. (2010). Metallicity of the massive protoplanets around HR 8799 If formed by gravitational instability. Icarus, 207(2):503–508.

Helled, R., Bodenheimer, P., Podolak, M., Boley, A., Meru, F., Nayakshin, S., Fortney, J. J., Mayer, L., Alibert, Y., and Boss, A. P. (2014). Giant Planet Formation, Evolution, and Internal Structure. In Beuther, H., Klessen, R. S., Dullemond, C. P., and Henning, T., editors, *Protostars and Planets VI*, page 643.

Helling, C., Woitke, P., Rimmer, P. B., Kamp, I., Thi, W.-F., and Meijerink, R. (2014). Disk Evolution, Element Abundances and Cloud Properties of Young Gas Giant Planets. *Life*, 4(2):142–173.

Heng, K. and Tsai, S.-M. (2016). Analytical Models of Exoplanetary Atmospheres. III. Gaseous C-H-O-N Chemistry with Nine Molecules. ApJ, 829:104.

Herndon, S. C., Froyd, K. D., Lovejoy, E. R., and Ravishankara, A. R. (1999). How Rapidly Does the SH Radical React with N2O? *The Journal of Physical Chemistry A*, 103(34):6778–6785.

Hindiyarti, L., Glarborg, P., and Marshall, P. (2007). Reactions of SO3 with the O/H Radical Pool under Combustion Conditions. *The Journal of Physical Chemistry A*, 111(19):3984–3991.

Hodgskiss, M. S. W., Crockford, P. W., Peng, Y., Wing, B. A., and Horner, T. J. (2019). A productivity collapse to end Earth's Great Oxidation. *Proceedings of the National Academy of Science*, 116(35):17207–17212.

Hu, R., Seager, S., and Bains, W. (2012). Photochemistry in Terrestrial Exoplanet Atmospheres. I. Photochemistry Model and Benchmark Cases. ApJ, 761(2):166.

Hu, R., Seager, S., and Bains, W. (2013). Photochemistry in Terrestrial Exoplanet Atmospheres. II. H_2S and SO_2 Photochemistry in Anoxic Atmospheres. ApJ, 769(1):6.

Hubeny, I. and Mihalas, D. (2014). *Theory of Stellar Atmospheres*. Princeton University Press.

Hwang, S. M., Cooke, J. A., De Witt, K. J., and Rabinowitz, M. J. (2010). Determination of the rate coefficients of the SO2 + O + M -> SO3 + M reaction. *International Journal of Chemical Kinetics*, 42(3):168–180.

Irwin, P. G. J. (1999). Cloud Structure And Composition Of Jupiter's Atmosphere. *Surveys in Geophysics*, 20(6):505–535.

Isshiki, N., Murakami, Y., Tsuchiya, K., Tezaki, A., and Matsui, H. (2003). High-Temperature Reactions of O + COS and S + SO2. Abstraction versus Substitution Channels. *The Journal of Physical Chemistry A*, 107(14):2464–2469.

Jordan, S., Rimmer, P. B., Shorttle, O., and Constantinou, T. (2021). Photochemistry of Venus-Like Planets Orbiting K- and M-Dwarf Stars. *arXiv e-prints, arXiv:2108.05778*.

Jourdain, J., Bras, G. L., and Combourieu, J. (1979). Kinetic study of some elementary reactions of sulfur compounds including reactions of S and SO with OH radicals. *International Journal of Chemical Kinetics*, 11(6):569–577.

Kley, W. and Nelson, R. P. (2012). Planet-Disk Interaction and Orbital Evolution. ARA&A, 50:211–249.

Knutson, H., Agol, E., Burrows, A., Charbonneau, D., Cowan, N., Deming, D., Fortney, J., Langton, J., Laughlin, G., Lewis, N., and Showman, A. (2008). Dynamic Studies of Exoplanet Atmospheres: From Global Properties to Local Physics. Spitzer Proposal.

Kobayashi, H., Tanaka, H., and Krivov, A. V. (2011). Planetary Core Formation with Collisional Fragmentation and Atmosphere to Form Gas Giant Planets. ApJ, 738(1):35.

Komacek, T. D., Showman, A. P., and Parmentier, V. (2019). Vertical Tracer Mixing in Hot Jupiter Atmospheres. ApJ, 881(2):152.

Krasnopolsky, V. and Pollack, J. (1994). H2O-H2SO4 System in Venus' Clouds and OCS, CO, and H2SO4 Profiles in Venus' Troposphere. Icarus, 109(1):58–78.

Krasnopolsky, V. A. (2007). Chemical kinetic model for the lower atmosphere of venus. *Icarus*, 191(1):25 – 37.

Kurbanov, M. and Mamedov, K. (1995). The role of the reaction CO + SH -> COS + H in hydrogen formation in the course of interaction between CO and HS. *Kinetics and Catalysis - KINET CATAL-ENGL TR*, 36:455–457.

Kurten, T., Lane, J. R., Jorgensen, S., and Kjaergaard, H. G. (2010). Nitrate radical addition - elimination reactions of atmospherically relevant sulfur-containing molecules. *Phys. Chem. Chem. Phys.*, 12:12833–12839.

Langford, R. and Oldershaw, G. (1972). Flash photolysis of H2S. *Journal of the Chemical Society, Faraday Transactions 1: Physical Chemistry in Condensed Phases*, 68:1550–1558.

Latham, D. W., Mazeh, T., Stefanik, R. P., Mayor, M., and Burki, G. (1989). The unseen companion of HD114762: a probable brown dwarf. Nature, 339(6219):38–40.

Lee, L. C., Wang, X., and Suto, M. (1987). Quantitative photoabsorption and fluorescence spectroscopy of H_2S and D_2S at 49-240 nm. J. Chem. Phys., 86(8):4353–4361.

Lewis, N., Cowan, N., Knutson, H., de Wit, J., Seager, S., Demory, B.-O., Fortney, J., and Showman, A. (2013). Exoplanet Atmospheres in High Definition: 3D Eclipse Mapping of HD 209458b and HD 189733b. Spitzer Proposal.

Liang, M.-C., Parkinson, C. D., Lee, A. Y. T., Yung, Y. L., and Seager, S. (2003). Source of Atomic Hydrogen in the Atmosphere of HD 209458b. ApJ, 596(2):L247–L250.

Lilenfeld, H. V. and Richardson, R. J. (1977). Temperature dependence of the rate constant for the reaction between carbon monosulfide and atomic oxygen. *The Journal of Chemical Physics*, 67(9):3991–3997.

Lindemann, F. A., Arrhenius, S., Langmuir, I., Dhar, N. R., Perrin, J., and McC. Lewis, W. C. (1922). Discussion on "the radiation theory of chemical action". *Trans. Faraday Soc.*, 17:598–606.

Linsky, J. L., Yang, H., France, K., Froning, C. S., Green, J. C., Stocke, J. T., and Osterman, S. N. (2010). Observations of Mass Loss from the Transiting Exoplanet HD 209458b. ApJ, 717:1291–1299.

Liou, K. (2002). *An Introduction to Atmospheric Radiation*. Academic Press.

Lissauer, J. J. and Stevenson, D. J. (2007). Formation of Giant Planets. In Reipurth, B., Jewitt, D., and Keil, K., editors, *Protostars and Planets V*, page 591.

Liu, B. and Showman, A. P. (2013). Atmospheric Circulation of Hot Jupiters: Insensitivity to Initial Conditions. ApJ, 770:42.

Lodders, K. and Fegley, B. (2002). Atmospheric Chemistry in Giant Planets, Brown Dwarfs, and Low-Mass Dwarf Stars. I. Carbon, Nitrogen, and Oxygen. Icarus, 155(2):393–424.

Lu, C.-W., Wu, Y.-J., and Lee, Y.-P. (2003). Experiments and Calculations on Rate Coefficients for Pyrolysis of SO2 and the Reaction O + SO at High Temperatures. *Journal of Physical Chemistry A - J PHYS CHEM A*, 107.

Lu, C.-W., Wu, Y.-J., Lee, Y.-P., Zhu, R. S., and Lin, M. C. (2006). Experimental and theoretical investigation of rate coefficients of the reaction S(P3)+OCS in the temperature range of 298 - 985K. *The Journal of Chemical Physics*, 125(16):164329.

Macdonald, F. A. and Wordsworth, R. (2017). Initiation of Snowball Earth with volcanic sulfur aerosol emissions. Geophys. Res. Lett., 44(4):1938–1946.

MacDonald, R. J. and Madhusudhan, N. (2017a). HD 209458b in new light: evidence of nitrogen chemistry, patchy clouds and sub-solar water. MNRAS, 469:1979–1996.

MacDonald, R. J. and Madhusudhan, N. (2017b). Signatures of Nitrogen Chemistry in Hot Jupiter Atmospheres. ApJ, 850(1):L15.

Madhusudhan, N. (2012). C/O Ratio as a Dimension for Characterizing Exoplanetary Atmospheres. ApJ, 758(1):36.

Madhusudhan, N. (2019). Exoplanetary Atmospheres: Key Insights, Challenges, and Prospects. ARA&A, 57:617–663.

Madhusudhan, N., Agúndez, M., Moses, J. I., and Hu, Y. (2016). Exoplanetary Atmospheres—Chemistry, Formation Conditions, and Habitability. Space Sci. Rev., 205(1-4):285–348.

Madhusudhan, N., Amin, M. A., and Kennedy, G. M. (2014a). Toward Chemical Constraints on Hot Jupiter Migration. ApJ, 794(1):L12.

Madhusudhan, N., Amin, M. A., and Kennedy, G. M. (2014b). Toward Chemical Constraints on Hot Jupiter Migration. ApJ, 794:L12.

Madhusudhan, N., Burrows, A., and Currie, T. (2011). Model Atmospheres for Massive Gas Giants with Thick Clouds: Application to the HR 8799 Planets and Predictions for Future Detections. ApJ, 737:34.

Malin, G. (1997). Sulphur, climate and the microbial maze. *Nature*, 387(6636):857–858.

Martín-Doménech, R., Muñoz Caro, G. M., Bueno, J., and Goesmann, F. (2014). Thermal desorption of circumstellar and cometary ice analogs. A&A, 564:A8.

Mayne, N. J., Baraffe, I., Acreman, D. M., Smith, C., Browning, M. K., Skålid Amundsen, D., Wood, N., Thuburn, J., and Jackson, D. R. (2014). The unified model, a fully-compressible, non-hydrostatic, deep atmosphere global circulation model, applied to hot Jupiters. ENDGame for a HD 209458b test case. A&A, 561:A1.

Mayor, M. and Queloz, D. (1995). A Jupiter-mass companion to a solar-type star. Nature, 378(6555):355–359.

McGuire, B. A., Bergin, E., Blake, G. A., Burkhardt, A. M., Cleeves, L. I., Loomis, R. A., Remijan, A. J., Shingledecker, C. N., and Willis, E. R. (2018). Observing the Effects of Chemistry on Exoplanets and Planet Formation. In Murphy, E., editor, *Science with a Next Generation Very Large Array*, volume 517 of *Astronomical Society of the Pacific Conference Series*, page 217.

Miller-Ricci Kempton, E., Zahnle, K., and Fortney, J. J. (2012). The Atmospheric Chemistry of GJ 1214b: Photochemistry and Clouds. ApJ, 745:3.

Mills, F. (1998). I. Observations and Photochemical Modeling of the Venus Middle Atmosphere. II. Thermal Infrared Spectroscopy of Europa and Callisto.

Miyoshi, A., Shiina, H., Tsuchiya, K., and Matsui, H. (1996). Kinetics and mechanism of the reaction of S(3P) with O2. *Symposium (International) on Combustion*, 26(1):535 – 541.

Montoya, A., Sendt, K., and Haynes, B. S. (2005). Gas-Phase Interaction of H2S with O2: A Kinetic and Quantum Chemistry Study of the Potential Energy Surface. *The Journal of Physical Chemistry A*, 109(6):1057–1062.

Mordasini, C., van Boekel, R., Mollière, P., Henning, T., and Benneke, B. (2016). The Imprint of Exoplanet Formation History on Observable Present-day Spectra of Hot Jupiters. ApJ, 832:41.

Moses, J. I., Allen, M., and Gladstone, G. R. (1995). Post-SL9 sulfur photochemistry on Jupiter. Geophys. Res. Lett., 22(12):1597–1600.

Moses, J. I., Line, M. R., Visscher, C., Richardson, M. R., Nettelmann, N., Fortney, J. J., Barman, T. S., Stevenson, K. B., and Madhusudhan, N. (2013). Compositional Diversity in the Atmospheres of Hot Neptunes, with Application to GJ 436b. ApJ, 777(1):34.

Moses, J. I., Marley, M. S., Zahnle, K., Line, M. R., Fortney, J. J., Barman, T. S., Visscher, C., Lewis, N. K., and Wolff, M. J. (2016). On the Composition of Young, Directly Imaged Giant Planets. ApJ, 829(2):66.

Moses, J. I., Visscher, C., Fortney, J. J., Showman, A. P., Lewis, N. K., Griffith, C. A., Klippenstein, S. J., Shabram, M., Friedson, A. J., Marley, M. S., and Freedman, R. S. (2011). Disequilibrium Carbon, Oxygen, and Nitrogen Chemistry in the Atmospheres of HD 189733b and HD 209458b. ApJ, 737(1):15.

Moses, J. I., Zolotov, M. Y., and Fegley, B. (2002). Photochemistry of a Volcanically Driven Atmosphere on Io: Sulfur and Oxygen Species from a Pele-Type Eruption. Icarus, 156(1):76–106.

Mousavipour, S. H., Namdar-Ghanbari, M. A., and Sadeghian, L. (2003). A theoretical study on the kinetics of hydrogen abstraction reactions of methyl or hydroxyl radicals with hydrogen sulfide. *The Journal of Physical Chemistry A*, 107(19):3752–3758.

Murray-Clay, R. A., Chiang, E. I., and Murray, N. (2009). Atmospheric Escape From Hot Jupiters. ApJ, 693:23–42.

Nee, J. B. and Lee, L. C. (1986). Vacuum ultraviolet photoabsorption study of SO. J. Chem. Phys., 84(10):5303–5307.

Nelson, B. E., Ford, E. B., and Rasio, F. A. (2017). Evidence for Two Hot-Jupiter Formation Paths. AJ, 154:106.

Nicholas, J. E., Amodio, C. A., and Baker, M. J. (1979). Kinetics and mechanism of the decomposition of H2S, CH3SH and (CH3)2S in a radio-frequency pulse discharge. *Journal of the Chemical Society, Faraday Transactions 1: Physical Chemistry in Condensed Phases*, 75:1868–1875.

Nikolov, N., Sing, D. K., Fortney, J. J., Goyal, J. M., Drummond, B., Evans, T. M., Gibson, N. P., De Mooij, E. J. W., Rustamkulov, Z., Wakeford, H. R., Smalley, B., Burgasser, A. J., Hellier, C., Helling, C., Mayne, N. J., Madhusudhan, N., Kataria, T., Baines, J., Carter, A. L., Ballester, G. E., Barstow, J. K., McCleery, J., and Spake, J. J. (2018). An absolute sodium abundance for a cloud-free 'hot Saturn' exoplanet. Nature, 557(7706):526–529.

Norwood, K. and Ng, C. Y. (1989). Photoion-photoelectron coincidence spectroscopy of the transient molecules SO and S $_2$O. *Chemical Physics Letters*, 156(2-3):145–150.

Öberg, K. I., Murray-Clay, R., and Bergin, E. A. (2011). The Effects of Snowlines on C/O in Planetary Atmospheres. ApJ, 743(1):L16.

Öberg, K. I. and Wordsworth, R. (2019). Jupiter's Composition Suggests its Core Assembled Exterior to the N_2 Snowline. AJ, 158(5):194.

Papaloizou, J. C. B., Nelson, R. P., Kley, W., Masset, F. S., and Artymowicz, P. (2007). Disk-Planet Interactions During Planet Formation. In Reipurth, B., Jewitt, D., and Keil, K., editors, *Protostars and Planets V*, page 655.

Penzhorn, R.-D. and Canosa, C. E. (1983). Second Derivative UV Spectroscopy Study of the Thermal and Photochemical Reaction of NO2 with SO2 and SO3. *Berichte der Bunsengesellschaft für physikalische Chemie*, 87(8):648–654.

Phillips, L. F. (1981). Absolute absorption cross sections for SO between 190 and 235 nm. *Journal of Physical Chemistry*, 85:3994–4000.

Pinhas, A., Madhusudhan, N., Gandhi, S., and MacDonald, R. (2019). H_2O abundances and cloud properties in ten hot giant exoplanets. MNRAS, 482(2):1485–1498.

Pollack, J. B., Hubickyj, O., Bodenheimer, P., Lissauer, J. J., Podolak, M., and Greenzweig, Y. (1996). Formation of the Giant Planets by Concurrent Accretion of Solids and Gas. Icarus, 124(1):62–85.

Redfield, S., Endl, M., Cochran, W. D., and Koesterke, L. (2008). Sodium Absorption from the Exoplanetary Atmosphere of HD 189733b Detected in the Optical Transmission Spectrum. ApJ, 673(1):L87.

Richardson, R. (1975). Carbon monosulfide-oxygen flame reaction chemistry. *The Journal of Physical Chemistry*, 79(12):1153–1158.

Rimmer, P. B. and Helling, C. (2016). A Chemical Kinetics Network for Lightning and Life in Planetary Atmospheres. ApJS, 224(1):9.

Rimmer, P. B., Jordan, S., Constantinou, T., Woitke, P., Shorttle, O., Hobbs, R., and Paschodimas, A. (2021). Hydroxide Salts in the Clouds of Venus: Their Effect on the Sulfur Cycle and Cloud Droplet pH. PSJ, 2(4):133.

Rimmer, P. B. and Rugheimer, S. (2019). Hydrogen cyanide in nitrogen-rich atmospheres of rocky exoplanets. Icarus, 329:124–131.

Rosenbrock, H. H. (1963). Some general implicit processes for the numerical solution of differential equations. *The Computer Journal*, 5(4):329–330.

Sánchez, M. B., de Elía, G. C., and Darriba, L. A. (2018). Role of gaseous giants in the dynamical evolution of terrestrial planets and water delivery in the habitable zone. MNRAS, 481:1281–1289.

Sander, S., Golden, D., Kurylo, M., Moortgat, G., Wine, P., Ravishankara, A., Kolb, C., Molina, M., Finlayson-Pitts, B., Huie, R., and Orkin, V. (2006). Chemical kinetics and photochemical data for use in atmospheric studies evaluation number 15.

Schofield, K. (1973). Evaluated chemical kinetic rate constants for various gas phase reactions. *Journal of Physical and Chemical Reference Data*, 2(1):25–84.

Schwarz, H., Brogi, M., de Kok, R., Birkby, J., and Snellen, I. (2015). Evidence against a strong thermal inversion in HD 209458b from high-dispersion spectroscopy. A&A, 576:A111.

Seager, S. and Deming, D. (2010). Exoplanet Atmospheres. ARA&A, 48:631–672.

Seager, S. and Sasselov, D. D. (2000). Theoretical Transmission Spectra during Extrasolar Giant Planet Transits. ApJ, 537:916–921.

Sendt, K. and Haynes, B. S. (2005). Role of the Direct Reaction H2S + SO2 in the Homogeneous Claus Reaction. *The Journal of Physical Chemistry A*, 109(36):8180–8186.

Shiina, H., Oya, M., Yamashita, K., Miyoshi, A., and Matsui, H. (1996). Kinetic Studies on the Pyrolysis of H2S. *The Journal of Physical Chemistry*, 100(6):2136–2140.

Showman, A. P., Fortney, J. J., Lian, Y., Marley, M. S., Freedman, R. S., Knutson, H. A., and Charbonneau, D. (2009a). Atmospheric Circulation of Hot Jupiters: Coupled Radiative-Dynamical General Circulation Model Simulations of HD 189733b and HD 209458b. ApJ, 699:564–584.

Showman, A. P., Fortney, J. J., Lian, Y., Marley, M. S., Freedman, R. S., Knutson, H. A., and Charbonneau, D. (2009b). Atmospheric Circulation of Hot Jupiters: Coupled Radiative-Dynamical General Circulation Model Simulations of HD 189733b and HD 209458b. ApJ, 699(1):564–584.

Shum, L. G. S. and Benson, S. W. (1985). The pyrolysis of dimethyl sulfide, kinetics and mechanism. *International Journal of Chemical Kinetics*, 17(7):749–761.

Sing, D. K., Fortney, J. J., Nikolov, N., Wakeford, H. R., Kataria, T., Evans, T. M., Aigrain, S., Ballester, G. E., Burrows, A. S., Deming, D., Désert, J.-M., Gibson, N. P., Henry, G. W., Huitson, C. M., Knutson, H. A., Lecavelier Des Etangs, A., Pont, F., Showman, A. P., Vidal-Madjar, A., Williamson, M. H., and Wilson, P. A. (2016). A continuum from clear to cloudy hot-Jupiter exoplanets without primordial water depletion. Nature, 529(7584):59–62.

Singleton, D. L. and Cvetanovic, R. J. (1988). Evaluated Chemical Kinetic Data for the Reactions of Atomic Oxygen O(3P) with Sulfur Containing Compounds. *Journal of Physical and Chemical Reference Data*, 17(4):1377–1437.

Sneep, M. and Ubachs, W. (2005). Direct measurement of the Rayleigh scattering cross section in various gases. J. Quant. Spec. Radiat. Transf., 92:293–310.

Spalding, C. and Batygin, K. (2017). A Secular Resonant Origin for the Loneliness of Hot Jupiters. AJ, 154(3):93.

Steinrueck, M. E., Parmentier, V., Showman, A. P., Lothringer, J. D., and Lupu, R. E. (2019). The Effect of 3D Transport-induced Disequilibrium Carbon Chemistry on the Atmospheric Structure, Phase Curves, and Emission Spectra of Hot Jupiter HD 189733b. ApJ, 880(1):14.

Stevenson, K. B., Bean, J. L., Madhusudhan, N., and Harrington, J. (2014). Deciphering the Atmospheric Composition of WASP-12b: A Comprehensive Analysis of its Dayside Emission. ApJ, 791:36.

Stock, J. W., Kitzmann, D., Patzer, A. B. C., and Sedlmayr, E. (2018). FastChem: A computer program for efficient complex chemical equilibrium calculations in the neutral/ionized gas phase with applications to stellar and planetary atmospheres. MNRAS, 479(1):865–874.

Swain, M. R., Tinetti, G., Vasisht, G., Deroo, P., Griffith, C., Bouwman, J., Chen, P., Yung, Y., Burrows, A., Brown, L. R., Matthews, J., Rowe, J. F., Kuschnig, R., and Angerhausen, D. (2009). Water, Methane, and Carbon Dioxide Present in the Dayside Spectrum of the Exoplanet HD 209458b. ApJ, 704:1616–1621.

Teyssandier, J., Lai, D., and Vick, M. (2019). Formation of hot Jupiters through secular chaos and dynamical tides. MNRAS, 486(2):2265–2280.

Thompson, S. D., Carroll, D. G., Watson, F., O'Donnell, M., and McGlynn, S. P. (1966). Electronic Spectra and Structure of Sulfur Compounds. J. Chem. Phys., 45(5):1367–1379.

Tiee, J. J., Wampler, F. B., Oldenborg, R. C., and Rice, W. W. (1981). Spectroscopy and reaction kinetics of HS radicals. *Chemical Physics Letters*, 82(1):80–84.

Titov, D. V., Ignatiev, N. I., McGouldrick, K., Wilquet, V., and Wilson, C. F. (2018). Clouds and Hazes of Venus. Space Sci. Rev., 214(8):126.

Tsai, S.-M., Lyons, J. R., Grosheintz, L., Rimmer, P. B., Kitzmann, D., and Heng, K. (2017). VULCAN: An Open-source, Validated Chemical Kinetics Python Code for Exoplanetary Atmospheres. ApJS, 228(2):20.

Tsai, S.-M., Malik, M., Kitzmann, D., Lyons, J. R., Fateev, A., Lee, E., and Heng, K. (2021). A Comparative Study of Atmospheric Chemistry with VULCAN. *arXiv e-prints*, page arXiv:2108.01790.

Tsuchiya, K., Kamiya, K., and Matsui, H. (1997). Studies on the oxidation mechanism of H2S based on direct examination of the key reactions. *International Journal of Chemical Kinetics*, 29(1):57–66.

Tsuchiya, K., Yamashita, K., Miyoshi, A., and Matsui, H. (1996). Studies on the Reactions of Atomic Sulfur (3P) with H2, D2, CH4, C2H6, C3H8, n-C4H10, and i-C4H10. *The Journal of Physical Chemistry*, 100(43):17202–17206.

Tsuchiya, K., Yokoyama, K., Matsui, H., Oya, M., and Dupre, G. (1994). Reaction mechanism of atomic oxygen with hydrogen sulfide at high temperature. *The Journal of Physical Chemistry*, 98(34):8419–8423.

Turrini, D., Schisano, E., Fonte, S., Molinari, S., Politi, R., Fedele, D., Panić, O., Kama, M., Changeat, Q., and Tinetti, G. (2021). Tracing the Formation History of Giant Planets in Protoplanetary Disks with Carbon, Oxygen, Nitrogen, and Sulfur. ApJ, 909(1):40.

Vandeputte, A. G., Reyniers, M.-F., and Marin, G. B. (2010). Theoretical study of the thermal decomposition of dimethyl disulfide. *The Journal of Physical Chemistry A*, 114(39):10531–10549.

Venot, O., Bénilan, Y., Fray, N., Gazeau, M.-C., Lefèvre, F., Es-sebbar, E., Hébrard, E., Schwell, M., Bahrini, C., Montmessin, F., Lefèvre, M., and Waldmann, I. P. (2018). VUV-absorption cross section of carbon dioxide from 150 to 800 K and applications to warm exoplanetary atmospheres. A&A, 609:A34.

Venot, O., Fray, N., Bénilan, Y., Gazeau, M.-C., Hébrard, E., Larcher, G., Schwell, M., Dobrijevic, M., and Selsis, F. (2013). High-temperature measurements of VUV-absorption cross sections of CO_2 and their application to exoplanets. A&A, 551:A131.

Venot, O., Hébrard, E., Agúndez, M., Dobrijevic, M., Selsis, F., Hersant, F., Iro, N., and Bounaceur, R. (2012). A chemical model for the atmosphere of hot Jupiters. A&A, 546:A43.

Verwer, J., Spee, E., Blom, J., and Hundsdorfer, W. (1999). A Second-Order Rosenbrock Method Applied to Photochemical Dispersion Problems. *SIAM Journal on Scientific Computing*, 20(4):1456–1480.

Visscher, C., Lodders, K., and Fegley, Bruce, J. (2006). Atmospheric Chemistry in Giant Planets, Brown Dwarfs, and Low-Mass Dwarf Stars. II. Sulfur and Phosphorus. ApJ, 648(2):1181–1195.

Visscher, C. and Moses, J. I. (2011). Quenching of Carbon Monoxide and Methane in the Atmospheres of Cool Brown Dwarfs and Hot Jupiters. ApJ, 738(1):72.

Wakelam, V., Herbst, E., Loison, J. C., Smith, I. W. M., Chandrasekaran, V., Pavone, B., Adams, N. G., Bacchus-Montabonel, M. C., Bergeat, A., Béroff, K., Bierbaum, V. M., Chabot, M., Dalgarno, A., van Dishoeck, E. F., Faure, A., Geppert, W. D., Gerlich, D., Galli, D., Hébrard, E., Hersant, F., Hickson, K. M., Honvault, P., Klippenstein, S. J., Le Picard, S., Nyman, G., Pernot, P., Schlemmer, S., Selsis, F., Sims, I. R., Talbi, D., Tennyson, J., Troe, J., Wester, R., and Wiesenfeld, L. (2012). A KInetic Database for Astrochemistry (KIDA). ApJS, 199(1):21.

Wakelam, V., Loison, J. C., Herbst, E., Pavone, B., Bergeat, A., Béroff, K., Chabot, M., Faure, A., Galli, D., Geppert, W. D., Gerlich, D., Gratier, P., Harada, N., Hickson, K. M., Honvault, P., Klippenstein, S. J., Le Picard, S. D., Nyman, G., Ruaud, M., Schlemmer, S., Sims, I. R., Talbi, D., Tennyson, J., and Wester, R. (2015). The 2014 KIDA Network for Interstellar Chemistry. ApJS, 217(2):20.

Wang, B. and Hou, H. (2005). Theoretical investigations on the SO2+HO2 reaction and the SO2-HO2 radical complex. *Chemical Physics Letters*, 410(4):235 – 241.

Wang, D., Miguel, Y., and Lunine, J. (2017). Modeling Synthetic Spectra for Transiting Extrasolar Giant Planets: Detectability of H_2S and PH_3 with the James Webb Space Telescope. ApJ, 850(2):199.

Wang, N.-S. and Howard, C. (1990). Kinetics of the reactions of HS and HSO with O3. *Journal of Physical Chemistry*, 94(25):8787–8794.

Watanabe, K. and Jursa, A. S. (1964). Absorption and Photoionization Cross Sections of H_2O and H_2S. J. Chem. Phys., 41(6):1650–1653.

Wei, C.-N. and Timmons, R. B. (1975). ESR study of the kinetics of the reactions of O(3P) atoms with CS2 and OCS. *The Journal of Chemical Physics*, 62(8):3240–3245.

Welbanks, L., Madhusudhan, N., Allard, N. F., Hubeny, I., Spiegelman, F., and Leininger, T. (2019). Mass-Metallicity Trends in Transiting Exoplanets from Atmospheric Abundances of H_2O, Na, and K. ApJ, 887(1):L20.

Wight, C. A. and Leone, S. R. (1983). Vibrational state distributions and absolute excitation efficiencies for T-V transfer collisions of NO and CO with H atoms produced by excimer laser photolysis. J. Chem. Phys., 79(10):4823–4829.

Woiki, D. and Roth, P. (1995). A shock tube study of the reaction S + H2 -> SH + H in pyrolysis and photolysis systems. *International Journal of Chemical Kinetics*, 27(6):547–553.

Wolszczan, A. and Frail, D. A. (1992). A planetary system around the millisecond pulsar PSR1257 + 12. Nature, 355(6356):145–147.

Wu, C. Y. R. and Chen, F. Z. (1998). Temperature-dependent photoabsorption cross sections of H_2S in the 1600-2600 Å region. J. Quant. Spec. Radiat. Transf., 60(1):17–23.

Wu, Y. and Lithwick, Y. (2011). Secular Chaos and the Production of Hot Jupiters. ApJ, 735(2):109.

Wu, Y. and Murray, N. (2003). Planet Migration and Binary Companions: The Case of HD 80606b. ApJ, 589(1):605–614.

Wyttenbach, A., Ehrenreich, D., Lovis, C., Udry, S., and Pepe, F. (2015). Spectrally resolved detection of sodium in the atmosphere of HD 189733b with the HARPS spectrograph. A&A, 577:A62.

Yoshimura, M., Koshi, M., Matsui, H., Kamiya, K., and Umeyama, H. (1992). Non-Arrhenius temperature dependence of the rate constant for the H + H2S reaction. *Chemical Physics Letters*, 189(3):199 – 204.

Youngblood, A., France, K., Loyd, R. O. P., Linsky, J. L., Redfield, S., Schneider, P. C., Wood, B. E., Brown, A., Froning, C., Miguel, Y., Rugheimer, S., and Walkowicz, L. (2016). The MUSCLES Treasury Survey. II. Intrinsic LYα and Extreme Ultraviolet Spectra of K and M Dwarfs with Exoplanets*. ApJ, 824:101.

Zahnle, K., Haberle, R. M., Catling, D. C., and Kasting, J. F. (2008). Photochemical instability of the ancient Martian atmosphere. *Journal of Geophysical Research (Planets)*, 113(E11):E11004.

Zahnle, K., Mac Low, M.-M., Lodders, K., and Fegley, Jr., B. (1995). Sulfur chemistry in the wake of comet Shoemaker-Levy 9. Geophys. Res. Lett., 22:1593–1596.

Zahnle, K., Marley, M. S., Freedman, R. S., Lodders, K., and Fortney, J. J. (2009). Atmospheric Sulfur Photochemistry on Hot Jupiters. ApJ, 701(1):L20–L24.

Zahnle, K., Marley, M. S., Morley, C. V., and Moses, J. I. (2016). Photolytic Hazes in the Atmosphere of 51 Eri b. ApJ, 824(2):137.

Zhang, X., Liang, M. C., Mills, F. P., Belyaev, D. A., and Yung, Y. L. (2012). Sulfur chemistry in the middle atmosphere of Venus. Icarus, 217(2):714–739.

Zhang, X. and Showman, A. P. (2017). Effects of Bulk Composition on the Atmospheric Dynamics on Close-in Exoplanets. ApJ, 836(1):73.

Zhang, X. and Showman, A. P. (2018). Global-mean Vertical Tracer Mixing in Planetary Atmospheres. II. Tidally Locked Planets. ApJ, 866(1):2.

A.1 A Discussion of Rates

Here we discuss some of the most significant sulfur chemical reaction rates in our network, their uncertainties, and where these uncertainties come from.

Photochemistry of H_2S

The photo-dissociation of H_2S is one of two photochemical sulfur reactions that form the explanation for sulfur's significant impact on other species in warm and hot Jupiters. There are a large number of works that have measured its UV cross-section, though not all of them agree upon the wavelength behaviour of the cross-section. The work of Lee et al. (1987) provides an effective "backbone" to the wavelength-dependent absorption cross-sections for H_2S, and provides the lowest measured estimates for H_2S absorption of all observations, diverging from other measurements at $\lambda < 172$ nm. Both Watanabe and Jursa (1964) and Wu and Chen (1998) find cross-sections below 172 nm that are a factor of 2-3 greater. Thompson et al. (1966) measures the absorption cross-section between 180 nm and 214 nm, in good agreement with other measurements at these wavelengths, though with a slight divergence between 210 – 214 nm. Wu and Chen (1998) generally agrees with most other measurements wherever one of the measurements diverges, and matches a measurement at a single (250 nm) wavelength very well (Wight and Leone, 1983). The measurements of Wu and Chen (1998) are clean and the results suggest few systematics and a very deep noise floor. For this reason the JPL database recommends using their H_2S cross-sections. More recently, Grosch et al. (2015) has made measurements at a higher resolution. These measurements diverge from Wu and Chen (1998) by a factor of 5 between 250 and 260 nm, suggesting the higher resolution has come at the cost of a higher noise floor.

Photo-chemistry of SO

The photo-dissociation of SO is the second of the important photochemical sulfur reactions. The most accurate cross-sections for SO were compiled by the Leiden database (Heays et al. 2017), based on Phillips (1981), Nee and Lee (1986) and Norwood and Ng (1989). The cross-sections all agree with each other reasonably well.

$H + SH \rightarrow H_2 + S$ vs $H_2 + S \rightarrow H + SH$

We found that the reaction $H + SH \rightarrow H_2 + S$ was significant in the pathway that lead to CO_2 destruction in 51 Eri b's atmosphere. However, in our network we choose to use this reaction's reverse, $H_2 + S \rightarrow H + SH$, even though it has an activation barrier. Our justification for this is that for $H + SH \rightarrow H_2 + S$ all the results are at room temperature, and all of them were measured in the 1970's and 1980's.

Cupitt and Glass (1970) performed a flow discharge with H_2S and O_2, and estimated the rate of $H + SH \rightarrow H_2 + S$ to be $k = 1.3 \times 10^{-10}\,\mathrm{cm^3\,s^{-1}}$. The experiment was subsequently

revisited, and the rate constant corrected to $k = 2.51 \times 10^{-11}\,\mathrm{cm^3\,s^{-1}}$ in (Cupitt and Glass, 1975).

Bradley et al. (1973) also performed a flow discharge with H_2S, controlling the overall reaction with NO, attempting to isolate the individual reactions, and constrained the HS hydrogen abstraction reaction to $k = 4.15 \times 10^{-11}\,\mathrm{cm^3\,s^{-1}}$. Their results do not indicate any kinetic barrier or polynomial temperature dependence.

Tiee et al. (1981) used a 193 nm UV laser to dissociate H_2S, forming HS, and then subsequently measured the decay of HS. They found a maximum rate of $k < 1.69 \times 10^{-11}\,\mathrm{cm^3\,s^{-1}}$.

Nicholas et al. (1979) used radio-frequency pulse discharge and found the measurement of HS decay to be $k = 2.16 \times 10^{-11}\,\mathrm{cm^3\,s^{-1}}$.

Langford and Oldershaw (1972) used flash photolysis and made the measurement of the HS decay to be $k = 1.1 \times 10^{-11}\,\mathrm{cm^3\,s^{-1}}$.

The reported rates are highly discordant, nor do they address the temperature dependence. In contrast, the reverse reaction, $H_2 + S \rightarrow H + SH$, was constrained much better by two experiments in the late 1990's. They were performed over a much larger temperature range, between 1000 K and 2000K, which is much more applicable to hot Jupiters.

Woiki and Roth (1995) used OCS/H_2 pyrolysis and CS_2/H_2 photolysis to generate S atoms that could then react with H_2. They found the reaction rate to be $k = 9.96 \times 10^{-10}\exp(-12070\mathrm{K/T})\,\mathrm{cm^3\,s^{-1}}$ for a temperature range of 1257 K to 3137 K.

Shiina et al. (1996) studied the thermal decomposition of H_2S and its subsequent reactions, and found the reaction between H_2 and S to be $k = 2.62 \times 10^{-10}\exp(-9920\mathrm{K/T})\,\mathrm{cm^3\,s^{-1}}$ over a temperature range of 1050 K to 1660 K.

As a result we decided that using the reaction $H_2 + S \rightarrow H + SH$ in our network was the choice offering the greatest accuracy in modelling hot Jupiters.

OH + S → H + SO

This reaction is the last reaction important to explaining the impact of sulfur in hot and warm Jupiters. It has been mentioned in several reviews, all based on a single experimental measurement by Jourdain et al. (1979). They used a flow discharge with SO_2 and H_2O, and found $k = 6.95 \times 10^{-11}\,\mathrm{cm^3\,s^{-1}}$. Without a second measurement, it is difficult to determine this reaction's uncertainties, and without uncertainties, there is no way to perform a sensitivity analysis accurately.

A.2 The Sulfur Network

No.	Reaction	$\alpha\,(m^6s^{-1}\,\text{or}\,m^3s^{-1})$	β	γ(K)	Reference
1	$S + S \rightarrow S_2$	3.95×10^{-45}			Du et al. (2008)
	$S + S \rightarrow S_2$	9.09×10^{-20}			Du et al. (2008)
2	$S + S_2 \rightarrow S_3$	1.11×10^{-42}	-2.00		Moses et al. (2002)
	$S + S_2 \rightarrow S_3$	3×10^{-17}			Moses et al. (2002)
3	$S + S_3 \rightarrow S_4$	1.11×10^{-42}	-2.00		Moses et al. (2002)
	$S + S_3 \rightarrow S_4$	3×10^{-17}			Moses et al. (2002)
4	$S + S_4 \rightarrow S_5$	1.11×10^{-42}	-2.00		Moses et al. (2002)
	$S + S_4 \rightarrow S_5$	3×10^{-17}			Moses et al. (2002)
5	$S + S_5 \rightarrow S_6$	1.11×10^{-42}	-2.00		Moses et al. (2002)
	$S + S_5 \rightarrow S_6$	3×10^{-17}			Moses et al. (2002)
6	$S + S_6 \rightarrow S_7$	1.11×10^{-42}	-2.00		Moses et al. (2002)
	$S + S_6 \rightarrow S_7$	3×10^{-17}			Moses et al. (2002)
7	$S + S_7 \rightarrow S_8$	1.11×10^{-42}	-2.00		Moses et al. (2002)
	$S + S_7 \rightarrow S_8$	3×10^{-17}			Moses et al. (2002)
8	$S_2 + S_2 \rightarrow S_4$	2.2×10^{-41}			Nicholas et al. (1979)
	$S_2 + S_2 \rightarrow S_4$	1×10^{-16}			Nicholas et al. (1979)
9	$S_2 + S_3 \rightarrow S_5$	1.11×10^{-42}	-2.00		Moses et al. (2002)
	$S_2 + S_3 \rightarrow S_5$	3×10^{-17}			Moses et al. (2002)
10	$S_2 + S_4 \rightarrow S_6$	1.11×10^{-42}	-2.00		Moses et al. (2002)
	$S_2 + S_4 \rightarrow S_6$	3×10^{-17}			Moses et al. (2002)
11	$S_2 + S_5 \rightarrow S_7$	1.11×10^{-42}	-2.00		Moses et al. (2002)
	$S_2 + S_5 \rightarrow S_7$	3×10^{-17}			Moses et al. (2002)
12	$S_2 + S_6 \rightarrow S_8$	1.11×10^{-42}	-2.00		Moses et al. (2002)
	$S_2 + S_6 \rightarrow S_8$	3×10^{-17}			Moses et al. (2002)
13	$S_3 + S_3 \rightarrow S_6$	1×10^{-42}			Mills (1998)
	$S_3 + S_3 \rightarrow S_6$	3×10^{-17}			Mills (1998)
14	$S_3 + S_4 \rightarrow S_7$	1.11×10^{-42}	-2.00		Moses et al. (2002)
	$S_3 + S_4 \rightarrow S_7$	3×10^{-17}			Moses et al. (2002)
15	$S_3 + S_5 \rightarrow S_8$	1.11×10^{-42}	-2.00		Moses et al. (2002)
	$S_3 + S_5 \rightarrow S_8$	3×10^{-17}			Moses et al. (2002)
16	$S_4 + S_4 \rightarrow S_8$	1×10^{-42}			Mills (1998)
	$S_4 + S_4 \rightarrow S_8$	3×10^{-17}			Mills (1998)

Table A.1 The 3-body reactions of the sulphur network used in this work. α, β and γ(K) refer to the three constants used in the arrhenius equation, such that the rate of reaction is $k = \alpha(T/300\,\text{K})^{\beta}\exp(-\gamma/T)\,\text{m}^3\text{s}^{-1}$. The reactions in this table are three body combination reactions that use a third body (M) as a catalyst. The first line of each reaction is the low pressure rate limit (k_0) and the second line is the high pressure rate limit (k_∞) that are combined to give an overall rate via $k = \frac{k_0[M]}{1+\frac{k_0[M]}{K_\infty}}$. Thus α_0 has units m^6s^{-1} and α_∞ has units m^3s^{-1}.

No.	Reaction					$\alpha\,(m^6s^{-1}\,\text{or}\,m^3s^{-1})$	β	γ(K)	Reference
17	S	+	O	→	SO	3.01×10^{-45}			Zhang et al. (2012)
	S	+	O	→	SO	7.27×10^{-20}	-1.00		Zhang et al. (2012)
18	S	+	SO	→	S_2O	3.67×10^{-43}	-2.00		Moses et al. (2002)
	S	+	SO	→	S_2O	8.86×10^{-19}	-3.00		Moses et al. (2002)
19	S	+	H_2	→	H_2S	1.4×10^{-43}	-1.9	2.3×10^{3}	Zahnle et al. (2016)
	S	+	H_2	→	H_2S	1×10^{-17}			Zahnle et al. (2016)
20	SO	+	HO	→	HOSO	6.45×10^{-41}	-3.48	4.90×10^{2}	Goumri et al. (1999)
	SO	+	HO	→	HOSO	8.75×10^{-17}	0.50		Goumri et al. (1999)
21	SO_2	+	O	→	SO_3	1.32×10^{-41}		1.00×10^{3}	Atkinson et al. (2004)
	SO_2	+	O	→	SO_3	5×10^{-18}			Atkinson et al. (2004)
22	SO_2	+	H	→	HSO_2	5.74×10^{-43}	-3.69	2.41×10^{3}	Goumri et al. (1999)
	SO_2	+	H	→	HSO_2	2.31×10^{-17}	0.62	1.82×10^{3}	Goumri et al. (1999)
23	SO_2	+	H	→	HOSO	9.43×10^{-40}	-4.36	5.44×10^{3}	Goumri et al. (1999)
	SO_2	+	H	→	HOSO	9.13×10^{-18}	0.96	4.32×10^{3}	Goumri et al. (1999)
24	SO	+	O	→	SO_2	4.82×10^{-43}	-2.17		Lu et al. (2003)
	SO	+	O	→	SO_2	3.5×10^{-17}	0.00		Lu et al. (2003)
25	SO_2	+	HO	→	HSO_3	3.3×10^{-43}	-4.30		Sander et al. (2006)
	SO_2	+	HO	→	HSO_3	1.6×10^{-18}	0.00		Sander et al. (2006)
26	HS	+	NO	→	HSNO	2.4×10^{-43}	-3.00		Demore et al. (1997)
	HS	+	NO	→	HSNO	2.71×10^{-17}			Demore et al. (1997)
27	HS	+	O_2	→	HSO_2	9.18×10^{-46}	-1.69		Goumri et al. (1995)
	HS	+	O_2	→	HSO_2	2.01×10^{-16}	0.31		Goumri et al. (1995)
28	HS	+	O_2	→	HSOO	9.06×10^{-46}	-2.01	1.00×10^{1}	Goumri et al. (1999)
	HS	+	O_2	→	HSOO	3.3×10^{-16}	-0.26	1.50×10^{2}	Goumri et al. (1999)
29	HS	+	H	→	H_2S	1×10^{-42}	-2.00		Krasnopolsky (2007)
	HS	+	H	→	H_2S	2.41×10^{-17}	-3.00		Krasnopolsky (2007)
30	CS_2	+	HO	→	CS_2OH	8×10^{-43}			Atkinson et al. (1992)
	CS_2	+	HO	→	CS_2OH	8×10^{-18}			Atkinson et al. (1992)
31	CO	+	S	→	OCS	3×10^{-45}		1.00×10^{3}	Krasnopolsky (2007)
	CO	+	S	→	OCS	7.24×10^{-20}	-1.00	1.00×10^{3}	Krasnopolsky (2007)
32	CH_3	+	HS	→	CH_3SH	6.88×10^{-43}	1.00		Shum and Benson (1985)
	CH_3	+	HS	→	CH_3SH	1.66×10^{-17}			Shum and Benson (1985)

Table A.2 The 3-body reactions of the sulfur network used in this work. α, β and γ(K) refer to the three constants used in the arrhenius equation, such that the rate of reaction is $k = \alpha(T/300\,\text{K})^{\beta}\exp(-\gamma/T)\,\text{m}^3\text{s}^{-1}$. The reactions in this table are three body combination reactions that use a third body (M) as a catalyst. The first line of each reaction is the low pressure rate limit (k_0) and the second line is the high pressure rate limit (k_∞) that are combined to give an overall rate via $k = \frac{k_0[M]}{1+\frac{k_0[M]}{K_\infty}}$. Thus α_0 has units m^6s^{-1} and α_∞ has units m^3s^{-1}.

No.	Reaction					$\alpha\,(m^3s^{-1}\,\text{or}\,s^{-1})$	β	γ(K)	Reference
33	HSO	→	H	+	SO	1.4×10^{-14}		2.95×10^{4}	Tsuchiya et al. (1994)
	HSO	→	H	+	SO	$3.38\times10^{+11}$	-1.00	2.95×10^{4}	Tsuchiya et al. (1994)
34	HOSO	→	HSO_2			3.18×10^{-09}	-5.64	2.79×10^{4}	Goumri et al. (1999)
	HOSO	→	HSO_2			$3.64\times10^{+11}$	1.03	2.52×10^{4}	Goumri et al. (1999)
35	HSOO	→	O	+	HSO	4.61×10^{-10}	-5.87	1.56×10^{4}	Goumri et al. (1999)
	HSOO	→	O	+	HSO	$4.53\times10^{+16}$	-1.07	1.43×10^{4}	Goumri et al. (1999)
36	H_2S_2	→	HS	+	HS	3.43×10^{-13}	1.00	2.87×10^{4}	Tsuchiya et al. (1994)
	H_2S_2	→	HS	+	HS	$8.28\times10^{+12}$		2.87×10^{4}	Tsuchiya et al. (1994)

Table A.3 The 3-body reactions of the sulfur network used in this work. α, β and γ(K) refer to the three constants used in the arrhenius equation, such that the rate of reaction is $k = \alpha(T/300\,\text{K})^{\beta}\exp(-\gamma/T)\,\text{m}^3\text{s}^{-1}$. The reactions in this table are three body decomposition reactions that use a third body (M) as a catalyst and a state shift reaction. The first line of each reaction is the low pressure rate limit (k_0) and the second line is the high pressure rate limit (k_∞) that are combined to give an overall rate via $k = \frac{k_0[M]}{1+\frac{k_0[M]}{K_\infty}}$. Thus α_0 has units m^3s^{-1} and α_∞ has units s^{-1}.

No.	Reaction				
1	S_3	→	S_2	+	S
2	S_4	→	S_2	+	S_2
3	SO_3	→	SO_2	+	O
4	OCS	→	S	+	CO
5	OCS	→	S	+	CO
6	OCS	→	S	+	CO
7	OCS	→	CS	+	O
8	OCS	→	CS	+	$O(^1D)$
9	S_2	→	S	+	S
10	S_2O	→	SO	+	S
11	S_2O	→	S_2	+	O
12	SO	→	S	+	O
13	CS_2	→	CS	+	S
14	SO_2	→	SO	+	O
15	SO_2	→	S	+	O_2
16	H_2S	→	HS	+	H
17	CH_3SH	→	CH_3	+	HS

Table A.4 The photo-chemical reactions of the sulfur network used in this work. The cross-sections for H_2S, SO, SO_2, OCS, CS_2 and CH_3SH were taken from PhIDrates (https://phidrates.space.swri.edu/), the cross-sections for S_3, S_4 and S_2 from the MPI-Mainz-UV-VIS Spectral Atlas of Gaseous Molecules (www.uv-vis-spectral-atlas-mainz.org) and the cross-section for S_2 from the Leiden database (Heays et al. 2017).

No.	Reaction	$\alpha\,(m^3s^{-1})$	β	γ(K)	Reference
1	$S + S_3 \rightarrow S_2 + S_2$	8×10^{-17}			Moses et al. (2002)
2	$S + S_4 \rightarrow S_2 + S_3$	8×10^{-17}			Moses et al. (2002)
3	$S + S_5 \rightarrow S_2 + S_4$	5×10^{-17}		2.00×10^{2}	Moses et al. (2002)
4	$S + S_6 \rightarrow S_2 + S_5$	5×10^{-17}		3.00×10^{2}	Moses et al. (2002)
5	$S + S_7 \rightarrow S_2 + S_6$	4×10^{-17}		2.00×10^{2}	Moses et al. (2002)
6	$S + S_8 \rightarrow S_2 + S_7$	4×10^{-17}		4.00×10^{2}	Moses et al. (2002)
7	$S + S_5 \rightarrow S_3 + S_3$	3×10^{-17}		2.00×10^{2}	Moses et al. (2002)
8	$S + S_6 \rightarrow S_3 + S_4$	3×10^{-17}		3.00×10^{2}	Moses et al. (2002)
9	$S + S_7 \rightarrow S_3 + S_5$	2×10^{-17}		2.00×10^{2}	Moses et al. (2002)
10	$S + S_8 \rightarrow S_3 + S_6$	2×10^{-17}		4.00×10^{2}	Moses et al. (2002)
11	$S + S_7 \rightarrow S_4 + S_4$	2×10^{-17}		2.00×10^{2}	Moses et al. (2002)
12	$S + S_8 \rightarrow S_4 + S_5$	2×10^{-17}		4.00×10^{2}	Moses et al. (2002)
13	$S_2 + S_8 \rightarrow S_5 + S_5$	1×10^{-17}		1.40×10^{3}	Moses et al. (2002)
14	$S_3 + S_5 \rightarrow S_2 + S_6$	4×10^{-17}		2.00×10^{2}	Moses et al. (2002)
15	$S_3 + S_7 \rightarrow S_2 + S_8$	3×10^{-17}		2.00×10^{2}	Moses et al. (2002)
16	$S_3 + S_7 \rightarrow S_4 + S_6$	1×10^{-17}		2.00×10^{2}	Moses et al. (2002)
17	$S_3 + S_4 \rightarrow S_2 + S_5$	4×10^{-17}		2.00×10^{2}	Moses et al. (2002)
18	$S_3 + S_6 \rightarrow S_2 + S_7$	4×10^{-18}		3.00×10^{2}	Moses et al. (2002)
19	$S_3 + S_7 \rightarrow S_5 + S_5$	1×10^{-17}		2.00×10^{2}	Moses et al. (2002)
20	$S_4 + S_5 \rightarrow S_2 + S_7$	2×10^{-18}		2.00×10^{2}	Moses et al. (2002)
21	$S_4 + S_6 \rightarrow S_2 + S_8$	2×10^{-18}		3.00×10^{2}	Moses et al. (2002)
22	$S_4 + S_5 \rightarrow S_3 + S_6$	2×10^{-18}		2.00×10^{2}	Moses et al. (2002)
23	$S_4 + S_7 \rightarrow S_3 + S_8$	5×10^{-18}		2.00×10^{2}	Moses et al. (2002)
24	$S_4 + S_6 \rightarrow S_5 + S_5$	2×10^{-18}		3.00×10^{2}	Moses et al. (2002)
25	$S_4 + S_7 \rightarrow S_5 + S_6$	5×10^{-18}		2.00×10^{2}	Moses et al. (2002)
26	$O + S_2 \rightarrow S + SO$	2×10^{-17}		8.40×10^{1}	Craven and Murrell (1987)
27	$O + S_3 \rightarrow S_2 + SO$	8×10^{-17}			Moses et al. (2002)
28	$O + S_4 \rightarrow S_3 + SO$	8×10^{-17}			Moses et al. (2002)
29	$O + S_5 \rightarrow S_4 + SO$	8×10^{-17}		2.00×10^{2}	Moses et al. (2002)
30	$O + S_6 \rightarrow S_5 + SO$	8×10^{-17}		3.00×10^{2}	Moses et al. (2002)
31	$O + S_7 \rightarrow S_6 + SO$	8×10^{-17}		2.00×10^{2}	Moses et al. (2002)
32	$O + S_8 \rightarrow S_7 + SO$	8×10^{-17}		4.00×10^{2}	Moses et al. (2002)
33	$S + O_2 \rightarrow SO + O$	2.51×10^{-17}		1.84×10^{3}	Miyoshi et al. (1996)
34	$S + SO_2 \rightarrow SO + SO$	9.77×10^{-18}		4.54×10^{3}	Isshiki et al. (2003)
35	$S + H_2 \rightarrow H + HS$	3.04×10^{-19}	2.70	6.46×10^{3}	Shiina et al. (1996) and Woiki and Roth (1995)

Table A.5 The 2-body reactions of the sulfur network used in this work. $\alpha\,(\mathrm{m^3s^{-1}})$, β and γ(K) refer to the three constants used in the arrhenius equation, such that the rate of reaction is $k = \alpha(T/300\,\mathrm{K})^{\beta}\exp(-\gamma/T)\,\mathrm{m^3s^{-1}}$. For the reactions with multiple sources, we have blended data from both sources to extend the applicable temperature range for the reaction.

No.	Reaction							$\alpha\,(m^3s^{-1})$	β	γ(K)	Reference
36	S	+	OCS	→	CO	+	S_2	1.35×10^{-19}	2.70	1.20×10^{3}	Shiina et al. (1996) and Lu et al. (2006)
37	S	+	CS_2	→	CS	+	S_2	2.82×10^{-16}		5.92×10^{3}	Woiki and Roth (1995)
38	S	+	C_2H_6	→	HS	+	C_2H_5	2.04×10^{-16}		7.42×10^{3}	Tsuchiya et al. (1996)
39	S	+	CH_4	→	HS	+	CH_3	3.39×10^{-16}		1.00×10^{4}	Tsuchiya et al. (1996)
40	S	+	HS	→	S_2	+	H	4.98×10^{-18}			Nicholas et al. (1979)
41	S	+	HO_2	→	SO	+	HO	5.84×10^{-17}			Zhang et al. (2012)
42	S	+	SO_3	→	SO_2	+	SO	1×10^{-22}			Moses et al. (2002)
43	S	+	HO	→	SO	+	H	6.6×10^{-17}			Demore et al. (1997)
44	S	+	S_2O	→	S_2	+	SO	1×10^{-18}		1.20×10^{3}	Moses et al. (2002)
45	S	+	O_3	→	SO	+	O_2	1.2×10^{-17}			Atkinson et al. (2004)
46	S_3	+	CO	→	OCS	+	S_2	1×10^{-17}		2.00×10^{4}	Krasnopolsky (2007)
47	S_3	+	H	→	HS	+	S_2	1.2×10^{-16}		1.95×10^{3}	Krasnopolsky (2007)
48	HS	+	HS	→	H_2S	+	S	1.5×10^{-17}			Schofield (1973)
49	HS	+	HO	→	H_2O	+	S	2.5×10^{-18}			Krasnopolsky (2007)
50	HS	+	O	→	H	+	SO	1.3×10^{-16}			Tsuchiya et al. (1994)
51	HS	+	NO_2	→	NO	+	HSO	6.49×10^{-17}			Atkinson et al. (2004)
52	HS	+	N_2O	→	N_2	+	HSO	5×10^{-22}			Herndon et al. (1999)
53	HS	+	O_3	→	O_2	+	HSO	1.1×10^{-17}		2.80×10^{2}	Wang and Howard (1990)
54	HS	+	O_2	→	O	+	HSO	3.11×10^{-17}		9.02×10^{3}	Tsuchiya et al. (1997)
55	HS	+	O_2	→	HO	+	SO	4×10^{-25}			Demore et al. (1997)
56	HS	+	CO	→	OCS	+	H	4.15×10^{-20}		7.66×10^{3}	Kurbanov and Mamedov (1995)
57	HS	+	H_2CS	→	H_2S	+	HCS	8.14×10^{-17}		3.18×10^{3}	Vandeputte et al. (2010)
58	H_2S	+	O	→	H	+	HSO	5×10^{-16}		3.85×10^{3}	Tsuchiya et al. (1994)
59	H_2S	+	O	→	HO	+	HS	2.01×10^{-16}		3.85×10^{3}	Tsuchiya et al. (1994)
60	H_2S	+	H	→	H_2	+	HS	3.07×10^{-18}	2.10	3.52×10^{2}	Yoshimura et al. (1992)
61	H_2S	+	O_2	→	HO_2	+	HS	3.1×10^{-18}	2.76	1.92×10^{4}	Montoya et al. (2005)
62	H_2S	+	HO	→	H_2O	+	HS	1.61×10^{-17}		5.40×10^{2}	Mousavipour et al. (2003)
63	H_2S	+	HO_2	→	H_2O	+	HSO	5×10^{-18}			Bulatov et al. (1990)
64	H_2S	+	CH_3	→	CH_4	+	HS	1.05×10^{-19}	1.20	7.22×10^{2}	Mousavipour et al. (2003)
65	H_2S	+	SO_2	→	H_2O	+	S_2O	1.09×10^{-19}	1.86	1.90×10^{4}	Sendt and Haynes (2005)
66	H_2S	+	S_2O	→	H_2O	+	S_3	7.08×10^{-19}	1.51	1.71×10^{4}	Sendt and Haynes (2005)
67	SO	+	HO_2	→	SO_2	+	HO	2.8×10^{-17}			Zhang et al. (2012)
68	SO	+	S_3	→	S_2O	+	S_2	1×10^{-18}			Moses et al. (2002)
69	SO	+	O_3	→	SO_2	+	O_2	4.5×10^{-18}		1.17×10^{3}	Atkinson et al. (2004)
70	SO	+	O_3	→	SO_2	+	$O_2(a^1\Delta g)$	3.6×10^{-19}		1.10×10^{3}	Sander et al. (2006)

Table A.6 The 2-body reactions of the sulfur network used in this work. $\alpha\,(\mathrm{m^3s^{-1}})$, β and γ(K) refer to the three constants used in the arrhenius equation, such that the rate of reaction is $k = \alpha(T/300\,\mathrm{K})^{\beta}\exp(-\gamma/T)\,\mathrm{m^3s^{-1}}$.

No.	Reaction									$\alpha\,(m^3s^{-1})$	β	γ(K)	Reference
71	SO	+	O_2	→	SO_2	+	O			4.37×10^{-20}	1.40	1.87×10^{3}	Garland (1998)
72	SO	+	CO_2	→	SO_2	+	CO			1.5×10^{-17}		2.20×10^{4}	Bauer et al. (1971)
73	SO	+	NO_2	→	SO_2	+	NO			1.4×10^{-17}			Atkinson et al. (2004)
74	SO	+	SO_3	→	SO_2	+	SO_2			2×10^{-21}			Chung et al. (1975)
75	SO_2	+	H	→	HO	+	SO			4.58×10^{-14}	-2.30	1.56×10^{4}	Blitz et al. (2006)
76	SO_2	+	NO_3	→	SO_3	+	NO_2			1.8×10^{-28}			Kurten et al. (2010)
77	SO_2	+	O_3	→	SO_3	+	O_2			3.01×10^{-18}		7.00×10^{3}	Demore et al. (1997)
78	SO_2	+	HO_2	→	HO	+	SO_3			2.26×10^{-19}		3.42×10^{3}	Hwang et al. (2010)
79	SO_2	+	HO_2	→	O_2	+	HOSO			8.6×10^{-16}		5.23×10^{3}	Wang and Hou (2005)
80	SO_2	+	O_3	→	SO_3	+	$O_2(a^1\Delta g)$			6×10^{-20}		7.00×10^{3}	Zhang et al. (2012)
81	SO_2	+	$O(^1D)$	→	SO	+	O_2			1.3×10^{-16}			Moses et al. (2002)
82	SO_2	+	NO_2	→	SO_3	+	NO			2×10^{-32}			Penzhorn and Canosa (1983)
83	SO_3	+	O	→	SO_2	+	O_2			1.06×10^{-19}	2.57	1.47×10^{4}	Hindiyarti et al. (2007)
84	SO_3	+	H	→	HO	+	SO_2			1.46×10^{-17}	1.22	1.67×10^{3}	Hindiyarti et al. (2007)
85	SO_3	+	S_2	→	S_2O	+	SO_2			2×10^{-22}			Moses et al. (2002)
86	SO_3	+	CO	→	CO_2	+	SO_2			1×10^{-17}		1.30×10^{4}	Krasnopolsky and Pollack (1994)
87	S_2O	+	O	→	SO	+	SO			1.7×10^{-18}			Mills (1998)
88	S_2O	+	S_2O	→	S_3	+	SO_2			1×10^{-20}			Mills (1998)
89	OCS	+	O	→	CO	+	SO			1.99×10^{-17}		2.15×10^{3}	Wei and Timmons (1975)
90	OCS	+	O	→	CO_2	+	S			8.3×10^{-17}		5.53×10^{3}	Singleton and Cvetanovic (1988)
91	OCS	+	C	→	CO	+	CS			1.01×10^{-16}			Dorthe et al. (1991)
92	OCS	+	NO_3	→	CO	+	SO	+	NO_2	1×10^{-22}			Atkinson et al. (2004)
93	OCS	+	HO	→	CO_2	+	HS			1.1×10^{-19}		1.20×10^{3}	Sander et al. (2006)
94	CS	+	O	→	CO	+	S			2.61×10^{-16}		7.58×10^{2}	Lilenfeld and Richardson (1977)
95	CS	+	HO	→	H	+	OCS			1.7×10^{-16}			Wakelam et al. (2015)
96	CS	+	HO	→	CO	+	HS			3×10^{-17}			Wakelam et al. (2015)
97	CS	+	C	→	S	+	C_2			1.44×10^{-17}	0.5	2.04×10^{4}	Wakelam et al. (2015)
98	CS	+	C_2H_3	→	H_2C_3S	+	H			1.7×10^{-18}		4.00×10^{2}	Wakelam et al. (2015)
99	CS	+	CH	→	S	+	C_2H			5×10^{-17}			Wakelam et al. (2015)
100	CS	+	HN	→	S	+	HNC			1×10^{-17}		1.20×10^{3}	Wakelam et al. (2015)
101	CS	+	NO_2	→	OCS	+	NO			7.61×10^{-23}			Black et al. (1983)
102	CS	+	O_3	→	OCS	+	O_2			3.01×10^{-22}			Black et al. (1983)
103	CS	+	O_2	→	OCS	+	O			2.62×10^{-22}		1.86×10^{3}	Richardson (1975)
104	CS_2	+	O	→	CS	+	SO			2.76×10^{-17}		6.44×10^{2}	Wei and Timmons (1975)
105	CS_2	+	O	→	CO	+	S_2			1.08×10^{-19}			Cooper and Hershberger (1992)
106	CS_2	+	O	→	OCS	+	S			3.65×10^{-18}		5.83×10^{3}	Singleton and Cvetanovic (1988)
107	CS_2	+	HO	→	OCS	+	HS			1.7×10^{-21}			Atkinson et al. (2004)
108	HSO_3	+	O_2	→	HO_2	+	SO_3			1.3×10^{-18}		3.30×10^{2}	Atkinson et al. (1992)
109	HSO	+	NO_2	→	NO	+	HSO_2			9.6×10^{-18}			Demore et al. (1997)
110	HSO	+	O_3	→	O_2	+	O_2	+	HS	2.54×10^{-19}		3.84×10^{2}	Wang and Howard (1990)
111	HSO_2	+	O_2	→	HO_2	+	SO_2			3.01×10^{-19}			Demore et al. (1997)
112	HSOO	+	O_2	→	HO_2	+	SO_2			3.01×10^{-19}			Demore et al. (1997)
113	H_2CS	+	H	→	H_2	+	HCS			9.33×10^{-17}		3.57×10^{3}	Vandeputte et al. (2010)
114	H_2CS	+	CH_3	→	CH_4	+	HCS			2.57×10^{-17}		4.93×10^{3}	Vandeputte et al. (2010)
115	CH_3SH	+	H	→	CH_3	+	H_2S			1.15×10^{-17}		8.41×10^{2}	Amano et al. (1983)

Table A.7 The 2-body reactions of the sulfur network used in this work. $\alpha\,(\mathrm{m^3s^{-1}})$, β and γ(K) refer to the three constants used in the arrhenius equation, such that the rate of reaction is $k = \alpha(T/300\,\mathrm{K})^{\beta}\exp(-\gamma/T)\,\mathrm{m^3s^{-1}}$.